UNIVERSITY COLLEGE LONDON

The role of the North Pacific Ocean in the deglacial CO_2 rise: insights from trace elements and boron isotopes in biogenic carbonates

William Gray

A thesis submitted for the
degree of Doctor of Philosophy

in the
Department of Geography
UCL

February 2015

Declaration of Authorship

I, William Gray, declare that this thesis titled, 'The role of the North Pacific Ocean in the deglacial CO_2 rise: insights from trace elements and boron isotopes in biogenic carbonates' and the work presented in it are my own. Where information has been derived from other sources, I confirm that this has been indicated in the thesis.

"The task of explaining the glacial to interglacial change in atmospheric CO_2 content suggested from studies of the air trapped in polar ice is a complex one which will occupy our attention for some time to come."

Wally Broecker, 1987
(The year I was born)

UNIVERSITY COLLEGE LONDON

Abstract

The ∼90 ppmv increase in atmospheric CO_2 over the last deglaciation was most likely driven by changes in the way the high latitude oceans regulate the exchange of dissolved inorganic carbon (DIC) between the surface and interior ocean, however the mechanisms involved in this repartitioning remain unclear. The subarctic Pacific Ocean is currently a significant source of CO_2 to the atmosphere due to mixing of DIC-rich intermediate waters into the surface ocean and incomplete nutrient utilisation. It is hypothesised that during the last glacial period increased stratification of the subarctic Pacific reduced CO_2 outgassing and increased DIC storage within the interior ocean, and over deglaciation this deeply sequestered DIC reservoir was returned back to the surface ocean and atmosphere.

This thesis provides the first quantitative reconstruction of changes in DIC storage within the interior North Pacific, and CO_2 outgassing from the subarctic Pacific over the last deglaciation. After demonstrating paired Li/Ca and Mg/Ca ratios in benthic foraminifera *Uvigerina* spp. can be used to reconstruct past changes in bottom water DIC with a core top calibration, Mg/Ca and Li/Ca ratios were measured in *Uvigerina senticosa* from marine sediment core MD01-2416, located at 2317m water depth in the subarctic Pacific. The results indicate a ∼200 μmol/kg increase in DIC within the interior North Pacific during glacial times. At ∼16 ka a rapid reduction in DIC, coeval with warmer bottom waters and an increase in benthic $\Delta^{14}C$, denotes the transfer of DIC out of the deep-intermediate subarctic Pacific Ocean. A reconstruction of surface ocean pCO_2 using boron isotopes measured on planktonic foraminifera *Neogloboquadrina pachyderma* (s) in the same core shows a ∼90 ppmv decrease during glacial times, and a major release of CO_2 to the atmosphere during deglaciation. These results suggest a significant role for the North Pacific Ocean in the deglacial atmospheric pCO_2 rise.

Acknowledgements

First and foremost I would like to thank my supervisor Jonathan Holmes. Without his continued support and advice this thesis would not have been possible. Jonathan, thank you for always 'having a minute'.

I would also like to thank my secondary supervisors Amelia Shevenell and Mark Maslin. Amelia, for sparking my initial interest in the North Pacific, and Mark for his advice over the past four years.

Many people, at UCL and beyond, have helped me greatly throughout the course of my thesis, and I am hugely grateful to them all. Immense thanks go to,

Mariette Wolthers and David Thornalley, for the interest and enthusiasm they have shown in my work, the knowledge they have imparted, and all the opportunites they have given me.

Katy Wilson, for her critical eye, and always having time to chat about the North Pacific.

Gary Tarbuck, John McArthur and Tony Osborn, for all their assistance with ICP-related matters.

Everybody who has made the microscope room a fun place to work over the past four years!

Janet Hope, Tula Maxsted and Ian Patmore, for their help in the labs.

Emma Wiik and Jorge Salgado Bonnet, for useful R scripts.

James Rae, as generating the boron isotope data (that makes up a significant part of this thesis) would not have been possible without his knowledge, enthusiasm, expertise, and 2 am peanut butter sandwiches. Thanks also for the use of unpublished model data, and many interesting discussions about the North Pacific.

Gavin Foster and the B Team, for being so accommodating in their labs (and homes).

Lennart de Nooijer, Gert-Jan Reichart, Karoliina Koho, Wim Boer, and Caroline Slomp for providing access to fantastic samples and unpublished pore water data, and assistance with LA-ICP-MS.

Mervyn Greaves, Anabel Morte Rodenas and Caroline Lear, for their cooperation in setting up trace element methods at UCL. Special thanks to Anabel and Carrie for enabling me to complete my analyses after disaster struck...

Maggi Simon, for putting up with me sleeping on the sofa for two weeks.

Aurora Elmore, for access to core top samples, the use of unpublished core top data, and plenty of ostracod related chats.

Michael Sarnthein and Lloyd Keigwin, for providing access to precious core material.

Sean Bryan and Tom Marchitto, for the use of their unpublished *Uvigerina peregrina* Sr/Ca dataset.

Finally thanks to all the friends at UCL, in London, and from further afield that have made the past four years so much fun, and to my family for their support.

This PhD was funded by NERC studentship NE/I528185/1. Additional funding came from a UCL Graduate School Grant and a UCL Fellowship. Further funding for data generated as part of this thesis came from grants awarded to Mariette Wolthers, James Rae, and Amelia Shevenell, for which I am very grateful.

Contents

List of Figures

List of Tables

Chapter 1

Glacial-Interglacial CO_2 and the North Pacific Ocean

Over the last deglaciation atmospheric CO_2 increased by 90 ppmv. The radiative forcing from this increase helped to bring the last glacial period a close, ushering in the interglacial epoch in which we currently find ourselves. The cause of the deglacial atmospheric CO_2 rise remains elusive, although the leading hypotheses center around changes in the efficency of the biological pump within the high latitude oceans. The deepwaters of the North Pacific are the largest reservoir of dissolved inorganic carbon (DIC) within the modern global ocean, and mixing of these deepwaters into the surface of the subarctic Pacific results a significant flux of CO_2 to the atmosphere. It is hypothesised that greater stratification of the North Pacific during glacial times sequestered more DIC within the deep ocean, lowering atmospheric CO_2, and that this isolated reservoir returned to the surface ocean and atmosphere over deglaciation. This thesis seeks to test this hypothesis by reconstructing the physical structure and carbonate chemistry of the interior and surface subarctic Pacific Ocean over deglaciation using trace elements and boron isotopes in biogenic carbonates.

1.1 Glacial-interglacial CO_2 cycling

Ice core records demonstrate that during the last 800 ka atmospheric pCO_2 has varied by 80-100 ppmv over glacial-interglacial (G-IG) cycles (Monnin et al., 2001; Lüthi et al., 2008; Lourantou et al., 2010). The deep ocean is the only reservoir large enough and sufficiently available to exchange with the atmosphere on millennial/sub millennial timescales (Figure 1.1) (Broecker, 1982). The reduction in atmospheric $\Delta^{14}C$ and

$\delta^{13}C$ (that is the ratio of $^{14}C/^{12}C$ and $^{13}C/^{12}C$ respectively) accompanying the ~90 ppmv rise in CO_2 over the last deglaciation documents the release of CO_2 back to the atmosphere from an isolated deep ocean reservoir (Figure 1.2) (Fairbanks et al., 2005; Broecker and Barker, 2007; Schmitt et al., 2012a). Although higher ΣCO_2 (ΣCO_2 is the sum of dissolved inorganic carbon species, used interchangeably with the term DIC here) solubility in the colder glacial ocean would have lowered atmospheric CO_2 by ~30 ppm, this effect would have been counteracted by a reduction in ΣCO_2 solubility from increased salinity, and a reduction in the size of the terrestrial biosphere. A more complex change in the marine carbon cycle is thus required to explain the G-IG atmospheric CO_2 shift (Broecker and Peng, 1989; Sigman and Boyle, 2000). The observation that the calcite lysocline was less than one kilometer deeper during glacial times limits the role of both whole-ocean alkalinity changes and surface-deep ocean alkalinity redistribution (Archer and Maier-Reimer, 1994). Any viable mechanism for increasing G-IG CO_2 storage must adhere to the constraint of a transient dissolution/preservation event and the inception/termination of glacial periods rather than a steady state shift in the lysocline (Broecker and Peng, 1987; Sigman and Boyle, 2000). These transient $CaCO_3$ dissolution/preservation events would have amplified any initial changes in atmospheric CO_2 through carbonate compensation (Broecker and Peng, 1987).

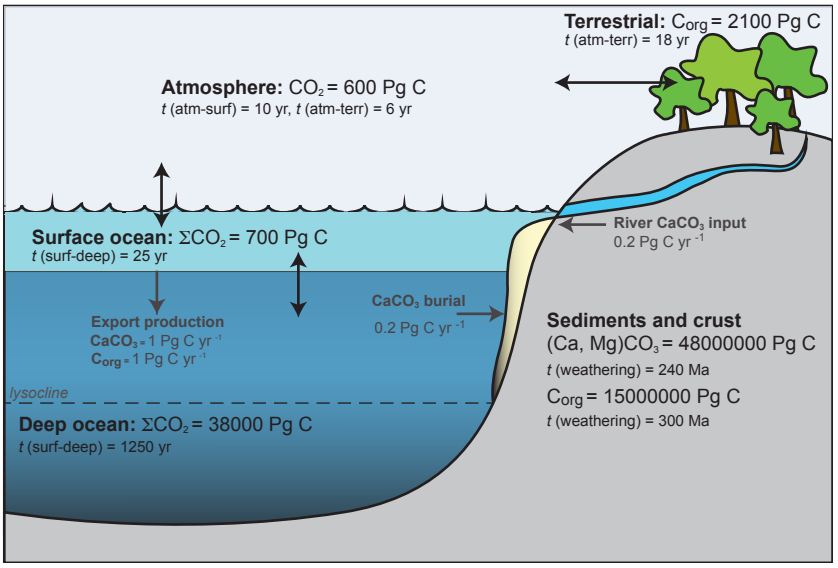

FIGURE 1.1: Major reservoirs and fluxes of the Holocene carbon cycle. Redrawn from Sigman and Boyle (2000).

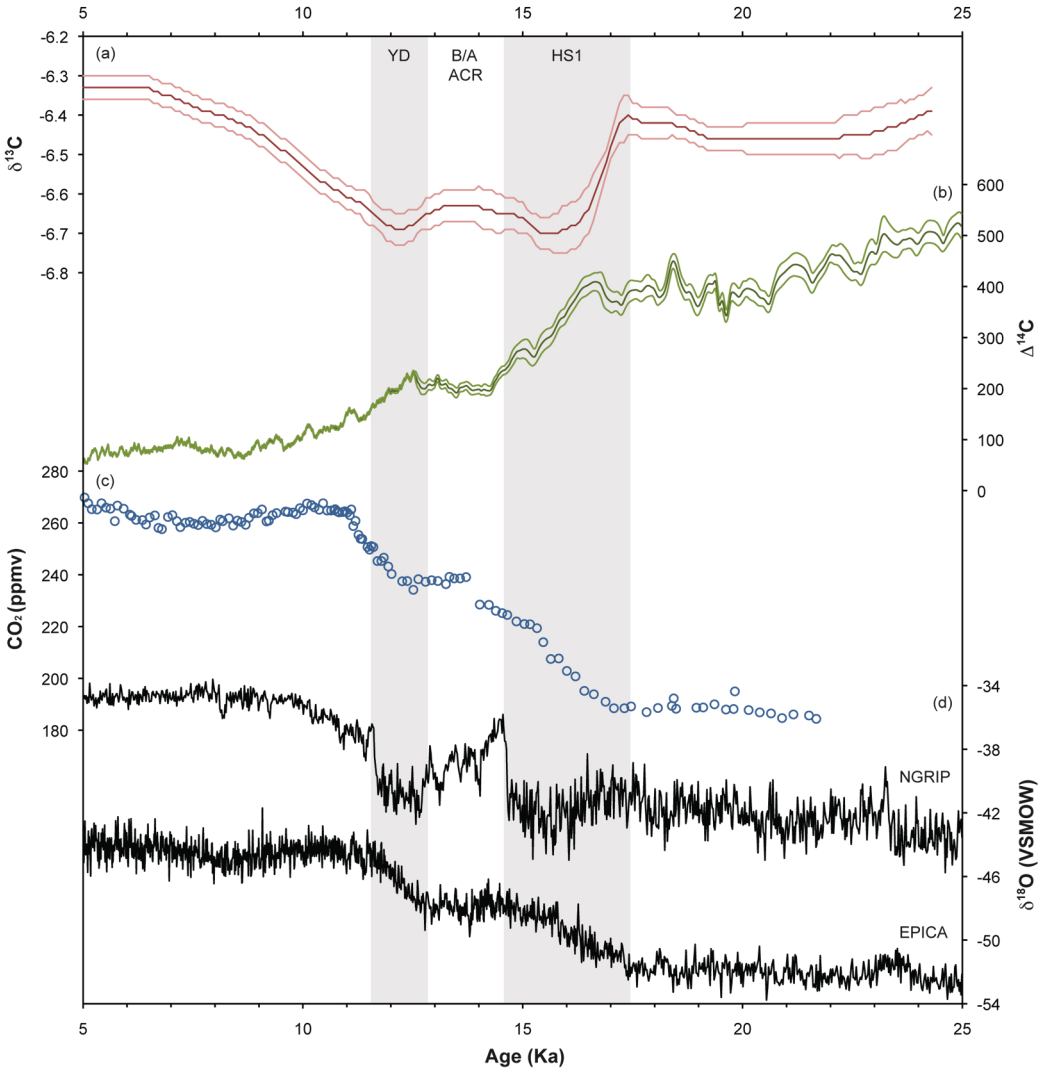

FIGURE 1.2: (a) Atmospheric $\delta^{13}C$ (Schmitt et al., 2012a) (b) atmospheric $\Delta^{14}C$ (Hughen et al., 2004) (c) atmospheric CO_2 (Monnin et al., 2001) and (d) $\delta^{18}O$ (VSMOW) from the NGRIP and EDML ice cores (Andersen et al., 2004; Rasmussen et al., 2006; Barbante et al., 2006).

1.1.1 The importance of the high latitude oceans in the marine carbon cycle

Excluding the effects of anthropogenic CO_2, the surface ocean and atmosphere can be considered in steady state equilibrium with regards to CO_2, with mixed layer CO_2 generally at $\pm 40\%$ saturation of atmospheric CO_2 (Tans et al., 1990). The pCO_2 of the surface ocean is mainly determined by temperature, ΣCO_2, alkalinity and salinity. Temperature (due to slow gas exchange) and ΣCO_2 concentration exert the strongest control on the disequilibria observed between the atmosphere and surface ocean (Takahashi et al., 1993). The concentration of ΣCO_2 in the surface ocean is

dependant on the balance between ΣCO_2 removal through the biological production of organic carbon (C_{org}) and $CaCO_3$ (the biological pump), and the input of high-ΣCO_2 deepwaters (Levy et al., 2013). Within the deep ocean C_{org} and $CaCO_3$ are returned to the inorganic carbon pool through the oxidation of C_{org} and dissolution of $CaCO_3$.

The biological pump results in both a vertical ΣCO_2gradient, with higher levels of ΣCO_2 in the deep ocean (~2300 μmol/kg) relative to the surface ocean (~2100 μmol/kg), and a lateral gradient, with ΣCO_2 concentration increasing within deepwaters as they progress away from the North Atlantic (~2100 μmol/kg), around the Southern Ocean (~2300 μmol/kg) and into the Pacific basin (~2500 μmol/kg) (Key, 2004). The export rain ratio of C_{org}:$CaCO_3$ (~4:1 in the modern ocean) plays an important role in determining the $[CO_2]$ of the surface ocean and $CaCO_3$ deposition within the deep ocean. The formation and export of $CaCO_3$ from the surface ocean removes alkalinity and ΣCO_2 in a 2:1 ratio, increasing $[CO_2]$ in the surface ocean and increasing alkalinity within the deep ocean. The formation and export of C_{org} lowers surface ocean ΣCO_2 with no effect on alkalinity, lowering $[CO_2]$ in the surface ocean and increasing it in the deep ocean (Archer and Maier-Reimer, 1994; Chikamoto et al., 2009).

The amount of ΣCO_2 taken up during the production of C_{org} and $CaCO_3$ is stoichiometrically defined in relation to the other major nutrients (NO_3^- and PO_4^{3-}) in the Redfield ratio (Redfield et al., 1963). Iron is also a vital nutrient, yet due to its lower solubility in oxic waters it has a residence time much shorter than that of NO_3^- and PO_4^{3-} and is depleted in upwelling waters (Martin, 1990). Aerial transport, shelf sediment inputs and remineralisation within the upper watercolumn instead constitute the main sources of Fe to the surface ocean (Jickells and Spokes, 2001; Elrod, 2004; Tagliabue et al., 2014). Thermal stratification in most of the low latitude oceans restricts the upwelling of PO_4^{3-} to the extent Fe inputs are sufficient not to limit primary productivity (Martin and Michael Gordon, 1988). The production of C_{org} and $CaCO_3$, and therefore the amount of ΣCO_2 sequestered by the biological pump, is instead limited by PO_4^{3-} availability (Broecker and Peng, 1982). Thus, in the low latitudes all upwelled ΣCO_2 is remineralised as C_{org} and $CaCO_3$ and there is no net loss or gain of ΣCO_2 from the surface ocean, with the biological pump approaching 100% efficiency. Here, only an increase in the total ocean nutrient budget could increase the sequestration of atmospheric CO_2. However the 16 Ma residence time of PO_4^{3-} is too long to provide a viable mechanism operating within G-IG timescales (Ruttenberg, 1993; Broecker and Henderson, 1998).

Due to the outcropping of the thermocline within the high latitude oceans, much of the ocean's deep waters return to the surface resulting in elevated surface ocean ΣCO_2 and nutrient concentrations. Annual average PO_4^{3-} concentrations are ~1.5 μmol/kg in the subarctic Pacific and >2 μmol/kg in the Southern Ocean, compared to <0.1 μmol/kg in

the western subtropical Pacific (Takahashi et al., 1993; Key, 2004). In these upwelling regions Fe and light concentrations limit primary productivity and nutrient utilisation is incomplete (Martin, 1990). In these high-nutrient low-chlorophyll (HNLC) zones unused 'preformed' nutrients return to the ocean's interior without forming C_{org} or $CaCO_3$. This represents a 'missed chance' for the deep ocean to sequester ΣCO_2 and a 'leakage from the biological pump, as for every mole of 'preformed' PO_4^{3-} that is subducted, 100-116 moles of ΣCO_2 remain in the surface ocean.

It should be noted that different processes drive elevated nutrient concentrations in the Southern Ocean and the subarctic Pacific; Ekman pumping brings nutrient rich deepwaters to the surface of the Southern Ocean (Marinov et al., 2006; Marshall and Speer, 2012), while tidal mixing fulfills an equivalent role in the subarctic Pacific (Kelley and Hood, 1971; Mordy et al., 2005). To borrow, and build upon Haug and Sigman's (2009) analogy, these polar twins are non-identical. The Southern Ocean is particularly important in this respect as it ventilates a large volume of the interior ocean and thus determines the ratio of preformed to remineralised nutrients throughout much of the deep ocean (Sigman and Boyle, 2000; Sigman et al., 2010). In fact, keeping all else equal, increasing the volume of the deep ocean that is ventilated by the Southern Ocean (as has widely been proposed for the LGM) would increase atmospheric CO_2 (Marinov et al., 2008). It is due to this high latitude ocean control on the efficiency of the biological pump that many hypotheses regarding to G-IG carbon cycling have focused on nutrient utilisation within the polar oceans (Knox and McElroy, 1984; Sarmiento and Toggweiler, 1984; Siegenthaler and Wenk, 1984; Broecker and Peng, 1989; Sigman and Boyle, 2000; Sigman et al., 2010).

1.2 Oceanography of the North Pacific

The interior North Pacific contains the oldest and most nutrient/ΣCO_2-rich waters in the global ocean. Volumetrically the Pacific dominates the worlds oceans, and is thus the largest nutrient/ΣCO_2 reservoir in the global ocean. Entering the basin via the Deep Western Boundary current, deepwaters flow northward before overturning and returning southward as Pacific Deepwater (PDW) (Figures 1.3 and 1.4). Broecker et al. (1998) suggested deepwater entering Pacific was a 1:1 mixture of recirculated North Atlantic Deepwater (NADW) and Antarctic Bottom Water (AABW), however Talley (2013) argue that it is almost all AABW. The formation of PDW (through diapycnal mixing) acts as the main return pathway of nutrients and ΣCO_2 from the deep ocean back to the intermediate depths Talley (2013). Furthermore, as PDW is upwelled to the surface of the Southern Ocean, formation of PDW through diapycnal mixing acts as an

integral step in the return of nutrient/ΣCO_2 rich deep waters to both the surface ocean, and the low latitude thermocline via the formation of AAIW/SAMW (Sarmiento et al., 2004; Talley, 2013) (Figure 1.3).

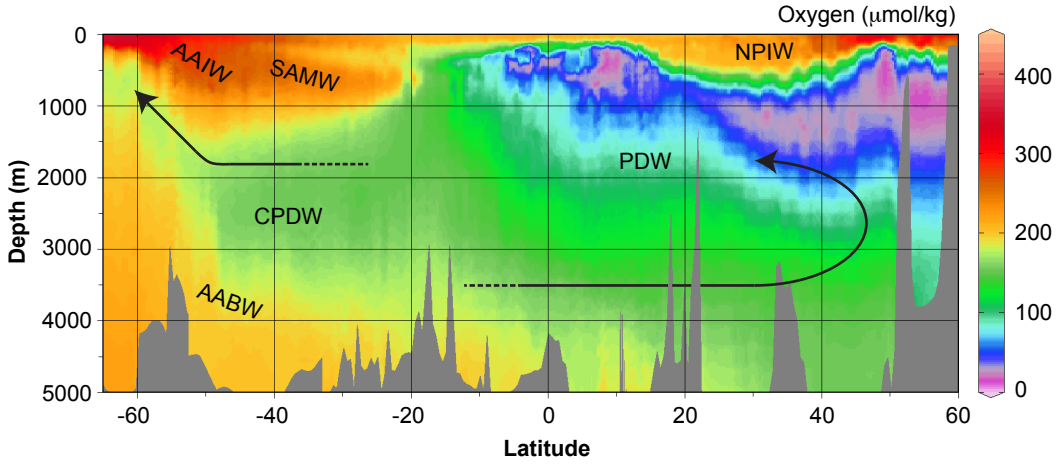

FIGURE 1.3: Latitudinal dissolved oxygen profile within the Pacific basin, data from (Key, 2004). Major watermasses are indicated; Antarctic Intermediate Water (AAIW), Sub Antarctic Mode Water (SAMW), Antarctic Bottom Water (AABW), Circumpolar Deepwater (CPDW), Pacific Deepwater (PDW) and North Pacific Intermediate Water (NPIW).

The high atmospheric moisture flux associated with the Asian monsoon and net transfer transfer of moisture from the Atlantic to the Pacific by the trade winds create a low-salinity cap over the North Pacific (Figure 1.5) (Emile-Geay, 2003). Surface circulation is dominated by the suptropical and subpolar gyres (Figure 1.5), which 'trap' the low salinity waters within the North Pacific (Talley, 2002). The low salinity of the surface ocean drives a strong perennial halocline at 150-200 m depth, stratifying the upper watercolumn (Figure 1.6). Due to the low salinity, the surface waters of the North Pacific remain below the density of PDW throughout the winter months, inhibiting the formation of deepwaters. The only subsurface watermass to form in the North Pacific today is North Pacific Intermediate Water (NPIW), a shallow (300-800m), low density (26.7-26.9 σ) watermass formed by brine rejection in Okhotsk Sea and modified by mixing processes along the Kuril Islands, that spreads eastwards throughout the North Pacific from the Okhotsk Sea (Emile-Geay, 2003; Warren, 1983; Yasuda, 1997). Although NPIW is initially separable from PDW by higher dissolved oxygen concentrations, a distinct productivity-driven oxygen minimum zone develops below $\sim$ 500 m (within the 26.7-26.9 σ isopycnal) as the watermass spreads eastwards below the subpolar gyre (Figure 1.3) (Talley, 1993).

The lack of any substantial watermass of North Pacific origin overlying PDW and reduction in density from diapycnal mixing allows the overturning of the watercolumn

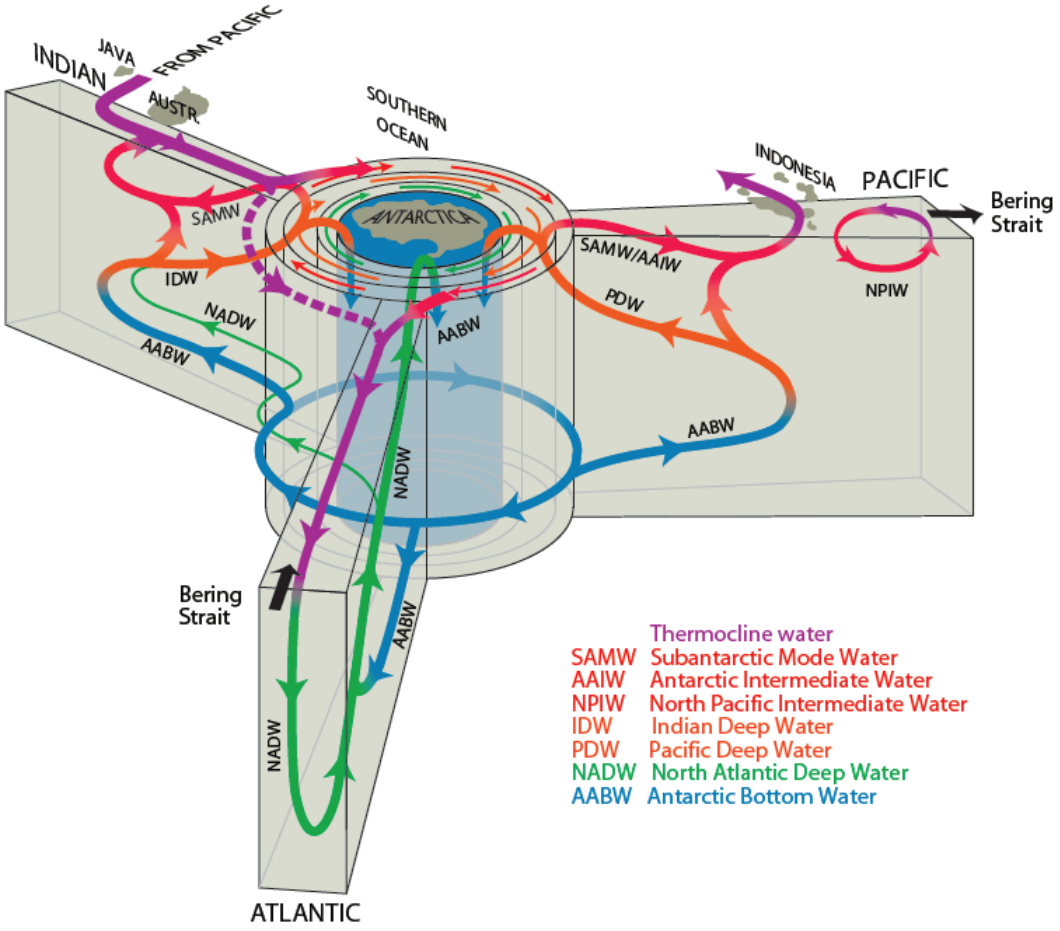

FIGURE 1.4: Schematic of global overturning circulation from Talley (2013)

at the northern end of the Pacific basin, upwelling nutrients and ΣCO_2 from the deep ocean into the intermediate depths (1000-2000m). This results in a reversed $\Delta^{14}C$ and ΣCO_2 profile with the oldest, most nutrient-rich waters located in the mid-depth ocean (Figure 1.7) (Key, 2004; Talley, 2013). Despite a stable upper water column from the perennial halocline at ~200 m depth (Figure 1.6), strong vertical mixing driven by tidal interactions in the Kuril and Aleutian Islands brings the nutrient/ΣCO_2-rich waters from the intermediate depths into the surface ocean. These nutrient/ΣCO_2-rich waters are entrained during the formation of NPIW and transported beneath the North Pacific subpolar and sub tropical gyres. NPIW thus forms an important nutrient source underlying the entire North Pacific thermocline that provides 70% of the silicic acid supply for diatom production within the equatorial Pacific (Dugdale et al., 2002; Sarmiento et al., 2004).

Within the subarctic Pacific, the input of old, nutrient-rich, deep waters into the surface ocean through vertical mixing in the winter months elevates $[CO_2]$, ΣCO_2 and nutrient concentrations and reduces the $\Delta^{14}C$ of ΣCO_2 (Figures 1.6 and 1.8). While stratification

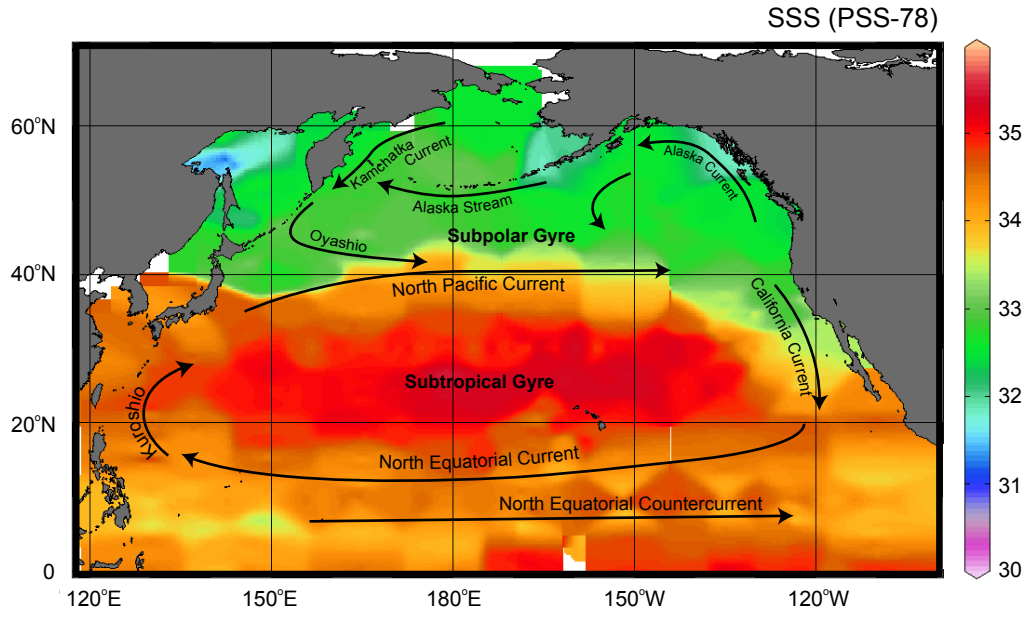

FIGURE 1.5: North Pacific sea surface salinity with major surface currents indicated. The minimal mixing between the gyres is evident from the sharp colour contrast north and south of ~40 °N. Data from (Key, 2004).

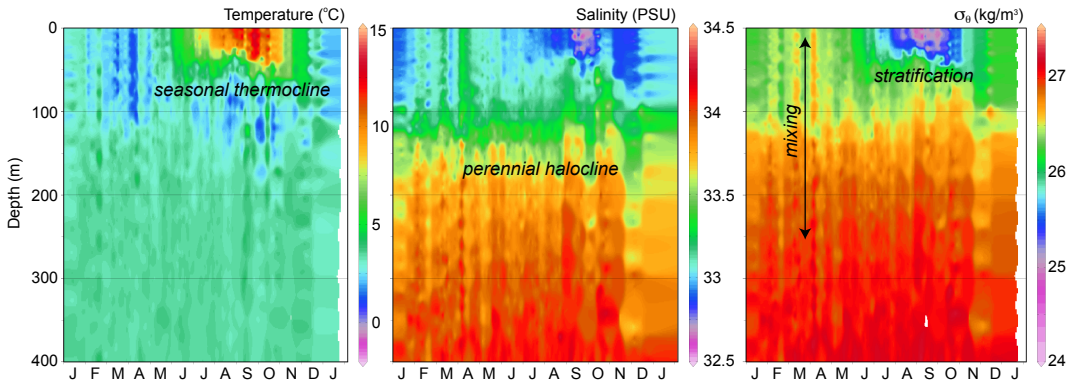

FIGURE 1.6: Seasonal changes in North Pacific upper ocean structure, showing the perennial halocline at 150-200 m and development of the seasonal thermocline at ~50 m. The watercolumn is highly stratified during the late summer, whereas the density gradient is much reduced in the early spring. Data from the World Ocean Database (Boyer et al., 2009)

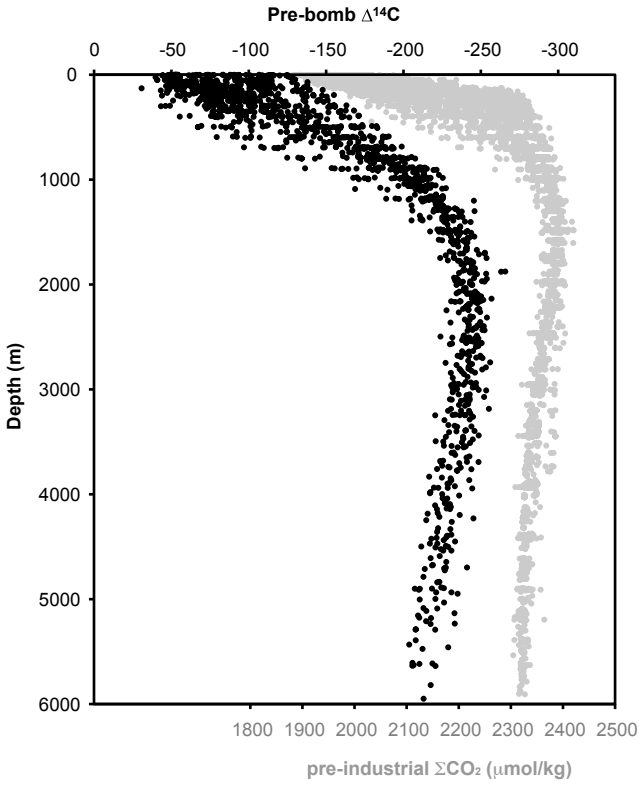

FIGURE 1.7: 'Reversed' North Pacific ΣCO_2 (grey) and $\Delta^{14}C$ (black) profiles. Data from (Key, 2004).

and photosynthesis in the summer months drive a reduction in $[CO_2]$, ΣCO_2 and nutrient concentrations (and an increase in $\Delta^{14}C$ from atmospheric CO_2 uptake), Fe limitation results in incomplete utilisation of the surface ocean nutrient pool (Martin, 1990; Takahashi et al., 1993; Tsuda, 2003) (Figure 1.6). The incomplete nutrient utilisation within the subarctic Pacific results in a flux of 4 moles CO_2 m^{-2} yr^{-1} to the atmosphere (Figure 1.9) (Takahashi et al., 1993, 2002). Within the temperate North Pacific the seasonal effects of temperature and upwelling/productivity are balanced such that there is no net flux of CO_2 between the surface ocean and atmosphere (Takahashi et al., 1993).

1.3 Hypotheses and evidence concerning the role of the North Pacific in glacial-interglacial CO_2 cycling

The potential role of the North Pacific in glacial-interglacial CO_2 cycling is twofold; (i) increasing the efficiency of the biological pump within the glacial subarctic Pacific (Sigman and Boyle, 2000; Jaccard et al., 2005; Galbraith et al., 2008; Sigman et al., 2010); (ii) increasing storage of ΣCO_2 within the deep glacial North Pacific (Galbraith et al., 2007; Jaccard et al., 2009). Greater stratification within the glacial North Pacific

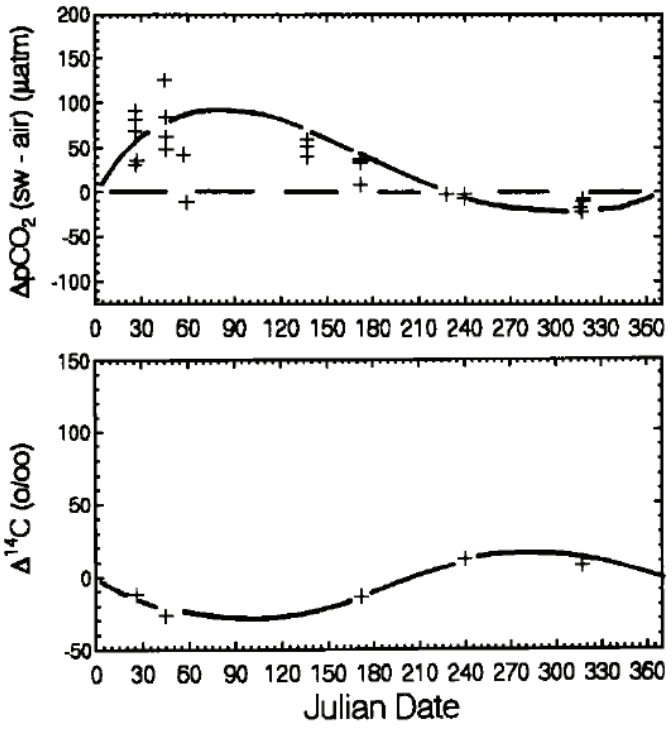

FIGURE 1.8: CO_2 outgassing from the subarctic Pacific. As CO_2 is released from the subarctic Pacific, the $\Delta^{14}C$ of the ΣCO_2 decreases, indicating it is of a deep ocean origin. Figure from Takahashi et al. (1993).

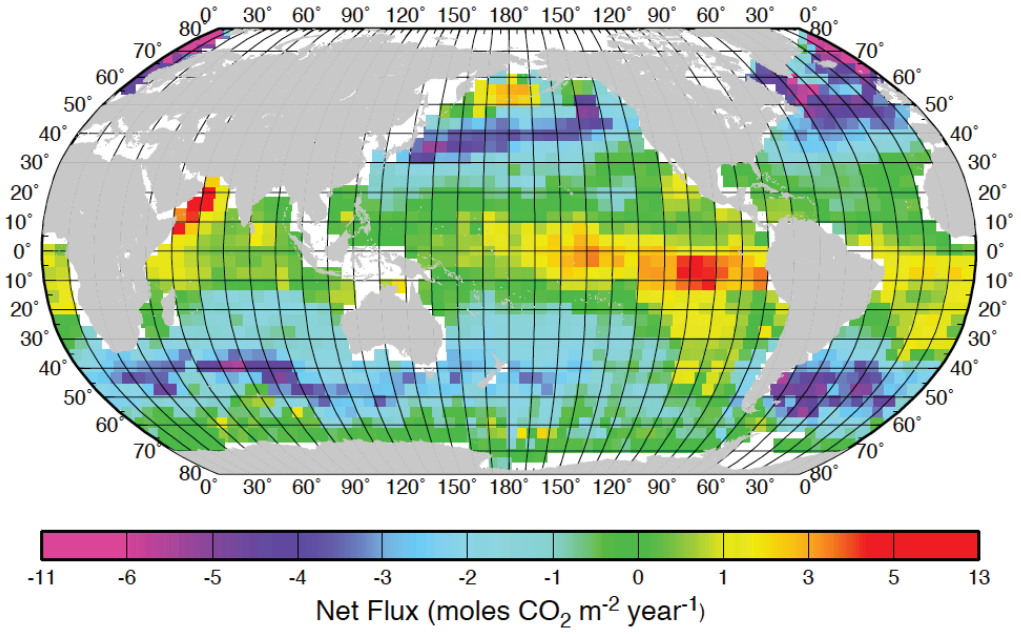

FIGURE 1.9: Global average annual sea-air CO_2 flux. Figure from Takahashi et al. (2002).

has been suggested as a mechanism to increase both the efficiency of the biological pump within the subarctic Pacific, and the storage of ΣCO_2 within the deep North Pacific Ocean (Sigman and Boyle, 2000; Jaccard et al., 2005; Galbraith et al., 2007, 2008; Jaccard et al., 2009; Sigman et al., 2010). Greater density stratification would reduce the input of nutrients/ΣCO_2 from the deep to surface ocean, driving an increase in nutrient utilisation and the efficiency of the biological pump by reducing the amount of 'excess' nutrient within the surface ocean (Sigman and Boyle, 2000; Jaccard et al., 2005; Galbraith et al., 2008; Sigman et al., 2010). Increasing the vertical density gradient would also work to decrease overturning circulation, increasing the concentration and reservoir time of ΣCO_2 in the deep Pacific (Boyle, 1988; Jaccard et al., 2009). The effects of increased deep ocean ΣCO_2 storage on decreasing atmospheric CO_2 would be amplified through carbonate compensation throughout the deep Pacific basin (Marchitto et al., 2005). A breakdown in stratification and ventilation of the deep ocean would then return this isolated ΣCO_2 reservoir to the atmosphere over deglaciation (Jaccard et al., 2005; Galbraith et al., 2007).

Analysis of diatom bound $\delta^{15}N$ ($\delta^{15}N_{db}$) shows increased nitrate utilisation in the subarctic Pacific during glacial times (Brunelle et al., 2007; Galbraith et al., 2008; Brunelle et al., 2010). As primary productivity was lower (Kienast et al., 2004; Jaccard et al., 2005; Galbraith et al., 2008; Gebhardt et al., 2008; Jaccard et al., 2010) (Figure 1.10), the increase in nitrate utilisation must have been driven by a decrease in nitrate availability, suggesting a more stratified watercolumn (Brunelle et al., 2007; Galbraith et al., 2008; Brunelle et al., 2010). Interior rather than surface stratification would seem a more plausible mechanism by which nutrient/ΣCO_2 upwelling could be reduced in the North Pacific as (i) the surface ocean is currently highly stratified yet tidal mixing of the intermediate and surface waters drives high nutrient concentrations in the surface ocean (Kelley and Hood, 1971; Mordy et al., 2005) (ii) the atmospheric monsoonal moisture flux that currently stratifies the North Pacific and limits sub-surface watermass formation appears to have been significantly reduced during glacial times, both reducing surface stratification and enabling the expansion of subsurface watermasses (Warren, 1983; Wang et al., 2001a; Emile-Geay, 2003). An inferred increase in salinity from paired Mg/Ca and stable isotope data (Sagawa and Ikehara, 2008; Riethdorf et al., 2013) suggests a reduction in the North Pacific halocline during the LGM. Surface ocean structure over deglaciation is debated, with planktonic foraminiferal $\delta^{18}O$ records suggesting increased surface ocean stratification during the Heinrich 1 Stadial (HS1) (Figure 1.10). However other authors have concluded the permanent halocline did not develop until the Holocene (Sarnthein et al., 2004; Riethdorf et al., 2013).

Higher glacial $\delta^{13}C$ (relative to the 0.34 $\pm$0.19‰ whole-ocean shift of Peterson et al.

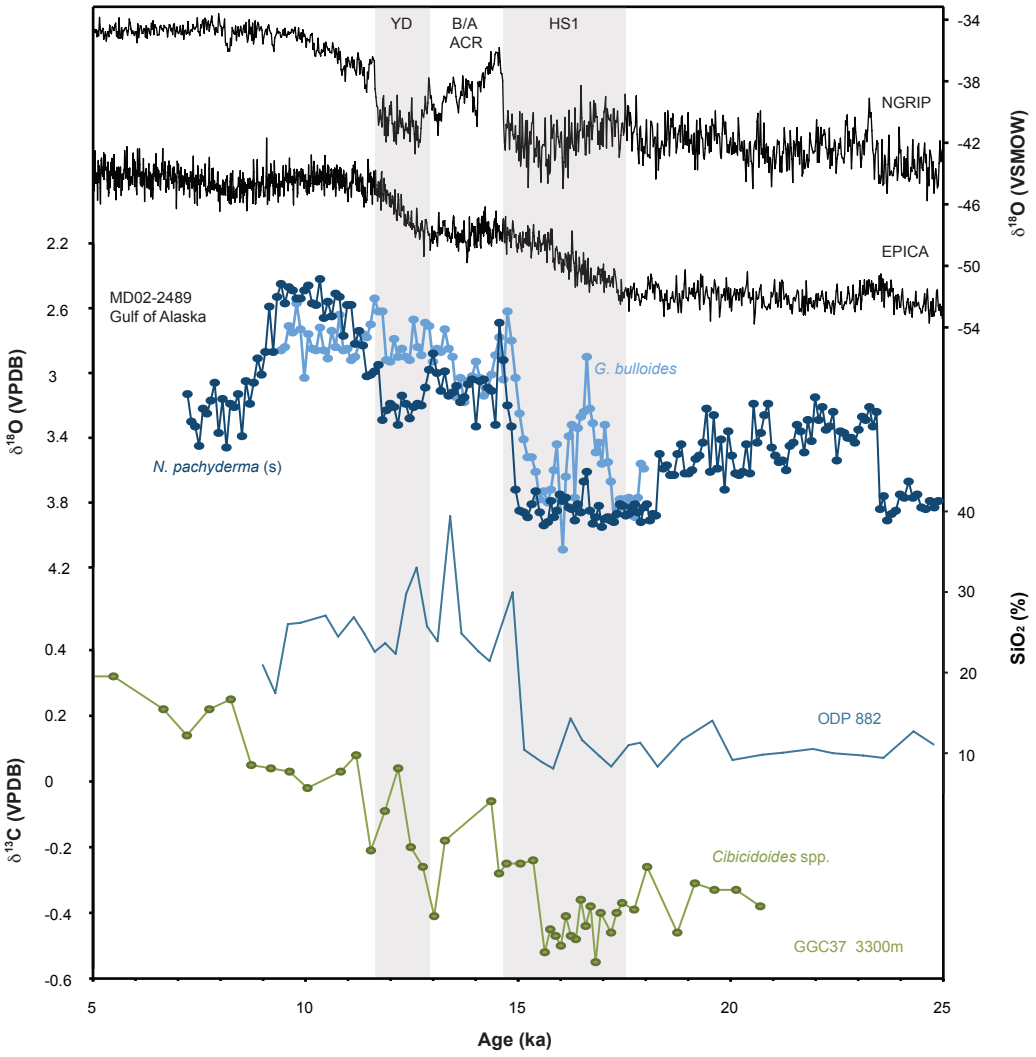

FIGURE 1.10: Deglaciation in the North Pacific. The $\delta^{18}O$ records from NGRIP on the GICC05 timescale (Rasmussen et al., 2006), and EPICA (Barbante et al., 2006) are shown for stratigraphic reference. Planktonic foraminiferal $\delta^{18}O$ records from MD02-2489 in the northeastern Pacific are shown in blue (Gebhardt et al., 2008), %Opal from ODP Site 882 (Jaccard et al., 2005) and *Cibicidoides* spp. $\delta^{13}C$ from GGC37 in the northwestern Pacific are shown in turquoise and green respecitively.

(2014)) and lower $\delta^{18}O$ values have been taken as evidence for a better ventilated watermass above ∼2000 m in the glacial ocean, suggested to represent a vertical expansion of NPIW (Figure 1.11) (Herguera et al., 1992; Keigwin, 1998; Matsumoto et al., 2002). Neodynium isotope and microfossil data support a Bering Sea source for this expanded glacial NPIW watermass (Ohkushi et al., 2003; Horikawa et al., 2010). The vertical expansion of what is currently a low salinity watermass provides a potential mechanism to increase stratification within the interior of the North Pacific Ocean. As the low density gradient within the North Pacific acts as the major pathway for the return of nutrients to the surface of the Southern Ocean today, increased interior ocean

stratification of the North Pacific from a glacial expansion of NPIW would have profound implications for nutrient and ΣCO_2 cycling throughout the global ocean. Below ~2000 m benthic foraminiferal $\Delta^{14}C$ and $\delta^{13}C$, and redox metal data indicate the presence of a larger and more isolated glacial ΣCO_2 reservoir (Galbraith et al., 2007; Jaccard et al., 2009; Lund et al., 2011). However, reconstructions using Cd/Ca indicate lower, not higher nutrient concentrations in the deep North Pacific during the LGM (Boyle, 1992; Ohkouchi et al., 1994).

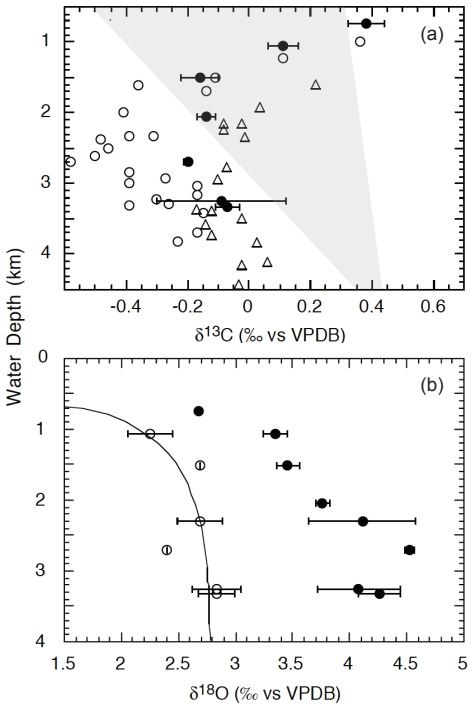

FIGURE 1.11: LGM North Pacific $\delta^{18}O$ and $\delta^{13}C$ profiles from Matsumoto et al. (2002)

Productivity maxima, which are observed at every major deglaciation since 2.7 Ma, are thought to document the upwelling of nutrient/ΣCO_2 rich deep waters into the surface ocean as the deep ocean is ventilated (Kienast et al., 2004; Sigman et al., 2004; Jaccard et al., 2005, 2010). The timing and physical mechanism by which this isolated ΣCO_2 reservoir returned to the surface ocean and atmosphere over the last deglaciation is poorly constrained. Opal, $CaCO_3$, benthic foraminiferal $\delta^{13}C$ and redox metal records indicate the deep ocean was ventilated at the onset of the Bolling-Allerod interstadial (B/A) (Figure 1.10) (Keigwin, 1998; Kienast et al., 2004; Jaccard et al., 2005, 2009). Productivity is not, however, a direct indicator of upwelling or CO_2 outgassing, as nutrient availability is only one of many controls on productivity (this is self evident from the high-nutrient low-chlorophyll status of the modern subarctic Pacific), and productivity reconstructions cannot discern between the proportion of the upwelled ΣCO_2 pool that is outgassed to the atmosphere, and the proportion that is remineralised

as C_{org} and $CaCO_3$. Furthermore, the effects of preservation on $CaCO_3$ and opal records may override any productivity signal (Archer et al., 1993; Serno et al., 2014). If the opal maximum at ∼14.5 ka does indicate greater productivity than observed at any point during the entire Holocene, the current Fe limitation must have been overcome. Inundation of Fe-rich shelf sediments following global sea level rise has been proposed (Davies et al., 2011), however radiogenic isotope work indicates no change in source of iron during this time (Lam et al., 2013), and thus the cause of this productivity remains enigmatic.

1.4 Aims and Objectives

The overarching aim of this thesis is to examine the role of the North Pacific Ocean in the deglacial CO_2 rise. It seeks to answer key questions concerning changes in the physical structure and carbonate chemistry of the surface and interior of the subarctic Pacific Ocean over deglaciation:

- Was more or less ΣCO_2 stored in the interior of the North Pacific during the LGM compared to the Holocene?
- Was the interior of the North Pacific Ocean more or less stratified than present during the LGM? How did any changes in physical stratification affect chemical stratification?
- Were the intermediate waters of the North Pacific better ventilated during the LGM than during the Holocene, and if so what was their origin?
- Did ventilation and ΣCO_2 storage in the interior North Pacific change over deglaciation? If so, what was the mechanism that drove these changes?
- Was CO_2 outgassing from the subarctic Pacific higher or lower during the LGM than during the Holocene?
- How did CO_2 outgassing from subarctic Pacific change over deglaciation? Was a deeply sequestered ΣCO_2 reservoir returned to the atmosphere through the surface waters of the subarctic Pacific?
- How did the physical properties of the North Pacific surface ocean change over deglaciation?
- How do changes in CO_2 outgassing from the subarctic Pacific relate to changes in stratification, deep ocean ventilation, and productivity?

This thesis attempts to answer these questions by generating quantative reconstructions of the physical properties (temperature and $\delta^{18}O_{seawater}$) and carbonate chemistry (surface ocean pCO_2 and deep ocean $\Sigma CO_2/[CO_3^{2-}]$) of the surface and interior subarctic Pacific Ocean over deglaciation using trace elements, oxygen isotopes, and boron isotopes in foraminifera. The theoretical framework underpinning the use of trace element/Ca ratios and boron isotopes in biogenic carbonates as proxies for the physical and chemical properties of seawater is outlined in Chapter 2, and details of the methods developed to measure trace element/Ca ratios in biogenic carbonates at UCL are given in Chapter 3.

Before applying trace element proxies downcore, studies were first conducted to understand the influence of contamination and cleaning procedures on Mg/Ca ratios in marine ostracod genus *Krithe* (Chapter 4), and the controls on the uptake of Li, B, Mg and Sr in benthic foraminifera *Uvigerina peregrina* (Chapter 5). Chapter 6 focusses on reconstructing deglacial changes in physical structure and carbon storage within the interior subarctic Pacific Ocean using trace element/Ca ratios in *Uvigerina peregrina*, while the reconstruction of deglacial surface ocean stratification and CO_2 outgassing with trace element/Ca ratios and boron isotopes in planktonic foraminifera is detailed in Chapter 7. The conclusions of this work are given in Chapter 8.

Chapter 4 may seem somewhat out of place within this thesis, because ultimately no analyses of *Krithe* were undertaken on any of the sediment cores analysed. It was originally intended that bottom water temperatures in the North Pacific would be reconstructed using Mg/Ca ratios in *Krithe*, hence the need for an evaluation of cleaning procedures. However, too few *Krithe* valves were found in any of the sediment cores, making this work unfeasible. The evaluation of cleaning procedures will be of value to subsequent work on fossil material, and so has been included in the thesis.

This thesis has been structured in a manner that chapters 4, 5,6 and 7 can be read as self contained papers.

Chapter 2

Trace elements and boron isotopes in foraminifera and ostracods as proxies for temperature, nutrient and the carbonate system

The uptake of Li, B, Mg and Sr into marine biogenic carbonates is dependent on both the temperature and carbonate chemistry of the seawater in which they precipitated, while the ratio of ^{11}B to ^{10}B within marine biogenic carbonates reflects seawater pH, and the distribution of Cd in seawater closely matches that of PO_4^{3-}. Trace elements and boron isotopes in marine biogenic carbonates can therefore potentially be used to reconstruct temperature, carbonate chemistry and nutrient composition in the past, all of which play fundamental roles within Earth's climate system. This chapter reviews the theoretical basis underpinning several trace element proxies and boron isotopes, detailing the controls on their (i) activity in seawater, (ii) speciation and isotopic fractionation in seawater and (iii) partition coefficients into inorganic calcite, before giving a background to calcite biomineralisation in foraminifera and ostracods, and the biological mediation of magnesium uptake in foraminifera. This is chapter provides a reference for recurrent topics in the proceeding chapters, however the specific details relating to the use of trace elements and boron isotopes as proxies for temperature and cabonate chemistry in ostracods and benthic and planktonic foraminifera are givien in chapters 4, 5 and 7 respectively.

2.1 Element activity in seawater

The activity (the activity coefficient (γ) corrected concentration) of elements within seawater is a primary control on their concentration within biogenic calcites precipitated from seawater. In seawater Lithium is mainly present as Li^+, Boron as $B(OH)_3$ and $B(OH)_4^-$ (boron speciation is discussed further in section 2.2.2), Magnesium as Mg^{2+}, Calcium as Ca^{2+}, Strontium as Sr^{2+}, Cadmium as $CdCl^+$ and Uranium as stable uranyl carbonate complexes discussed in section 2.2.3 (Riley and Chester, 1971). The activity of Li, B, Mg, Ca, Sr, Cd and U within seawater reflects the balance between the inputs and outputs of each element in the ocean system. Fluvial transport of the dissolved constituents of carbonate and silicate rocks provides the main input for B, Mg, Ca, Sr, Cd and U (Table 2.1). Hydrothermal fluids provide a further source of B, Sr and Ca although several orders of magnitude lower than riverine inputs (Stoffyn-Egli and Mackenzie, 1984; Von Damm et al., 1985; Spivack and Edmond, 1987; Spivack et al., 1987). Li is unusual in that hydrothermal input constitues a greater proportion of the total Li input than riverine, and dissolved Li in rivers is almost entirely derived from silcate minerals (Huh et al., 1998; Chan and Edmond, 1988).

TABLE 2.1: Ocean residence time (τ) of selected elements

Element	Mean river concentration[1] (μmol/kg)	Mean ocean concentration[2] (μmol/kg)	τ[3] (yrs)
Li	3.0×10^{-1}	2.5×10^{1}	1.2×10^{6}*
B	1.7	4.2×10^{2}	9.4×10^{6}
Mg	1.6×10^{2}	5.3×10^{4}	1.3×10^{7}
Ca	3.6×10^{2}	10.3×10^{3}	1.1×10^{6}
Sr	6.9×10^{-1}	8.7×10^{1}	4.8×10^{6}
Cd	5.0×10^{-4}	6.2×10^{-4}	5.0×10^{4}
U	1.2×10^{-3}	1.3×10^{-2}	4.0×10^{5}

[1]Values from Turekian (1969), Martin and Meybeck (1979), Palmer and Edmond (1993) and Huh et al. (1998).
[2]Values from Bruland (1983) and Chan and Edmond (1988).
[3]Calculated using an ocean volume of 1.4×10^9 km^3 and an annual river water flux of $3.7 \times 10^4 km^3$.
*including hydrothermal input in calculation.

B/Ca, Mg/Ca and Sr/Ca ratios in seawater are respectively 8.6, 11.6 and 4.4 times higher than in typical river water, reflecting an inbalance of the outputs of B, Mg and Sr compared to Ca (Li, 2000). Ca is removed by the formation of $CaCO_3$ (and to a lesser extent $CaSO_4$), which constitutes the largest authigenic mineral formation

within the ocean. Conversely very little B, Mg or Sr is removed by any of the major authigenic minerals (FeS_2, $CaSO_4$, $CaCO_3$, NaCl, SiO_2). Instead B, Mg and Sr are removed from seawater during basaltic alteration within hydrothermal vents, where seawater is heated at high pressure (350 °C, 400atm) in the presence of basalts (Mackenzie and Garrels, 1966; Seyfried et al., 1984; Spivack and Edmond, 1987; Li, 2000). Reverse weathering may be an important process in removing Mg in near-shore/clay-rich sediments (Michalopoulos and Aller, 1995), and B is also removed from seawater through adsorption onto clays and coprecipitation with calcium carbonate (Schwarcz et al., 1969; Ishikawa and Nakamura, 1993). The major sinks for Li from seawater are the formation of marine authigenic alumino-silicate (MAAC) clays by 'reverse weathering' (∼70%) (Chan et al., 2002), and through basaltic alteration (∼30%) (Seyfried et al., 1984). Both processes involve the formation of Mg-rich smectites, in which Li can readily substitute octhedral Mg due to the similarity of their ionic radii (Chan et al., 2006).

The flux of uranium to and from the crust is not significant (Hart and Staudigel, 1982). Instead the major sink of U in seawater is the reduction of soluble U(VI) to insoluble U(IV) in suboxic porewaters (Anderson, 1982; Barnes and Cochran, 1990; Klinkhammer and Palmer, 1991). Cadmium is removed from seawater through incorporation into organic matter (Bruland, 1983). As the relative fluxes of Cd and U out of seawater are larger than that of Ca, the residence times are shorter (45 ka and 400 ka respectively) and the Cd/Ca and U/Ca ratios of seawater are lower than that of riverwater.

Li, B, Mg and Ca are conservative elements with ocean residence times of >1 Ma (Table 2.1) (Broecker and Peng, 1982). Seawater therefore has a near constant Li/Ca, B/Ca and Mg/Ca ratio of 0.0024, 0.040 and 5.2 mol/mol respectively on timescales of less than 1 Ma. Over longer timescales Li, B and Mg concentrations in seawater will reflect variations in the fluxes to and from the respective sources and sinks, and trace elemental ratios in biogenic carbonates can be used to reconstruct these hydrothermal and weathering processes over such timescales (Delaney et al., 1985). While uranium is conservative in oxic waters (Ku et al., 1977), redox-driven changes in U solubility can lead to non-linearity in the U-salinity relationship (McKee et al., 1987). While there are constraints on the Mg/Ca and Sr/Ca of seawater over the Cenozoic, the past concentration of Li, B and U in seawater is more poorly understood (Figure 2.1) (Wilkinson and Algeo, 1989; Lear et al., 2003; Coggon et al., 2010).

As Li, B, Mg and U are bio-unlimited, little variation in activity is expected both vertically within the watercolumn and between ocean basins. Calcium is biologically utilised in the formation of $CaCO_3$; however the ratio of Ca relative to PO_4^{3-} and NO_3^- exported out of the surface ocean within biological material is considerably lower than the ratio of Ca to PO_4^{3-} and NO_3^- within upwelling deepwater. As such, only a very

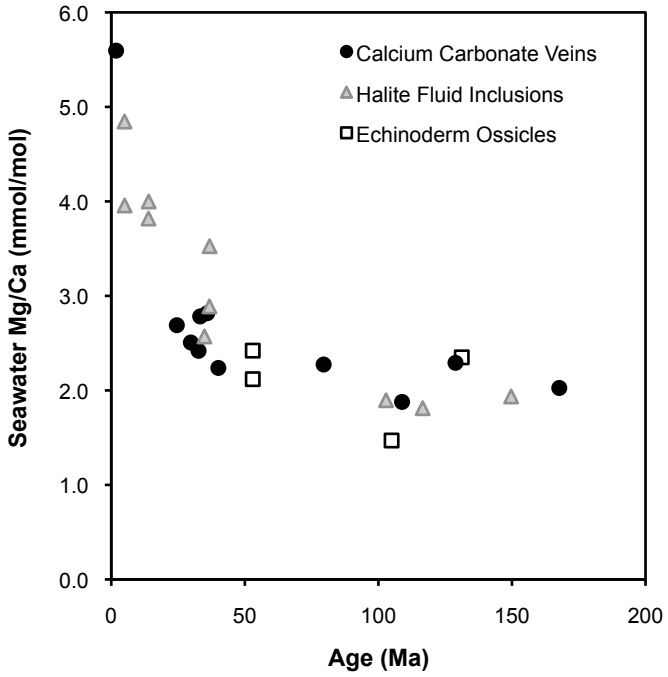

FIGURE 2.1: The Mg/Ca of seawater over the past 200 Ma. See Coggon et al. (2010) for details.

small depletion (0.5%) is observed in Ca^{2+} concentration within the surface of the modern ocean (Broecker and Peng, 1982). Variations in the utilisation of calcium by $CaCO_3$ producing organisms are unlikely to have significantly affected the distribution of Ca^{2+} within the water column over glacial-interglacial time scales. It has been suggested that $CaCO_3$ export was lower during glacial periods, resulting in increased Ca^{2+} concentrations within the surface ocean (Dymond and Lyle, 1985). However, even if $CaCO_3$ production ceased completely during glacial times, it would only result in a 0.5% increase in Ca^{2+} (it would also be a great shame as we would have nothing to study!). Sr is bioactive and exhibits a spatial variability of 2-3% relative to salinity, with higher values in the deep ocean and upwelling regions. Sr inclusion into celestite ($SrSO_4$) skeletons and a shallow dissolution cycle mean the upper ocean residence time is much shorter than its global ocean residence time (de Villiers, 1999).

Cadmium is a bioactive element utilised as a redox catalyse in enzymes and the concentration of Cd varies non-linearly with salinity (Boyle et al., 1976). Due to its role in metabolic processes, Cd correlates strongly with PO_4^{3-} (Boyle et al., 1976; de Baar et al., 1994) (Figure 2.2). As such there is both a large vertical and horizontal Cd gradient within the oceans following the build up of the constituent parts of organic matter, with low values in the surface ocean and the Atlantic, and enrichment in the deep ocean and the Pacific (Figure 2.3). The relationship between Cd and PO_4^{3-} appears

to break down in oxygen minimum zones (OMZs) (Anderson, R.F., 11^{th} International Conference on Paleoceanography, Barcelona, 2013).

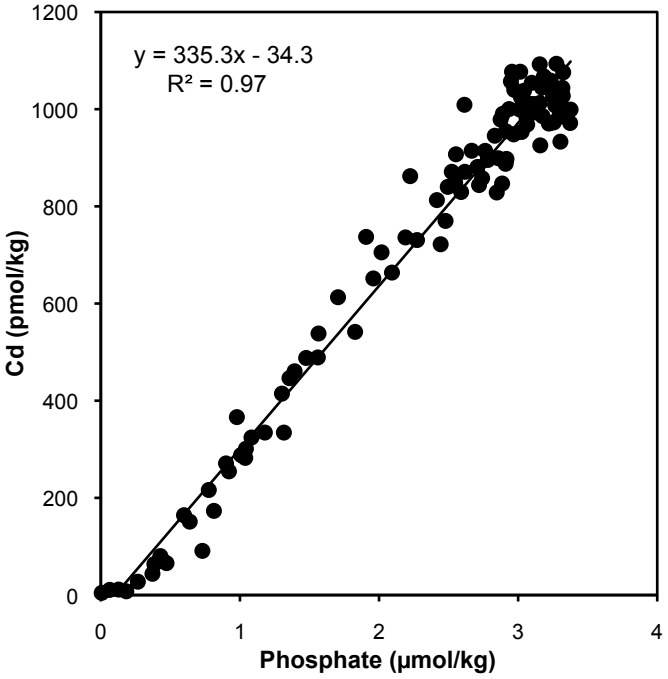

FIGURE 2.2: Relationship between Cd and PO_4^{3-} in the North Pacific Ocean. Data from de Baar et al. (1994).

2.2 Inorganic controls on partition coefficents and elemental speciation

2.2.1 Thermodynamic control on uptake of Mg within inorganic calcite

Mg^{2+} is a divalent cation that can substitute Ca^{2+} during the formation of $CaCO_3$ to form $MgCO_3$ compounds within the calcite lattice (Equation 2.1). $MgCO_3$ is isostructural with calcite, forming a rombohederal lattice system (Driessens and Verbeeck, 1981).

$$Mg^{2+} + CaCO_3 \longrightarrow MgCO_3 + Ca^{2+} \tag{2.1}$$

The incorporation of Mg relative to Ca within calcite is dependant on the activity ratio of each element in solution and the temperature-dependant distribution coefficient (D_{Mg}) between calcite and seawater.

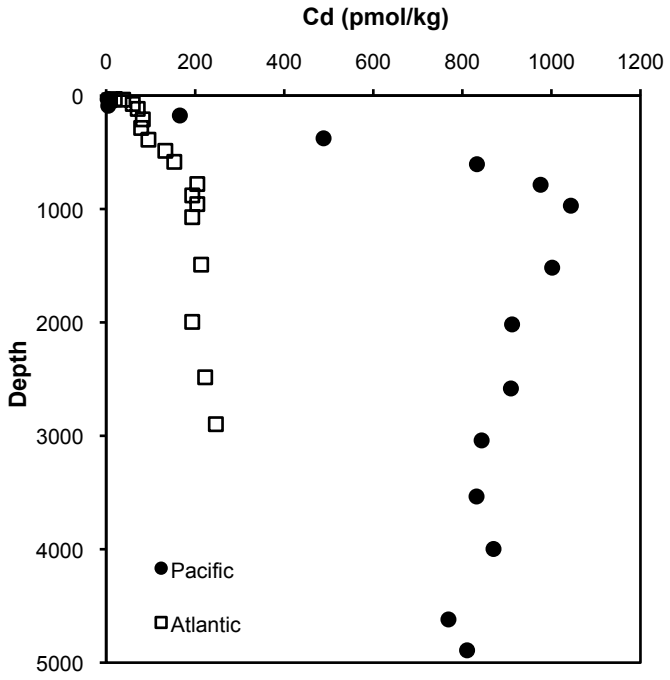

FIGURE 2.3: Dissolved Cd profiles of the Atlantic and Pacific oceans. Higher Cd concentrations in the Pacific correspond with higher PO_4^{3-}. Data from Boyle and Huested (1983).

$$D_{Mg} = \frac{\mathrm{MgCO_3/CaCO_3}}{[Mg^{2+}/Ca^{2+}]_{seawater}} \tag{2.2}$$

The van't Hoff equation (2.3) shows that any reaction with an associated enthalpy change (ΔH) will be exponentially sensitive to temperature (Garrels and Christ, 1965):

$$\frac{d\ln K}{d(1/T)} = -\frac{\Delta H}{R} \tag{2.3}$$

where T is temperature in Kelvin, R is the gas constant and K is the equilibrium constant for the reaction. The substitution of Mg into calcite is an endothermic reaction with a ΔH° of 21kJ/mol (Koziol and Newton, 1995). At equilibrium, theory predicts that the uptake of Mg within a thermodynamically ideal calcite will increase exponentially by $\sim$3 °C between 0 and 30 °C (Lea et al., 1999), with inorganic calcite precipitates empirically supporting this relationship (Figure 2.4) (Katz, 1973; Oomori et al., 1987).

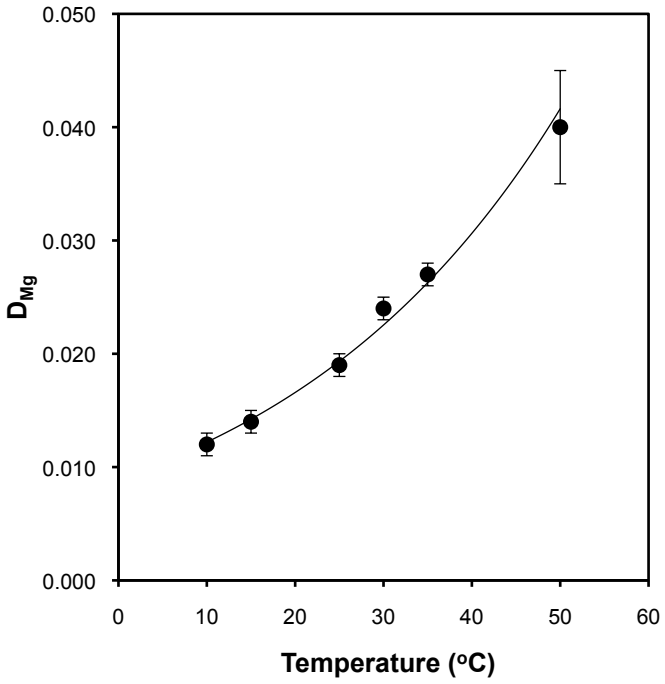

FIGURE 2.4: Temperature dependence of D_{Mg} in inorganic calcite, D_{Mg}= $0.009exp(0.031T)$. Data from Oomori et al. (1987).

2.2.2 Boron and the carbonate system

Boron exists as two main species in seawater, boric acid (triagonal coordination) and borate (tetrahedral coordination) (Equation 2.4), the proportions of which are pH dependent (Equation 2.5). They are the acid-base pair with the second highest concentration in seawater and a *p*K near the pH of seawater, and alongside the carbonate system play an important role in determining the acid-base chemistry of seawater (Figure 2.5).

$$B(OH)_3 + H_2O \leftrightharpoons B(OH)_4^- + H^+ \tag{2.4}$$

$$K_B = [B(OH)_4^-][H^+]/[B(OH)_3] \tag{2.5}$$

$B(OH)_4^-$ is thought to be primary species incorporated into carbonates, and Hemming and Hanson (1992) put forward the following mechanism for boron substitution in the CO_3^{2-} site in carbonate:

$$CaCO_3 + B(OH)_4^- \rightarrow Ca(HBO_3) + HCO_3^- + H_2O \tag{2.6}$$

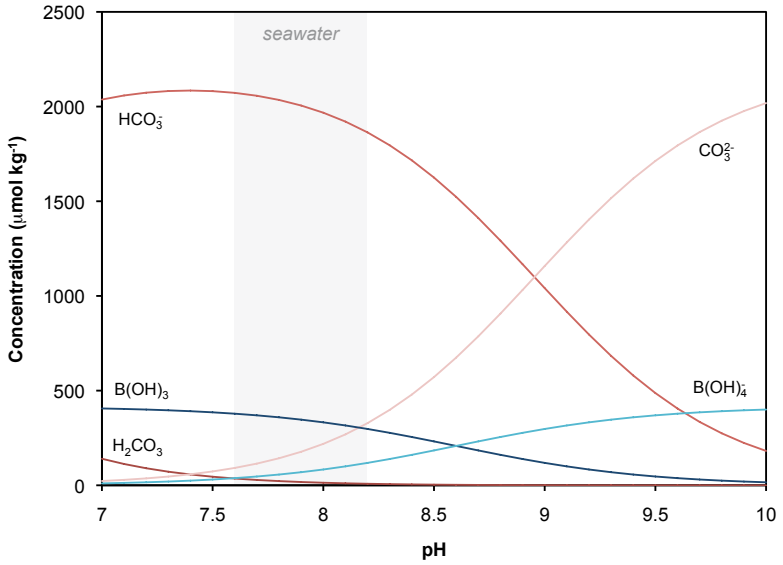

FIGURE 2.5: Speciation of ΣCO_2 and boric acid/borate with pH (25 °C, 35 PSU, ΣCO_2 = 2200 μmol kg^{-1}). Seawater total boron concentration was calculated by [B]total μmol kg^{-1} = 416 * S/35 (Uppström, 1974), pKB from DOE (1994), carbonate system disassociation constants from Millero and Roy (1997). Typical range of seawater pH (7.6-8.2) highlighted by the grey box.

The presence of HCO_3^- in equation 2.6 indicates that B/Ca ratios in $CaCO_3$ are likely to be influenced by both the activity of $B(OH)_4^-$ and HCO_3^- in seawater. The exchange distribution coefficient (D_B) for boron substitution in carbonate can be expressed as:

$$D_B = \frac{[HBO_3^{2-}/CO_3^{2-}]_{CaCO_3}}{[B(OH)_4^-/HCO_3^-]_{seawater}} \tag{2.7}$$

$$= \frac{[B/Ca]_{CaCO_3}}{[B(OH)_4^-/HCO_3^-]_{seawater}} \tag{2.8}$$

Hemming and Hanson (1992). CO_3^{2-} is replaced by Ca in equation 2.8 because their molar ratios are essentially in stoichiometric unity within $CaCO_3$ (Yu et al., 2007b). If the exchange distribution coefficient is constant, the B/Ca ratio in calcite can be used to determine pH (Figure 2.6).

Boron has two stable isotopes ^{11}B (80.18%) and ^{10}B (19.82%), the ratio of which is normally expressed in delta notation (in ‰) relative to NIST 951 ($^{11}B/^{10}B$ = 4.04367 (Catanzaro et al., 1970). There is a large isotopic fractionation between $B(OH)_4^-$ and $B(OH)_3$, with $B(OH)_3$ enriched in the heavier isotope. The fractionation factor between $B(OH)_4^-$ and $B(OH)_3$ (α_B),

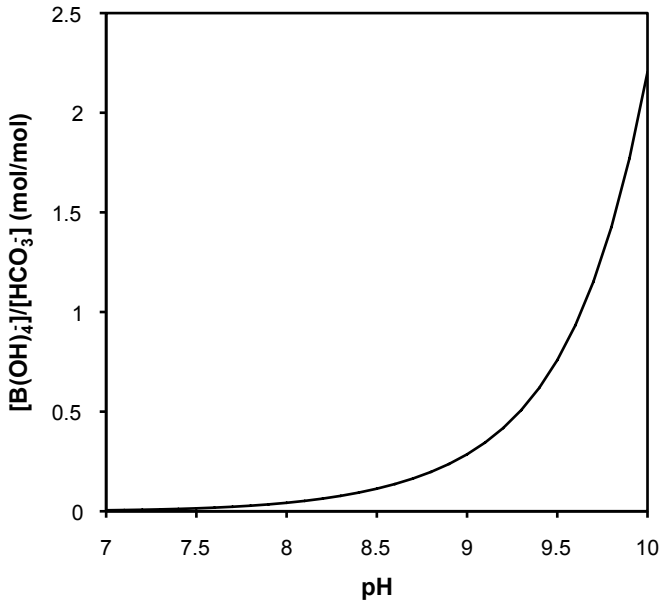

FIGURE 2.6: Molar ratios of borate and bicarbonate with pH (25 °C, 35 PSU, ΣCO_2 = 2200 μmol kg^{-1}). Seawater total boron concentration was calculated from by [B]total μmol kg^{-1} = 416 * S/35 (Uppström, 1974), pK_B (25 °C, 35 PSU) from DOE (1994), carbonate system disassociation constants from Millero and Roy (1997).

$$\alpha_B = \frac{^{11}B(OH)_3/^{10}B(OH)_3}{^{11}B(OH)_4^-/^{10}B(OH)_4^-} \tag{2.9}$$

has been measured at 1.0272 ± 0.0006 at 25 °C in artificial seawater (Klochko et al., 2006). As the proportions of $B(OH)_4^-$ and $B(OH)_3$ vary with pH, so too does the $\delta^{11}B$ of the $B(OH)_4^-$ and $B(OH)_3$ such that the sum of the two equals the isotopic composition of seawater ($\delta^{11}B_{sw}$) at 39.61 ‰ (Foster et al., 2010) (Figure 2.7). At low pH boron is almost entirely $B(OH)_3$ and $\delta^{11}B(OH)_3 \approx \delta^{11}B_{sw}$. At high pH boron is almost entirely $B(OH)_4^-$ and $\delta^{11}B(OH)_4^- \approx \delta^{11}B_{sw}$. As it is only the $B(OH)_4^-$ that is incorporated into calcite, $\delta^{11}B_{calcite}$ can be used to calculate pH if $\delta^{11}B_{sw}$ is known (Zeebe and Wolf-Gladrow, 2001) (Equation 2.10).

$$pH = pK_B - \log\left(-\frac{\delta^{11}B_{sw} - \delta^{11}B_{borate}}{\delta^{11}B_{sw} - (\alpha_B \times \delta^{11}B_{borate}) - 1000(\alpha_B - 1)}\right) \tag{2.10}$$

2.2.3 Uranium speciation in seawater

Uranium very soluble in well-oxygenated water as U(VI) and forms uranyl-carbonate complexes through the following reactions (Djogic et al., 1986; Krestou et al., 2003):

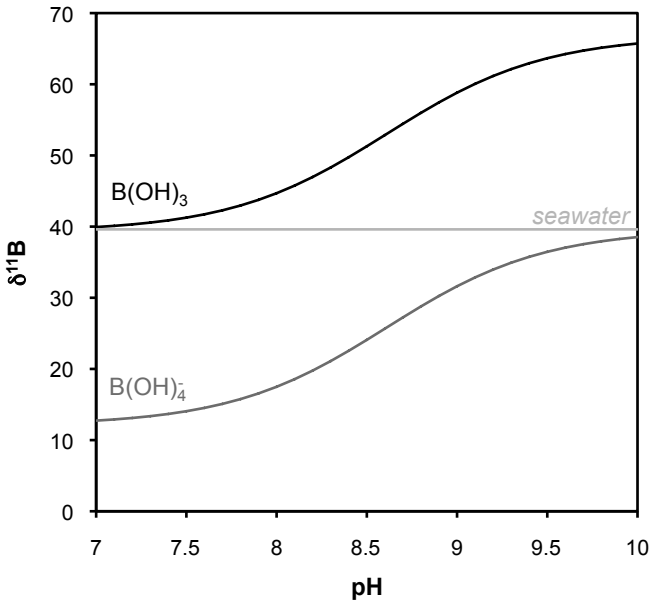

FIGURE 2.7: Effect of pH on the $\delta^{11}B$ of $B(OH)_4^-$ and $B(OH)_3$. pK_B (25 °C, 35 PSU) from DOE (1994), $\alpha_B = 1.0272$ from Klochko et al. (2006) and $\delta^{11}B_{sw} = 39.61‰$ from Foster et al. (2010).

$$UO_2^{2+} + CO_3^{2-} \leftrightharpoons UO_2CO_3 \tag{2.11}$$

$$UO_2CO_3 + CO_3^{2-} \leftrightharpoons UO_2(CO_3)_2^{2-} \tag{2.12}$$

$$UO_2(CO_3)_2^{2-} + CO_3^{2-} \leftrightharpoons UO_2(CO_3)_3^{4-} \tag{2.13}$$

The abundance of each complex is strongly dependent on $[CO_3^{2-}]$, with $UO_2(CO_3)_2^{2-}$ and $UO_2(CO_3)_3^{4-}$ being the predominant species in the pH range of seawater (Swart and Hubbard, 1982; Djogic et al., 1986; Krestou et al., 2003). Uranium may be incorporated into calcite by either replacing Ca^{2+} with UO_2^{2+}, or as a urynal-carbonate complex replacing one or more CO_3^{2-} ion (Swart and Hubbard, 1982; Russell et al., 2004).

2.3 Biomineralisation in foraminifera

Despite both the surface ocean and the interior ocean above the calcite saturation horizon being supersaturated in respect to calcite, kinetic constraints imposed by the high Mg^{2+} concentration of seawater inhibit the spontaneous precipitation of calcite (Morse and Mackenzie, 1990). Calcifying organisms must overcome these kinetic constraints during

biomineralisation of calcite, and the mechanisms underlying calcite biomineralisation are fundamental to understanding the incorporation of trace metals within foraminifera.

Radiotracer experiments have highlighted a large internal carbon pool in perforate foraminifera utilised for calcification (Kuile and Erez, 1987; Kuile et al., 1989b). Biological uptake of carbon has been demonstrated, showing that metabolic carbon enters both the internal carbon pool and skeleton (Kuile et al., 1989a). An internal Ca pool has also been observed within planktonic foraminifera, connected to small polarizing granules within the endoplasm (Anderson and Faber, 1984; Bentov and Erez, 2006). The existence of an internal carbon pool is thought to play a crucial role in controlling the trace metal partition coefficents between seawater and calcite (Elderfield et al., 1996; Erez, 2003).

Foraminifera secrete several discrete calcite layers during their lifetime, dependent on the number of chambers within the test (Reiss, 1957). Erez (2003) presents a two-phase working hypothesis for the biomineralisation of calcite in perforate foraminifera. During the primary phase of chamber formation the organism is partially separated from the environment by ectoplasmic pseudopods, before a cytoplasmic bulge is formed, acting as both an organic matrix and a template for nucleation. Granules composed of Ca, Mg, P provide Ca for the first $CaCO_3$ crystals, forming a 2-dimensional Mg-rich calcitic microspherulite wall embedded within the organic matrix. This initial high-Mg (>10 mmol/mol) primary calcitic lamellar represents only a small fraction of the calcite deposited during a growth instar.

In the second phase, vacuolised seawater is modified in the cytoplasm to reduce the Mg activity, and the intracellular pH is elevated to >9 (De Nooijer et al., 2009) (Figure 2.8). Carbon may enter the internal pool through either diffusion of CO_2 into the basic vacuoles, or direct CO_3^{2-} ion transportation across the membrane. In order to prevent the spontaneous precipitation of aragonite inside the vacuoles as pH increases (Zeebe and Sanyal, 2002), the total alkalinity and DIC must increase in a 1:1 relationship after pH reaches 8.5 ($\Omega_{Aragonite}$ is reached at pH ~9), or the organism must provide an inorganic/organic inhibitor to the vacuoles. Mg^{2+} may play a role in slowing the kinetics of $CaCO_3$ precipitation until the high pH vacuole reaches the site of biomineralisation, where Mg is complexed in a way to precipitate low-Mg calcite. The secondary, low-Mg (~3 mmol/mol), calcitic layer (covering the whole test) makes up around 90% of the newly deposited calcite.

A major criticism of 'vacuolised seawater' model of biomineralisation is that the number of Ca^{2+} ions required for the observed rate of calcification in foraminifera is far higher than the number available given the vacuole volume and the vacuolisation rate (Nehrke

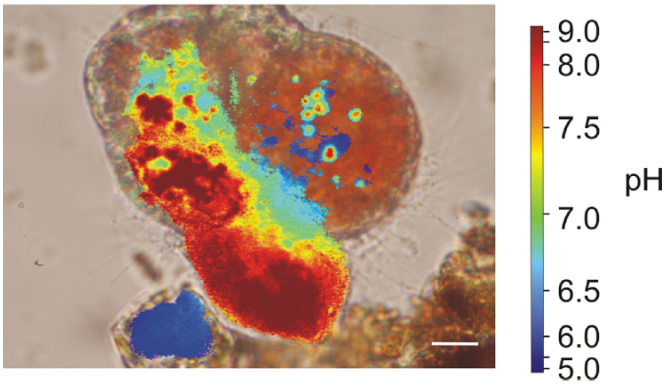

FIGURE 2.8: The pH of foraminiferal cytoplasm during calcification increases to >pH 9. Figure from De Nooijer et al. (2009).

et al., 2013; De Nooijer et al., 2014). Nehrke et al. (2013) instead suggest trans-membrane transport as the predominant transport path for Ca^{2+} during calcification.

2.3.1 Biological mediation of Mg uptake in foraminifera

Compared to Li, B and Sr, the uptake of Mg in foraminifera appears to have a much greater biological control; the biochemical mechanisms thought to be involved in regulating Mg uptake, and their effect on foraminiferal Mg/Ca are discussed briefly below.

Early studies demonstrated a strong temperature sensitivity of Mg/Ca in benthic and planktonic foraminifera. However, Mg/Ca ratios in foraminifera are 1-2 orders of magnitude lower and temperature dependence of Mg uptake is generally higher than inorganic calcite precipitates (Chave, 1954; Delaney et al., 1985). As with inorganic calcite Mg is present as $MgCO_3$ in foraminifera (Branson et al., 2013), however there are the significant differences in Mg concentration and temperature sensitivity between foraminiferal and inorganic calcite (Figure 2.9). These differences indicate a significant biological control on Mg uptake, and thus equilibrium thermodynamics cannot be directly applied to foraminiferal calcite (Lea et al., 1999; Anand, 2003). The Mg^{2+} content of foraminiferal calcite is much closer to the Mg^{2+} concentration of cytoplasm than seawater (Williams, 2008), suggesting most species of foraminifera have Mg^{2+} channels or pumps in order to actively remove Mg from vacuolized seawater against a large electrochemical gradient (de Nooijer et al., 2009). Mg/Ca values in benthic and planktonic foraminifera are in the same order of magnitude, indicating a similar biological control.

The offsets from inorganic equilibrium, or vital effects, observed within foraminifera are likely due to three main mechanisms during biomineralisation: (1) involvement of organic

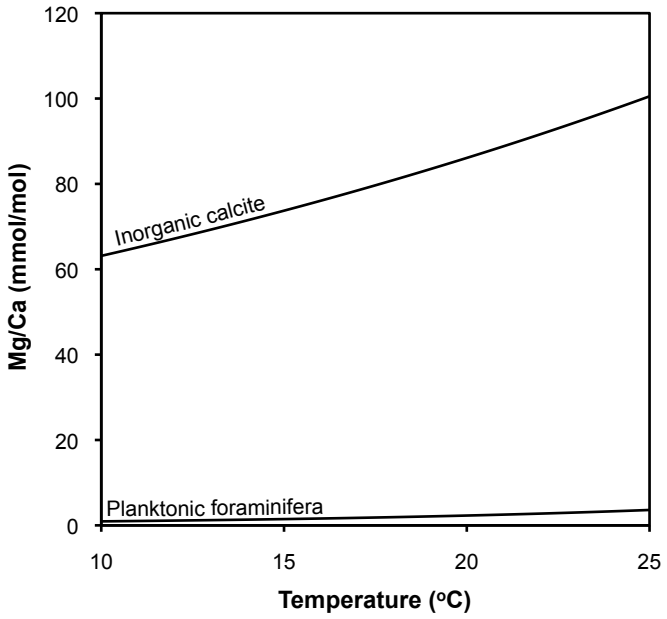

FIGURE 2.9: The thermal dependence of Mg partitioning into foraminiferal and inorganic calcite. Calculated using a D_{Mg} for inorganic calcite of $0.038exp(0.09T)$ (Oomori et al., 1987), the for multiple species of planktonic foraminifera of $0.009exp(0.0031T)$ (Anand, 2003), and a seawater Mg/Ca ratio of 5.15 mol/mol.

matrix in the precipitation process that may alter the D_{Mg} within biogenic calcite, (2) controlled conversion of transient amorphous phases to calcite, and (3) modification of Mg concentration in the parent solution. Whereas (1) and (2) are likely to increase Mg concentrations, (3) acts to lower Mg concentration in foraminiferal calcite (Bentov and Erez, 2006). Higher sensitivity of Mg/Ca ratios to temperature in foraminiferal calcite relative to inorganic calcite indicates temperature-dependant processes must play a role in biomineralisation, and it has been suggested this increased sensitivity may be due to a temperature-mediated increase in the proportion of the primary high-Mg phase (Bentov and Erez, 2006).

2.4 Biomineralisation in ostracods

Ostracods deposit $CaCO_3$ as a low-Mg (5−25 mmol/mol Mg/Ca) calcite carapace (Kesling, 1951), made up of small crystallites embedded in a chitanous/protein matrix (around 2-15 % of the carapace) (Rosenfeld, 1979). The carapace consists of two valves and is formed by two lateral folds of the epidermis, each fold having inner and outer lamellae. The valves are shed during each molt, with rapid calcification of new valves within several hours following molting (Chave, 1984). In podocopans, valves are secreted by the epidermis of the outer lamella and peripheral inner lamella (Horne et al., 2002).

^{45}Ca studies show that it is a simple process with no specialised cells, and in contrast to other Crustacea there is no re-absorption of Ca before molting (Turpen and Angell, 1971). The work of Keyser and Walter (2010) suggests that prior to molting, a large amount of calcium phosphate granules and chitin precursors are stored in the outer epidermal cells. Once released outside of the cell these calcium phosphate granules form amorphous $CaCO_3$ platelets that disintegrate into the $CaCO_3$ granules used to form the carapace.

Chapter 3

Development of trace element methodologies at UCL

This chapter details the development of methodologies to measure trace element/Ca ratios in biogenic carbonates at UCL. The analysis of trace element/Ca ratios forms a central part the research detailed in subsequent chapters, however before this research could be carried out trace element methodologies had to first be developed and tested at UCL. Other analytical methods used in this thesis are listed in the relevant chapters.

3.1 Standard preparation, acids and acid washing

All trace element/Ca ratio standards were prepared volumetrically using single element solution standards of known concentration. Optima grade HNO_3 and Millipore Milli Q 18 Ω water was used throughout. All volumetric flasks, standard bottles (PTFE), and microcentrifuge tubes were acid leached in HNO_3 at 80 °C for 48 hrs and rinsed five times with Millipore Milli Q 18.2 Ωwater. All standard and sample preparation took place in a laminar flow hood fitted with an American Air Filters International PTFE (low boron) HEPA filter.

3.2 ICP-OES analysis

Methods were developed to analyse Mg/Ca, Al/Ca, Mn/Ca, Fe/Ca and Sr/Ca by ICP-OES. The Varian 720 axial ICP-OES gives simultaneous coverage of wavelengths in the range 167 to 785 nm using an Echelle chip, with anti booming protection allowing the

simultaneous measurement of trace elements in the presence of a concentrated Ca matrix. Sample introduction is via peristaltic pump (0.48 mm tubing), low flow concentric glass nebuliser (Micromist 0.2 ml/min) and a glass cyclonic spray chamber. Instrument settings followed de Villiers et al. (2002), with wavelengths selected to minimise matrix effects (self absorbtion in the case of Ca) while maximising sensitivity. The detection limit, calculated as 3*standard deviation of the blank (Harris, 2010), was 3 ppb for Mg and 1 ppb for Sr.

Calcium is the most sensitive element in ICP-OES, resulting in both self absorption and high background counts (interferences) on other element lines (Ramsey et al., 1987). Line curvature has been observed within the relatively low concentrations typical of foraminifera (de Villiers et al., 2002). The use of the least sensitive Ca line (315.887nm) minimises line curvature, however signal suppression at typical foraminiferal and ostracodal Ca concentrations significantly impacts analysis of Mg/Ca and Sr/Ca ratios (Figure 3.1). Careful matrix matching of standards and samples is thus required for the accurate determination of Mg/Ca ratios. Long term analysis of calcite standard BSC-CRM 393 by ICP-OES gives a Mg/Ca value of 3.72±0.01 mmol/mol (RSD=0.3% at 60 ppm Ca) in very good agreement (±0.02 mmol/mol) with published values of Greaves (2005). Analysis of calcite standard PE3 gives a Mg/Ca value of 8.5±0.05 mmol/mol (RSD=0.6% at 5 ppm Ca) in very good agreement (±0.01 mmol/mol) with Dwyer et al. (1995).

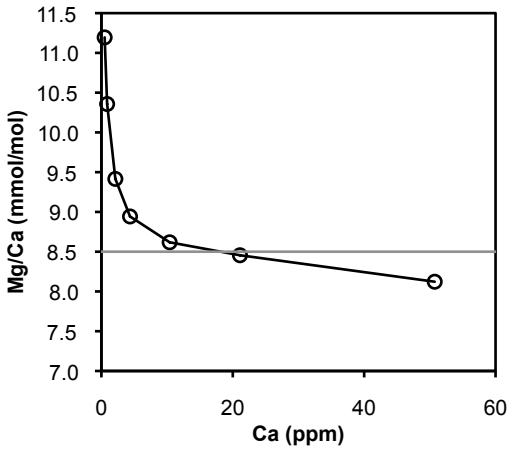

FIGURE 3.1: The effect of changing Ca concentration on the measured Mg/Ca ratio of calcite standard PE3. The published Mg/Ca ratio of 8.5 mmol/mol (Dwyer et al., 1995) is shown by the grey line.

3.3 ICP-MS analysis

ICP-MS is required for the analysis of Li, B, Cd and U due to their relatively low concentration in foraminifera. The Varian 820 MS is a quadrupole ICP-MS that allows the rapid and precise measurements of several elemental ratios over a wide range of atomic masses. Similarly to the ICP-OES method of de Villiers et al. (2002) the count ratio method of Yu (2005) utilises matrix matched Ca standards with varying trace elemental ratios. An aliquot of sample is initially measured in order to determine Ca concentration within the sample, before the samples are diluted to match the Ca concentration of the standards (typically 160 ppm) for trace element/Ca ratio analysis. The determination of elemental concentrations based on single masses assumes a similar isotopic distribution within a sample and standards. The isotopes selected for analysis where chosen to ensure maxiumum sensitivity, while avoiding polyatomic interferences. Build up of Ca on cones can lead to within run drift. In order to minimise this effect cones were Ca conditioned for ∼1hr before analysis using a pure 160 ppm Ca solution following Yu (2005). To avoid memory effects a rinse time of 3 mins was allocated between all samples. Blank and drift monitors are analysed between every five unknown samples and drift is corrected using a polynomial fit technique. No increase is seen in background boron counts through the course of the run (see section 3.6). The instrument was tuned regularly to ensure greatest signal/background ratio (rather than absolute signal) for the elements of interest, while CeO/Ce and Ba^{2+}/Ba^{+} were used to ensure oxides and doubly charged ions remained below 2%. Count ratio calibrations for selected elements of interest are shown in figure 3.2.

Interlaboratory calibrations were carried out by analysis of trace element standards at UCL, Cambridge (M. Greaves) and Cardiff (A. Morte Rodenas). Measure trace element/Ca ratios at UCL show very good agreement with both Cambridge (Figure 3.3) and Cardiff (Figure 3.4). Differences in intercept most likely relate to differences in blank concentrations between labs. Please note the Cd/Ca and U/Ca methodologies were not set up at UCL when the interlaboratory calibration took place with Cardiff.

3.4 Foraminiferal trace element cleaning protocol

The cleaning procedure outlined below is a version of the foraminiferal trace element cleaning procedure developed by Boyle and Keigwin (1985).

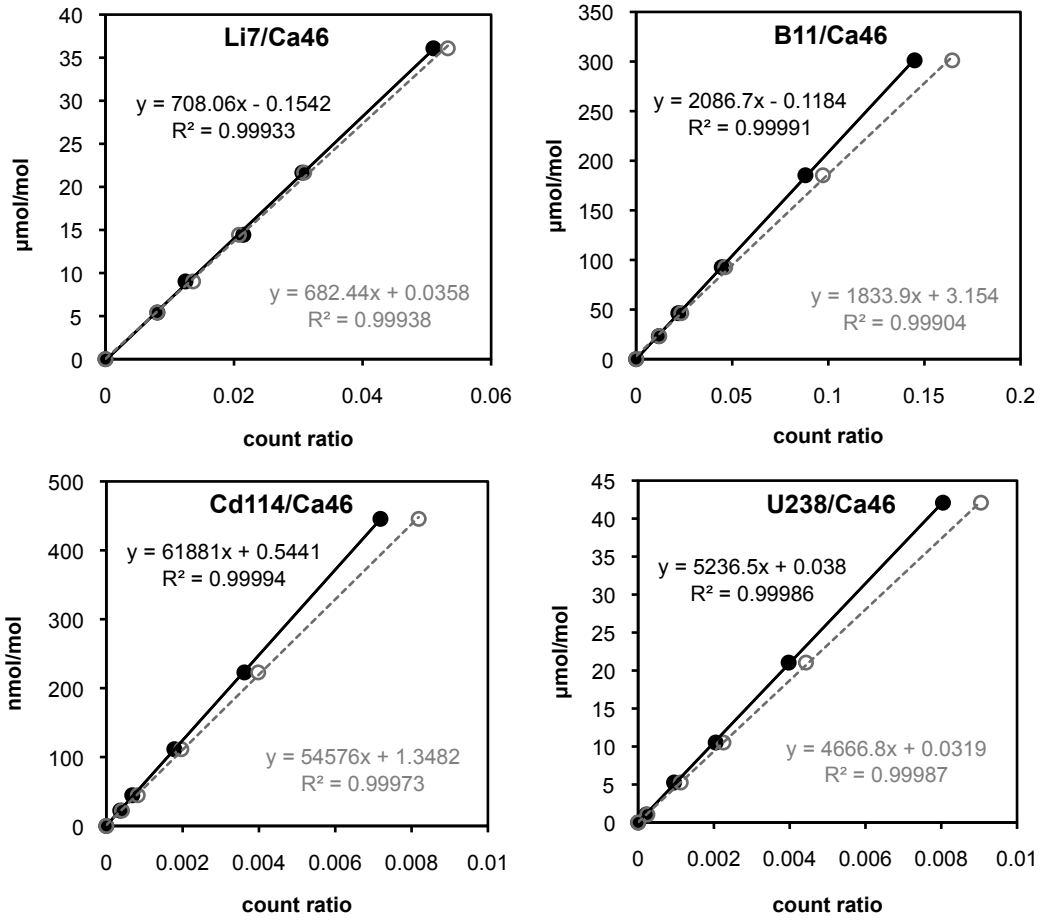

FIGURE 3.2: Count ratio calibrations for selected elements of interest using the UCL (2014) trace element standards at 160 ppm Ca (black) and 80 ppm Ca (grey) to highlight the effect of the Ca matrix.

3.4.1 Chamber opening and visible particulate removal

Place foraminifera on a clean microscope slide and submerge in a few drop of Milli Q (or similar ultrapure) water. Using a second microscope slide apply pressure to the foraminifera until all the chambers are open, being careful not to over crush the sample. Remove any visible non-calcite particulates using a soft hair paintbrush under a transmitted-light microscope. Transfer crushed sample to an acid-leached 600µl micro-centrifuge tube.

3.4.2 Clay removal

Add 300µl of Milli Q into the micro-centrifuge tube. Tap micro-centrifuge tubes firmly to ensure all calcite fragments settles to the bottom. Place in ultrasonic bath for 30s (increase to 60s if samples are large or robust benthics). Using an acid-leached pipette

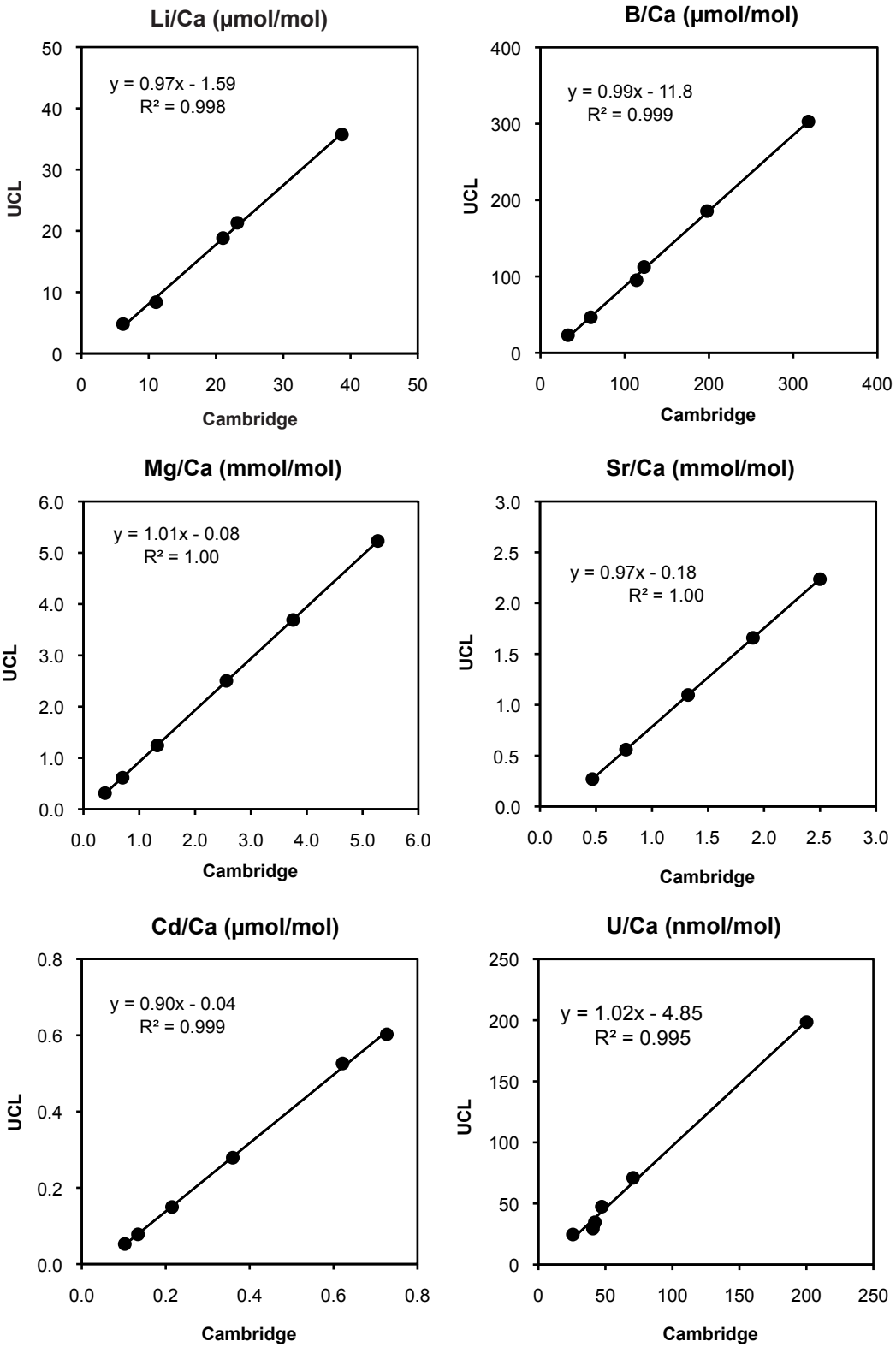

FIGURE 3.3: Comparison of measured trace element/Ca ratios of solution standards at UCL and Cambridge.

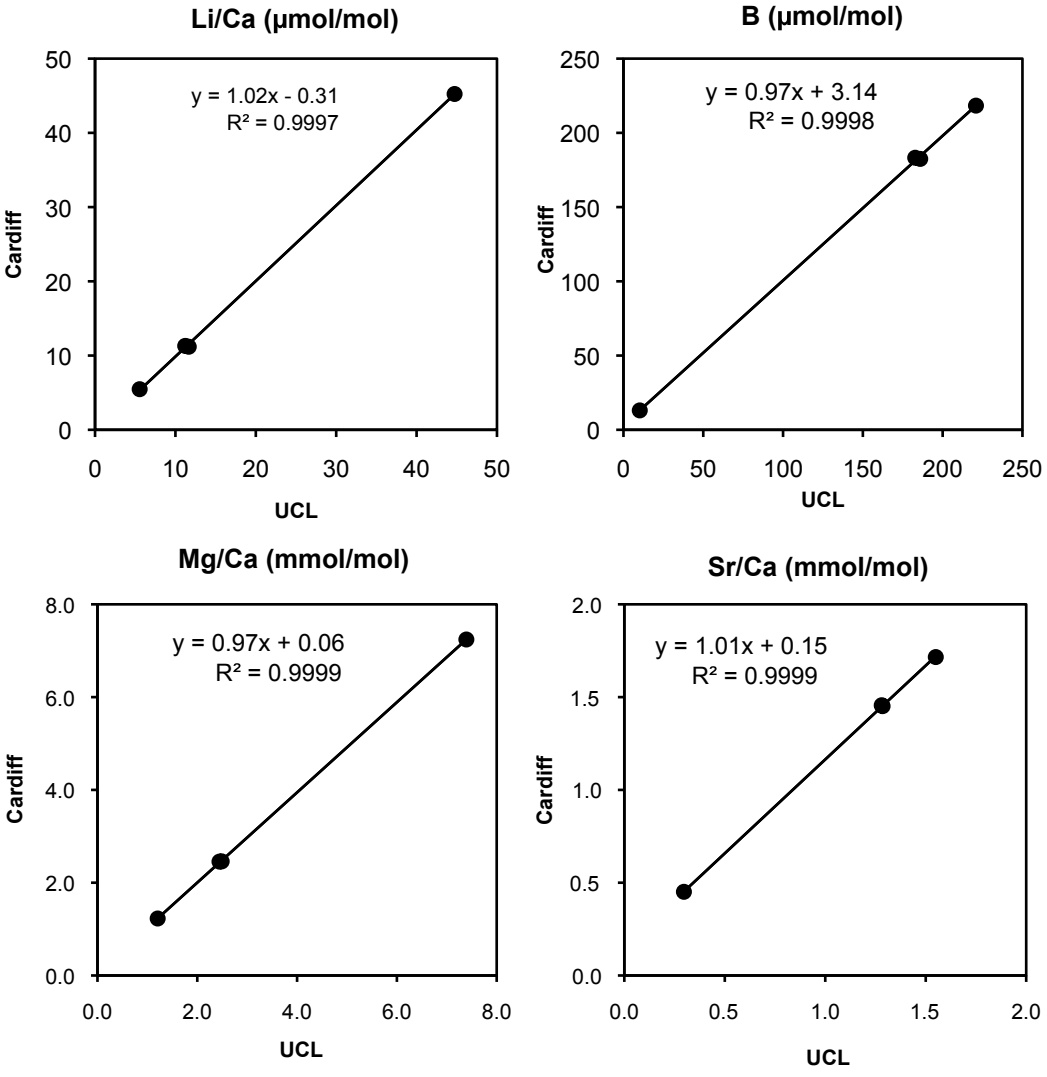

FIGURE 3.4: Comparison of measured trace element/Ca ratios of solution standards at UCL and Cardiff.

tip, re-circulate Milli Q within the micro-centrifuge tube to re-suspend clays before removing. Repeat sonication in Milli Q two more times. Add 500µl of trace metal grade methanol into the micro-centrifuge tube. Tap micro-centrifuge tubes firmly to ensure all calcite fragments settles to the bottom. Place in ultrasonic bath for 30s (or 60s). Using an acid-leached pipette tip, re-circulate methanol within the micro-centrifuge tube to re-suspend clays before removing. Repeat sonication with methanol one more time. Add 500µl of Milli-Q water and repeat sonication step. Remove Milli Q water with an acid-leached pipette tip. Rinse once with 500µl of Milli Q water. Increase number of methanol steps if sediments are clay-rich.

3.4.3 Fe-Mn oxyhydroxide coating removal

Add 100µl of hydrous hydrazine/ammonium citrate solution (150µl of 20 M $N_2H_4 \cdot H_2O$ + 2ml of 15M NH_4OH and 2ml of $(NH_4)_2C_6H_8O_7$. The $(NH_4)_2C_6H_8O_7$ solution should be prepared prior to cleaning by adding 25g of citric acid to 500ml of 15M ammonium hydroxide solution in an ice bath. Secure microcentrifuge caps tightly and place in hot water bath at 80 °C for 30 mins, flipping and sonicating for ∼2 s every 2 mins. Remove micro-centrifuge tubes from the hot water bath and remove the hydrous hydrazine/ammonium citrate solution with an acid-leached pipette tip. Rinse three times with 500µl of Milli Q water, ensuring insides of the caps are also rinsed.

3.4.4 Organic matter removal

Add 250 µl of buffered hydrogen peroxide (prepared with 10ml of 0.1 M NaOH and 100µl of 30% H_2O_2) to the micro-centrifuge tubes and secure caps tightly. Place in hot water bath at 90 °C for 10 mins, flipping once at 5 mins to ensure maximum contact between the sample and reagent. Remove micro-centrifuge tubes from the hot water bath and rap firmly until all visible bubbles are gone (this ensures less sample is lost when removing the buffered hydrogen peroxide solution). Remove the buffered hydrogen peroxide with an acid-leached pipette tip. Rinse three times with 500µl of Milli Q water.

Transfer the sample into a new acid leached 600µl micro-centrifuge tube using an acid-leached 100µl pipette tip with the bottom $1/8^{th}$ removed. Rinse with 500µl of Milli-Q water. Check sample sizes and add either 100 µl (if small sample) or 200 µl (if large sample) of 0.001 M Optima HNO_3 to the samples. Fill to 500 µl volume with Milli Q water before removing the HNO_3/Milli Q with an acid-leached pipette tip. Rinse one final time with 500 µl Milli Q and ensuring as little solution remains in the microcentrifuge tubes as possible.

3.4.5 Sample transfer and acid leach

3.5 Interlaboratory foraminiferal trace element/Ca comparison

Differences in cleaning and analytical procedure have the potential to cause significant varibility in measured trace element/Ca ratios between laboratories (Martin, 2002; Barker, 2003; Rosenthal, 2004). In order to assess the foraminiferal cleaning and

analytical procedures at UCL foraminiferal samples with previously publised trace element/Ca ratios were re-analysed at UCL. *Uvigerina peregrina* with previously published Mg/Ca and Li/Ca data from Bryan and Marchitto (2008), and *Globigerinoides ruber* and *Globigerinoides sacculifer* with previously published Mg/Ca data from Dekens (2002) were reanalysed at UCL using the cleaning and analytical methods described above, ensuring the same foraminiferal size fraction was used. The previous studies were chosen as both studies used reductive cleaning, thus minimising the potential of cleaning related offsets. Foraminiferal Mg/Ca ratios measured at UCL show very good agreement with previously published results (Figure 3.5). Li/Ca ratios measured at UCL also show good agreement (Figure 3.6), despite the low Li/Ca range in the comparison study.

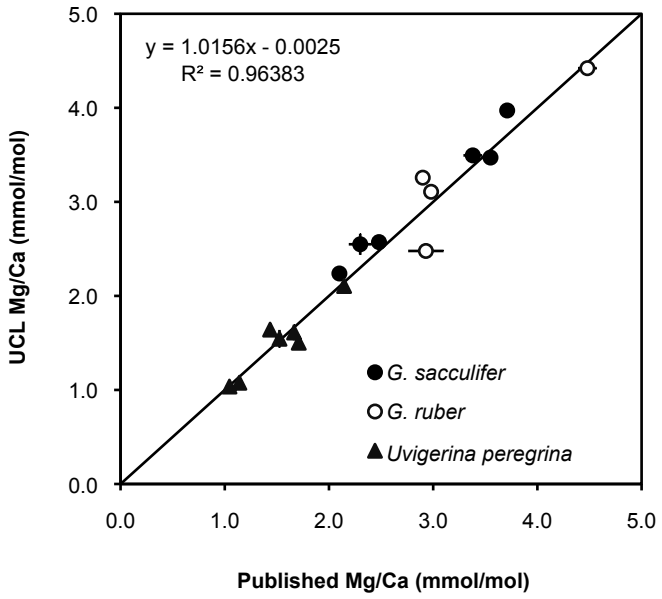

FIGURE 3.5: Comparison of UCL and previously published foraminiferal Mg/Ca ratios. Published data are from Bryan and Marchitto (2008) and Dekens (2002). The 1:1 line is shown in black. The regression line is also shown but is not visible as it is indistinguishable from the 1:1 line.

3.6 Boron blanks

High background counts and long memory effects are known to impact the analysis of boron (Al-Ammar et al., 1999). A quartz spray chamber was used to minimise boron blanks following Yu (2005). In order to overcome memory effects a long rinse time of 3 minutes at a higher perastaltic pump speed was used. It was found that the best rinseout and lowest blanks was achieved using relatively dilute (0.01 M) but high quality (Optima grade) HNO_3. While the boron blank is relatively high (<300 ppt), it remains

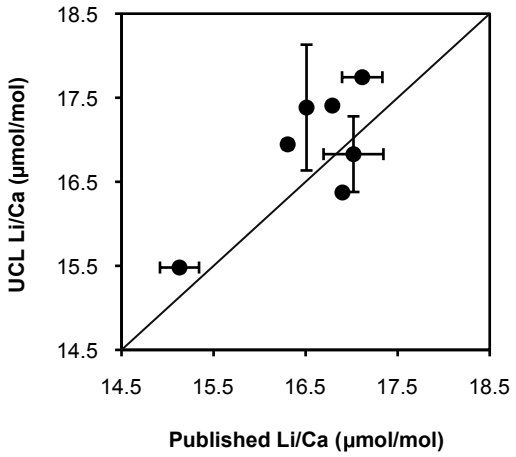

FIGURE 3.6: Comparison of UCL and previously published foraminiferal Li/Ca ratios. Published data are from Bryan and Marchitto (2008). The 1:1 line is shown in black.

~10 times lower than typical *Uvigerina* (a low boron genera) samples analysed in this study (B/Ca = 20 µmol/mol, 160 ppm Ca), and is remarkably consistent through the duration of a run, resulting in an equivalent detection limit of ~5 µmol/mol at 160 ppm Ca.

While previous tests had shown the total procedural blank (TBP), which is the blank following the full foraminiferal cleaning procedure, to be equal to that of the acid blank, during a long run of foraminiferal samples it was discovered that the TPB systematically increased over the course of the run while the acid blank remained constant (Figure 3.7). The TPBs had been cleaned over the course of three days, and analysed in order they had been cleaned. While the increase was sytematic and highly predictable, and could thus be corrected for, the correction becomes a significant part of the total boron within small samples towards the end of the run (up to ~25%). A series of tests was conducted to determine the source of the boron contamination.

The possibility that the boron contamination was due to analytical reagents was examined by running TBPs with varying amounts of $(NH_4)_2C_6H_8O_7$ and NaOH. There was no difference in B concentration within TPBs cleaned with different amounts of reagents (Figure 3.8), indicating the contamination was not from the analytical reagents.

The systematic nature of the B increase with run time, and the initial similarity of the acid blank and TPB suggests the addition of boron to the TBPs occurs during the run. During ICP-MS analysis the samples are housed in a ESI SCµ microautosampler fitted with a perspex cover, and this is the only time the samples are exposed to the atmosphere for a significant period of time. The amount of boron accumulation that occurs from inside the autosampler cover was investigated by exposing the acid

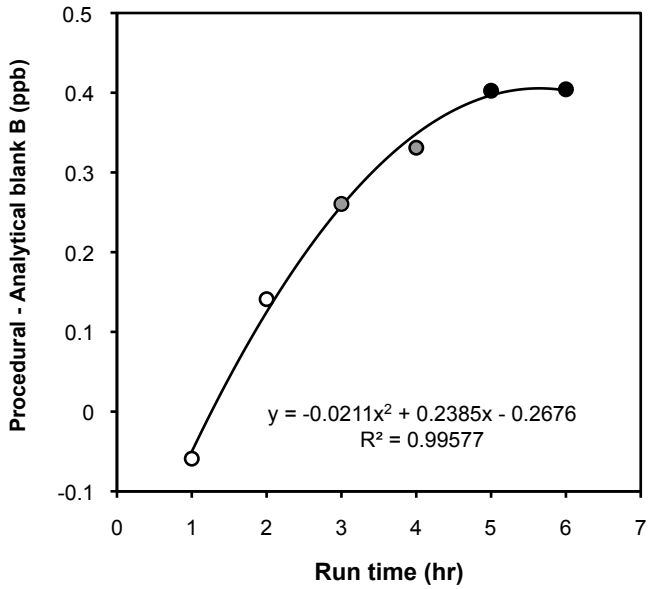

FIGURE 3.7: Total procedural blank increase relative to the acid blank over the course of a run. TPBs cleaned during day 1 are shown by the open symbols, day 2 by the grey symbols and day 3 by the black symbols.

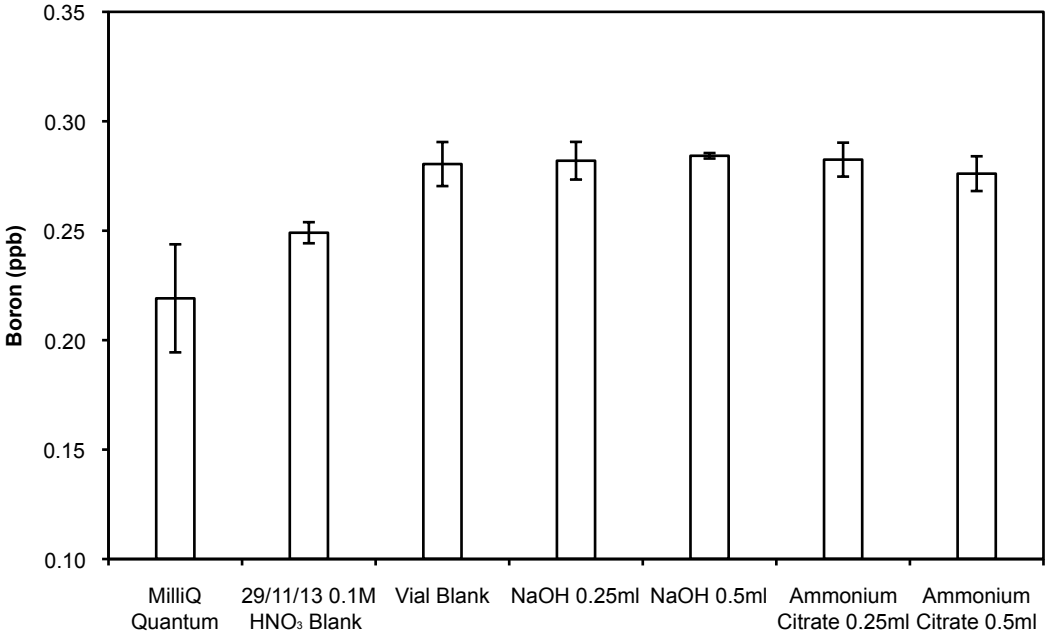

FIGURE 3.8: Boron concentration in total procedural blanks cleaned with varying volumes of the main analytical reagents.

blank to the atmosphere within the autosampler cover for varying amounts of time. 600 µl microcentrifuge tubes containing 500 µl of 0.1 M Optima HNO_3 were exposed to the atmosphere within the autosampler cover, which contained open foraminiferal trace element standards within it to replicate the conditions during a run of samples. Acid blanks were also exposed directly to the atmosphere of the ICP-MS lab as a control. Figure 3.8 shows that the boron concentration within the acid blanks increases systematically with exposure time, and while most of the accumulation is coming from the ICP-MS lab air, the rate of boron accumulation is higher within the autosampler cover than in the atmosphere of the lab. As boron is volatile, the increased rate of boron accumulation within the autosampler cover is most likely due to the evaporation of boron from the trace element standards and re-deposition within the microcentrifuge tubes. The increase is not observed within the acid blank (also exposed to the atmosphere of the autosampler cover) as the ratio of the exposure area (the opening) to the volume of the PTFE acid blank container is significantly lower than the exposure area/volume ratio of the microcentrifuge tubes. The rate of B increase observed in figure 3.9 is 0.01 ng/hr, similar, although slightly lower than the rate of 0.035 ng/hr observed in figure 3.7, suggesting the accumulation of airborne B is the source of the increase observed in figure 3.7. The difference in accumulation rate between the two studies may relate to the use of the autosampler probe in the initial study, which would reduce the surface tension of the trace element standards while entering and leaving the solutions, thus making B more volatile. In order to reduce boron contamination during ICP-MS analysis at UCL microcentrifuge tubes should be opened in small batches (∼10) for analysis, and a minimal number of trace element standards should be left open within the autosampler cover during the analysis of samples.

Unfortunately as I analysed the first acid blank at the start of a run of samples and TPBs I had cleaned as the final test of the method outlined above before commencing with down core analysis, I discovered that the instrument had been contaminated with significant levels of boron (and lithium) from a lithium-borate fusion. The contamination from the lithium borate fusion was so great that the boron counts in the blank now saturated the detector, making the steps to reduce the 0.2 ng B increase from 8 hrs of airfall somewhat unnecessary. The contamination from the lithium-borate fusion rendered the ICP-MS at UCL unusable for the analysis of Li and B in foraminifera. All subsequent trace element determinations (constituting the data for chapters 6 and 7) were conducted on a Thermo Finnigan Element II HR-ICP-MS at Cardiff University; the method used for these analyses is listed in section 6.2.

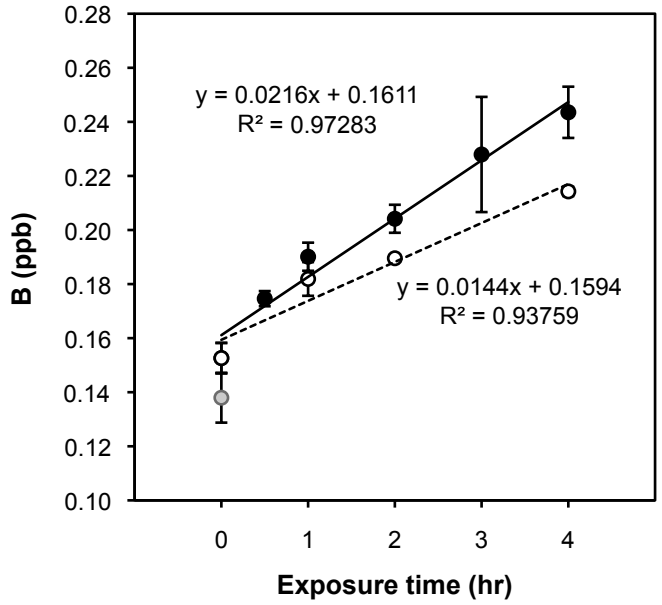

FIGURE 3.9: Boron concentration with exposure time to the atmosphere. The grey circle is the acid blank, the open circles are vial blanks that have been exposed to the atmosphere of the ICP-MS lab, and the black symbols are vial blanks that have been exposed to the atmosphere within the autosampler cover with open trace element standards inside.

3.7 *Krithe* trace element cleaning protocol

The cleaning procedure outlined below is a version of the foraminiferal trace element cleaning procedure developed by Boyle and Keigwin (1985), modified to account for the lower weight and increased fragility of single ostracod valves, with the exception of step 3.7.1 which was developed for cleaning non-marine ostracod valves by Chivas et al. (1983).

3.7.1 Visible particulate removal *(B)*

Place valve on microscope slide and submerge in a few drops of trace metal grade ethanol. Remove all visible particulates using a soft hair paintbrush under a transmitted-light microscope. Unlike foraminifera, ostracods do not have closed chambers and it is not necessary to crush the valves during cleaning. Rinse with Milli Q (or other ultra high quality) water and transfer to acid-washed 600µl micro-centrifuge tubes.

3.7.2 Clay removal *(S)*

Add 500µl of trace metal grade methanol into the micro-centrifuge tube. Tap micro-centrifuge tubes firmly to ensure ostracod valve settles to the bottom. Place in ultrasonic bath for 60s (reduce to 30s if valves are small/fragile). Using an acid leached pipette tip, re-circulate methanol within the micro-centrifuge tube to re-suspend clays before removing the methanol. Add 500µl of Milli Q water. Place in ultrasonic bath for 30s. Remove Milli Q water with an acid leached pipette. Rinse once with 500µl of Milli Q water. Increase number of methanol steps if sediments are clay-rich.

3.7.3 Fe-Mn oxyhydroxide coating removal *(R)*

Add 50µl of hydrous hydrazine/ammonium citrate solution (150µl of 20 M $N_2H_4 \cdot H_2O$ + 2ml of 15M NH_4OH and 2ml of $(NH_4)_2C_6H_8O_7$. The $(NH_4)_2C_6H_8O_7$ solution should be prepared prior to cleaning by adding 25g of citric acid to 500ml of 15M ammonium hydroxide solution in an ice bath. Secure microcentrifuge caps tightly and place in hot water bath at 80 °C for 10 mins, flipping once at 5 mins. Remove micro-centrifuge tubes from the hot water bath and remove the hydrous hydrazine/ammonium citrate solution with an acid leached pipette tip. Rinse three times with 500µl of Milli Q water.

3.7.4 Organic matter removal *(O)*

Add 100 µl of buffered hydrogen peroxide (prepared with 10ml of 0.1 M NaOH and 100µl of 30% H_2O_2) to the micro-centrifuge tubes and secure caps tightly. Place in hot water bath at 90 °C for 5 mins, flipping once at 2.5 mins to ensure maximum contact between the sample and reagent. Remove micro-centrifuge tubes from the hot water bath and siphon off the buffered hydrogen peroxide with an acid leached pipette tip. Rinse three times with 500µl of Milli Q water.

Chapter 4

Evaluation of foraminiferal trace element cleaning protocols on the Mg/Ca of marine ostracod genus *Krithe*

A version of this chapter has been published in Chemical Geology.

Gray, W., Holmes, J., Shevenell, A. (2014) Evaluation of foraminiferal trace element cleaning protocols on the Mg/Ca of marine ostracod genus *Krithe*. *Chemical Geology* 382, 14-23.

4.1 Introduction

The oxygen isotope ($\delta^{18}O$) composition of marine calcite ($CaCO_3$) is a standard proxy for past climate and oceanographic change. However, the ratio of $^{18}O/^{16}O$ in the $CaCO_3$ of marine calcifiers is controlled by both calcification temperature and the $\delta^{18}O$ of the seawater ($\delta^{18}O_{sw}$) in which calcification occurred (see review in Bemis et al. 1998). For decades paleoceanographers have focused on deconvolving the temperature and $\delta^{18}O_{sw}$ signals preserved in marine $CaCO_3$ to better understand past climate forcings and feedbacks (e.g. global ice volume, surface and deep ocean temperatures, and local salinity) (Shackleton, 1967; Schrag et al., 1996; Elderfield and Ganssen, 2000). The Mg/Ca of marine $CaCO_3$ is a robust and commonly employed paleotemperature proxy (Dwyer et al., 1995; Nürnberg et al., 1996; Rosenthal et al., 1997; Lea et al., 1999;

Elderfield and Ganssen, 2000; Lear et al., 2000), with the thermal dependence of Mg uptake into marine $CaCO_3$ first demonstrated by Chave (1954). Importantly, Mg/Ca and $\delta^{18}O$ can be measured on the same marine $CaCO_3$, allowing the simultaneous reconstruction of temperature and seawater $\delta^{18}O$ (Lea, 2000; Lear et al., 2000). Mg/Ca ratios in marine carbonates are also influenced by the activity of Mg and Ca in seawater. Due to the long residence times of Ca and Mg in the ocean (1 and 12 Myr, respectively), seawater Mg/Ca may be considered constant on timescales of ~1Myr. Over longer timescales past ocean temperatures may be reconstructed with knowledge of past seawater [Ca] and [Mg] (Lear et al., 2000; Shevenell et al., 2004; Coggon et al., 2010).

Bottom water temperature (BWT) reconstructions based on Mg/Ca ratios in marine carbonates may provide important insights into past ocean circulation changes, ocean heat transport, ice volume, and seawater carbonate chemistry. While benthic foraminiferal Mg/Ca is most often employed as a BWT proxy (Lear et al., 2000, 2010; Martin et al., 2002; Elderfield et al., 2006; Marchitto et al., 2007b), the Mg/Ca of marine ostracod calcite has also been established as a BWT proxy at temperatures between -1.5 and 16 °C (Chave, 1954; Dwyer et al., 1995; Elmore et al., 2012; Farmer et al., 2012). Ostracods are benthic crustaceans that molt their $CaCO_3$ valves every 1-3 days and are often recovered where suitable benthic foraminifera taxa are limited or absent. They have a higher overall Mg concentration than benthic foraminifera, and also generally a higher Mg/Ca-temperature sensitivity, as well as exhibiting species-specific Mg/Ca-temperature relationships (Turpen and Angell, 1971; Dwyer et al., 1995, 2002; Farmer et al., 2012).

To date, marine ostracod paleotemperature research has focused on the genus *Krithe*, due to its relatively smooth carapace structure, which makes it less prone to contamination, its ubiquitous geographic and depth (150-4000m) distribution, resistance to dissolution (Swanson and Van der Lingen, 1994), and long duration in the marine stratigraphic record (97.5 Ma to present) (Cadot and Kaesler, 1977; Coles et al., 1994; Dwyer et al., 1995, 2002; Elmore et al., 2012; Farmer et al., 2012). Core top calibration studies of Mg/Ca in Krithe versus calcification temperature document both linear and exponential relationships (Dwyer et al., 2002; Elmore et al., 2012; Farmer et al., 2012), and *Krithe* Mg/Ca has been applied downcore in numerous orbital and millennial scale BWT reconstructions in the North Atlantic and Arctic Oceans (Dwyer et al., 1995, 2000; Cronin et al., 2012). While temperature is thought to be the primary driver of Mg incorporation in *Krithe*, the influence of seawater carbonate ion saturation (ΔCO_3^{2-}) on *Krithe* Mg/Ca is debated. Elmore et al. (2012) proposed a ΔCO_3^{2-} effect at low temperatures (<3 °C), while Farmer et al. (2012) concluded that ΔCO_3^{2-} state does not influence Mg uptake in *Krithe*.

4.1.1 Mg contaminants and cleaning procedures

Sedimentary contaminants, including clays, organic matter, and iron- and manganese-rich oxyhydroxide coatings (Mn-Fe oxyhydroxides), have the potential to bias elemental ratios in ostracod $CaCO_3$. Yet, rigorous reductive-oxidative trace element cleaning protocols developed for foraminifera (Boyle, 1981; Boyle and Keigwin, 1985; Lea and Boyle, 1991; Hastings et al., 1996) are not traditionally employed in marine ostracod-based paleotemperature studies because ostracod valves are not composed of enclosed chambers and thus, are thought to be less prone to contamination (Cronin et al., 2005). However, as in foraminifera, the morphological features of *Krithe* (e.g., lips, canals, and pores) may also trap clays and organic material, introducing the potential for contamination.

Marine clays (e.g., illite, kaolinite, montmorillonite, and chlorite) contain 1-10 % Mg by weight (Riley and Chester, 1971; Barker, 2003). In foraminiferal-based trace element cleaning protocols, clays are removed using multiple methanol/deionised-water sonication steps (Boyle and Keigwin, 1985; Barker, 2003). Four approaches have been used to remove clays in ostracod-based Mg/Ca studies; (i) rinsing with ethanol using a fine haired-brush (Chivas et al., 1983); (ii) sonication in ethanol (Correge, 1993); (iii) sonication in deionised water (Dwyer et al., 1995; Farmer et al., 2012); (iv) sonication in deionised water and methanol (Elmore et al., 2012). Incomplete removal of clays has the potential to introduce significant errors in analyses of deep-sea benthic ostracods, where BWTs are cold and Mg/Ca ratios are typically low. For example, the presence of 0.05 µg of clay (∼10% Mg w/w) could increase the Mg/Ca-derived temperature of a typical adult *Krithe* valve (average $CaCO_3$ weight: ∼20 µg; average Mg/Ca of ∼12 mmol/mol) by ∼1 °C, which is significant given the low range in BWTs typical of deep-sea locations and the *Krithe* paleotemperature calibration error of ±0.3 °C.

Organic matter may also provide a source of Mg, from both the organic matter itself, and from adhering clay particles (Hastings et al., 1996; Barker, 2003). The chitin matrix of ostracod valves, in which the calcite is embedded, also contains significant levels of Mg (Chivas et al., 1983). To oxidise organic matter, foraminiferal trace element cleaning protocols include an alkali-buffered hydrogen peroxide step (Boyle, 1981; Boyle and Keigwin, 1985). Marine ostracod studies have oxidised organic matter by; (i) a multi-day soak of bulk sediment in 3% hydrogen peroxide (Correge, 1993); (ii) soaking valves overnight in a 5% NaClO solution (Dwyer et al., 1995; Farmer et al., 2012), which has been shown to have no effect on the Mg/Ca ratio of inorganic spar calcite (Dwyer et al., 2002), and effectively removes organic matter without causing $CaCO_3$ dissolution (Gaffey and Bronnimann, 1993); and (iii) application of the alkali-buffered hydrogen

peroxide step (Elmore et al., 2012), originally developed for foraminifera (Boyle, 1981; Boyle and Keigwin, 1985).

Fe-Mn oxyhydroxide coatings form on marine biogenic calcite under suboxic sedimentary conditions below the Mn redox boundary or when Mn^{2+} is remobilised in sediments (Lynn and Bonatti, 1965; Froelich et al., 1979). Boyle (1981, 1983) concluded Fe-Mn oxyhydroxide coatings were a significant source of trace element contamination in foraminiferal $CaCO_3$ when Mn/Ca ratios were <0.1 mmol/mol. Thus, the standard foraminiferal trace element cleaning protocol employs a reductive (hydrazine) treatment step to remove Fe-Mn oxyhydroxide coatings from foraminifera (Boyle and Keigwin, 1985).

While the reductive step has been questioned for foraminiferal Mg/Ca studies due to the partial dissolution of $CaCO_3$ (Barker, 2003; Barker et al., 2005; Vetter et al., 2013), laser ablation of individual foraminifera has revealed both $MnCO_3$ coatings with Mg/Ca ratios up to 50 mmol/mol (Pena, 2005), and regions of high Mn, Fe and Mg on the calcite surface (thought to be Fe-Mn oxyhydroxides) (Pena et al., 2008). Moreover, a flow-through method developed to sequentially leach contaminant phases before dissolving foraminiferal calcite demonstrated the presence of Mn-oxide coatings containing high levels of Mg (Benway et al., 2003; Haley and Klinkhammer, 2002), further highlighting the importance of reductive cleaning in foraminiferal Mg/Ca studies.

With the exception of one recent study of *Krithe* Mg/Ca (Elmore et al., 2012), the reductive cleaning step is not routinely employed to remove Fe-Mn oxyhydroxide coatings in ostracod Mg/Ca studies because the higher concentrations of Mg in ostracods compared with foraminifera suggests that the Mg associated with Fe-Mn oxyhydroxide coatings may not affect ostracod Mg/Ca as profoundly as in foraminiferal studies (Elmore et al., 2012). This hypothesis is supported for lacustrine ostracods (Jin et al., 2006), but has not been adequately assessed in the marine environment (Elmore et al., 2012), where the sedimentary redox conditions under which Fe-Mn oxyhydroxide coatings form are widespread.

Reconstructions of BWTs using the Mg/Ca of ostracod valves are typically based on multiple, single-shell trace element determinations at each individual stratigraphic horizon. Not unexpectedly, inter-valve variability at each horizon is pronounced (Dwyer et al., 2002). Along with physiological, environmental and taphonomic factors, contamination resulting from incomplete or improper removal of Mg-rich sedimentary contaminants may cause the observed variability (Holmes, 2008). The existing global *Krithe* Mg/Ca-temperature calibration comprises datasets made up of values cleaned by three different cleaning protocols, as outlined above. To improve the utility of the

Krithe Mg/Ca paleothermometer a systematic study of the sequential cleaning steps on ostracod calcite is required.

The most common Mg-bearing marine clay minerals also contain Al and Fe, and Fe-Mn oxyhydroxide coatings comprise Fe and Mn. Al/Ca, Fe/Ca and Mn/Ca ratios are routinely measured in foraminiferal trace element studies as indicators of clay and Fe-Mn oxyhydroxide contamination (Boyle, 1981, 1983; Barker, 2003). In this study foraminiferal cleaning procedures are applied to individual *Krithe* valves, and use Al/Ca, Fe/Ca and Mn/Ca ratios to monitor contamination from clays and Fe-Mn oxyhydroxide coatings in order to (1) evaluate the effects of contamination as a bias on Mg/Ca ratios in *Krithe*, and (2) assess the efficacy of foraminiferal trace-element cleaning procedures on the removal of contamination, and the effect of these procedures on valve chemistry.

4.2 Study Location and Methodology

4.2.1 Site selection and sample preparation

This study is based on core top (0-2 cm) sediments from a box core (OCE205-50BC; 26.23 °N, 77.7 °W) raised from 817m of water, west of Great Abaco, Bahamas. The site has a BWT of 8.4 °C (Slowey and Curry, 1995), and bottom-waters have a dissolved oxygen content of ∼150 µmol/kg (Key, 2004). The core was chosen to give bottom-water temperature and redox conditions representative of deep-sea paleoceanographic studies, while ensuring sufficient numbers of well-preserved *Krithe* were present for the study. Benthic foraminifera in the coretop have $\delta^{18}O$ values expected from the measured seawater $\delta^{18}O$ value and BWT at the site, indicating the sediment is of late-Holocene age (Slowey and Curry, 1995). Furthermore, the presence of complete *Krithe* carapaces and other ostracod species with remaining setae suggests the ostracods were living close to the time of collection.

Sediments were washed through a 63µm sieve and the residues were oven dried. To eliminate potential Mg-variability associated with species and gender, only male adult and A-1 juvenile (the final molt stage before adult) *Krithe pernoides* valves were selected for analysis (Coles et al., 1994) (Fig. 4.1). Valve length and height were measured using a stage micrometer and valves were classified as adult or A-1 juvenile according to the criteria of McKenzie et al. (1989). Valve preservation was assessed via the visual preservation index (VPI) of Dwyer et al. (1995), in which a value of one (1) indicates a translucent carapace and seven (7) indicates an opaque carapace. To minimise potential dissolution effects, only valves with a VPI between one and three were selected for Mg cleaning tests.

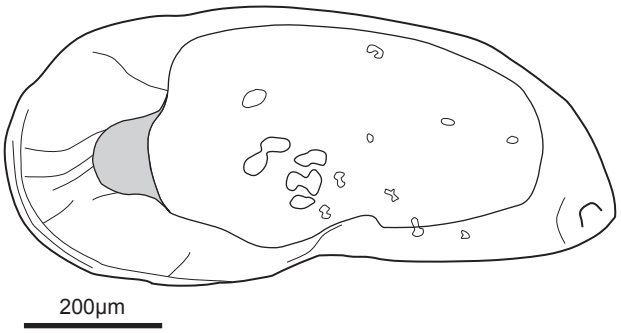

FIGURE 4.1: A male *Krithe pernoides* valve drawn under light microscrope. The characteristic 'pocket' shaped vestibule that defines this species is highlighted in grey.

Cleaning experiments were carried out on individual ostracod valves (n=43). The preliminary cleaning tests indicated that the full trace metal cleaning procedure of Boyle and Keigwin (1985) (excluding the final acid leach) resulted in excessive sample loss in delicate *Krithe* valves. Therefore, we applied the Boyle and Keigwin (1985) methodology with modifications outlined in section 3.7, which included reducing the number of sonication steps and decreasing the volume of, and exposure time to, the oxidising and reducing reagents. When applied, the reductive step preceded the oxidative step following Martin (2002). In order to assess the impact of each cleaning step on valve chemistry, between 8 and 16 valves were removed from the cleaning procedure after each cleaning step and the individual valves were analysed by ICP-OES for a suite of major and trace elements.

4.2.2 ICP-OES analysis

For analysis by ICP-OES, single ostracod valves were dissolved in 350µl of 0.1 M HNO_3 (Optima Grade) in an acid-leached (48 hrs in warm 2.2 M HNO_3) Molecule BioProducts 0.6 ml microcentrifuge tube and centrifuged at 5000 rpm for 5 mins. After centrifuging, 300µl of supernatant was transferred to an acid-leached 0.6 ml microcentrifuge tube for analysis. The Mg/Ca, Sr/Ca, Al/Ca, Fe/Ca and Mn/Ca ratios of acidified samples were analysed at University College London (UCL) by Varian 720 ES ICP-OES using the intensity ratio calibration method of de Villiers et al. (2002). Trace metal/Ca ratios were corrected for matrix effects relating to differences in Ca concentration using matrix-matched standards; all Mg/Ca matrix corrections were less than 1 mmol/mol (7%), with the majority of corrections <0.3 mmol/mol (2%). Analysis of carbonate standard PE3 during the run gave a Mg/Ca value of 8.51±0.06 mmol/mol (n=7), in good agreement

with the value of 8.50±0.04mmol/mol reported by Dwyer et al. (1995). Over the 6 month study interval, Mg/Ca reproducibility of the BSC-CRM 393 calcite standard on UCLs Varian ICP-OES was 3.74±0.05 mmol/mol (<1.4%), based on 92 determinations. The detection limit, calculated as 3*standard deviation of the blank (Harris, 2010), at average ostracod Ca concentrations after acidification is 0.01 mmol/mol (adults) and 0.04 mmol/mol (A-1 juveniles) for Fe, 0.14 and 0.55 mmol/mol for Al, and <0.01 and 0.01 mmol/mol for Mn. Analytical precision ($\pm 1\sigma$) for each element/Ca at typical concentrations is displayed in Figs. 4.2, 4.3, 4.4 and 4.5. The full dataset is given in the data appendix.

4.2.3 Statistical analyses

A Student's *t*-test was employed to evaluate the significance of differences in mean Mg/Ca ratios of valves cleaned with each subsequent cleaning treatment, and between adult and A-1 valves. All *t*-tests were one-tailed, and either a homoscedastic (equal-variance) or heteroscedastic (unequal-variance) t-test was chosen depending on the result of a preceding analysis of variance (ANOVA) F-Test.

4.3 Results and discussion

4.3.1 Contamination indicators

Al and Fe concentrations are below detection limit in most samples (Figs. 4.3 and 4.4), and the proportion of samples with Al, Fe and Mn concentrations below detection generally increases with each subsequent cleaning step. Several valves have very high Al/Ca ratios, of up to 12.9 mmol/mol. As Al is more difficult to measure using ICP-OES and more abundant in contaminant phases than Mg (Kaolinite comprises 20% Al (w/w) and no Mg: Riley and Chester 1971), high Al/Ca values are not necessarily indicative of Mg-bearing contaminants (Elderfield et al., 2010). Fe/Ca is below 0.3 mmol/mol in all samples and Mn/Ca is below 0.4 mmol/mol in all but one outlying sample. The mean concentration of Fe and Mn contained directly within the calcite of *Krithe*, as determined by LA-ICP-MS, equates to an Fe/Ca ratio <0.1 mmol/mol and a Mn/Ca ratio of <0.02 mmol/mol (Fig. 4.11) (Ito et al., 2003). Fe/Ca and Mn/Ca ratios measured above these values in this study suggests the presence of contaminants. Elevated Al/Ca, Fe/Ca and Mn/Ca values are generally not associated with higher Mg/Ca values, and no relationship is observed between Mg/Ca and Al/Ca, Fe/Ca or Mn/Ca (Figs. 4.6, 4.7 and 4.8. These results suggest that levels of contamination

in *Krithe* valves are generally low, supporting the assumption that the morphology of ostracod valves makes them less prone to contamination than foraminifera (Cronin et al., 2005). However, the general decrease in the proportion of samples with detectable Al, Fe and Mn concentrations with each subsequent cleaning step indicates that clay particles and Fe-Mn oxyhydroxides are being removed during the cleaning procedure.

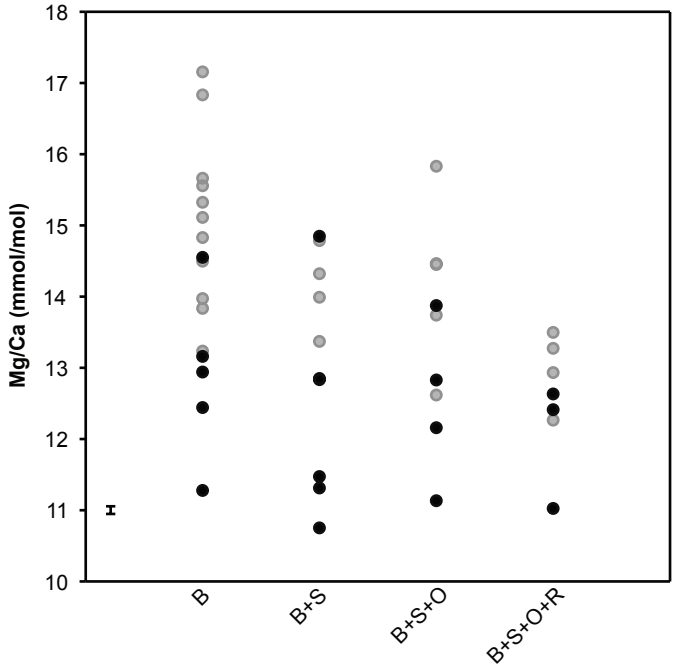

FIGURE 4.2: Effect of foraminiferal trace element cleaning procedures on *Krithe* Mg/Ca. A-1 juveniles are shown by the light symbols and adults by the dark symbols. The cleaning steps are: ***B*** brush with ethanol, ***S*** sonication in methanol, ***O*** oxidation with hydrogen peroxide, ***R*** reduction with hydrous hydrazine/ammonium citrate. A full description of the procedure is given in section 3.7. Analytical precision (±1σ) for each element/Ca at typical concentrations is shown by the black error bar.

4.3.2 Effects of cleaning

Following sonication in methanol, the mean Mg/Ca ratio decreases significantly from 14.8±1.8 to 13.2±1.9 mmol/mol (11%) (p=<0.01). However, inter-valve variability remains high, with a relative standard deviation (RSD) of 14% (Fig. 4.2). As sonication is a purely mechanical process and does not directly affect the chemistry of the ostracod calcite, the decrease in Mg/Ca can only be attributable to the removal of Mg-bearing clays. Mean Mg/Ca ratios and inter-valve Mg/Ca variability show no significant differences following oxidation with buffered hydrogen peroxide, indicating that oxidative cleaning has little effect on Mg-contaminant removal or valve chemistry at the study site. Rigorous testing across a wide range of bottom water oxygen, productivity, and water

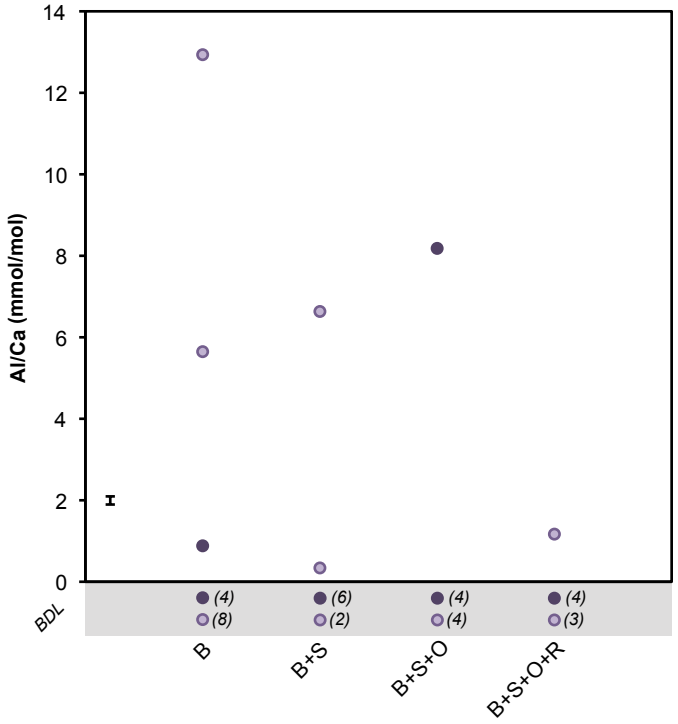

FIGURE 4.3: Effect of foraminiferal trace element cleaning procedures on *Krithe* Al/Ca. A-1 juveniles are shown by the light symbols and adults by the dark symbols. The cleaning steps are: ***B*** brush with ethanol, ***S*** sonication in methanol, ***O*** oxidation with hydrogen peroxide, ***R*** reduction with hydrous hydrazine/ammonium citrate. A full description of the procedure is given in section 3.7. Analytical precision ($\pm 1\sigma$) for each element/Ca at typical concentrations is shown by the black error bar. The number of valves with Al concentrations below the detection limit (BDL) is given in parentheses within the grey shaded area of the graph.

depth conditions is required to further assess the effects of oxidative cleaning on *Krithe* Mg/Ca.

Excluding the outlying valve with anomalously high Mn/Ca (>1 mmol/mol), there is a significant relationship between samples with above-detection Mn/Ca and Fe/Ca (including one reductively cleaned valve with a detectable Fe/Ca ratio of 0.08 mmol/mol) in a ∼1:1 molar relationship suggesting a detectable presence of Fe-Mn oxyhydroxides in the samples (Fig. 4.9). Under scanning electron microscope (SEM), secondary overgrowths are visible on the calcite surface of ostracods that have not been reductively cleaned (Fig. 4.10). After reductive cleaning, all Mn/Ca values fall below 0.1 mmol/mol (Fig. 4.5), mean Mg/Ca values show a statistically significant decrease from 13.6±.6 to 12.7±0.6 mmol/mol (p=<0.05), and inter-valve variability also decreases substantially, with a reduction in RSD from 12% to 5% (Fig. 4.2). The decrease in Mn/Ca values and the reduction in Mg/Ca variability suggest the removal of Mg-bearing Fe-Mn oxyhydroxide overgrowths during reductive cleaning. This decrease in inter-valve

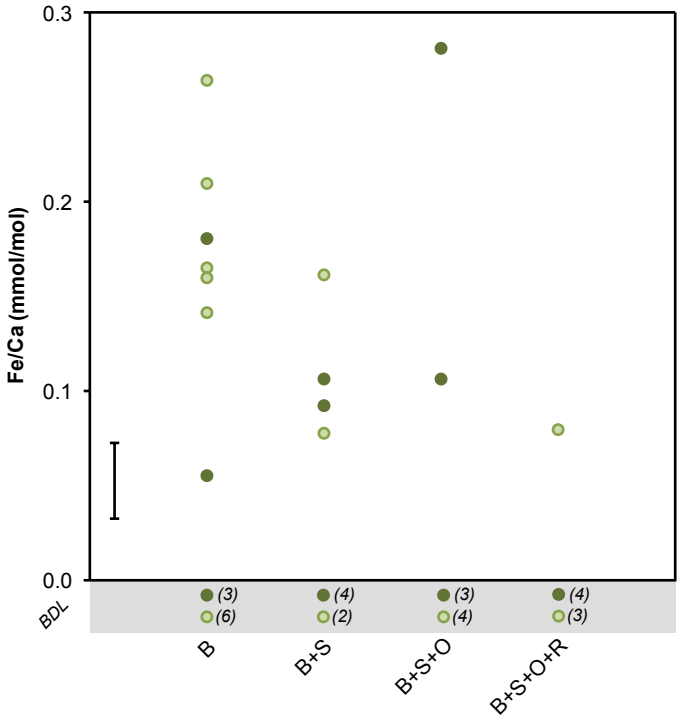

FIGURE 4.4: Effect of foraminiferal trace element cleaning procedures on *Krithe* Fe/Ca. A-1 juveniles are shown by the light symbols and adults by the dark symbols. The cleaning steps are: ***B*** brush with ethanol, ***S*** sonication in methanol, ***O*** oxidation with hydrogen peroxide, ***R*** reduction with hydrous hydrazine/ammonium citrate. A full description of the procedure is given in section 3.7. Analytical precision ($\pm 1\sigma$) for each element/Ca at typical concentrations is shown by the black error bar. The number of valves with Fe concentrations below the detection limit (BDL) is given in parentheses within the grey shaded area of the graph.

variability delimits contamination from Fe-Mn oxyhydroxide overgrowths as one of the potential causes of Mg/Ca variability observed between *Krithe* valves within the same stratigraphic interval (Dwyer et al., 2002).

Examination of the ostracod calcite surface under SEM also reveals that the reductive cleaning process partially removes the outer calcite layer (Fig. 4.10). LA-ICP-MS studies have revealed the outer 2 μm layer of calcite in adult *Krithe* is enriched in Mg by ~8 mmol/mol, and complete removal of this layer results in a net Mg/Ca reduction of ~1.2 mmol/mol) (Ito et al., 2003). The observed 0.9 mmol/mol decrease in Mg/Ca following reductive cleaning is therefore likely caused both by the removal of high-Mg overgrowths, and the partial removal of the Mg-enriched outer calcite layer. While the outer-layer of calcite is also enriched in Mn by ~0.02 mmol/mol and Fe by ~0.25 mmol/mol (as well as many other trace elements), the mass of Mn in the outer 2 μm of calcite is insufficient to account for the high Mn/Ca ratios observed before reductive cleaning. It is unlikely that the trace element-enriched outer layer of calcite is due to secondary

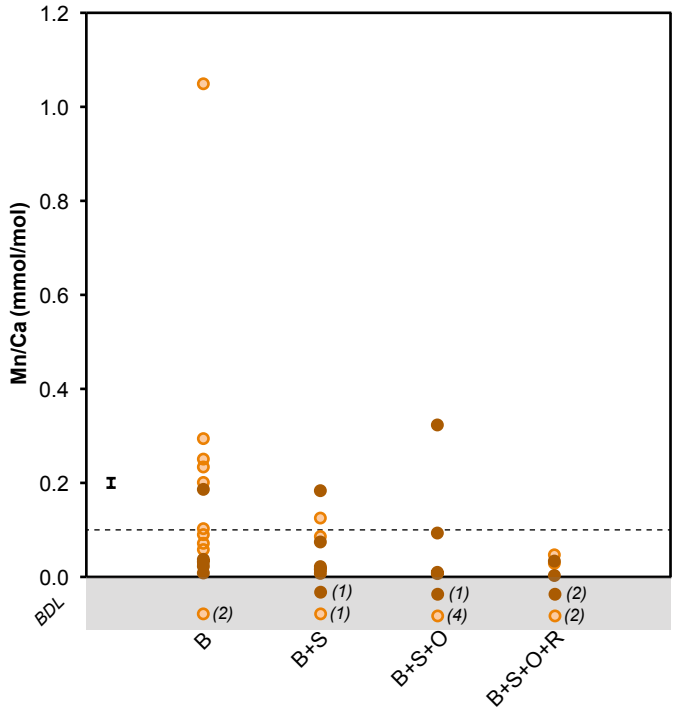

FIGURE 4.5: Effect of foraminiferal trace element cleaning procedures on *Krithe* Mn/Ca. The number of valves with Mn concentrations below the detection limit (BDL) is given in parentheses within the grey shaded area of the graph. The dashed line indicates Mn/Ca ratios of 0.1 mmol/mol, the value above which Boyle (1981, 1983) concluded that foraminiferal calcite contained significant Fe-Mn oxyhydroxide contamination.

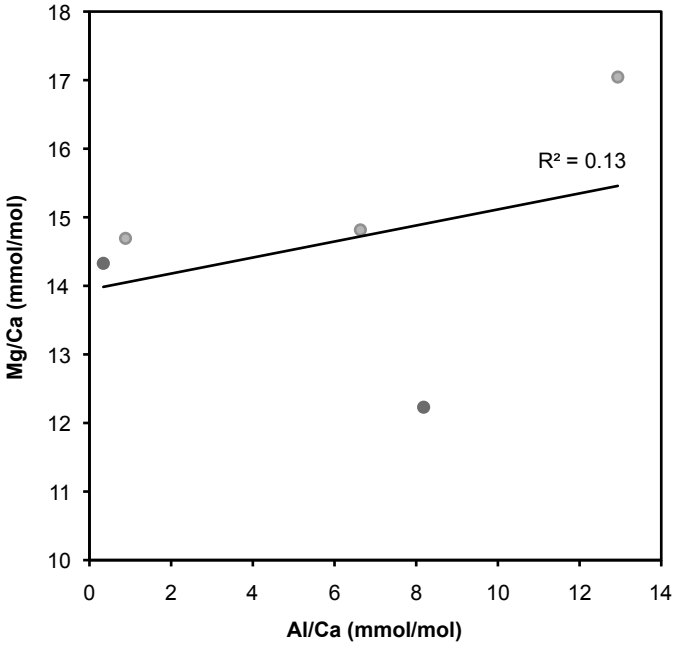

FIGURE 4.6: Regression of Al/Ca against Mg/Ca. The relationship is not significant.

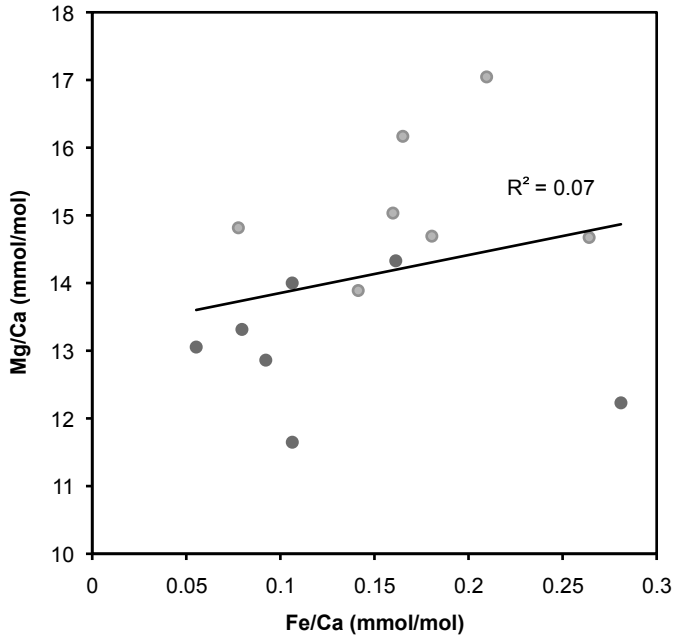

FIGURE 4.7: Regression of Fe/Ca against Mg/Ca. The relationship is not significant.

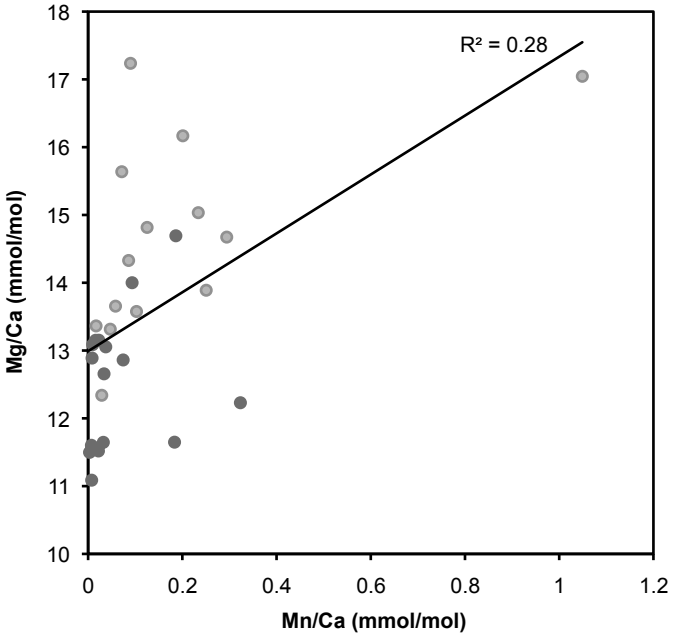

FIGURE 4.8: Regression of Mn/Ca against Mg/Ca. The relationship is not significant.

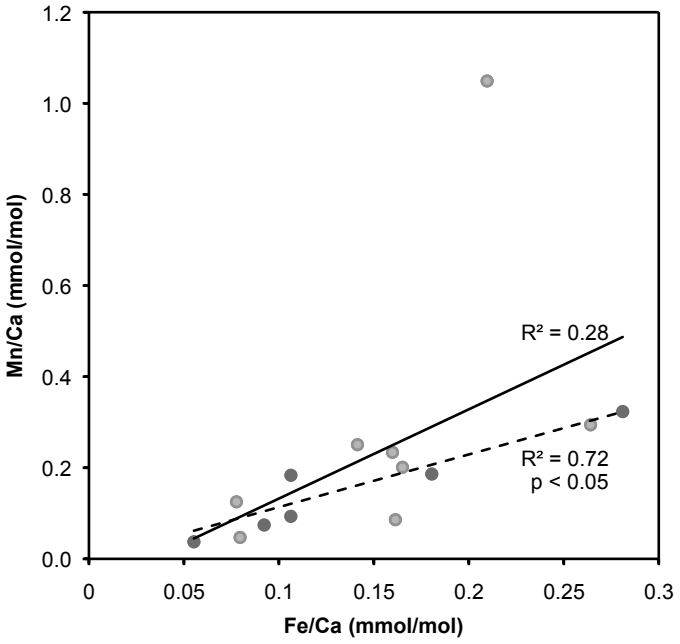

FIGURE 4.9: Regression of Mn/Ca against Fe/Ca, including one reductively cleaned valve with a detectable Fe/Ca ratio of 0.08 mmol/mol. If the outlying valve with high (>1 mmol/mol) Mn/Ca is excluded (dashed line), the relationship between Mn/Ca and Fe/Ca is significant to 95%, indicating a detectable presence of Fe-Mn oxyhydroxides.

overgrowths as trace-element enrichment is also observed in the outer calcite layer of laboratory-cultured ostracods belonging to the same superfamily as *Krithe* (Ito et al., 2003).

4.3.3 Differential effects of cleaning on adult and A-1 juvenile valves

Adult and A-1 *Krithe* valves are often used interchangeably in Mg/Ca paleotemperature reconstructions because there is no significant difference in Mg/Ca ratios between these lifestages (Dwyer et al., 2002). However, by assessing adult and A-1 valves separately, clear differences in the effects of cleaning on valves from the two molt stages emerge (Fig. 4.2). The mean Mg/Ca ratio of brush cleaned A-1 juvenile valves is 2.5 mmol/mol higher than that of brush cleaned adult valves ($p=<0.01$). A-1 juveniles show a significant ($p=<0.05$) 1.5 mmol/mol (9%) decrease in Mg/Ca following sonication, whereas adult valves show no significant change ($p=0.27$). It is only after oxidative cleaning that the Mg/Ca ratio of A-1 juvenile and adult valves becomes statistically indistinguishable. The greater Mg/Ca decrease in A-1 juvenile valves compared to adult valves following sonication indicates a greater influence of clay contamination in the former. Contamination would be expected to play a greater role in A-1 juveniles owing to their lower mass. In this study average adult valves weighed ~20µg, while A-1 juveniles

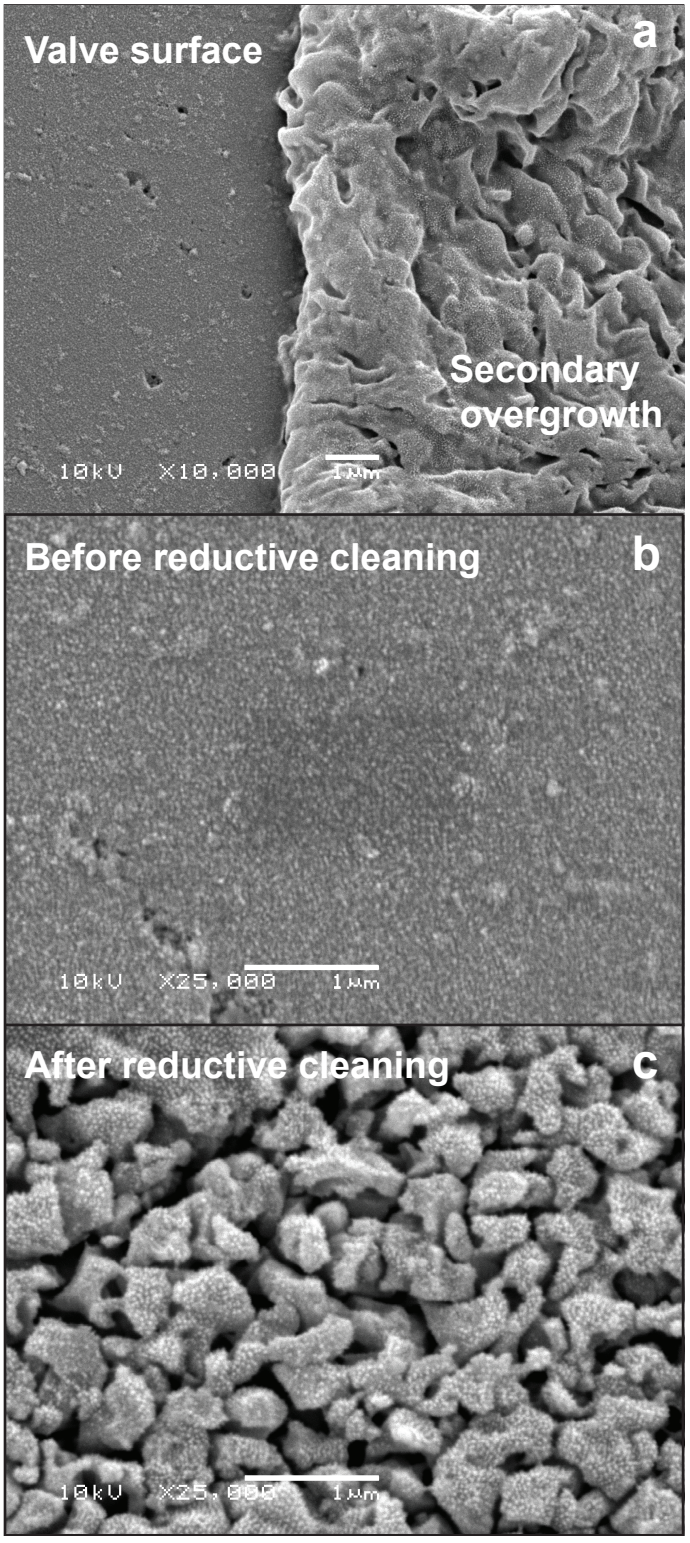

FIGURE 4.10: SEM images of the calcite surface showing **(a)** an overgrowth on a valve that has not been reductively cleaned, **(b)** the surface calcite structure before reductive cleaning and **(c)** the surface calcite structure after reductive cleaning. Partial dissolution of the valve surface is clearly visible after reductive cleaning. While not from the same carapace, valves chosen for SEM imaging had similarly excellent preservation (VPI = 1) before any cleaning procedures took place. Scale bar indicates 1µm.

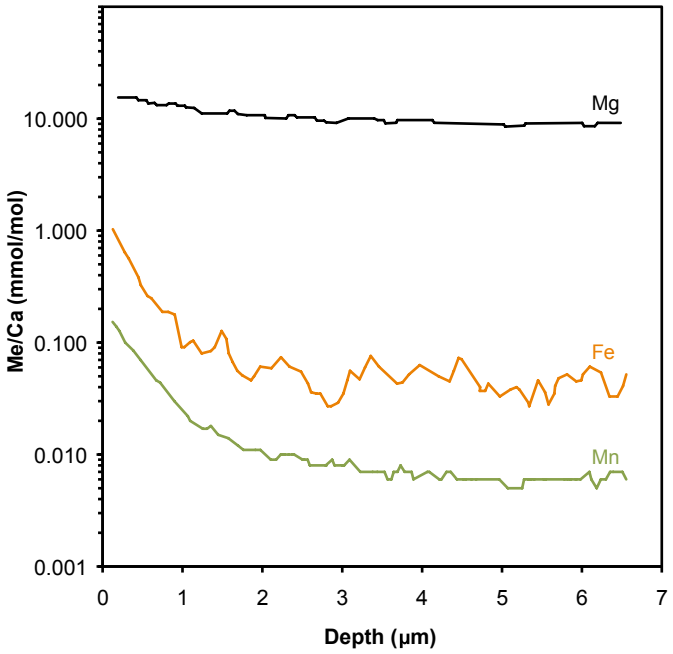

FIGURE 4.11: LA-ICP-MS profile of a *Krithe* valve, showing trace element enrichment in the outer 2 µm. Data digitised from Ito et al. (2003)

weighed just ∼5µg; any contaminating Mg in A-1 juvenile valves therefore represents a much greater proportion of the Mg contained within the ostracod calcite (Fig. 4.12).

By assessing adult and A-1 valves separately, the sample sizes become relatively small (the low abundance of well-preserved adult and A-1 juvenile single species *Krithe* valves in the sediment sample used in this study limits any further increase in sample size). However the differences in the data on which the conclusions are based remain statistically robust. This result confirms adult and A-1 valves can be used interchangeably, but only after effective clay removal.

4.3.4 Implications for paleotemperature reconstructions

We convert *Krithe* Mg/Ca values to equivalent temperatures using the calibrations of Elmore et al. (2012) for BWTs >3 °C,

$$Mg/Ca = 0.97 * BWT + 7.95 \tag{4.1}$$

Farmer et al. (2012) for the North Atlantic,

$$Mg/Ca = 1.13 * BWT + 6.43 \tag{4.2}$$

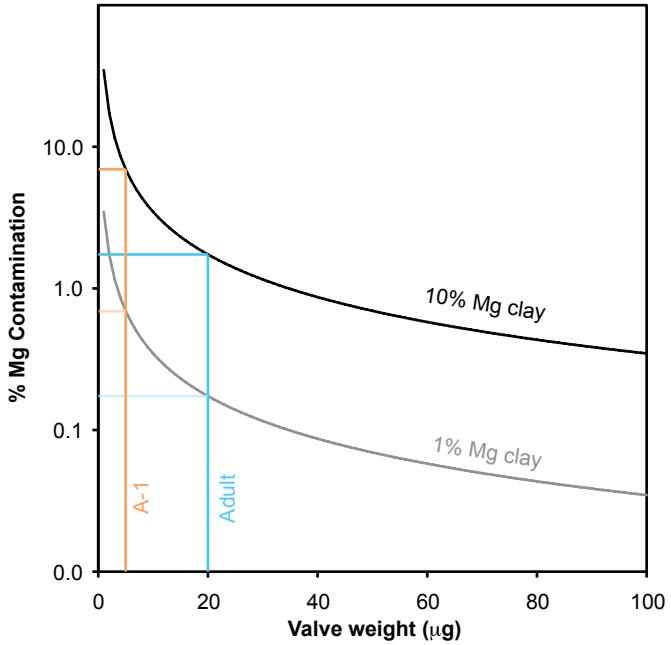

FIGURE 4.12: The effect of 0.01µg of clay (containing 1% Mg and 10% Mg by weight) as a percentage of the total Mg in a *Krithe* valve with a Mg/Ca of 12 mmol/mol across a range of valve weights. The average weight of adult (20µg) and A-1 juvenile (5µg) valves in this study is indicated.

and the species-specific calibration of Farmer et al. (2012) for *Krithe pernoides*,

$$Mg/Ca = 1.12 * BWT + 7.06 \tag{4.3}$$

where Mg/Ca is in mmol/mol, and BWT is in °C. Uncertainty in reconstructed BWT is given as the 1σ Mg/Ca inter-valve variability divided by the slope of the calibration equation (Eqs. 4.1, 4.2 and 4.3). The three paleotemperature equations show good agreement with each other, and reconstructed BWTs range between 7.4±1.6 to 4.8±0.7 °C (Fig. 4.13). The reconstructed temperature of brush cleaned valves is between 1.0±1.6 to 1.5±1.6 °C below the measured BWT at our site. After sonication reconstructed temperatures fall to between 2.4±1.6 to 3.0±1.9 °C below the measured BWT, and the equivalent temperature of reductively cleaned valves is between 2.9±0.6 to 3.6±0.7 °C below measured BWT. Taking the mean reconstructed temperature from the three calibrations, the decrease in Mg/Ca following sonication is equivalent to a temperature decrease of 1.5 °C, and the decrease in Mg/Ca following reductive cleaning is equivalent to a temperature decrease of 0.9 °C. These apparent temperature decreases are significant given the calibration error of ±0.3 °C for Elmore et al. (2012), and ±0.7 °C for the North Atlantic calibration of Farmer et al. (2012) (based on 10 replicate single-valve analyses).

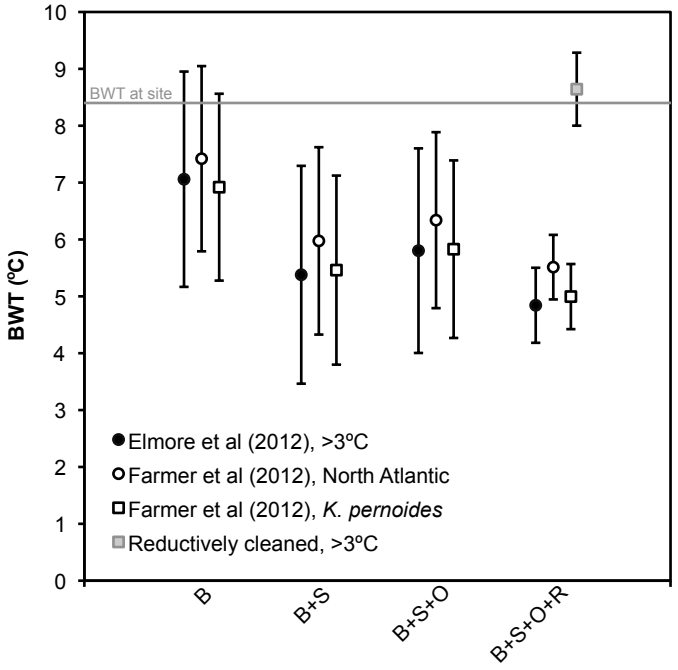

FIGURE 4.13: The effect of cleaning procedures on reconstructed BWT (see text for calibration details), error bars are $\pm 1\sigma$. The measured bottom-water temperature at the core site is indicated by the grey line. The cleaning steps are: ***B*** brush with ethanol, ***S*** sonication in methanol, ***O*** oxidation with hydrogen peroxide, ***R*** reduction with hydrous hydrazine/ammonium citrate. A full description of the procedure is given in ection 3.7

Krithe valves used in the calibration of Farmer et al. (2012) were cleaned by sonication in deionised water and oxidisation with 5% NaClO. While Elmore et al. (2012) used the reductive cleaning procedure of Rosenthal et al. (1999) (modified after Boyle and Keigwin (1985)), the data for reductively cleaned valves were combined with several previously-published datasets for non-reductively cleaned valves. As such, only 10% of the material comprising the Elmore et al. (2012) >3 °C calibration dataset was reductively cleaned, with the majority of the valves making up the dataset being cleaned by sonication in deionised water and oxidisation with 5% NaClO.

Reconstructed temperatures for brush cleaned valves are within error of measured BWT using the temperature calibrations of Elmore et al. (2012) and Farmer et al. (2012). The data from valves cleaned by sonication should provide the most direct comparison to the calibrations of Elmore et al. (2012) and Farmer et al. (2012); however a large offset is observed between reconstructed and measured BWT for this dataset (Fig. 4.13). The large offset is likely the result of increased clay removal by sonication in methanol compared to sonication in deionised water. Jin et al. (2006) demonstrated a 0.5 - 1 mmol/mol decrease in Mg/Ca following sonication in methanol, even after multiple sonication steps in deionised water. The lower viscosity of methanol may more readily

dislodge clay particles adhering to the valve surface, making it a more effective clay-removal agent. The large decrease in reconstructed temperature following sonication in methanol highlights the necessity of effective clay removal in order to avoid significantly biasing paleotemperature reconstructions. This result suggests that previous *Krithe*-Mg/Ca paleotemperature reconstructions studies that have not utilised methanol could potentially be biased to warmer temperatures, particularly in ocean basins (or periods of the geological past) where clay input, or the Mg-content of clay, is elevated. Future Mg/Ca determinations of *Krithe* should include a methanol sonication step as outlined in **??**.

Using the temperature calibrations of Elmore et al. (2012) and Farmer et al. (2012) reconstructed BWT from reductively cleaned valves is significantly below measured BWT (Fig. 4.13). However, the data from reductively cleaned valves in the Elmore et al. (2012) calibration are systematically lower than that for non-reductively cleaned valves. Regressing only the data for reductively cleaned valves from Elmore et al. (2012) for sites with BWT >3 °C, including the mean Mg/Ca value for reductively cleaned valves from this study, against BWT gives the relationship,

$$Mg/Ca = 1.00 * BWT + 4.02 \tag{4.4}$$

with a standard error equivalent to ±1.81 °C (Fig. 4.14). Calibrating the mean Mg/Ca value for reductively cleaned valves from this study with 4.4 gives a reconstructed BWT of 8.64±0.64 °C, in good agreement with measured BWT at the site (Fig. 4.13). It is important to note that removing the data point generated in this study from Equation 4.4 results in no significant difference to the calibration equation or reconstructed BWT.

The slope of the calibration in Eq. 4.4 above is very similar to the >3 °C calibration of Elmore et al. (2012) (Eq. 4.1) and the North Atlantic calibration of Farmer et al. (2012) (Eq. 4.2), although the intercept is 3.93 mmol/mol lower than in Eq. 4.1 and 2.40 mmol/mol lower than in Eq. 4.2. The similarity in slope, but reduction in intercept suggests that the calibrations based on non-reductively cleaned valves are systematically biased to higher Mg/Ca values due to the influence of clay and Fe-Mn oxyhydroxide contamination. Although some fraction of the difference in intercept is due to partial dissolution of the Mg-enriched valve surface, it is unlikely to account for more than ∼1.2 mmol/mol, the resulting decrease following total removal of the Mg-enriched layer (Ito et al., 2003). Due to the relatively small dataset available, the calibration for reductively cleaned valves at sites with BWT >3 °C presented here is tentative, and further coretop data from reductively cleaned *Krithe* are needed to confirm the Mg/Ca-BWT relationship.

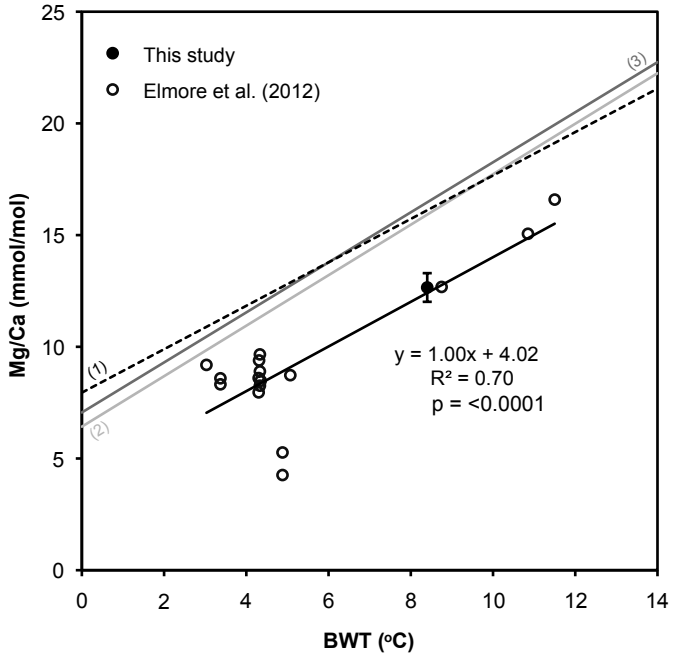

FIGURE 4.14: Mg/Ca-temperature calibration of reductively cleaned valves. The calibrations of **(1)** Elmore et al. (2012) for sites with BWT >3 °C, **(2)** Farmer et al. (2012) for the North Atlantic and **(3)** Farmer et al. (2012) for *Krithe pernoides* are shown.

Elmore et al. (2012) ascribed anomalously high Mg/Ca values from sites with BWTs <3 °C to the influence of ΔCO_3^{2-} below this temperature. Much of the data for reductively cleaned valves from <3 °C also lies above the calibration line for reductively cleaned valves from sites >3 °C. This suggests it is not an artefact of contamination, and thus likely results from a secondary influence on Mg uptake into ostracod calcite, such as ΔCO_3^{2-} as indicated by Elmore et al. (2012).

The reduction in inter-valve Mg/Ca variability following reductive cleaning represents a large increase in equivalent BWT precision, with reduction in error from ±1.7 °C to ±0.6 °C. Reductive cleaning therefore has the potential to improve *Krithe* Mg/Ca BWT reconstruction precision by >1 °C. While bottom waters bathing the core site are oxic, the importance of removing Fe-Mn oxyhydroxide overgrowths will increase in regions (or during periods in the geological past) of high productivity and/or reduced bottom water ventilation, where sedimentary redox conditions are more conducive to Fe-Mn oxyhydroxide formation. Given the prevalence of Fe-Mn oxyhydroxide formation on marine carbonates, the low range in BWTs expected at deep-sea locations, and the potential of reductive cleaning to improve *Krithe* Mg/Ca BWT reconstructions, future *Krithe* Mg/Ca paleotemperature reconstructions should include a reductive cleaning step. However, further experiments to better constrain the effects of partial dissolution

of the valve surface and determine the optimum exposure time to the reducing reagents should also be conducted.

4.4 Conclusions

- While the data suggest generally low levels of Al, Fe and Mn in *Krithe*, Mg bearing clays and Fe-Mn oxyhydroxide overgrowths are present, detectable, and exert a significant influence on the Mg/Ca of *Krithe* valves.
- Sonication in methanol lowers Mg/Ca by 1.6 mmol/mol (11%), due to the removal of clays. This Mg/Ca reduction is equivalent to a decrease in reconstructed temperature of 1.5 °C, emphasising the importance of sonication in methanol as a critical step in the preparation of *Krithe* valves for Mg/Ca analysis.
- Clay contamination exerts a greater influence on the Mg/Ca of A-1 juvenile valves compared to adult valves, due to the lower mass of the former.
- Oxidation with buffered hydrogen peroxide does not influence Mg/Ca ratios in valves from the study site. Future work should assess the effects of contamination from organic matter and oxidative cleaning across different oceanographic and sedimentary settings.
- Reduction with hydrous hydrazine/ammonium citrate decreases Mg/Ca by 0.9 mmol/mol (7%), equivalent to a decrease in reconstructed temperature of 1 °C, due both to the removal of Fe-Mn oxyhydroxide overgrowths, and the partial dissolution of the valve surface.
- The lowest inter-valve Mg/Ca variability of ±0.6 mmol/mol (5%) (±0.6 °C) is achieved following reductive cleaning, indicating the high Mg/Ca variability previously observed in non-reductively cleaned *Krithe* valves is, in part, due to contamination. The data demonstrate the potential of reductive cleaning to improve the precision of BWT reconstructions based on multiple, single-valve determinations of *Krithe* Mg/Ca per stratigraphic level. Future work should aim to better constrain the effects of partial dissolution of the valve surface and determine the optimum exposure time to the reducing reagents.
- Future *Krithe* Mg/Ca studies should employ the full cleaning procedure outlined in this study, namely sonication in methanol/deionised water, oxidation with alkali-buffered hydrogen peroxide and reduction with hydrous hydrazine/ammonium citrate. Further coretop data from *Krithe* that have been cleaned according

to this protocol should be generated to improve the *Krithe* Mg/Ca-temperature calibration.

Chapter 5

Controls on the uptake of Li, B, Mg and Sr in benthic foraminifera *Uvigerina peregrina*

Trace element/Ca ratios in benthic foraminifera can be used to reconstruct the temperature and carbonate chemistry of the deep ocean in the past, provided the controls on their uptake into benthic foraminiferal calcite are well understood. Uvigerina peregrina is a cosmopolitan species, widely used in paleoceanographic research. Core top calibrations show a correlation between Mg/Ca and Li/Ca in Uvigerina peregrina and both bottom water temperature (BWT) and carbonate ion saturation (ΔCO_3^{2-}), and studies of Uvigerina spp. indicate a ΔCO_3^{2-} control on the uptake of B and Sr in this genus. However, current core top calibration studies are predominantly based in the North Atlantic, where deepwaters are super saturated with respect to calcite. A coretop calibration study of Li/Ca, B/Ca, Mg/Ca and Sr/Ca ratios in Uvigerina peregrina, predominantly based in the calcite-undersaturated waters of North Pacific was conducted in order that the controls on trace element uptake across a wide calcite saturation range could be understood.

5.1 Introduction

The deep ocean contains nearly all of the heat and carbon within the ocean-atmosphere system, and as such understanding its behaviour in the past is paramont to understanding the mechanisms driving past climatic change (Adkins, 2013). Determining the temperature of the deep ocean in the past is necessary to understand

past changes in the physical structure of, and heat transport within, the deep ocean, while an understanding of past changes in the oceanic carbonate system can elucidate the processes within the carbon cycle that have driven past changes in atmospheric CO_2 (and thus Earth's radiative forcing). Trace elements in benthic foraminifera can potentially be used to understand both the temperature and carbonate chemistry of the deep ocean in the past, as the uptake of trace elements has been demonstrated to be dependent upon both the temperature and chemistry of the water in which calcification occurs (Lear et al., 2002; Elderfield et al., 2006; Yu and Elderfield, 2007; Rae et al., 2011).

Much work has focussed on determining the controls on trace element incorporation in the epifaunal genus *Cibicidoides* spp. as it is thought to faithfully record past changes in bottomwater chemistry. However, *Cibicidoides* spp. is often absent in poorly ventilated deep waters, and is therefore not universally applicable as a paleoenvironmental recorder. *Uvigerina peregrina* is a more cosmopolitan species of benthic foraminifera with a shallow infaunal habitat, usually found at maximum abundance at 0-2 cm within the sediment (Corliss, 1991; Rathbuml and Corliss, 1994). *Uvigerina peregrina* can be found in sediments underlying poorly ventilated deep waters, and can potentially be used to reconstruct the temperature and carbonate chemistry of deepwaters, providing the microhabitat of *Uvigerina peregrina* is significantly related to bottomwater conditions.

5.1.1 Benthic foraminferal Mg/Ca paleothermometry

Mg is incorporated into foraminiferal calcite as $MgCO_3$ (Branson et al., 2013) (see section 2.3.1), and as with planktonic foraminifera (Nürnberg et al., 1996; Elderfield and Ganssen, 2000; Anand, 2003), species specific relationships between water temperature and the ratio of Mg to Ca within the calcite of benthic foraminifera have been empirically determined (Lear et al., 2000; Elderfield et al., 2006; Marchitto et al., 2007b). Core-top calibration studies indicate a linear temperature sensitivity of Mg uptake in perforate benthic foraminifera of between ~0.08-0.12 mmol/mol/ °C (Elderfield et al., 2006; Marchitto et al., 2007b; Lear et al., 2010). Both the observed temperature sensitivity and total amount of Mg in benthic foraminifera are 1-2 orders of magnitude lower than inorganic calcite, suggesting the uptake of Mg is strongly biologically mediated (Figure 5.1).

Coretop calibration studies of *Uvigerina* spp. suggest a linear temperature sensitivity of between 0.071±0.005 to 0.084±0.005 mmol/mol/ °C, and in contrast to the genus *Cibicidoides*, there appears to be little inter-species variability (Elderfield et al., 2010). In order to explain the observed variability in the Florida Straits *Uvigerina peregrina*

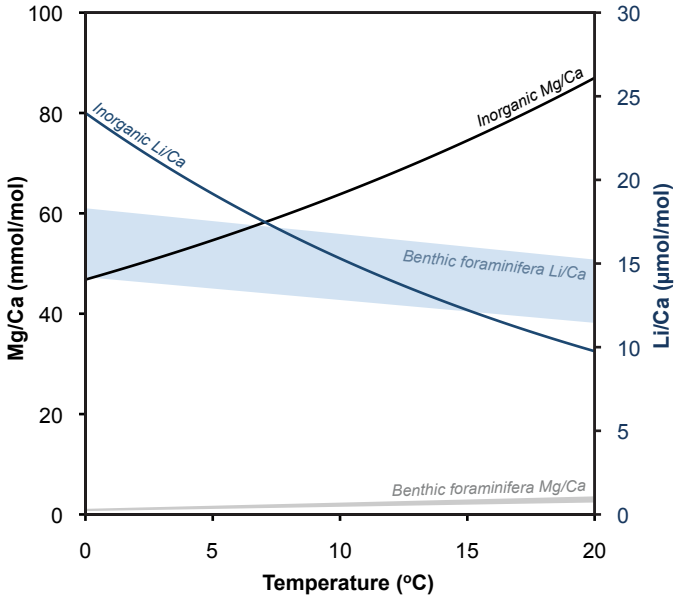

FIGURE 5.1: The thermal control on Mg and Li uptake in inorganic and benthic foraminiferal calcite. For both Mg and Li the inorganic relationship represented by a single line and the range measured in benthic foraminifera is represented by the shaded area. The inorganic Mg/Ca line is derived from D_{Mg} of Oomori et al. (1987) and a seawater Mg/Ca of 5.2 mol/mol, and the inorganic Li/Ca relationship is derived from D_{Mg} of Marriott et al. (2004b) and a seawater Li/Ca of 0.0024 mol/mol. Benthic foraminiferal values are for both *Cibicidoides pachyderma* and *Uvigerina peregrina* from Marchitto et al. (2007b) and Bryan and Marchitto (2008).

calibration Bryan and Marchitto (2008) suggested a greater temperature sensitivity of 0.096 mmol/mol/ °C at temperatures <11 °C, and a lower sensitivity of 0.044 mmol/mol/ °C above 11 °C. Using a novel approach Elderfield et al. (2010) assessed the temperature sensitivity of *Uvigerina* spp. by comparing Mg/Ca and foraminiferal $\delta^{18}O$ derived temperatures from ODP Site 1123, where porewater measurements allow LGM seawater $\delta^{18}O$ to be independently constrained (Adkins, 2002). Through extension of the calibration back to glacial temperatures Elderfield et al. (2010) proposed a temperature sensitivity of 0.1±0.013 mmol/mol/ °C for *Uvigerina* spp., similar to the <11 °C sensitivity of Bryan and Marchitto (2008).

Inital work suggested a higher temperature sensitivity in *Cibicidoides* spp (Lear et al., 2002; Martin et al., 2002). However Elderfield et al. (2006) hypothesised that the higher apparent temperature sensitivity in *Cibicidoides* spp. was due to a carbonate ion saturation (ΔCO_3^{2-}) effect (the difference between $[CO_3^{2-}]_{seawater}$ and $[CO_3^{2-}]_{saturation}$) of ∼0.01 mmol/mol/µmol/kg at low temperatures in this genus. The observation of a ΔCO_3^{2-} effect on Mg uptake in *Cibicidoides* spp called into question its reliability as a BWT proxy. However ΔCO_3^{2-} does not appear to influence Mg uptake in *Uvigerina* spp, suggesting that Mg/Ca_{Uvi} may be more reliable bottom water temperature (BWT)

proxy than Mg/Ca_{Cib} (Elderfield et al., 2006, 2010). There is however a paucity in *Uvigerina* spp coretop data from waters at low- (<30 μmol/kg) and under- saturation states, and coretop *Uvigerina* spp Mg/Ca data from watermasses at low- and under-saturation states are needed to fully test this ascertion and assertain if Mg/Ca_{Uvi} can reliably be used as a proxy for deep ocean temperature in the past.

5.1.2 Li uptake in benthic foraminifera

The observation that the incorporation of alkali metals within calcite decreased with increasing ionic radius led (Okumura and Kitano, 1986) to conclude that Li (and all alkali metals) occupy interstitial sites rather than substituting Ca within the lattice. Busenberg and Plummer (1985) proposed the following model for sodium incorporation,

$$a_{M^+}/C_{M^+} = K(a_{M^+})^n \tag{5.1}$$

where a_{M^+} is the activity of Na^+ in solution, C_{M^+} is the concentration of Na^+ in calcite, and K and n are constants, and (Okumura and Kitano, 1986) demonstrated that this model also accurately describes Li incorporation within calcite. The amount of lithium co-precipitation within calcite is therefore dependent on the activity of lithium, but not calcium, in the parent solution (Okumura and Kitano, 1986). Li uptake in inorganic calcite decreases exponentially with increasing temperature (Marriott et al., 2004a,b; Hall and Chan, 2004), and core top studies of Li/Ca in benthic foraminifera also suggest a negative relationship with temperature, with Li incorporated in an amount, and with a temperature sensitivity close to inorganic calcite (Figure 5.1). Furthermore, the $\delta^{11}Li$ of foraminiferal calcite is close to that of inorganic calcite, indicating any biological mediation of Li uptake in foraminiferal calcite is limited Marriott et al. (2004b). While a negative relationship between Li/Ca and temperature has been observed in multiple species of benthic and planktonic foraminifera, the Li/Ca-temperature relationship appears to vary between species (Delaney et al., 1985; Hall and Chan, 2004; Marriott et al., 2004b), indicating some biological mediation.

Downcore studies show that during the LGM Li/Ca in planktonic foraminifera was significantly higher than predicted by a decrease temperature alone, leading Hall and Chan (2004) to hypothesise that Li uptake in foraminifera was also controlled by the carbonate ion concentration of seawater, with lower atmospheric CO_2 necessitating higher $[CO_3^{2-}]$ in the surface of the glacial ocean. Increased incorporation of Li within inorganic calcite has also been observed with higher Mg activity in the parent solution. Okumura and Kitano (1986) proposed substitution of the smaller Mg ion

for Ca leads to significant distortion of calcite lattice, which is more favourable for alkali metal ion incorporation. The amount of Na within inorganic calcite has also been demonstrated to increase linearly as a function of the logarithm of crystal growth rate (Busenberg and Plummer, 1985), suggesting that faster crystal growth rate may also lead to increased lattice distortion. Hall and Chan (2004) proposed a mechanism where increasing seawater $[CO_3^{2-}]$ increases the calcification rate of foraminifera; faster calcification rates lead to more distortion of the calcite lattice, resulting in more Li being incorporated within the calcite. Using a holothermal depth transect in the Nordic Seas, Lear and Rosenthal (2006) proposed a Li/Ca-ΔCO_3^{2-} sensitivity of 0.047 µmol/mol/µmol/kg in *Oridorsalis umbonatus*, empirically demonstrating $[CO_3^{2-}]$ controls Li uptake in benthic foraminifera, and highlighting its potential as a proxy for deep ocean carbonate chemistry. At present the only published coretop *Uvigerina peregrina* Li/Ca data comes from waters highly saturated with respect to calcite (ΔCO_3^{2-} >50 µmol/mol/µmol/kg) in the North Atlantic (Bryan and Marchitto, 2008), and as such behaviour of Li/Ca at low- and under- saturated states is unknown.

5.1.3 Sr/Ca in benthic foraminifera

As a divalent cation, Sr^{2+} is thought to substitute Ca within the calcite lattice. Sr uptake in inorganic calcite varies with precipitation rate (Tang et al., 2008), and is unaffected by salinity/ionic strength (Tang et al., 2012). Coretop studies of benthic foraminifera demonstrate a positive relationship between Sr/Ca and ΔCO_3^{2-}, although with different relationships in the Atlantic and Pacific basins (Dawber and Tripati, 2012; Yu et al., 2014). In the calibrations of Dawber and Tripati (2012) and Yu et al. (2014) Sr/Ca values are ~0.1 mmol/mol higher in the Pacific compared to the Atlantic at similar saturation states. This may be the result of augmented seawater Sr/Ca in the Pacific from celestite remineralisation, and, if this is the case, indicates non-conservative behaviour of Sr in seawater. The controls on Sr/Ca in benthic foraminifera may therefore be more complex than suggested by Yu et al. (2014), who concluded Sr/Ca in foraminifera could effectively be used as a proxy for ΔCO_3^{2-}. At present, the published coretop *Uvigerina peregrina* Sr/Ca dataset is extremely small, although a significant relationship between Sr/Ca and ΔCO_3^{2-} is suggested, highlighting the potential of Sr/Ca as a carbonate system proxy (Yu et al., 2014).

5.1.4 B/Ca in benthic foraminifera

The speciation of $B(OH)_3$ and $B(OH)_4^-$, which together account for almost all boron in seawater, is pH dependent (see section 2.2.2). As only $B(OH)_4^-$ is incorporated within

carbonates (Hemming and Hanson, 1992), B/Ca ratios in foraminifera were initally proposed as proxy for pH. However, empirical calibrations have demonstrated that benthic foraminiferal B/Ca is more strongly correlated with ΔCO_3^{2-} than pH (Yu and Elderfield, 2007; Rae et al., 2011). Coretop data indicate a lower B/Ca sensitivity to ΔCO_3^{2-} in *Uvigerina* spp. (0.27 µmol/mol/µmol/kg) relative to *Cibicidoides* spp. (0.69-1.15 µmol/mol/µmol/kg) (Yu and Elderfield, 2007; Rae et al., 2011). The lower sensitivity may relate to the infaunal habitat of *Uvigerina* spp, as porewater pH (and ΔCO_3^{2-}) can be buffered by $CaCO_3$ dissolution in the upper few centimeters of sediment. Current core top data for *Uvigerina* spp. is very limited, with only 13 published values of mixed *Uvigerina* species, and more data is needed to accurately define the sensitivity of B uptake to ΔCO_3^{2-} in this genus.

5.1.5 Aims and objectives

The current calibrations for *Uvigerina peregrina* Li/Ca and Mg/Ca are predominantly based in the highly saturated waters of the North Atlantic, and the published coretop Sr/Ca and B/Ca dataset is extremely small. This study extends these calibrations to low and undersaturated waters in order to determine the extent to which Li/Ca, B/Ca, Mg/Ca and Sr/Ca in *Uvigerina peregrina* can be used to reconstruct the temperature and carbonate chemistry of the deep ocean in the past. The objectives of this study are to (i) assess the effects of temperature and deep water carbonate chemistry on trace element uptake in *Uvigerina peregrina* (ii) determine to what extent the changing chemistry of porewaters influences these relationships.

5.2 Materials and Methods

5.2.1 Sediments and sample preparation

Core top (0-2 cm) sediments from the Florida Straits, Gulf of California, Southern Californian Margin, Bering Sea and Okhotsk Sea were chosen to span a wide range of BWTs and carbonate ion saturation states (n= 50). The samples were predominantly selected from low-saturation, and under-saturated waters in order to complement the exisiting *Uvigerina peregrina* dataset of Bryan and Marchitto (2008). Samples from the Florida Straits had previously been analysed by Bryan and Marchitto (2008), and were re-analysed in this study to ensure there were no inter-laboratory analytical differences. Where possible, only multicore and gravity coretops where used in the study to ensure material was of late-Holocene age. Multicore sediments from the North Arabian Sea

were sampled at half centimeter resolution and stained with rose-bengal to identify foraminifera living at each depth (n= 8). All samples are listed in the data appendix.

Foraminifera were picked from the 150-500 μm fraction of washed core top sediments (>63 μm) and identified to species level. For a single core top (KNR166-2 55), the test length of each individual was measured using the Zeiss AxioVision software package. For this sample foraminifera were seperated into groups of 400-500, 500-600, 600-700 and 700-800 μm test length for trace element analysis.

5.2.2 Hydrographic data

For each site dissolved inorganic carbon (ΣCO_2), total alkalinity (ALK), major nutrients (PO_4 and SiO_3), salinity (S), bottom water temperature (BWT), and anthropogenic CO_2 were taken from nearby Global Ocean Data Analysis Project (GLODAP) sites (Key, 2004), except for the Florida Straits where hydrographic data came from bottle data taken during the KNR166-2 cruise, and the North Arabian Sea porewaters, which were measured by C. P. Slomp and P. Kraal at Utrecht University. Pre-industrial ΣCO_2 was calculated by subtracting anthropogenic CO_2 from ΣCO_2. Pre-industrial ΣCO_2 was used in all subsequent calculations, as coretop material will be of dominantely pre-industrial age, with the exception of the North Arabian Sea where stained (recently living) foraminifera were analysed. For the North Arabian Sea sites, therefore, anthropogenic CO_2 was not subtracted from ΣCO_2. Carbonate system parameters were calculated using the *seacarb* package within R using the following constants: K_1K_2 from Millero et al. (2006) for S ranging between 0.1 and 50 and T ranging between 1 and 50 °C, KSO_4 from Dickson (1990a) for S ranging between 5 and 45 and T ranging between 0 and 45 °C, and pH on total scale. Assuming constant $[Ca^{2+}]$ in seawater, $[CO_3^{2-}]_{sat}$ is calculated as $[CO_3^{2-}]/\Omega_{calcite}$, and carbonate saturation state (ΔCO_3^{2-}) is given as $[CO_3^{2-}]$ - $[CO_3^{2-}]_{sat}$. Seawater total boron concentration was calculated from by [B]total (μmol/kg) = 416*S/35 (Uppström, 1974), and KB was from DOE (1994) with the pressure corrections of Millero (1995) and the temperature corrections of Dickson (1990b). Hydrographic data for all sites are given in the data appendix.

5.2.3 $\delta^{18}O$ analysis

Foraminiferal $\delta^{18}O$ was analysed from coretops that did not have previously published data in order to asses if they were late Holocene age. Between 5-10 *Uvigerina peregrina* individuals were analysed on a ThermoFinnigan DeltaPLUS XP stable isotope mass spectrometer coupled to a ThermoScientific Gas Bench II at the Bloomsbury

Environmental Isotope Facility (BEIF). Precision of internal and external standards over a large isotopic range is ±0.06‰ for $\delta^{18}O$. All values are reported in the Vienna Pee Dee Belemnite notation (VPDB) relative to NBS-19. Modern equilibrium $\delta^{18}O$ values were calculated using the North Pacific seawater $\delta^{18}O$-salinity relationship of LeGrande and Schmidt (2006), and the *Uvigerina* spp. temperature-fractionation factor relationship of Marchitto et al. (2014). All $\delta^{18}O$ data is given in the data appendix.

5.2.4 Trace element analysis

Between 10 and 25 monospecific *Uvigerina* individuals were cleaned according to the protocol outlined in section 3.4 and Li/Ca, B/Ca, Mg/Ca, Al/Ca, Mn/Ca and Sr/Ca ratios were analysed on UCL's Varian 820 MS according to methods listed in section 3.3. ∼ 30% of samples were analysed with replicates. Trace element/Ca ratios measured in this study are given in the data appendix.

Due to the low abundance of foraminifera from the North Arabian Sea sediments, these samples were analysed by Laser Ablation-Inductively Coupled Plasma-Mass Spectrometry (LA-ICP-MS) at the Royal Netherlands Institue for Sea Research. Individual foraminifera were cleaned with repeated methanol and ultrapure water rinses and single chamber Li/Ca, Mg/Ca, Al/Ca, Mn/Ca and Sr/Ca ratios were determined using ^{7}Li, ^{24}Mg, ^{26}Mg, ^{27}Al, ^{43}Ca, ^{44}Ca, ^{55}Mn and ^{88}Sr, assuming natural isotope abundances (Reichart et al., 2003). ^{11}B was below detection for most samples. All laser spots were 100 µm in diameter, repetition rate was 7 Hz and laser energy density was set at 1 J/cm^2. Time resolved signals were selected for integration, background subtracted, internally standardized to ^{43}Ca, and trace element ratios were calibrated against glass standard NIST 610, which was ablated at 5 J/cm^2). Integration windows in the Qtegra software package were used to seperate the calcite signal from background, and detect contaminants on the test surface. Analytical uncertainty (±1 σ) during the run, based on multiple analyses of in house foraminiferal standard BRUM, was ±2µmol/mol for Li/Ca, ±0.2mmol/mol for Mg/Ca, and ±0.06 mmol/mol for Sr/Ca. An ablated *Uvigerina peregrina* specimen is shown in Figure 5.2, and a typical LA-ICP-MS profile is shown in Figure 5.3. All foraminiferal LA-ICP-MS data is given in the data appendix.

5.2.5 Statistical analysis

Correlations between trace element/Ca ratios and hydrographic variables were assessed using redundancy analysis (RDA) in the *vegan* package in R. All hydrographic data

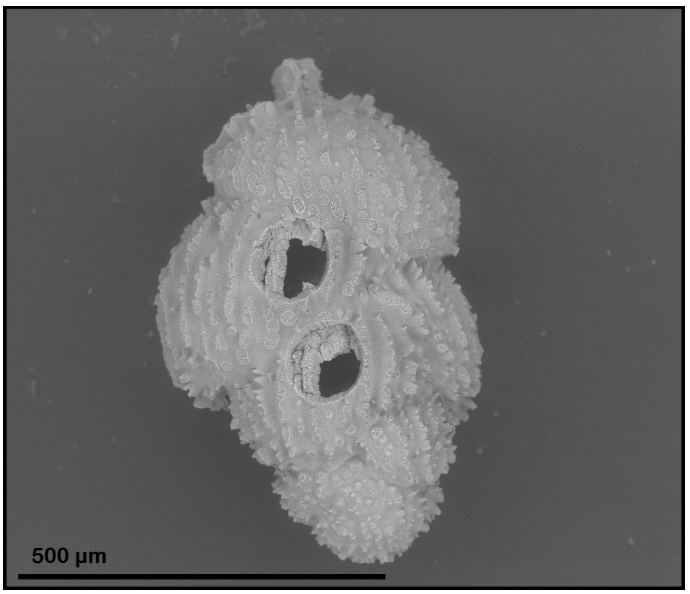

FIGURE 5.2: A *Uvigerina peregrina* specimen following laser ablation.

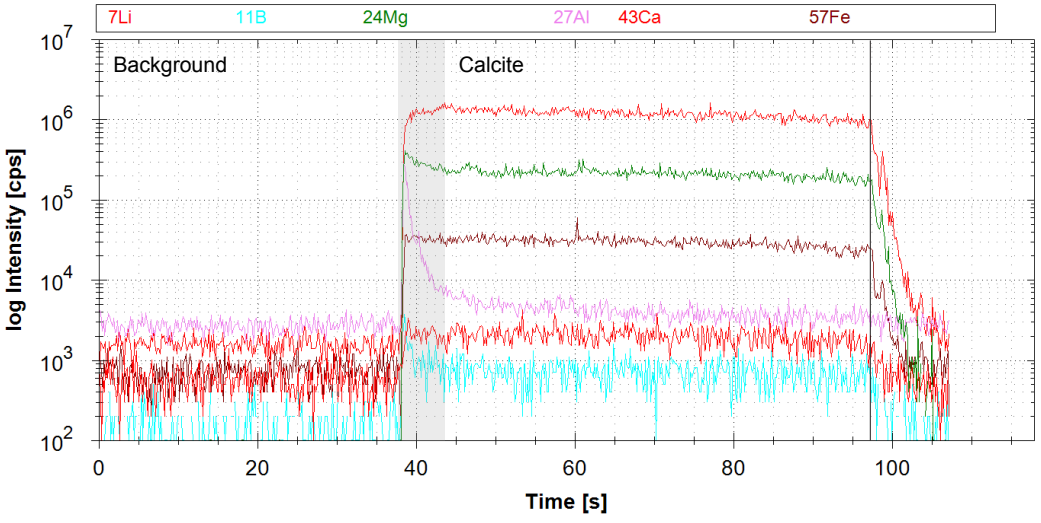

FIGURE 5.3: A typical LA-ICP-MS profile. Contamination on the outside of the test, indicated by high Al, is shown in grey. This part of the profile is not included when calculating elemental ratios.

was scaled and elemental/Ca ratios were assessed both together (as a population) and individually. When assessed together, trace element/Ca ratios were also scaled.

5.3 Results and Discussion

5.3.1 $\delta^{18}O$ analysis

Results are displayed in Figure 5.4. The maximum 1σ variability displayed by replicate foraminiferal samples is ±0.22‰, and the 6 measured samples sitting above the +0.5‰ line (shown in grey) are thus >2σ above modern equilibrium values, implying they are likely older than late Holocene (with seawater enriched in ^{18}O during glacial times, and increased fractionation of ^{18}O into calcite due to colder glacial temperatures), and were excluded from trace element calibrations.

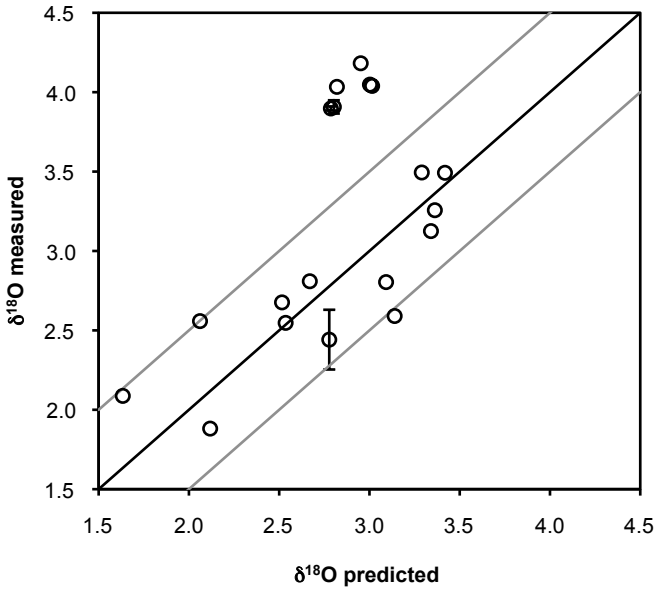

FIGURE 5.4: Measured *Uvigerina peregrina* $\delta^{18}O$ against predicted $\delta^{18}O$. The 1:1 line is shown in black, with ±0.5‰ indicated by the grey lines.

5.3.2 Contamination

Clays and Mn-Fe oxyhydroxide coatings can lead to contamination in trace element studies. However, Al/Ca and Mn/Ca may be used to assess contamination levels as clays contain significant levels of Al, and Mn-Fe oxyhydroxide coatings contain significant levels of Mn (See Chapter 4). Intra-test Mn/Ca and Al/Ca values can be measured by LA-ICP-MS and be used as a base-line against which to compare solution ICP-MS

results. In this study the average Mn/Ca value, as measured by LA-ICP-MS, was 30 μmol/mol, and excluding two anomalously high values of ∼200 μmol/mol, all values were below 70 μmol/mol. This is inkeeping with an upper limit on intra-test Mn of 100 μmol/mol, as suggested by Boyle (1983). The average Al/Ca value, as measured by LA-ICP-MS, was 27 μmol/mol, and excluding four anomalously high values of ∼100 - 300 μmol/mol, all values were below 60 μmol/mol, suggesting an upper limit on intra-test Al/Ca of <100 μmol/mol.

Trace element/Ca ratios measured by solution ICP-MS are shown against Al/Ca and Mn/Ca in Figure 5.5 and Figure 5.6 respectively. Al/Ca ratios are typically below 50 μmol/mol and Mn/Ca ratios typically below 100 μmol/mol, suggesting minimal contamination from clays and Mn-Fe oxyhydroxides. Although Al/Ca ratios of ∼100 μmol/mol and Mn/Ca ratios between ∼200-300 μmol/mol are observed, Al/Ca and Mn/Ca do not correlate with any of the trace element/Ca ratios, suggesting limited influence of contamination within the samples. One coretop sample with high Mn/Ca also has anomalously high Li/Ca (AII125-8 - GGC71), and was removed from the dataset. The samples with high Mn/Ca ratios are all from intermediate depths in the Gulf of California and Okhotsk Sea, where there is a strong oxygen minimum zone, and the suboxic conditions are favourable to Mn-Fe oxyhydroxide precipitation (Lynn and Bonatti, 1965; Froelich et al., 1979).

5.3.3 Ontogenetic variability

Trace element/Ca ratios are plotted against test length in Figure 5.7. As *Uvigerina* spp grow they sequentially add chambers along their length, and as such test length is an approximation to age in this genus. Li/Ca shows a significant negative relationship with test length, with a total decrease of 1 μmol/mol from 450 to 750 μm. B/Ca and Mg/Ca show no relationship with test length, however Mg/Ca ratios are significantly higher by ∼0.2 mmol/mol between 550-650 μm. Sr/Ca decreases with test length, although the relationship is not significant. Augmented Mg incorporation during the mid-development stages has been observed in culture studies of *Bulimina aculeata* (Hintz et al., 2006a), supporting an ontogenetic control on Mg uptake. Inter-chamber Li/Ca, Mg/Ca and Sr/Ca varibility was measured by LA-ICP-MS on two specimens. No variability was seen for Li/Ca and Sr/Ca, however the analytical error was considerably higher than for solution ICP-MS. One individual showed significantly higher Mg/Ca values in its central chamber, while another showed a steady decrease with chamber number, confirming an apparent ontogentic control on Mg uptake in *Uvigerina* spp. (Figure 5.8).

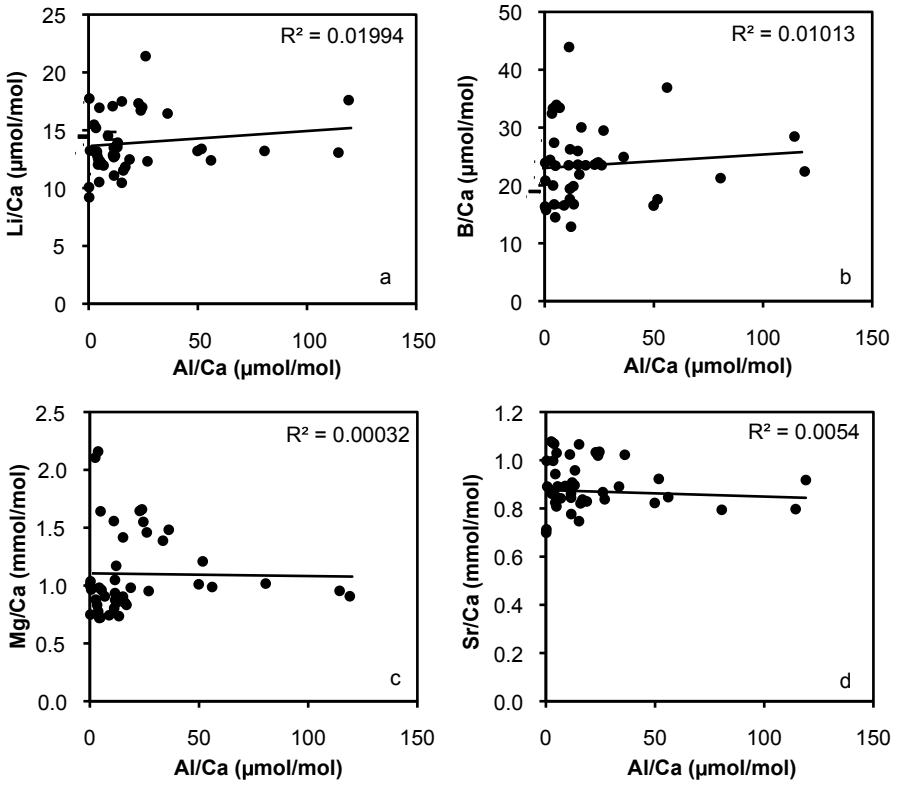

FIGURE 5.5: Al/Ca against (a) Li/Ca (b) B/Ca (c) Mg/Ca (d) Sr/Ca for all coretop samples measured by solution ICP-MS. No relationship is seen between Al/Ca and any of the trace element/Ca ratios.

5.3.4 Multivariate statistical analysis

The *Uvigerina peregrina* Li/Ca, Mg/Ca and Sr/Ca values measured in this study were combined with the *Uvigerina peregrina* Li/Ca, Mg/Ca and Sr/Ca dataset from the Florida Straits. The Li/Ca and Mg/Ca data has previously been publised in Bryan and Marchitto (2008); however the Sr/Ca data are unpublished and I gratefully acknowledge S. Bryan and T. Marchitto for allowing it to be used in this study. Unpublished Li/Ca, B/Ca, Mg/Ca and Sr/Ca values from one coretop sample from the Challenger Plateau were also included, and I acknowledge Aurora Elmore for allowing it to be used in this study. All further discussions will be based around the larger combined dataset, except B/Ca as Bryan and Marchitto (2008) did not measure B/Ca on the Florida Straits coretops. Due to potential differences arising from analytical method, LA-ICP-MS data were not included in the calibrations.

Correlations between hydrographic variables and the first RDA axis of the Li/Ca, Mg/Ca and Sr/Ca dataset are shown in table 5.1, and summarised in a figure 5.9. DIC explains the highest proportion of the total trace element/Ca dataset, with the highest correlation observed between DIC and RDA Axis 1. This is visualised in figure 5.9, where DIC falls

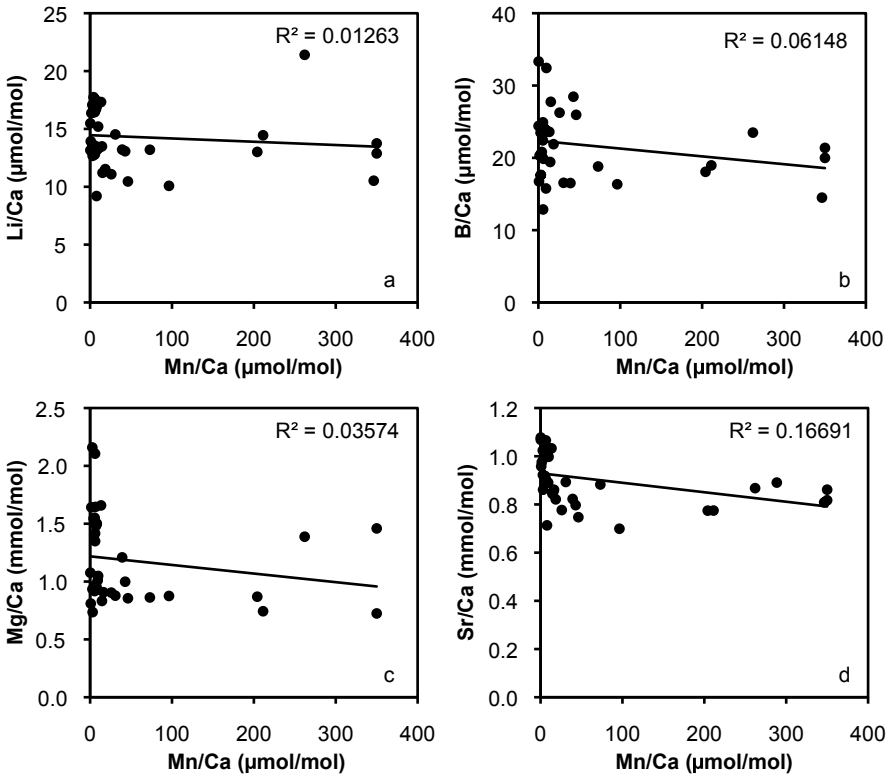

FIGURE 5.6: Mn/Ca against (a) Li/Ca (b) B/Ca (c) Mg/Ca (d) Sr/Ca for all coretop samples measured by solution ICP-MS. No relationship is seen between Mn/Ca and any of the trace element/Ca ratios.

parallel to RDA Axis 1 in the biplot. Correlations between hydrographic variables and each seperate trace element/Ca ratio are also given in table 5.1. Li/Ca and Sr/Ca are most strongly correlated with DIC, while Mg/Ca is most strongly correlated with temperature. It should be noted that significant correlations are observed between both RDA Axis 1, and each trace element/Ca ratio seperately, with several parameters of the carbonate system. This is due to the large degree of auto-correlation between the carbonate system parameters (with all parameters lying close to RDA Axis 1 in figure 5.9), and thus it is not possible to say definitively which parameter is driving the relationship. In each instance it is only possible to say which variable explains the greatest proportion of the trace element/Ca data, and assume this parameter is driving the relationship.

5.3.5 Controls on the uptake of Mg

Redundancy analysis demonstrates temperature explains the greatest proportion of the Mg/Ca data (Table 5.1). Regressing Mg/Ca against temperature using a linear least squares regression gives the relationship,

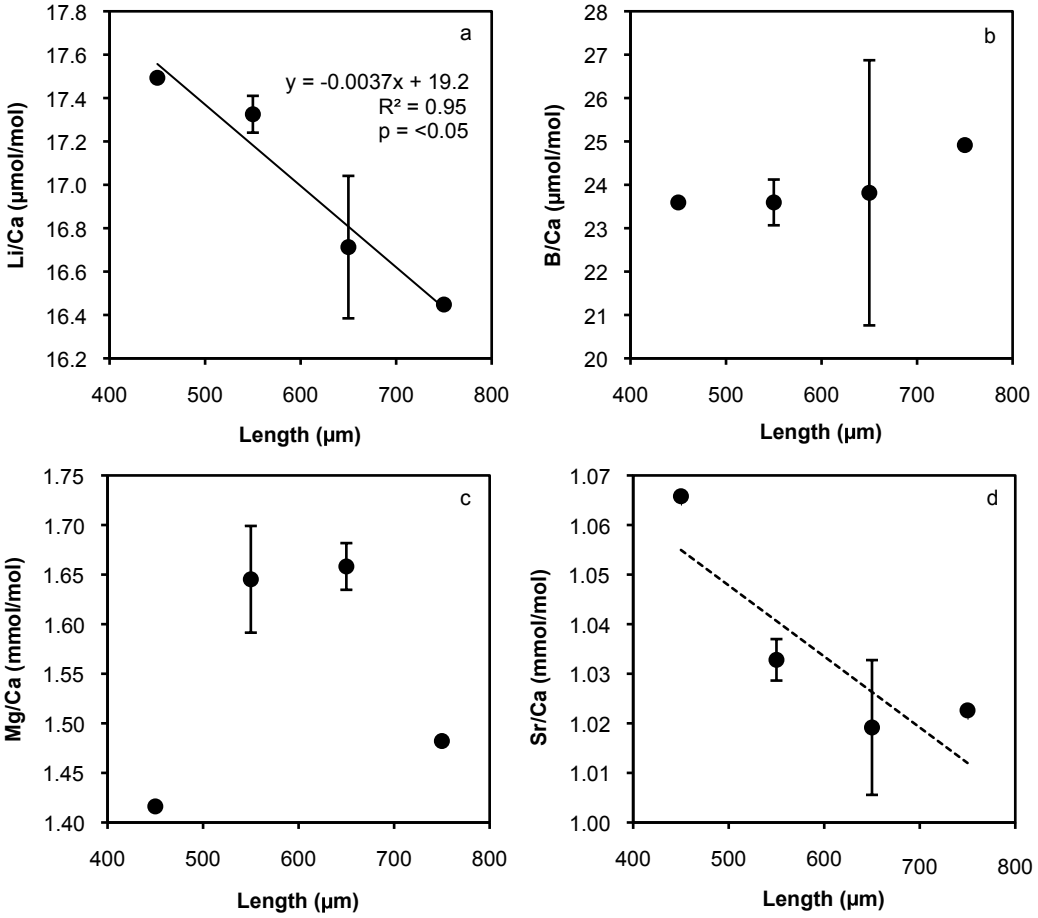

FIGURE 5.7: Test length against (a) Li/Ca (b) B/Ca (c) Mg/Ca (d) Sr/Ca. Foraminifera were seperated into groups of 400-500, 500-600, 600-700 and 700-800 µm test length for analysis.

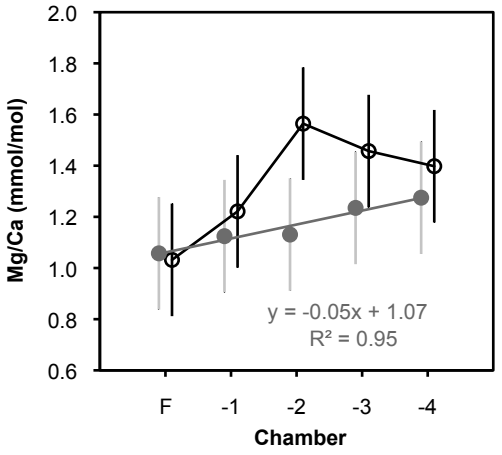

FIGURE 5.8: Variability of Mg/Ca with chamber number of two *Uvigerina peregrina* individuals, measured by LA-ICP-MS.

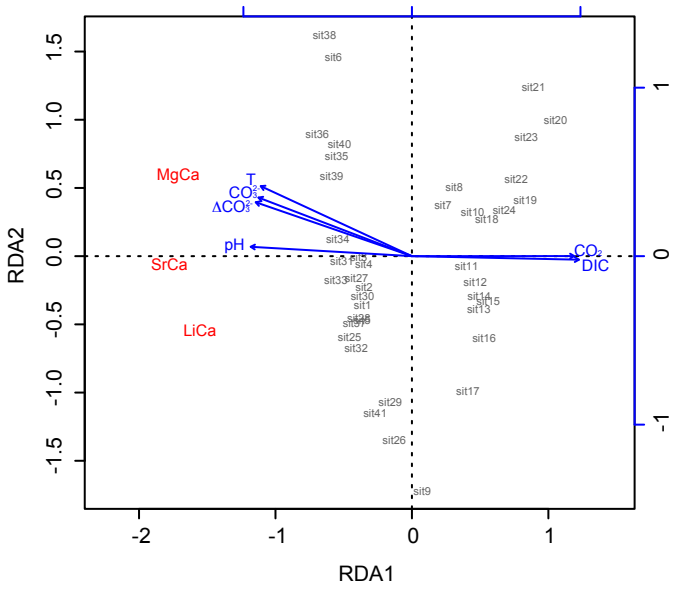

FIGURE 5.9: Biplot of results from redundancy analysis (RDA) of all trace element data (excluding B/Ca) and selected hydrographic variables.

$$Mg/Ca = 0.088 \pm 0.004 * BWT + 0.63 \pm 0.04 \tag{5.2}$$

where Mg/Ca is in mmol/mol and BWT in °C ($R^2 = 0.9$, p =1.6*10^{-22}) (Figure 5.10). The relationship is linear, with the correlation coefficent decreasing significantly if an exponential curve is fitted. The standard error of y in the calibration is ±0.13 mmol/mol ($\sim$ 10%), equivalent to a temperature error of ±1.4 °C. The 1σ standard error is four times higher than the typical 1σ reproducibility of foraminiferal Mg/Ca ($\sim$0.03 mmol/mol), indicating that there are secondary controls on Mg uptake in *Uvigerina peregrina*.

Regressing the Mg/Ca data from $>$ 10 °C and $<$ 10 °C against temperature seperately gives the relationship,

$$Mg/Ca = 0.071 \pm 0.011 * BWT + 0.84 \pm 0.14 \tag{5.3}$$

for sites $>$ 10 °C ($R^2 = 0.81$, p =6.1*10^{-5}) and,

$$Mg/Ca = 0.096 \pm 0.009 * BWT + 0.54 \pm 0.05 \tag{5.4}$$

TABLE 5.1: Results of redundancy analysis of all trace element data except B/Ca (RDA1), and individual element/Ca ratios, with hydrographic variables. tnLi/Ca is temperature normalised Li/Ca (see section 5.3.6). The highest correlation coefficent in each column is shown in bold.

	RDA1	Li/Ca	tnLi/Ca	Mg/Ca	Sr/Ca
Salinity	-0.814	0.599	0.821	0.913	0.770
Temperature	-0.880	0.631	0.914	**0.970**	0.864
Pressure	0.773	-0.675	-0.800	-0.692	-0.795
pH	-0.942	0.783	0.900	0.910	0.945
CO_2	0.950	-0.810	-0.903	-0.903	-0.945
HCO_3^-	0.960	-0.771	-0.947	-0.957	-0.960
CO_3^{2-}	-0.894	0.658	0.886	0.958	0.888
ALK	0.525	-0.650	-0.503	-0.266	-0.549
DIC	**0.977**	**-0.822**	**-0.954**	-0.932	**-0.979**
$\Omega_{Calcite}$	-0.904	0.667	0.900	0.966	0.899
ΔCO_3^{2-}	-0.910	0.679	0.905	0.964	0.906
PO_4^{3-}	0.839	-0.604	-0.820	-0.885	-0.860
SiO_2	0.869	-0.776	-0.854	-0.751	-0.902

for sites $< 10\,^{\circ}C$ ($R^2 = 0.79$, p =2.6*10^{-11}), where Mg/Ca is in mmol/mol and BWT in $^{\circ}C$. Although difference in temperature sensitivity above and below $10\,^{\circ}C$ is less than proposed by Bryan and Marchitto (2008), the difference between the slopes is significant, supporting their asscertion of a higher Mg/Ca-temperature sensitivity below $10\,^{\circ}C$.

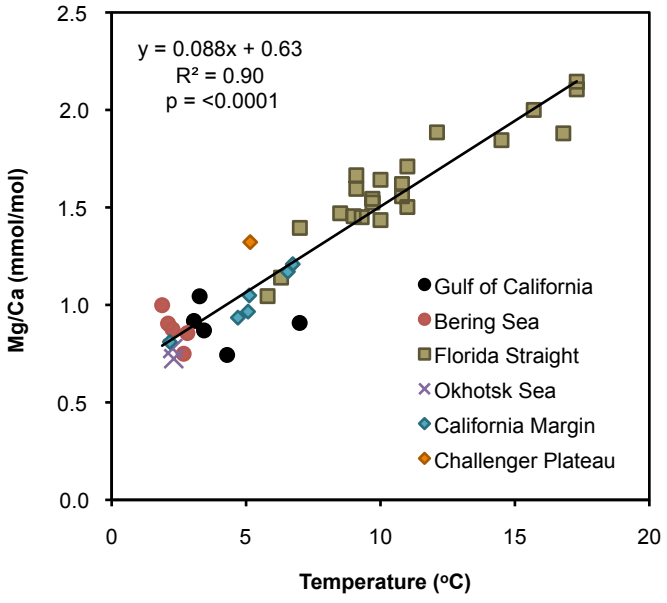

FIGURE 5.10: Linear least squares regression between Mg/Ca and bottom water temperature.

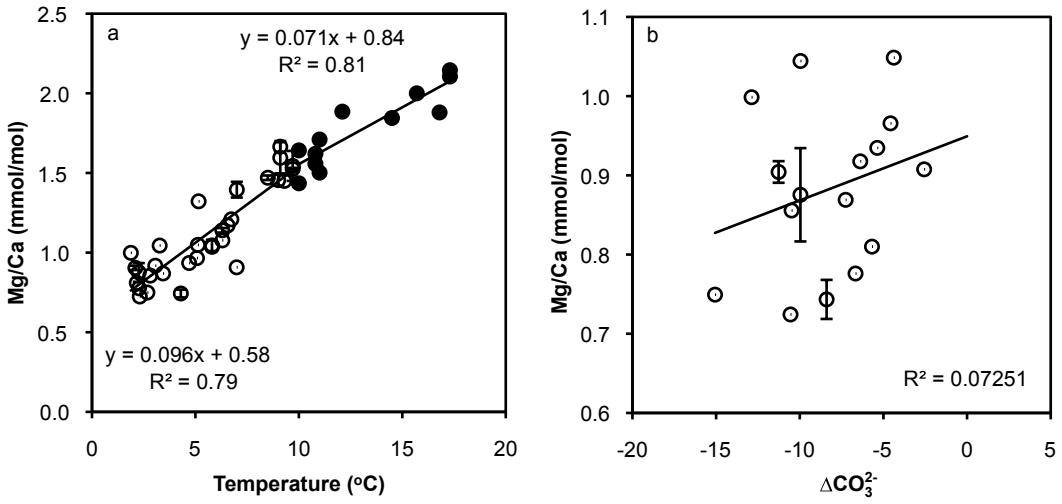

FIGURE 5.11: (a) Mg/Ca regressed against temperature above and below 10 °C (b) Mg/Ca regressed against ΔCO_3^{2-} from sites undersaturated with respect to calcite.

No significant inter-basin offset is seen in *Uvigerina peregrina* Mg/Ca between the North Atlantic and North Pacific (Figure 5.10), despite the deep waters of the North Pacific being at a considerably lower carbonate saturation state (10 to -15 µmol/kg) than the North Atlantic (50-180 µmol/kg), indicating little influence of ΔCO_3^{2-} in the calibration. Furthermore, no relationship is seen between Mg/Ca and ΔCO_3^{2-} in undersaturated waters, where the effect of ΔCO_3^{2-} is hypothesised to be greatest (Figure 5.11). This result suggests no, or very limited, influence of carbonate ion saturation on Mg uptake in *Uvigerina peregrina*, confirming that Mg/Ca_{Uvi} can reliably used as a proxy for deep ocean temperature.

These results pose two further questions (i) why is there a different temperature sensitivity above and below 10 °C and (ii) why is there no ΔCO_3^{2-} effect in *Uvigerina peregrina* when it is observed in other species? Bryan and Marchitto (2008) proposed that the difference in temperature sensitivity above and below 10 °C could be due to either an influence of ΔCO_3^{2-} at low temperatures increasing the apparent temperature sensitivity, or reduced Mg inclusion in super-saturated waters, as observed in cultured planktonic and benthic foraminifera (Lea et al., 1999; Russell et al., 2004; Hintz et al., 2006b). Given that ΔCO_3^{2-} does not seem to influence Mg uptake at low temperatures/saturation states, a reduced apparent temperature sensitivity due to inhibited Mg incorporation in super-saturated waters seems the most plausible explanation. This hypothesis could be tested by analysing foraminifera grown at temperatures above 10 °C, but at low saturation states (<50 µmol/kg). However currently, this scenario does not occur anywhere naturally in the ocean and thus would

have to be tested using cultured foraminifera (or we could just give anthropogenic CO_2 emmissions a few more years!).

Elderfield et al. (2006, 2010) proposed that the lack of a ΔCO_3^{2-} effect in *Uvigerina peregrina* was due to their infaunal habitat, which would be buffered against under-saturated waters by $CaCO_3$ dissolution. While this could explain the Mg/Ca data, the strong influence of seawater carbonate system parameters on other trace elements in *Uvigerina peregrina* (see table 5.1 and discussion below), makes this mechanism unlikely. The lack of ΔCO_3^{2-} effect on *Uvigerina peregrina* Mg/Ca is therefore more likely a result of differences in biomineralisation compared to *Cibicidoides* spp. The more common occurance of *Uvigerina peregrina* in low- and under- saturated waters suggests they have developed biochemical advantages to calcifying in low- and under- saturated waters, which in turn may involve, or have indirectly affected, the incorporation of Mg.

5.3.6 Controls on the uptake of Li

When Li/Ca ratios are plotted against ΔCO_3^{2-} considerable differences can be seen between the North Atlantic and North Pacific basins (Figure 5.12). While the North Atlantic data fall along a gentle negative slope, Li/Ca increases steeply with increasing ΔCO_3^{2-} in the North Pacific ocean. Redundancy analysis shows DIC explains the greatest proportion of the Li/Ca data (Table 5.1), although the significant change relationship observed between ocean basins indicates that Li uptake is not a simple, singular function of temperature, carbonate ion saturation, or any other parameter of the carbonate system. Taking the Li/Ca-ΔCO_3^{2-} sensitivity of Lear et al. (2010) and normalising the data to a constant saturation state, Li/Ca values fall very close ot the inorganic temperature line in highly-saturated waters. However, the data from low- and under-saturation states fall below the inorganic temperature line (Figure 5.13).

If the difference between expected Li/Ca based on measured BWT and the inorganic calcite Li/Ca-temperature relationship of Marriott et al. (2004a), and measured *Uvigerina peregrina* Li/Ca is plotted against ΔCO_3^{2-} a significant, non linear relationship can be seen (Figure 5.13). This suggests that Li uptake is controlled both by temperature, with a similar sensitivity as inorganic calcite, and also some parameter of the carbonate system, with the linear ΔCO_3^{2-} sensitivity of Lear et al. (2010) inadequately explaining the data at low- and under- saturated states. Redundancy analysis of temperature normalised Li/Ca (normalised using the inorganic calcite Li/Ca-temperature sensitivity of Marriott et al. (2004a)) shows DIC explains the greatest proportion of the Li/Ca data after the effects of temperature are removed (Table

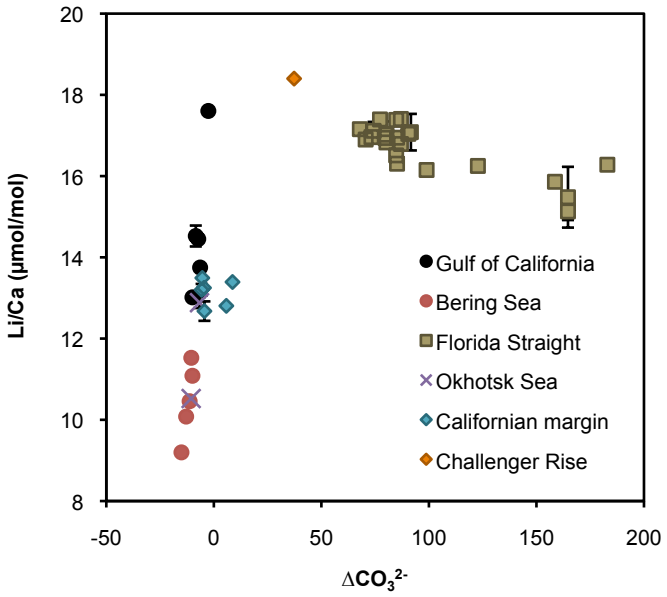

FIGURE 5.12: Li/Ca plotted against ΔCO_3^{2-}, with the different basins indicated.

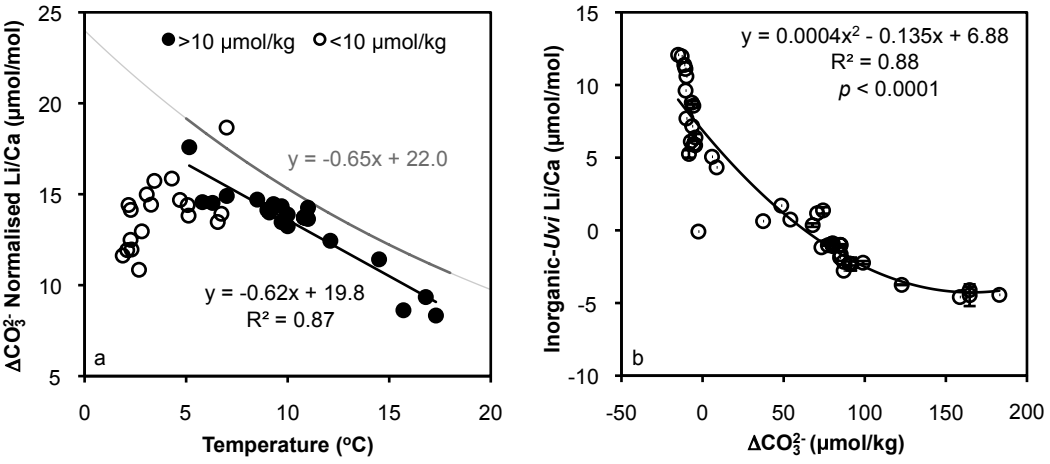

FIGURE 5.13: (a) ΔCO_3^{2-} normalised Li/Ca plotted against bottom water temperature. Li/Ca was normalised with the ΔCO_3^{2-} sensitivity of Lear et al. (2010). Sites from high saturation states (> 10 µmol/kg) are shown by the filled circles, and sites with low- and under- saturated bottom waters (< 10 µmol/kg) are shown by the open circles. The inorganic calcite Li/Ca-temperature line of Marriott et al. (2004a) is shown in light grey. The first order linear approximation of the inorganic temperature sensitivity in the temperature range of the high-saturation sites is shown in heavy grey (b) The difference betwen expected Li/Ca based on measured BWT and the inorganic calcite Li/Ca-temperature relationship of Marriott et al. (2004a), and measured *Uvigerina peregrina* Li/Ca plotted against ΔCO_3^{2-}. Removing the outlying sample results in no significant difference to the relationship, and R^2 increases to 0.93.

5.1). Removing the outlying sample in figure 5.14, a linear least squares regression of temperature normalised Li/Ca (Li/Ca_{TN}) and DIC gives the relationship,

$$Li/Ca_{TN} = -0.045 \pm 0.002 * DIC + 123 \pm 4.0 \tag{5.5}$$

where Li/Ca_{TN} is in μmol/mol and DIC in μmol/kg ($R^2 = 0.94$, $p = 2.2 * 10^{-26}$). Including the outlying sample results in no significant change to the relationship, however R^2 decreases to 0.91. The standard error of y in the calibration is ±1.3 μmol/mol (∼ 6%), equivalent to a DIC error of ±28 μmol/kg.

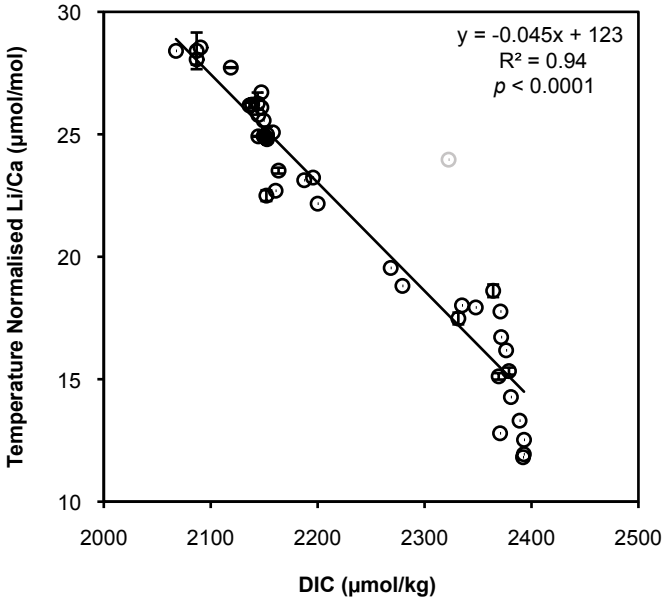

FIGURE 5.14: Temperature normalised Li/Ca plotted against DIC. The data were normalised using the inorganic calcite Li/Ca-temperature relationship of Marriott et al. (2004a). Including the outlying sample (shown in grey) results in no significant difference to the relationship ($y = -0.044x + 120$), however R^2 decreases to 0.91.

The strong correlation between DIC and Li/Ca_{TN} in equation 5.5 suggests that if temperature is known, Li/Ca_{TN} can be used to reconstruct DIC. Lear et al. (2010) used a simultaneous approach to reconstruct past BWT and ΔCO_3^{2-} using Mg/Ca and Li/Ca in *Cibicidoides pachyderma*. The same approach can be used with *Uvigerina peregrina*, except as demonstrated in section 5.3.5, the sensitivity of *Uvigerina peregrina* Mg/Ca to ΔCO_3^{2-} is ∼0. Using the quadratic approximation to the exponential inorganic calcite Li/Ca temperature relationship of Marriott et al. (2004a), and the Mg/Ca temperature relationship in equation 5.2 gives the following relationship,

$$DIC = \frac{\left(Li/Ca - \left(0.0157 * \left(\frac{Mg/Ca - 0.63}{0.088}\right)^2 - 1.019 * \left(\frac{Mg/Ca - 0.63}{0.088}\right)\right)\right) - 123}{-0.045} \quad (5.6)$$

where DIC is in μmol/kg, Li/Ca in μmol/mol and Mg/Ca in mmol/mol. The slope and intercept of the Mg/Ca-temperature relationship can be substituted for those in equations 5.3 and 5.4 if reason dictates temperatures were likely to be above or below 10 °C respectively. Propagating the Mg/Ca and Li/Ca calibration errors quadratically results in a total DIC error of ±34 μmol/kg.

5.3.7 Controls on the uptake of Sr

Redundancy analysis shows DIC explains the greatest proportion of the Sr/Ca data (Table 5.1). A linear least squares regression of Sr/Ca and DIC gives the relationship,

$$Sr/Ca = -0.00116 \pm 0.0001 * DIC + 3.77 \pm 0.13 \quad (5.7)$$

where Sr/Ca is in mmol/mol and DIC in μmol/kg ($R^2 = 0.90$, $p = 1.6 * 10^{-21}$) (Figure 5.15 and 5.9). The standard error of y in the calibration is ±0.04 mmol/mol (∼ 4%), equivalent to a DIC error of ±37 μmol/kg. Planktonic foraminiferal culturing studies have demonstrated that Sr/Ca increases with both increasing temperature and pH (Lea et al., 1999). While temperature does show a significant relationship with Sr/Ca, it is most likely due to the autocorrelation of temperature and DIC in the calibration, as the correlation with DIC is considerably higher (Figure 5.15).

No inter-basin differences are seen between Sr/Ca in the Atlantic and Pacific. This is contrary to the findings of Yu et al. (2014) for the *Cibicidoides* genus, where y intercept offsets are seen between basins. The lack of interbasin differences seen in this study suggest the differences seen by Yu et al. (2014) may relate to inter-basin differences in *Cibicidoides* morpho- or geno-type, rather than differences in seawater Sr/Ca, which would be manifested across genera. The strong correlation between Sr/Ca and DIC indicates the potential of *Uvigerina peregrina* Sr/Ca to reconstruct past DIC concentrations.

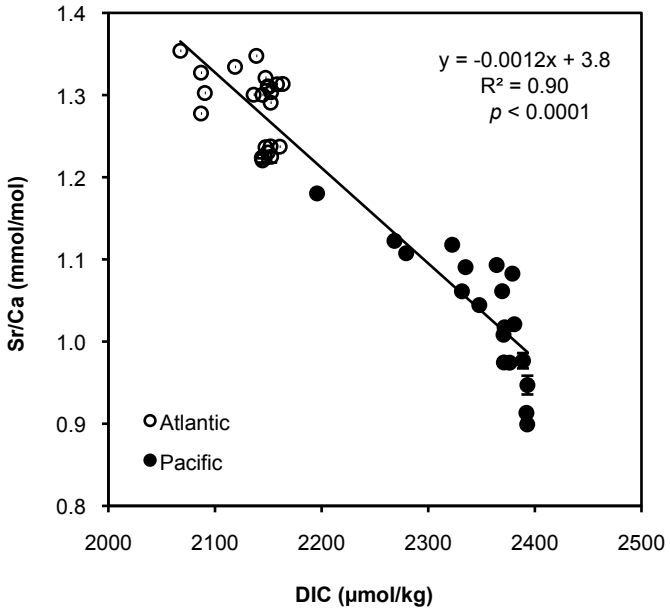

FIGURE 5.15: Sr/Ca plotted against DIC. Atlantic sites are shown by open circles and Pacific sites are shown by closed circles.

5.3.8 Controls on the uptake of B

B/Ca was not measured on the Florida Straits coretops by Bryan and Marchitto (2008), so the B/Ca dataset (n = 25) is considerably smaller than for Li, Mg and Sr. Redundancy analysis of B/Ca and hydrographic variables shows DIC explains the highest proportion of the B/Ca data (Table 5.2). A linear least squares regression of B/Ca and DIC gives the relationship,

$$B/Ca = -0.038 \pm 0.005 * DIC + 103 \pm 11.5 \tag{5.8}$$

where B/Ca is in µmol/mol and DIC in µmol/kg ($R^2 = 0.72$, $p = 7.8 * 10^{-8}$) (Figure 5.15). The standard error of y in the calibration is ±1.2 µmol/mol (∼ 14%), equivalent to a DIC error of ±55 µmol/kg. When regressed against ΔCO_3^{2-} the resulting slope is 0.08 µmol/mol/µmol/kg. This is considerably lower than previosuly published studies have found for *Uvigerina* spp., with a sensitivity of 0.27 µmol/mol/µmol/kg in the calibration of Yu and Elderfield (2007). The difference in sensitivies may be due to interspecies differences as the calibration of Yu and Elderfield (2007) used mixed species *Uvigerina*, rather than monospecific *Uvigerina*. The significant correlation between B/Ca and DIC suggests *Uvigerina peregrina* B/Ca may be used to reconstruct past ocean DIC concentration. However, as the correlation is weaker than observed with Li/Ca and Sr/Ca, the equivalent error in reconstructed DIC will be considerably higher.

TABLE 5.2: Results of redundancy analysis of B/Ca with hydrographic variables. The highest correlation coefficent is shown in bold.

	B/Ca
Salinity	0.737
Temperature	0.766
Pressure	-0.648
pH	0.828
CO_2	-0.823
HCO_3^-	-0.850
CO_3^{2-}	0.775
ALK	-0.543
DIC	**-0.866**
ΔCO_3^{2-}	0.8108
$\Omega_{Calcite}$	0.794
Kb	0.604
TBoron	0.737
$B(OH)_4^-$	0.782
$B(OH)_4^-/HCO_3^-$	0.779

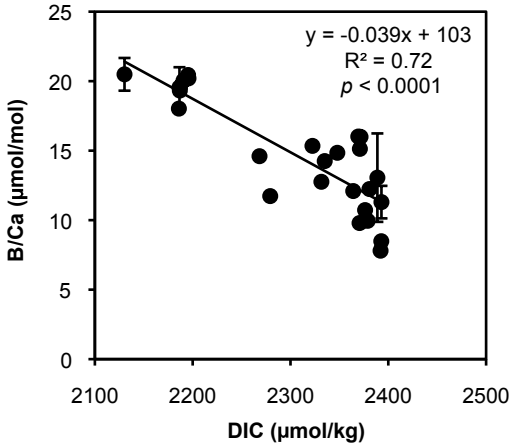

FIGURE 5.16: *Uvigerina peregrina* B/Ca plotted against DIC.

5.3.9 Mechanisms for a carbonate system control on trace element incorporation

If trace element/Ca ratios are to be used as environmental proxies it is necessary to develop a mechanistic understanding of their incorporation in order that the relationships can confidently be applied in the past. Due to the greater size of the datasets, most of the discussion will be focussed on mechanisms for the incorporation of Li and Sr.

Regressing Sr/Ca and B/Ca against Li/Ca_{TN} shows there is a high degree of auto-correlation between the trace element/Ca ratios (Figure 5.17), suggesting a similar control on Li/Ca_{TN}, B/Ca and Sr/Ca in *Uvigerina peregrina*. As discussed above, DIC best explains the uptake of these trace elements (Table 5.1 and 5.2), with Li/Ca_{TN}, Sr/Ca and B/Ca all displaying highly significant correlations with DIC (Figures 5.14, 5.15, and 5.16). However, due to the high degree of auto-correlation between carbonate system parameters, Li/Ca_{TN}, Sr/Ca and B/Ca also all show highly significant positive correlations with ΔCO_3^{2-} (R^2=0.93, 0.89 and 0.63 respectively), and negative correlations with HCO_3^- (R^2=0.93, 0.87 and 0.7 respectively).

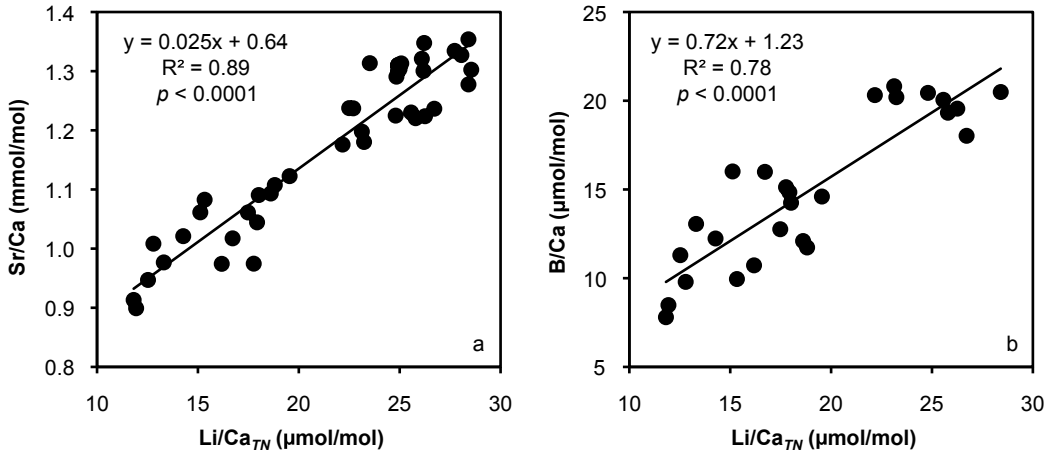

FIGURE 5.17: Li/Ca_{TN} plotted against (a) Sr/Ca and (b) B/Ca

It is the variation in DIC that predominantly drives changes in ΔCO_3^{2-} (through $[CO_3^{2-}]$) within the dataset (R^2=0.99), and as almost all DIC is present as HCO_3^- at the pH of seawater, these parameters are also highly positively correlated (R^2=0.99). As such, it is not possible to say it is DIC that is directly driving the relationship with Li/Ca_{TN}, Sr/Ca and B/Ca. However, a direct control is implied by the strongest correlation occurring between the trace element/Ca ratios and DIC.

The unusual hydrography of the intermediate depth (600-2000 m) Southern California margin offers an opportunity to begin to deconvolve the effects of different carbonate system parameters on trace element uptake. The hydrography in this region is such that between $\sim$ 600 and 2000 m water depth DIC increases with depth, but ΔCO_3^{2-} remains constant ($\pm$ 1 µmol/kg (Figure 5.18). This is because the increase in calcite solubility with depth (due to pressure and temperature) is balanced by an increase in alkalinity relative to DIC (and thus $[CO_3^{2-}]$), due to the deeper remineralisation of $CaCO_3$ compared to C_{org} (Figure 5.18).

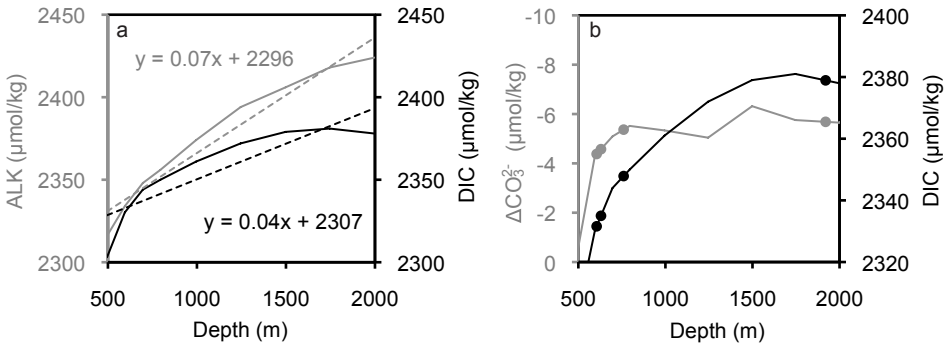

FIGURE 5.18: Seawater carbonate chemistry of the Southern Califronia margin (a) Alkalinity and DIC and (b) ΔCO_3^{2-} and DIC plotted against water depth. The depths of the coretops in this study are shown by circles.

At present the dataset is very limited from this region (n = 4), however this still provides some indication of whether ΔCO_3^{2-}, or some other parameter of the carbonate system, is controlling trace element uptake. Li/Ca_{TN} and Sr/Ca are plotted against CO_3^{2-}, HCO_3^-, CO_2 and DIC in figures 5.19 and 5.20. Relationships can be seen between each of the carbonate system parameters and Li/Ca_{TN}, but not with Sr/Ca. This suggets ΔCO_3^{2-} is not driving the relationship observed between DIC and Li/Ca_{TN}, and is likely to be driving the relationship observed with Sr/Ca. At present this dataset is too small to draw significant conclusions, but does suggest that the mechanisms controlling the uptake of Li and Sr maybe subtely different, as well as highlight the potential of the Southern Californian margin (and other regions with unusual hydrography) in deconvolving the controls on trace element uptake, if the dataset can be expanded.

Elderfield et al. (1996) proposed a Rayleigh distillation model for the incorporation of trace elements into foraminiferal calcite, where trace elements are incorporated into calcite from vacuolised seawater with the inorganic calcite partition coefficients. In the model the element/Ca ratio of the vacuole begins at (or close to) that of seawater, and becomes progressively enriched in the element if the partition coefficent (D) is < 1, or depleted in the element if D is > 1. Both the flushing rate of the calcification reservoir and calcification rate control the fraction remaining of the calcification pool (f), and thus the degree of Rayleigh distillation. If the calcification rate or flushing rate are a function of some parameter of the carbonate system (most likely ΔCO_3^{2-}), that parameter will control the degree of Rayleigh distillation and thus the element/Ca ratio of the calcite. The following Rayleigh distillation model was used to assess the controls on the uptake of Sr and Li in *Uvigerina peregrina*,

$$X/Ca_{calcite} = \left(X/Ca_{sw} \cdot f^{D_X - 1}\right) \cdot D_X \tag{5.9}$$

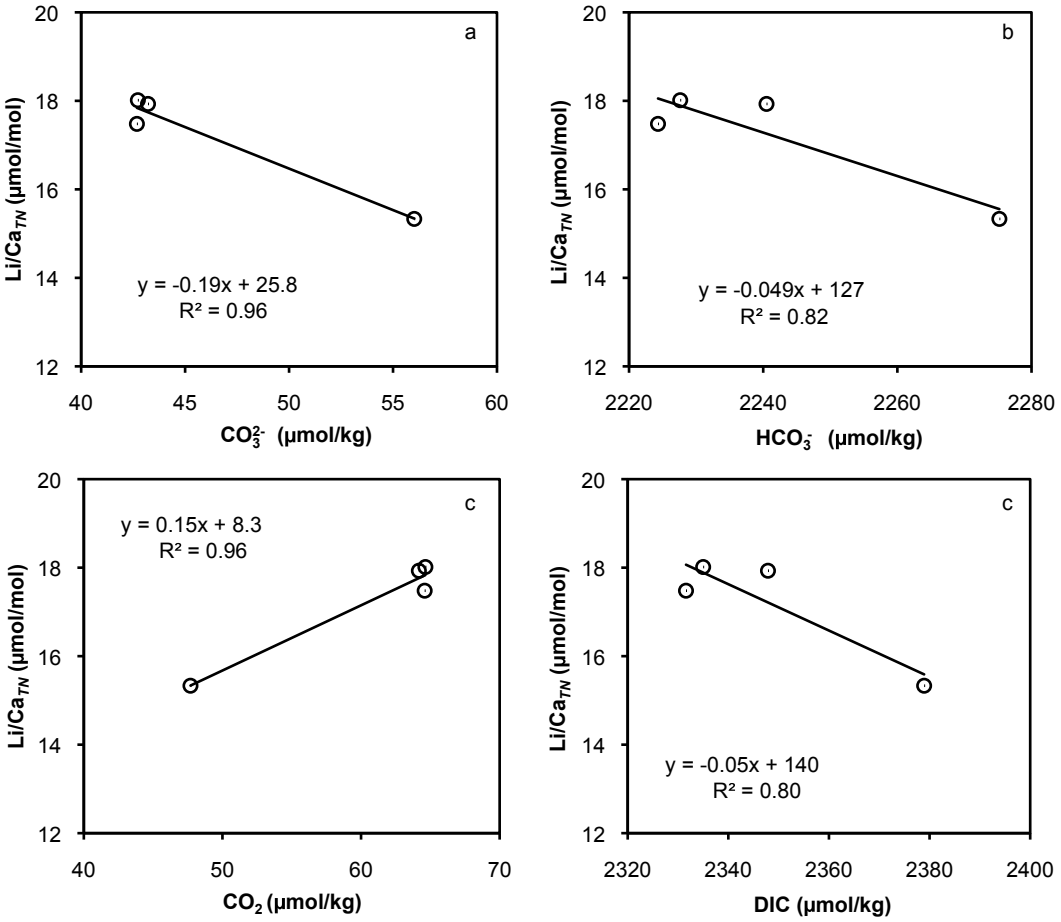

FIGURE 5.19: Li/Ca_{TN} plotted against (a) CO_3^{2-} (b) HCO_3^- (c) CO_2 (d) DIC from > 600 m water depth in the Southern California margin, below which ΔCO_3^{2-} remains ~ constant.

where $X/Ca_{calcite}$ is the element/Ca ratio of calcite, X/Ca_{sw} is the element/Ca ratio of seawater, f is the fraction of the calcification reservoir remaining, and D_X is the elemental partition coefficent for inorganic calcite. For lithium, the 2 and 20 °C inorganic calcite Li partition coefficients of Marriott et al. (2004b) were used. For strontium D_{Sr} was calculated using the 5 °C D_{Sr}-calcification rate relationship of Tang et al. (2008), and foraminiferal calcification rates of 4 and 40 µmol m^{-2} hr^{-1} (Erez, 2003) were adopted. A calcification rate of 40 µmol m^{-2} hr^{-1} has been measured in planktonic foraminifera, although the calcification rate of benthic foraminifera is likely to be considerably (up to an order of magnitude) lower (Erez, 2003), hence the range used here. The model adequately describes Sr/Ca ratios in *Uvigerina peregrina*, with measured Sr/Ca values falling within the range predicted by the model (Figure 5.21), necessitating that between 55 to 85 % of the calcification reservoir is used in order to match the measured Sr/Ca values. The model suggests DIC (via ΔCO_3^{2-}) could control Sr/Ca through either a control on vacuole flushing time, and thus f, or simply by the calcification rate control

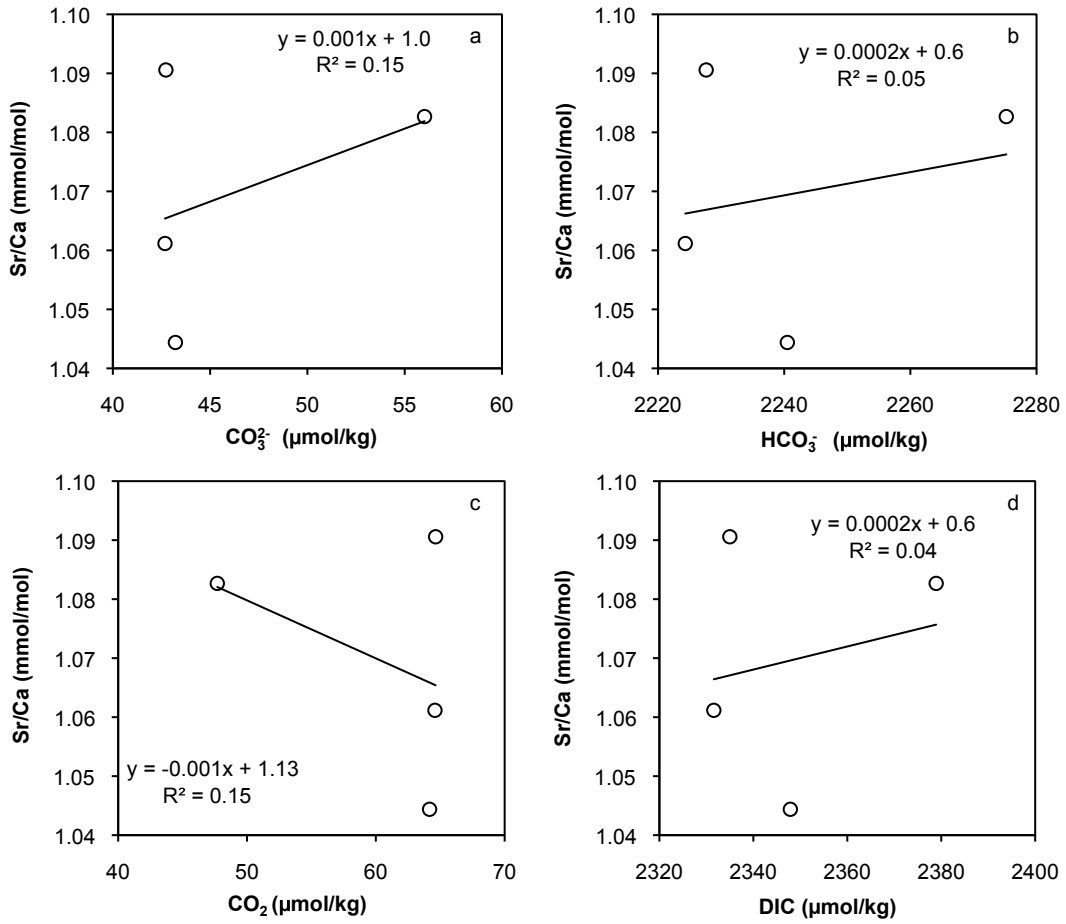

FIGURE 5.20: Sr/Ca plotted against (a) CO_3^{2-} (b) HCO_3^- (c) CO_2 (d) DIC from > 600 m water depth in the Southern California margin, below which ΔCO_3^{2-} remains ∼ constant.

on D_Sr, which can vary Sr/Ca in the measured range at a constant f, and at feasible foraminiferal calcification rates (highlighted by the 4 and 40 µmol m^{-2} hr^{-1} calcification rate lines in figure 5.21).

While the model predicts Li/Ca within the measured range for the 20 °C inorganic calcite partition coefficient, necessitating that between ∼ 0 and 24 % of the internal reservoir is utilised, predicted Li/Ca ratios using the 2 °C partition coefficient lie above measured values. This discrepency is most likely due to different calcification rates of inorganic and benthic foraminiferal calcite, with foraminifera generally calcifying more slowly than inorganic calcite by a factor of at least ∼2.5 (Erez, 2003) (unless the inorganic calcites are precipitated from artificial seawater), and the uptake of other alkali metals into inorganic calcite being highly sensitive to calcification rate and impurity concentration (Busenberg and Plummer, 1985). Until the sensitivity of Li uptake to calcification rate in inorganic calcite is known it is not possible to assess if the discrepency

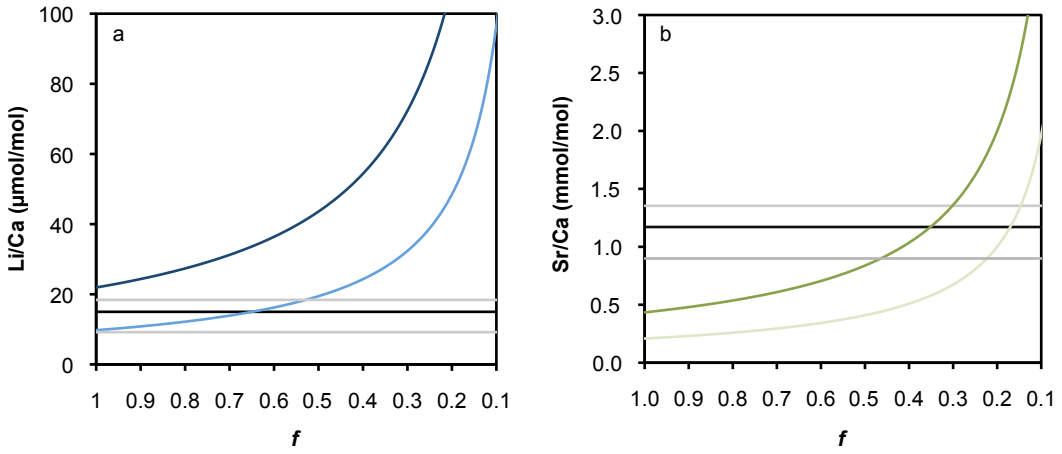

FIGURE 5.21: Rayleigh model results for (a) Li/Ca with the inorganic calcite D_{Li} from Marriott et al. (2004b) at 2 °C in dark blue and 20 °C in light blue (b) Sr/Ca with the inorganic calcite D_{Sr} from Tang et al. (2008) for calcification rates of 4 (light green) and 40 (dark green) µmol m^{-2} hr^{-1}. Average measured *Uvigerina peregrina* Li/Ca and Sr/Ca ratios from this study are indicated by the horizontal black line, with the full measured range shown by the grey lines.

between f predicted by Li/Ca and Sr/Ca is real (which would imply a different uptake mechanism for the two elements), or an artefact of different foraminiferal and inorganic calcification rates. Assuming it is an artefact of calcification rate, DIC (via ΔCO_3^{2-} or some other carbonate system parameter) could control Li/Ca through either a control on flushing time, and thus f, or directly via the calcification rate control on D_Li. Different calcification rates between foraminifera and inorganic calcite are unlikely to affect the temperature sensitivity of Li, although this warrants further testing.

The rayleigh distillation model provides a possible mechanism to directly relate DIC to the observed Li/Ca and Sr/Ca trends, if the ability of foraminifera to regulate vacuole pH during calcification is considered. Given that foraminifera can regulate their internal pH during calcification (De Nooijer et al., 2009) (Figure 2.8), all DIC species within the vacuolised seawater can be speciated to $[CO_3^{2-}]$, and used during calcification. The dependency on vacuole fluching time could thus depend on the initial DIC concentration, rather than the initial $[CO_3^{2-}]$ of the vacuolised seawater. At low seawater DIC concentrations flushing rate would be reduced, leading to a higher degree of distillation, and increased trace element/Ca ratios in the foraminiferal calcite.

Taking the empirical results and model findings together, Sr uptake in *Uvigerina peregrina* is most likely driven by the influence of DIC (probably via its control on ΔCO_3^{2-}) on calcification rate or vacuole flushing time. Li uptake is controlled by DIC (most probably via some other parameter of the carbonate system) through its effects

on either calcification rate or vacuole flushing time. Due to the high degree of auto-correlation between carbonate system parameters it is not possible to draw further conclusions regarding the exact mechanisms driving the relationships seen between trace element/Ca ratios and DIC, and a greater understanding of Li uptake in inorganic calcite is required before a mechanistic understanding of Li uptake in foraminifera can be developed. A potentially interesting outcome of these findings is that if Li and Sr do have slightly different carbonate system controls, and if they can be deconvolved and understood, then several parameters of seawater carbonate chemistry could be reconstructed simultaneously using multiple trace elements in foraminifera - an exciting prospect!

5.3.10 Porewater influence

Due to the infaunal habitat of *Uvigerina peregrina*, trace element uptake in this species may be sensitive to changes in porewater chemistry, as suggested by the $\delta^{13}C$ and $\delta^{11}B$ offsets observed between infaunal and epifaunal foraminifera (McCorkle et al., 1997; Rae et al., 2011). Modelling work indicates changes in porewater carbonate chemistry relative to seawater can occur at, or immediately below, the sediment-water interface (Zeebe, 2007), and large changes in saturation state can be seen within the upper few centimeters of the North Arabian sea multicore profile (Figure 5.22). The ΔCO_3^{2-} changes within the porewaters are mainly driven by changing pH, due to respiration of organic matter within the sediments.

With the exception of one Sr/Ca data point, all measured foraminiferal Li/Ca and Sr/Ca values are within error of the Li/Ca and Sr/Ca ratios predicted using the trace element/Ca-ΔCO_3^{2-} relationships presented in this study, and measured GLODAP seawater ΔCO_3^{2-} for the site (dashed line, figure 5.22). A muted response to changing porewater ΔCO_3^{2-} can be seen in the foraminiferal Li/Ca data, with slightly lower Li/Ca values at the depths of the most under-saturated porewaters, and slightly higher values where porewaters are super-saturated, but the values remain within error of Li/Ca predicted from seawater throughout. Sr/Ca values show no response to porewater ΔCO_3^{2-}. This suggests that despite the large changes in porewater ΔCO_3^{2-}, the foraminifera are mainly responding to the ΔCO_3^{2-} of seawater. Infaunal foraminifera are known to migrate through the sediment during their lifecycle (McCorkle et al., 1997). As the overlying seawater is more saturated with respect to calcite than the porewaters at this site, the foraminifera may be migrating upwards towards the seawater to calcify (as this would be the most energy efficient place to precipitate calcite), and thus the foraminiferal calcification would occur at, or close to, the ΔCO_3^{2-} state of seawater.

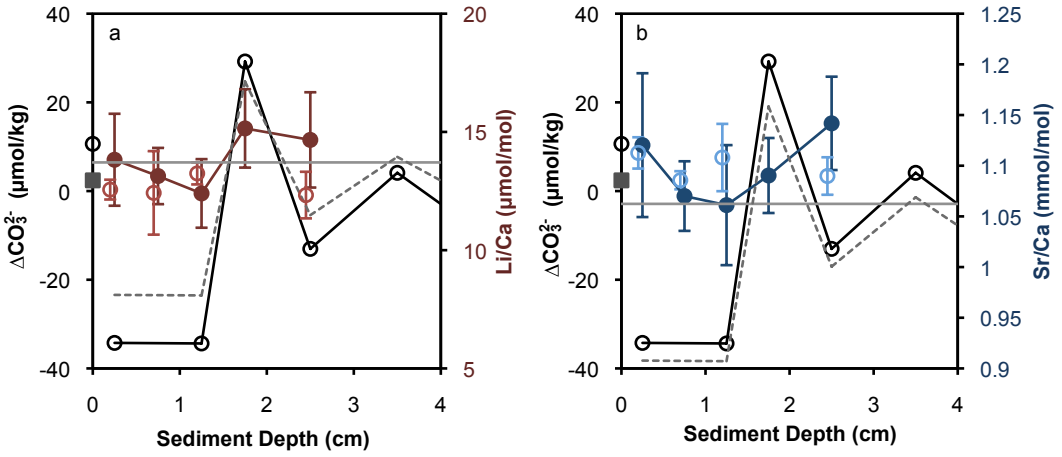

FIGURE 5.22: Porewater profile from the North Arabian Sea showing the effects of porewater chemistry on (a) Li/Ca and (b) Sr/Ca. Seawater ΔCO_3^{2-} is shown by the filled squares (GLODAP) and open circles (Utrecht University), and porewater ΔCO_3^{2-} is indicated by the solid black line and open circles. Element/Ca ratios, predicted by the relationships presented in this study, are indicated for GLODAP seawater ΔCO_3^{2-} (solid grey line) and porewater ΔCO_3^{2-} (dashed grey line). Measured foraminiferal element/Ca ratios are shown by the coloured circles for both living (filled circles) and dead (open circles) foraminifera.

Figure 5.22 also shows Li/Ca and Sr/Ca ratios from dead foraminifera are always within error of recently living foraminifera, indicating any effects of dissolution are minimal. These results indicate dissolution and changing porewater carbonate chemistry have little influence on Li/Ca and Sr/Ca in *Uvigerina peregrina*, demonstrating they may be used to reconstruct seawater carbonate chemistry in the past. However, care should be taken when interpreting seawater chemistry reconstructions when large changes in organic matter or $CaCO_3$ have occurred within the sediment.

5.4 Conclusions

- The uptake of Mg in *Uvigerina peregrina* is mainly controlled by temperature, with a higher Mg/Ca temperature sensitivity below 10 °C, likely due to the supression of Mg inclusion at high saturation states. ΔCO_3^{2-} does not affect Mg/Ca in *Uvigerina peregrina* at low temperatures/saturation states indicating it can reliably be used as a proxy for bottom water temperature in the past.

- Li uptake is controlled by both temperature and seawater carbonate chemistry. The temperature sensitivity of Li uptake appears to be close to that of inorganic calcite, and if the effects of temperature are accounted for by normalisation to a constant temperature (Li/Ca_{TN}), a strong correlation is observed with

several carbonate system parameters, but most significantly with DIC. Mg/Ca temperature can be used to correct Li/Ca ratios for the effects of temperature, enabling it to be used as a proxy for past seawater DIC concentrations.

- Sr/Ca shows a highly significant relationship with several carbonate system parameters, but most significantly with DIC, implying it can be used as a proxy for past past seawater DIC concentrations.

- B/Ca shows is well correlated with several carbonate system parameters. The sensitivity to ΔCO_3^{2-} is considerably lower than published elsewhere, most likely due to inter-species effects.

- The auto-correlation of carbonate system parameters within the dataset means the specific carbonate system parameter driving the observed relationships cannot be deconvolved. A Rayleigh distillation model and inorganic calcite trace element partition coefficients can adequately explain the observed Li/Ca and Sr/Ca data. A DIC control, on the rate of calcification or vacuole flushing rate (either directly, or more likely through ΔCO_3^{2-}), provides a viable mechanism for Li and Sr incorporation within *Uvigerina peregrina*. Further experiments to determine the sensitivity of Li uptake to calcification rate in inorganic calcite are needed to progess the understanding of Li uptake in foraminifera.

- Porewater chemistry and dissolution appear to have a limited effect on *Uvigerina peregrina* Li/Ca and Sr/Ca ratios, indicating they can effectively be used to reconstruct past bottomwater chemistry.

Chapter 6

Deglacial watermass structure and carbon storage in the interior North Pacific

6.1 Introduction

The radiative forcing resulting from the ~90 ppmv increase in atmospheric CO_2 over the last deglaciation was a major factor in bringing the last glacial period to a close, and the strong correlation observed between atmospheric CO_2 and temperature inferred from δD in Antarctic ice cores suggests that atmospheric CO_2 has been an important feedback process, amplifying orbital forcing and regulating Earth's temperature over at least the past 800 ka (Augustin et al., 2004; Schneider von Deimling et al., 2006). The contraction of the terrestrial biosphere and the combined effects of changes in the physical properties of seawater (temperature, salinity, volume) on CO_2 solubility leaves only increased DIC storage within the interior ocean as a viable mechanism to reduce atmospheric CO_2 during glacial times, while adhering to the observed constraint of a minimal change in lysocline depth (Archer et al., 2000; Sigman and Boyle, 2000; Sigman et al., 2010). The depletion of ^{13}C and ^{14}C isotopes within atmospheric CO_2 documents the release of carbon from an isolated deep ocean reservoir to the atmosphere over the last deglaciation (Figure 1.2) (Hughen et al., 2004; Schmitt et al., 2012b). However the exact set of mechanisms resulting in the differential partitioning of DIC between the surface and deep ocean over glacial-interglacial cycles remains elusive.

The North Pacific Ocean currently contains the most DIC-rich deepwaters in the global ocean. Deep waters (predominantly AABW) enter the Pacific basin from the south

via a western boundary current, and due to the lack of any significant watermasss overlying the southern source deepwaters and the strong physical mixing along the numerous island chains, nutrients and DIC are mixed from the deep ocean into the intermediate depths (Warren, 1973; Talley, 2013). This results in a 'reversed' $\Delta^{14}C$ and DIC profile, with the highest DIC concentrations/lowest $\Delta^{14}C$ values found between 1000-2000 m (Figure 1.7) (Key, 2004). The formation of Pacific Deepwater (PDW) via these dipycnal mixing processes is an important pathway for the return of DIC (and other nutrients) from the deep to intermediate depths within the modern global ocean (Figure 1.4) (Sarmiento et al., 2004; Talley, 2013), with the isolated DIC eventually being released to the atmosphere both directly through tidal mixing in the subarctic Pacific (Kelley and Hood, 1971; Takahashi et al., 1993; Mordy et al., 2005), and by upwelling of PDW into the surface of the Southern Ocean (Marinov et al., 2006; Talley, 2013). A more detailed account of the modern oceanography of the North Pacific is given in section 1.2.

It is hypothesised that greater stratification of the North Pacific (along with the Southern Ocean) increased DIC storage in the deep ocean and reduced CO_2 outgassing during the LGM, and overturning of the watercolumn released the deeply sequestered DIC back to the atmosphere during deglaciation (Boyle, 1988; Sigman and Boyle, 2000; Jaccard et al., 2005). Benthic foraminiferal $\delta^{18}O$ and $\delta^{13}C$ profiles show an ^{18}O-depleted (warmer/fresher) and ^{13}C-enriched (more recently ventilated) watermass above ~2000 m in the North Pacific during the LGM (Figure 1.11), and this has been taken as evidence of a glacial expansion of NPIW to depths of >2000m (Keigwin, 1998; Matsumoto et al., 2002; Herguera et al., 2010). Due to the breakdown of the simple relationship between denisty and $\delta^{18}O_{calcite}$ at low temperatures (Lynch-Stieglitz et al., 1999), the increase in $\delta^{18}O$ gradient observed in the glacial North Pacific may or may not represent an increase in density gradient, depending on the extent to which the $\delta^{18}O$ differences are driven by temperature or salinity. Lower $\delta^{13}C$ values below 2000m and increased authigenic U concentrations suggest a more poorly ventilated watermass in the deep ocean (Keigwin, 1998; Matsumoto et al., 2002; Herguera et al., 2010), which Jaccard et al. (2009) took as evidence for a deepening of the respired carbon pool. Conversely, lower Cd/Ca values suggest less, not more, nutrients within the deep North Pacific during glacial times (Boyle, 1992; Ohkouchi et al., 1994).

Downcore increases in sedimentary $\%CaCO_3$ and %Opal over deglaciaiton demonstrate a rapid rise in productivity at ~15 ka (Kienast et al., 2004). This increase in productivity has been suggested to indicate overturning of the watercolumn, ventilation of the deep ocean, and the return of deeply sequestered nutrients and DIC to the surface ocean (Jaccard et al., 2005). Similar productivity events are observed during every major

deglaciation since the intensification of northern hemisphere glaciation ~ 2.7 Ma (Haug and Sigman, 2009). The cause of these productivity increases remain enigmatic, with productivity observed above Holocene levels indicating the current Fe-limitation was overcome (Lam et al., 2013). While productivity is not a direct measure of deep ocean ventilation, sedimentary redox and benthic foraminiferal $\Delta^{14}C$ studies do suggest an increase in ventilation over deglaciation, although the timing and magnitude varies between sites, and is often contradictory (Jaccard et al., 2009; Okazaki et al., 2010; Lund et al., 2011; Rae et al., 2014). Several authors have suggested that deep water formation occurred within the North Pacific over deglaciation, although its existence and vertical/lateral extent are debated (Okazaki et al., 2010; **?**; Rae et al., 2014). Marchitto et al. (2007a) proposed very depleted benthic foraminiferal $\Delta^{14}C$ values in the intermediate depth northeastern Pacific represent the return of an isolated deep ocean DIC reservoir back to the surface ocean through the intermediate depth North Pacific, although subsequent modelling work has determined this explanation highly unlikely (Hain et al., 2011).

This study aims to answer three main questions about the North Pacific ocean during the LGM and over deglaciation (i) how did physical structure of the interior subarctic Pacific Ocean differ during glacial times? (ii) was more or less CO_2 sequestered in the interior North Pacfic? (iii) how and when did ventilation change over deglaciation?

6.1.1 Approach

The degree of mixing within the interior ocean is determined by bathymetry (~constant on G-IG timescales) and the density gradient within the watercolumn. Mg/Ca ratios in *Uvigerina* spp can be used to reconstruct past bottom water temperature (BWT), with the uptake of Mg unaffected by ΔCO_3^{2-} (Section 5.3.5), allowing the temperature and $\delta^{18}O_{sw}$ (~salinity) components of $\delta^{18}O_{calcite}$ to be deconvolved. Reconstructed BWT and $\delta^{18}O_{sw}$ can then be used to approximate density.

Temperature-normalised Li/Ca in *Uvigerina* spp shows a strong correlation with ΔCO_3^{2-} (and also DIC, see section 5.3.6), and ΔCO_3^{2-} is a function of calcite solubility ($\Omega_{Calcite}$) and $[CO_3^{2-}]$. The magnitude of apparent changes in temperature, salinity, and pressure (sea level) have a negligible effect on $\Omega_{Calcite}$, allowing $[CO_3^{2-}]$ to be reconstruct reconstructed, and hence DIC with an estimation of alkalinity (Yu et al., 2010, 2013a).

6.2 Materials and methods

Three cores spanning ∼ 3300 to 1000 m water depth were selected to reconstruct the physical and chemical structure of the subarctic Pacific watercolumn over deglaciation; Nesmeyanov GGC27, 46.9 N, 151.2 E, 995 m; MD01-2416, 51.3 N, 167.7 E, 2317 m; Roundabout PC11, 51.1 N, 168.0 E, 3225 m. The two deepest sites (Roundabout PC11 and MD01-2416) are located on the Emperor Seamounts in the open NW Pacific, however as there are no hemipelagic sediments above ∼2300 m in the open NW Pacific, the shallowest site (Nesmeyanov GGC27) is located in the Okhotsk Sea (Figure 6.1). The deepwaters in the Okhotsk Sea are well mixed with the open NW Pacific below ∼1000m, and so Nes GGC27 should be representative of the open NW Pacific (Keigwin, 1998). All cores have published benthic foraminiferal $\delta^{18}O$ stratigraphies (Keigwin, 1998; Gebhardt et al., 2008), although the resolution of the Nes GGC27 $\delta^{18}O$ record was increased for this study. It was not possible to generate a high resolution deglacial trace-element record for the deepest site as RNDB PC11, and all alternative deep NW Pacific sites (ODP 882 and Vinograd GGC37) have been oversampled and no useable material is remaining (Keigwin, WHOI, pers comm). This highlights a significant paucity in material from the deep NW Pacific, and further coring campaigns should be directed around the aim of retrieving more material from this important region.

All sediment samples were washed at >63 μm, and *Uvigerina* spp were picked from the >150 μm size fraction and identified to species level. PC11 and MD01-2416 contained exclusively *Uvigerina senticosa*, while GGC27 contained both *Uvigerina hispida* and *Uvigerina peregrina*, with a switch from *Uvigerina peregrina* to *Uvigerina hispida* below ∼ 50 cm in the core. Only two depth intervals contained both species found concurrently. GGC27 was sampled at a continuous 1-2 cm resolution between 38-79 cm depth. For samples without exisiting $\delta^{18}O$ values (n=23), between 5-12 individual *Uvigerina* were analysed for $\delta^{18}O$ and $\delta^{13}C$ at the Bloomsbury Environmental Isotope Facility following the methods listed in section 5.2.3. Three samples previously analysed by Keigwin (1998) spanning a large range in $\delta^{18}O$ were re-analysed at UCL in order to assess, and correct for, any inter-laboratory differences in the measurement of $\delta^{18}O$. All newly generated $\delta^{18}O$ data are presented in the data appendix.

MD01-2416 was sampled at a 2-5 cm resolution, and four intervals at 47, 79, 124 and 145 cm depth with sufficent individuals were sampled from PC11. Between 8-30 monospecific *Uvigerina* individuals were cleaned at UCL in a laminar flow hood fitted with a boron-free PTFE HEPA filter following the oxidative/reductive protocol of Boyle and Keigwin (1985), as outlined in section 3.4. Cleaned foraminiferal samples were analysed for a suite of major and trace elements at Cardiff University. Samples were dissolved in 0.065

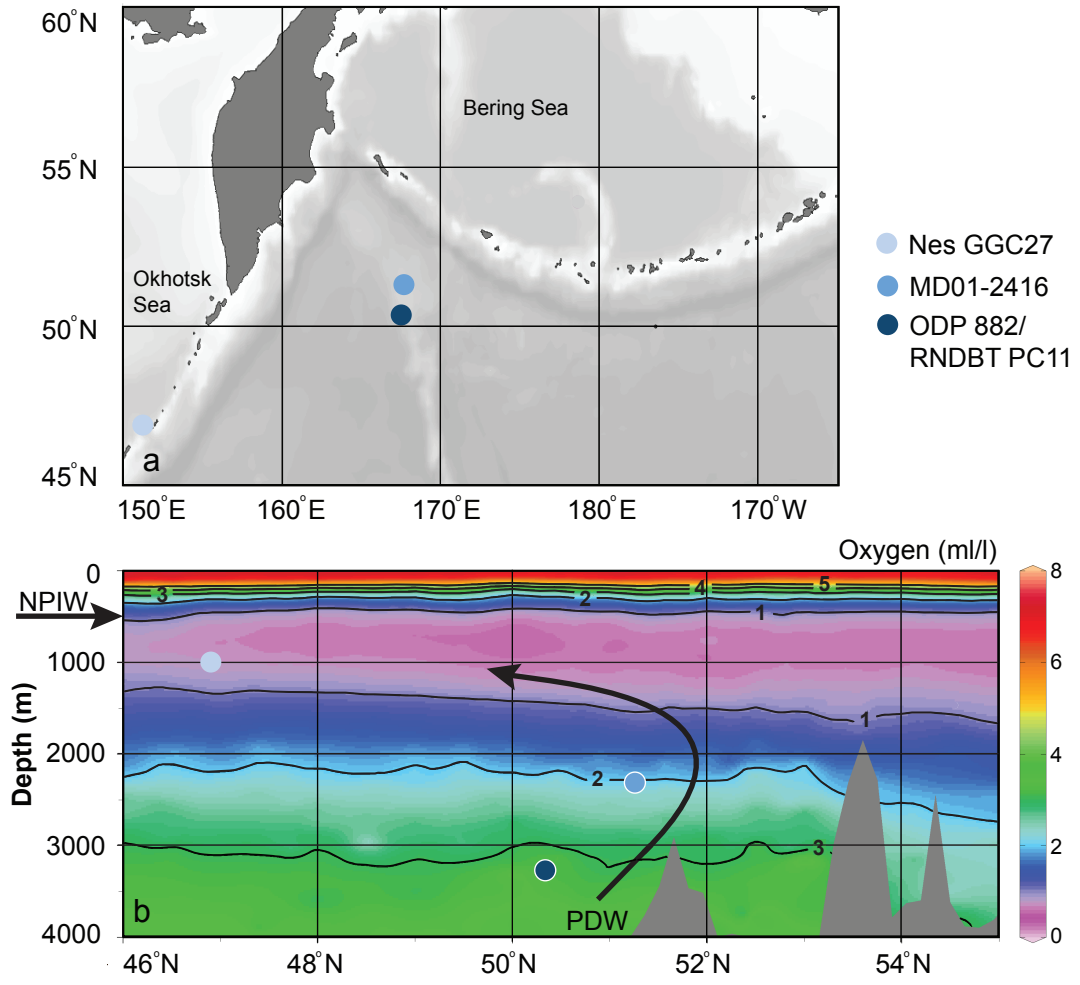

FIGURE 6.1: Location of the cores used in this study. PDW is Pacific Deepwater, and NPIW is North Pacific Intermediate Water.

M Optima Grade HNO_3 and centrifuged at 3000 rpm for 5 mins. Ca concentration in the supernatant was determined by ICP-MS and the acidified samples were diluted to a final volume of 350 µl, and a maximum Ca concentration of 4 mM using 0.5 M Optima Grade HNO_3. Element/Ca ratios were determined using a Thermo Finnigan Element II HR-ICP-MS by count ratio calibration against matrix matched standards (Lear et al., 2002). All trace element data are presented in the data appendix.

6.2.1 Age model

New age models were generated for all of the cores. Previously-published planktonic ^{14}C dates (Keigwin, 1998; Gebhardt et al., 2008) were recalibrated with the OXCAL software package (Bronk Ramsey, 2013) using the INTCAL13 calibration curve (Reimer, 2013) and a constant reservoir age of 950±250 years. This range in reservoir ages brackets

both the modern range within the North Pacific, and available estimates for the LGM in the northeastern Pacific (Kovanen and Easterbrook, 2002). The minima and maxima of major events within the high-resolution *Neogloboquadrina pachyderma* $\delta^{18}O$ record from MD01-2416 (Gebhardt et al., 2008) were then tied to the NGRIP $\delta^{18}O$ record on the GICC05 timescale (Andersen et al., 2004; Rasmussen et al., 2006), with the constraint of remaining within the 2 σ radiocarbon age range, which is typically around $\pm$1000 yr. A link between $\delta^{18}O$ in the North Pacific and Greenland could be caused by (i) a temperature link between the North Pacific and Greenland (Hendy et al., 2002), or (ii) a North Pacific precipitation source to Greenland (Kiefer et al., 2002). The previously published age model for the core by Gebhardt et al. (2008), and updated by Sarnthein et al. (2013), is based on the ^{14}C plateau tuning approach and results in considerably larger reservoir ages below 150 cm depth than the independent reservoir estimates for the LGM (Kovanen and Easterbrook, 2002). The age models agree later than $\sim$15 ka, but diverge prior to this (Figure 6.3).

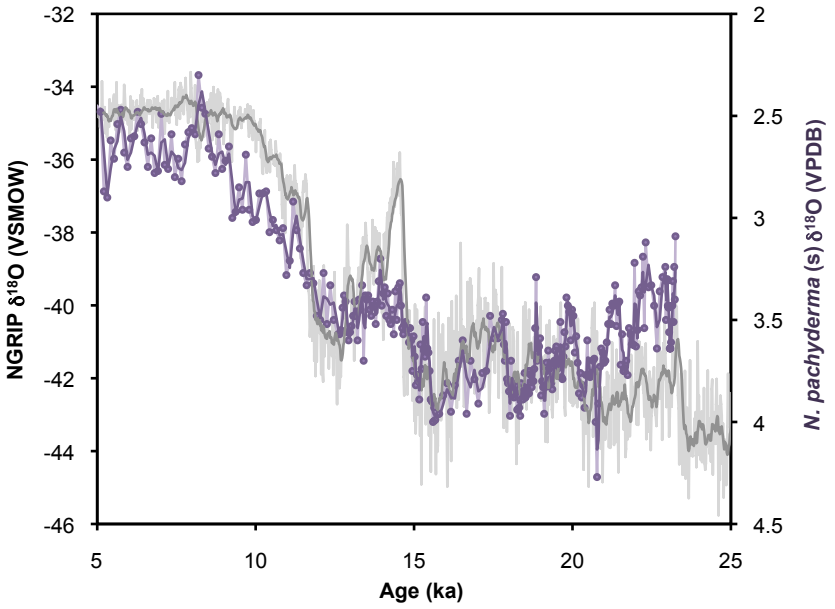

FIGURE 6.2: NGRIP $\delta^{18}O$ on the GICC05 timescale (Andersen et al., 2004; Rasmussen et al., 2006) and *N. pachyderma* $\delta^{18}O$ from MD01-2416 (Gebhardt et al., 2008), which has been tied to the NGRIP record based on the major events. A moving average is shown for both records.

Due to the higher resolution of the *N. pachyderma* $\delta^{18}O$ record and ^{14}C dates, the age model for MD01-2416 was used as a basis to construct age models of the other cores. The *N. pachyderma* $\delta^{18}O$ record from RNDBT PC11 (Keigwin, 1998) was tied to the *N. pachyderma* $\delta^{18}O$ record from MD01-2416, while staying within the error of the PC11 ^{14}C age range (Figure 6.4). There is no planktonic $\delta^{18}O$ record for Nes GGC27, so

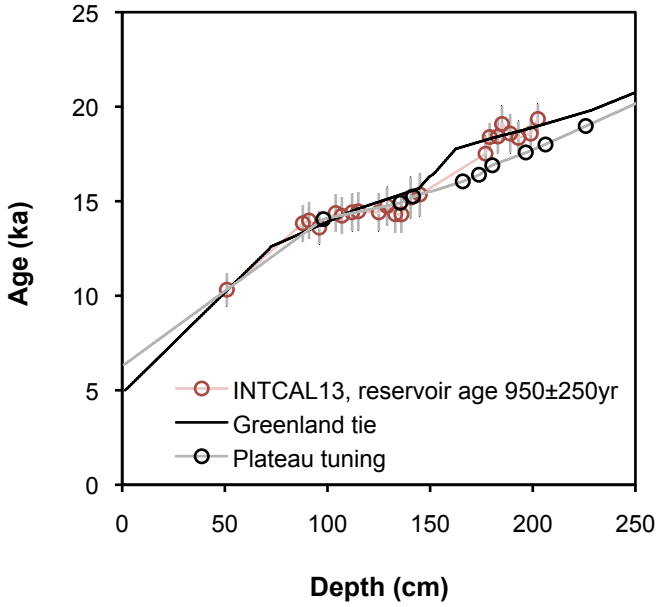

FIGURE 6.3: Age/depth plot for core MD01-2416 showing the (i) ^{14}C dates calibrated with the INTCAL14 calibration curve (Reimer, 2013) and a constant reservoir age of 950±250 yr (ii) Greenland tuned age model described in the text above (iii) ^{14}C Plateau tuning model of Sarnthein et al. (2013)

the age model was based soley on the radiocarbon chronology, although the increase in $CaCO_3$ within the core agrees very well with that in MD01-2416 (Figure 6.5).

6.3 Results and discussion

6.3.1 Benthic $\delta^{18}O$ data

Previously published *Uvigerina* spp $\delta^{18}O$ data for cores MD01 and PC11, and previously published and newly generated data for GGC27, are shown on the new age models generated in this study in Figure 6.6. Unpublished *Uvigerina* spp $\delta^{18}O$ data from ODP Site 882 (W. Gray, 2009 MSc Thesis) from 3244 m on the Detroit Seamounts (adjacent to PC11, Figure 6.1) is also shown on the age model of Jaccard et al. (2009). The *Uvigerina* spp $\delta^{18}O$ data for PC11 and GGC27 of Keigwin (1998) were corrected for interlaboratory offsets with the relationship $\delta^{18}O_{UCL} = 1.074 \times \delta^{18}O_{Keigwin1998} + 0.048$ (R^2=0.999). The corrected $\delta^{18}O$ data from PC11 shows very good agreement with the ODP 882 record prior to ~10 ka. After this PC11 shows an ^{18}O depletion relative to ODP 882, although the proximity of these cores strongly suggests that this disagreement is due to discrepencies between age models rather than a difference in the physical properties

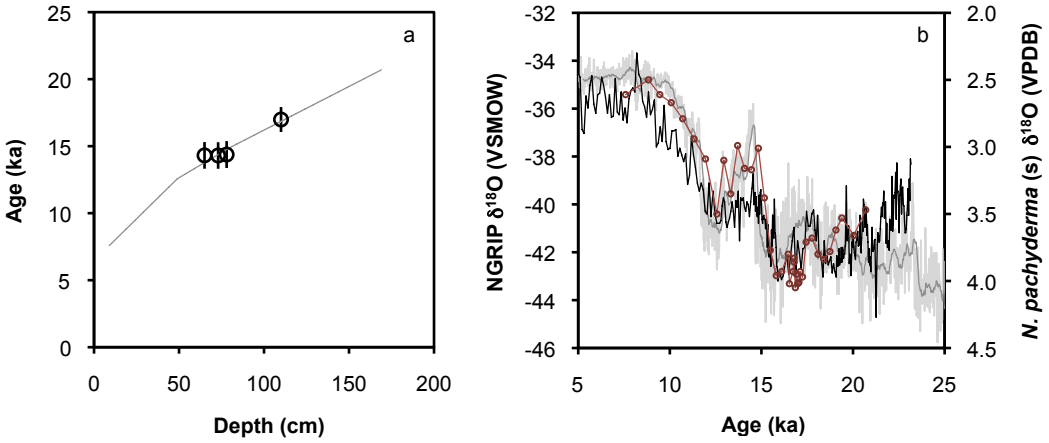

FIGURE 6.4: (a) Age/depth plot for PC11 based on the tie to MD01-2416. ^{14}C dates, calibrated with the INTCAL14 calibration curve (Reimer, 2013), are shown in black (b) NGRIP δ^{18}O on the GICC05 timescale (grey) (Andersen et al., 2004; Rasmussen et al., 2006), *N. pachyderma* δ^{18}O from MD01-2416 (Gebhardt et al., 2008) (black), which has been tied to the NGRIP record based on the major events, and *N. pachyderma* δ^{18}O from PC11 (Keigwin, 1998) , which has been tied to the MD01-2416 *N. pachyderma* δ^{18}O record.

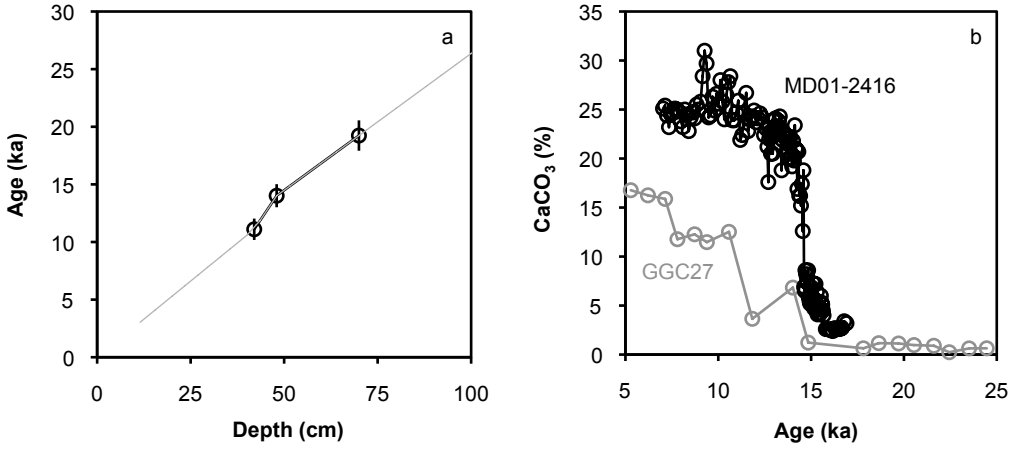

FIGURE 6.5: (a) Age/depth plot for GGC27, with the constrained sections of the age depth plot shown in heavy grey (b) %CaCO3 from GGC27 (Keigwin, 1998), on the age model developed in this study (grey) and %CaCO3 from MD01-2416 (Gebhardt et al., 2008), on the age model developed in this study.

of seawater within the water column (i.e. its an x axis rather than a y axis issue), as the age model for PC11 is poorly constrained in this interval.

The *Uvigerina* spp $\delta^{18}O$ records show a ~70% increase in $\delta^{18}O$ difference between ~1000 and ~3300 m during the LGM, compared to that expected from modern hydrographic data (referred to hear as the 'expected' difference). At present the same watermass is found in both the deep (~3300 m) and deep-intermediate (~2300 m) North Pacific, as indicated by the similarity of the $\delta^{18}O$ 'expected' at both depths. However, the $\delta^{18}O_{Uvi}$ records from PC11 and MD01-2416 show a 0.46 ‰ depletion at 2300m relative to 3300 m during the LGM; that is as large as the expected $\delta^{18}O_{Uvi}$ difference between 1000 m and 3300 m today, and demonstrates that an isotopically lighter (fresher) and/or warmer watermass was found in the deep-intermediate compared to the deep North Pacific Ocean during the LGM. Over deglaciation the $\delta^{18}O_{Uvi}$ difference between the deep and deep-intermediate sites decreased, first at ~20 ka, and then at ~16 ka, after which the deep and deep-intermediate records become almost identical, suggesting a return to modern circulation conditions. Despite the increased resolution of the GGC27 $\delta^{18}O_{Uvi}$ record to ~1 cm, the resolution of the record is still limiting with respect to PC11 and MD01-2416. However, it does suggest that the watermass at within the intermediate depths remained warmer and/or fresher than the deep-intermediate and deep ocean throughout deglaciation. As previously discussed, this increase in *Uvigerina* spp $\delta^{18}O$ gradient during the LGM could represent either an increase or decrease in density stratification within the watercolumn, depending on which variable (temperature or $\delta^{18}O_{sw}$) had changed. Deconvolution of the temperature and $\delta^{18}O_{sw}$ components from $\delta^{18}O_{Uvi}$ is therefore required to determine the degree of interior ocean stratification during the LGM.

6.3.2 Trace element contamination

In order to assess the impact of contamination on the trace element/Ca ratios from each core, Al/Ca, Fe/Ca and Mn/Ca were compared to intra-test values, as outlined in section 5.3.2. In the limited dataset for core PC11 all Al/Ca values are below 6 μmol/mol, and all Fe/Ca values are below 12 μmol/mol. With the exception of one sample with Mn/Ca ratio of ~190 μmol/mol, Mn/Ca values are below 50 μmol/mol, and the sample with elevated Mn/Ca shows similar trace element/Ca values to the other low-Mn/Ca samples indicating that the influence of contamination on these samples is minimal (Figure 6.7).

Al/Ca in core MD01-2416 are very low, with values generally below 5 μmol/mol, and Mn/Ca and Fe/Ca ratios are generally below 80 and 10 μmol/mol respectively (Figures 6.8 and 6.9). There is no correlation between the contamination indicators

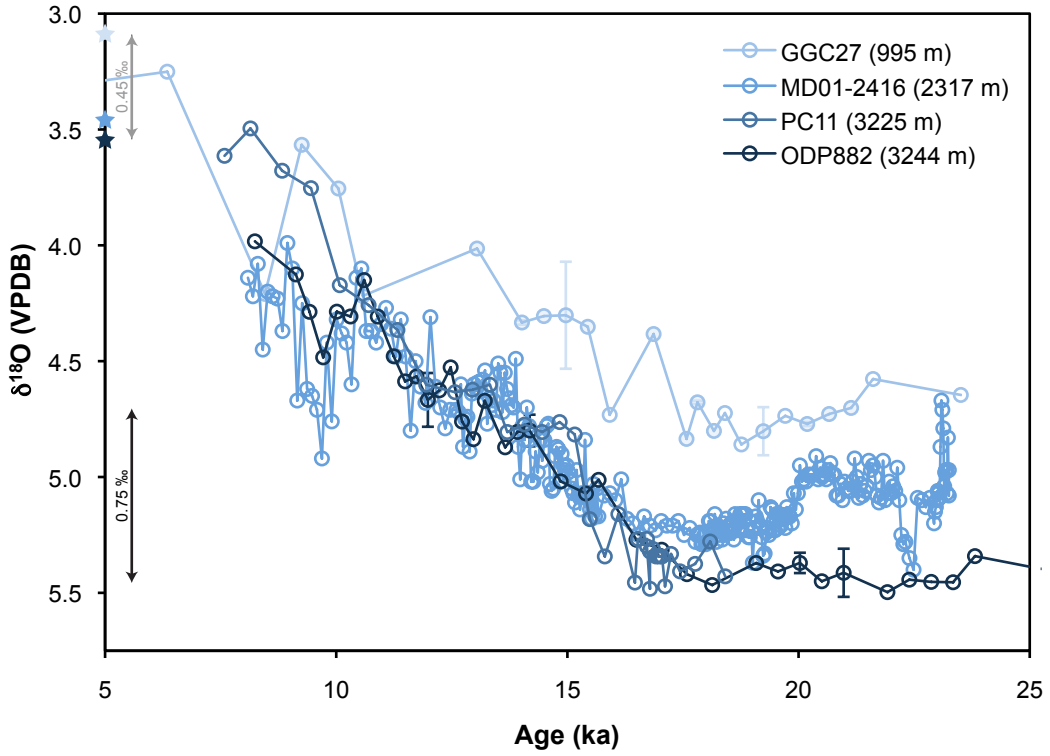

FIGURE 6.6: North Pacific benthic $\delta^{18}O$ records. Data from MD01-2416 are from Gebhardt et al. (2008), PC11 and GGC27 are from Keigwin (1998) corrected for inter-laboratory differences (except filled circles which are data generated in this study), and ODP 882 are unpublished data from the authors MSc thesis. The modern $\delta^{18}O_{Uvi}$ value expected at each depth in the open northwestern Pacific, calculated using the North Pacific $\delta^{18}O_{sw}$-salinity relationship of LeGrande and Schmidt (2006) and the *Uvigerina* spp temperature-α relationship of Marchitto et al. (2014), is indicated with a star. The difference in $\delta^{18}O_{Uvi}$ between 995 and 3244 m expected based on modern hydrographic data is shown by the grey arrow, and that measured for the LGM is shown in black.

and Li, B, Mg, Sr or Cd. However, several data points with only slightly elevated Al (> 10 µmol/mol) and Mn (> 100 µmol/mol) clearly have anomously high Li, B, Mg, Sr and Cd (Figures 6.8 and 6.9), indicating some influence from clay and Mn-Fe oxyhydroxide contamination; these samples were removed from the dataset. The large trace element/Ca anomalies associated with the moderate Al/Ca increases indicates the presence of clay with very high (Mg,Li,Sr,B)/Al ratios, and suggest rather than judging the influence of contamination an absolute intra-test based Al/Ca, Mn/Ca or Fe/Ca value across all sites, a site- and interval- specific approach should be used.

Below ~55 cm depth in core GGC27 Mn/Ca is consistently < 40 µmol/mol, however at 52 cm depth there is a large increase in Mn/Ca values to a maximum of 1900 µmol/mol at 48 cm (Figure 6.10). Li/Ca, B/Ca, Mg/Ca, and Cd/Ca all increase concurrently with Mn/Ca, and a significant relationship exisits between all trace elements and Mn/Ca (R^2= 0.74, 0.72, 0.57 and 0.7 respective to the ordering above). Despite reductive

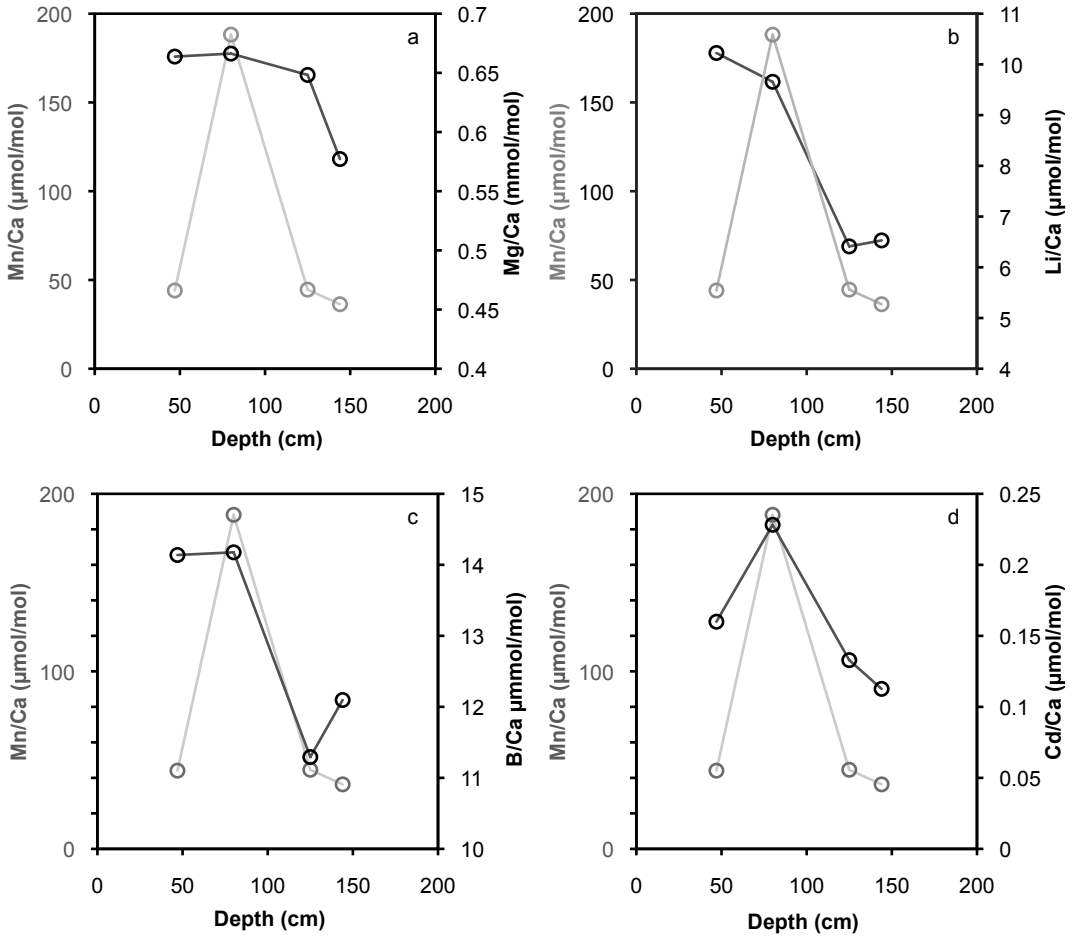

FIGURE 6.7: PC11 (a) Mg/Ca (b) Li/Ca (c) B/Ca and (d) Cd/Ca ratios plotted downcore with Mn/Ca (grey).

cleaning there is clearly a significant influence of contamination on the samples above 52 cm depth in the core. Interestingly, the onset of high Mn/Ca values occurs at the switch from *U. hispida* to *U. peregrina*, with *U. peregrina*. In the two intervals where both species were analysed only the *U. peregrina* have high Mn/Ca values. In these intervals the abundance of *U. hispida* was very low, and its likely that the individuals that were present were bioturbated upward from the lower interval, where they are much more abundant.

6.3.3 Last Glacial Maximum watercolumn profile

Due to the lack of deglacial material available from the deepest sites, and the influence of contamination on the shallowest site in the later half of the record, it is not possible to reconstruct temperature, $\delta^{18}O_{sw}$ and DIC storage for the watercolumn across the

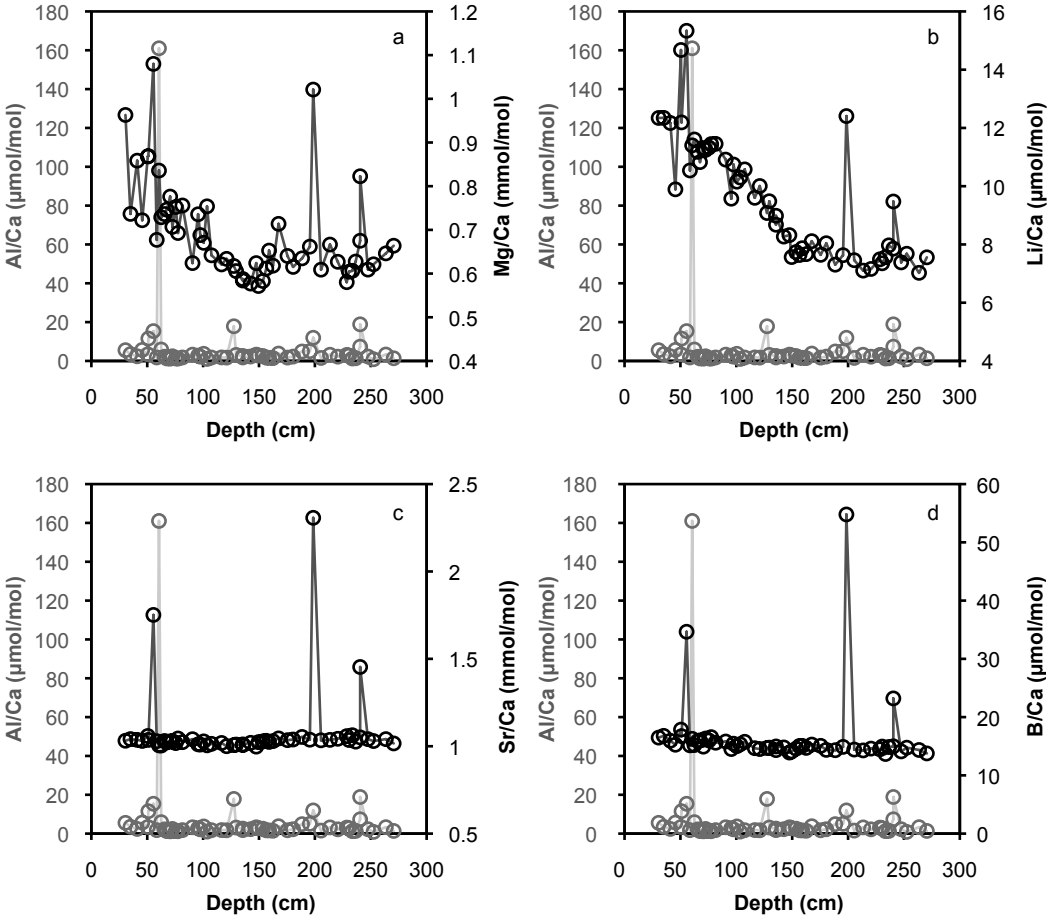

FIGURE 6.8: MD01-2416 (a) Mg/Ca (b) Li/Ca (c) Sr/Ca and (d) B/Ca ratios (black) plotted downcore with Al/Ca (grey). Samples with on slightly evelvated Al/Ca ratios show very large anomalies in (Mg,Li,Sr,B)/Ca.

deglaciation. However there is trace element/Ca and $\delta^{18}O$ data for all sites between 19-21 ka, and so it is possible to construct watercolumn profiles for the LGM. For the deepest interval in PC11 $\delta^{18}O$ data from ODP882 was used as there is no $\delta^{18}O$ for PC11. Mg/Ca values were converted to temperature using the Mg/Ca-BWT relationship in equation 5.2 and $\delta^{18}O_{sw}$ was derived using the *Uvigerina* spp. fractionation factor (α) of Marchitto et al. (2014). The porewater derived LGM salinity of Adkins (2002) from ODP Site 1123 in the South Pacific was used for PC11, assuming the same salinity in the deep North and South Pacific; this assumption is supported by porewater salinity reconstructions spanning the North and South Pacific, which indicate a similar salinity throughout the deep basin (Insua et al., 2014), and that the reconstructed $\delta^{18}O_{sw}$ value for the deep North Pacific in this study of 1.0±0.1‰ is identical to Adkins's (2002) porewater-based esimate for the deep South Pacific of 1.0±0.1 ‰. The salinity of the intermediate and shallowest sites were calculated using the difference in reconstructed $\delta^{18}O_{sw}$ between GGC27, MD01-2416 and PC11, and the global $\delta^{18}O_{sw}$-salinity relationship of LeGrande

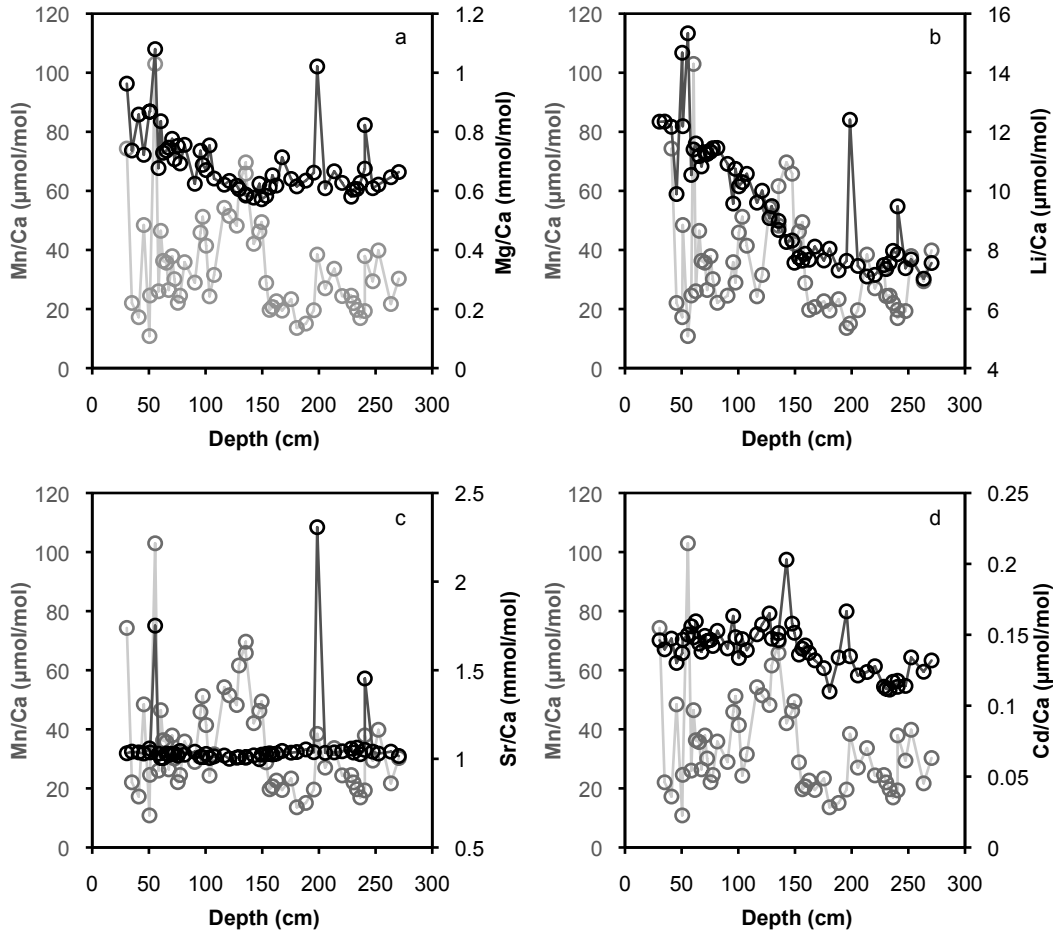

FIGURE 6.9: MD01-2416 (a) Mg/Ca (b) Li/Ca (c) Sr/Ca and (d) Cd/Ca ratios (black) plotted downcore with Mn/Ca (grey).

and Schmidt (2006). Temperature error is given as $\pm 1\sigma$ of reconstructed temperatures between 19-21 ka. Salinity error is the $\pm 1\sigma$ of reconstructed $\delta^{18}O_{sw}$ between 9-21 ka, divided by the slope of the $\delta^{18}O_{sw}$-salinity relationship, plus the ± 0.07 PSU salinity error of Adkins (2002). The reconstructed BWT and salinity estimates (Figure 6.11) were used to calculate the LGM potential density anomaly for each depth with the *oce* package in R (Figure 6.12).

DIC for each site was calculated using two methods; DIC was derived directly from Li/Ca and Mg/Ca using equation 5.6. This assumes that DIC directly controls the relationship observed with Li/Ca_{TN} (Figure 5.14). However, if the relationship between Li/Ca and the carbonate system is driven by a ΔCO_3^{2-} control on calcification rate (see discussion in section 5.3.9), DIC must be calculated by firstly calculating $[CO_3^{2-}]$, using the relationship between Li/Ca and ΔCO_3^{2-} in Figure 5.13. Changes in $[CO_3^{2-}]_{sat}$ during the LGM due to the effects pressue and temperature are minimal ($< \pm 2$ µmol/kg), and are ignored. Knowledge of alkalinity is required if DIC is to be calculated from

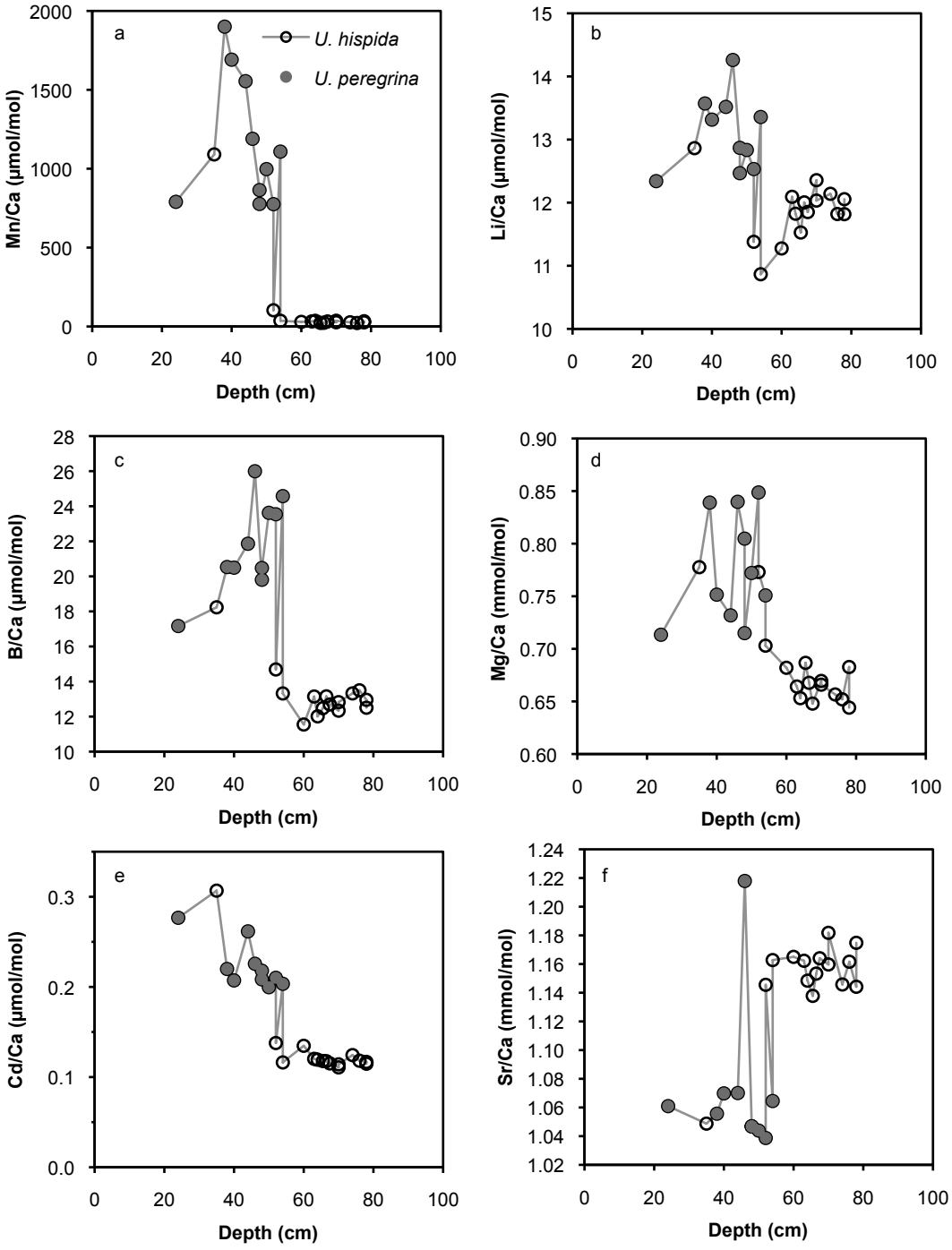

FIGURE 6.10: GGC27 (a) Mn/Ca (b) Li/Ca (c) B/Ca (d) Mg/Ca (e) Cd/Ca (f) Sr/Ca plotted downcore. The large increase Mn/Ca at ∼50cm is accompanied by significant increases in (Li,B,Mg,Cd)/Ca ratios, suggesting these elements are associate with a contaminant phase, rather than foraminiferal calcite.

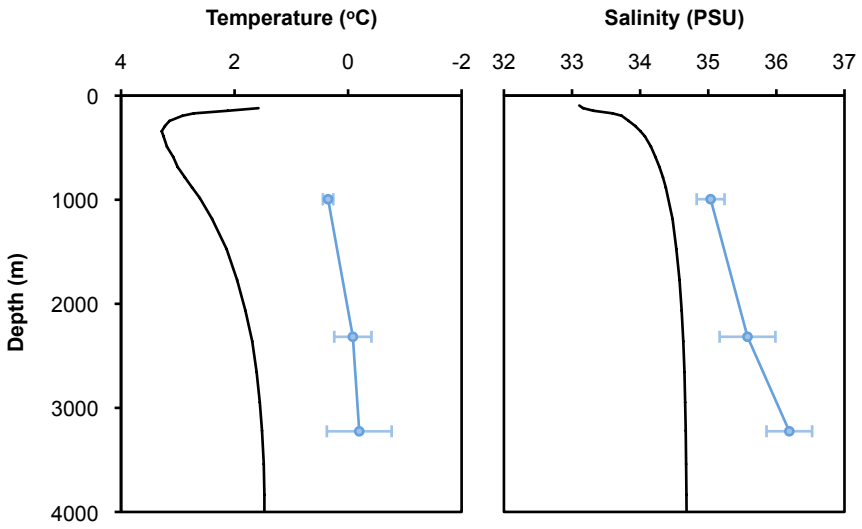

FIGURE 6.11: Modern (black) and LGM (light blue) BWT and salinity profiles of the northwestern North Pacific Ocean. Modern hydrographic data comes from GLODAP station 6017 B (Key, 2004). See text for details of LGM profiles.

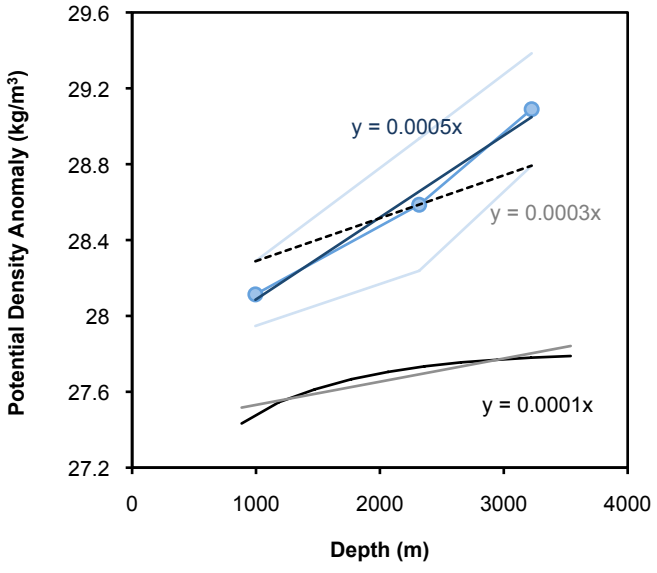

FIGURE 6.12: Modern (black) and LGM (blue) potential density anomaly gradients in the North Pacific Ocean. Even at the lowest limit of the LGM density anomaly gradient (dashed line), the gradient is still three times higher than modern. The modern density gradient was calculated using hydrographic data from GLODAP station 6017 B (Key, 2004) and the *oce* package in R. See text for details of LGM profile.

$[CO_3^{2-}]$. There are no independent estimates for alkalinity for the glacial North Pacific, so modern values were used, although both the reduction in sea level and shoaling of the Atlantic lysocline would have worked to increase alkalinity within the North Pacific during the LGM (Ridgwell et al., 2003, 2007). In order to assess how alkalinity may have changed, estimates of alkalinity from GENIE, an intermediate-complexity earth system model (Ridgwell et al., 2007) run under several modern and LGM circulation scenarios provided a likely range of LGM alkalinity at each core depth (I gratefully acknowledge James Rae at the University of St Andrews for providing the output of these model runs). The model estimates of alkalinity generally show an increase during the LGM, and with the exception of the deepest site, measured alkalinity falls within the range of modelled alkalinity, and measured alkalinity at the deepest site is only 5 μmol/mol lower than the modelled range.

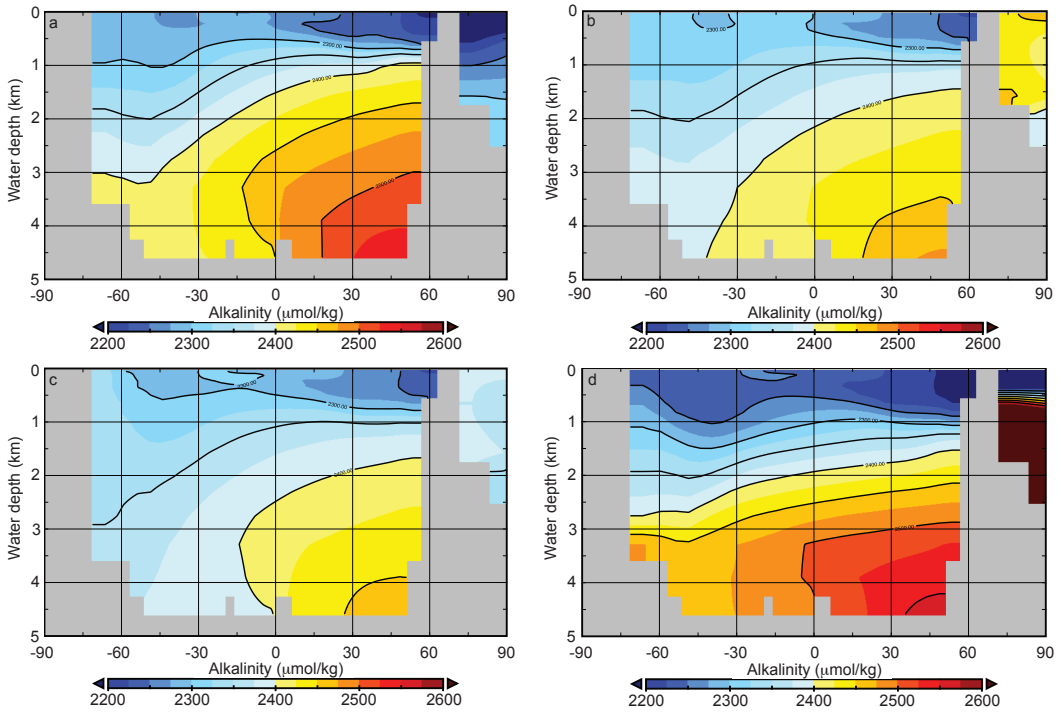

FIGURE 6.13: Modelled Pacific alkalinity transect using GENIE for modern (a and b) and LGM (c and d) circulation, and with closed (a and d) and open (b and c) sediments.

Both the direct DIC reconstruction, and that using the reconstructed $[CO_3^{2-}]$ and modern alkalinity (using the modelled alkalinity range to calculate the uncertainty), are shown in figure 6.14. A watercolumn $\Delta\Delta^{14}C$ (that is the difference between radiocarbon activity in the deep ocean and atmosphere, scaled to modern) profile was constructed by compiling published deglacial North Pacific benthic foraminiferal radiocarbon records that span the entire North Pacific basin (Ahagon, 2003; Galbraith et al., 2007; Marchitto et al., 2007a; Gebhardt et al., 2008; Lund et al., 2011; Okazaki et al., 2012), and includes

unpublished data from MD02-2496 in the northeastern Pacific. For cores MD01-2416 and MD02-2489 (Gebhardt et al., 2008), and the unpublished data from core MD02-2496, benthic $\Delta^{14}C$ was calculated using new age models for the cores based on tying the planktonic $\delta^{18}O$ data to NGRIP, as outlined in section 6.2.1.

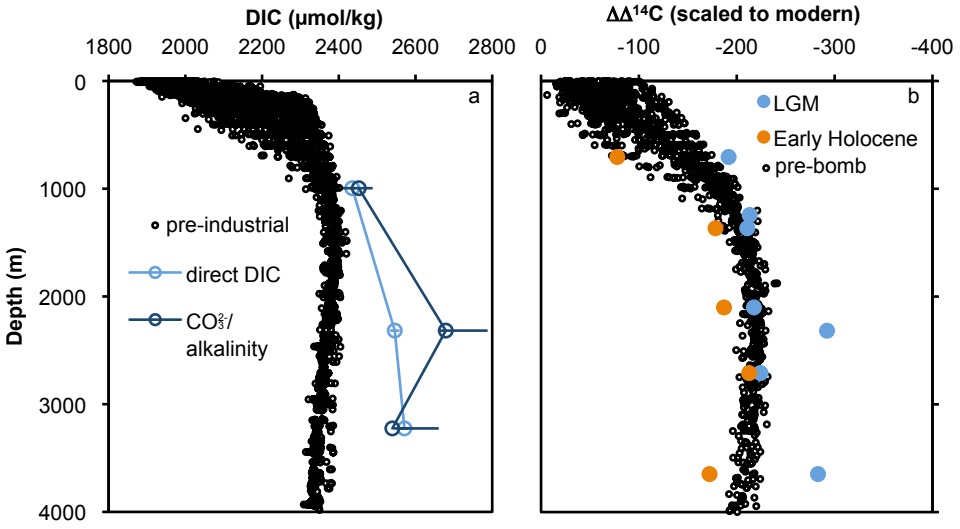

FIGURE 6.14: Modern and LGM North Pacific modern and LGM DIC and $\Delta\Delta^{14}C$ profiles. (a) Pre-industrial DIC is shown by the black circles, DIC calculated directly using equation 5.6 is shown in light blue, and DIC calculated using reconstructed $[CO_3^{2-}]$ and modern alkalinity is shown in dark blue, with the modelled range in modern and LGM alkalinity indicated by the dark blue horizontal line (b) The difference between atmospheric and deep ocean $\Delta^{14}C$ scaled to modern for the LGM (light blue), early Holocene (orange) and modern (black circles)

The LGM profile shows almost uniform temperatures throughout the water column, with BWT decreasing from 0.35±0.1 to -0.2±0.6 °C with increasing depth (Figure 6.11). The deep ocean temperature of -0.2±0.6 °C is ∼1 °C warmer (although within error) of Adkins's (2002) porewater-calcite $\delta^{18}O$ derived temperature for the deep South Pacific of -1.2±0.5 °C. The warmer temperatures in the North Pacific may be due to geothermal heating, which currently warms the deepwaters of the subarctic Pacific by ∼0.4 °C relative to the deepwaters entering the Pacific basin in the south (Joyce et al., 1986). Due to the uniform watercolumn profile, the observed decrease in $\delta^{18}O_{calcite}$ in the upper watercolumn (Keigwin, 1998; Matsumoto et al., 2002; Herguera et al., 2010) must represent a lower salinity (more depleted $\delta^{18}O_{sw}$) watermass rather than a warmer one. The increased salinity gradient results in a much larger density gradient within the interior glacial subarctic Pacific, with a threefold increase in potential density gradient, even at the lower limits of the error range (Figure 6.12).

The two approaches to reconstructing LGM DIC give very similar results for the shallowest and deepest site, but there is a discrepency between them at the intermediate

site, with the direct approach resulting in ∼130 μmol/kg less DIC. Both approaches cannot be right, and it is not possible to say which is correct at present. The discrepency between the approaches may be due to a deviation from the modern DIC-alkalinity relationship in the deep-intermediate depths during the LGM. DIC and ΔCO_3^{2-} are very well correlated in the modern ocean, as it is the changing ratio of DIC to alkalinity that results in variations in $[CO_3^{2-}]$, and thus ΔCO_3^{2-}. Deviation from the modern DIC-alkalinity relationship would cause a discrepency between the two approaches as it would result in a different relationship between DIC and ΔCO_3^{2-} than observed within the calibrations presented in section 5.3.6.

LGM DIC at the shallowest site is within error of modern, and the $\Delta\Delta^{14}C$ profile indicates similar ventilation to modern above ∼ 2000 m. Using both DIC reconstruction approaches, both MD01-2416 and PC11 show increases in DIC during the LGM. MD01-2416 shows an increase of between 180-420 μmol/kg and PC11 shows in increase of 200-320 μmol/kg. Although the depth of the most DIC-rich waters within the LGM watercolumn does change depending on which approach is used, all approaches show a deepening of the DIC pool within the LGM ocean, supporting the nutrient deepening hypothesis of Boyle (1988) as the mechanism by which atmospheric CO_2 was lowered during glacial times. The DIC and $\Delta\Delta^{14}C$ profiles suggest more poorly ventilated deepwaters, and increased DIC storage below 2000 m during the LGM. This result is supported by increased authigenic U (Jaccard et al., 2009) and lower $\delta^{13}C$ values (Keigwin, 1998; Matsumoto et al., 2002; Herguera et al., 2010) which also indicate a more poorly ventilated watermass occupied the deep North Pacific. In order to reconcile the apparent reduction in nutrients implied by lower Cd/Ca ratios (Boyle, 1992; Ohkouchi et al., 1994), also observed in this study (Figure 6.7), a ΔCO_3^{2-} effect on Cd uptake at low saturation states may be invoked, where lower Cd/Ca ratios result from more under-saturated waters (higher DIC), as suggested by the Li/Ca, rather than a canonical interpretation of lower nutrients. Bryan and Marchitto (2010) suggested a lower Cd partion coefficent in the deep ocean; this is likely to be driven by ΔCO_3^{2-}.

While previous studies have suggested better ventilated intermediate waters than present within the glacial North Pacific based on $\delta^{13}C$ (Keigwin, 1998; Matsumoto et al., 2002; Herguera et al., 2010), both the DIC and $\Delta\Delta^{14}C$ reconstructions show a watermass that was as similarly poorly ventilated as at present, however with a lower salinity ($\delta^{18}O_{sw}$) than the deep ocean. The poor ventilation of the intermediate waters suggested by the DIC and $\Delta\Delta^{14}C$ data does not indicate a vertical expansion of NPIW during the LGM, and implies a more distal origin for the intermediate waters (possibly Glacial North Atlantic Intermediate Water), requiring air-sea gas exchange processes at the time of watermass formation to explain the higher $^{13}C/^{14}C$ ratio (Lynch-Stieglitz et al.,

1995). Taken together the density and DIC profiles of the LGM North Pacific indicate greater density stratification of the interior ocean, reduced mixing, and increased DIC storage in the deep and deep-intermediate North Pacific. The relationship between density stratification and DIC storage is not straightforward however, with the deep-intermediate ocean as equally poorly ventilated as the deep ocean, despite the salinity being lower.

6.3.4 Temperature, $\delta^{18}O_{sw}$ and carbon in the deep-intermediate subarctic Pacific over deglaciation

The *Uvigerina senticosa* Mg/Ca and Li/Ca records from site MD01-2416 were used to reconstruct BWT, $\delta^{18}O_{sw}$ and DIC/$[CO_3^{2-}]$ in the deep-intermediate North Pacific across deglaciation. Before reconstructing seawater carbonate sytem parameters from Li/Ca in the infaunal species *Uvigerina senticosa*, the effects of potential changes in porewater chemistry on Li/Ca were assessed by comparing Li/Ca to %Opal and $\%CaCO_3$ within the core (Figure 6.15). The increase in Li/Ca within the core occurs earlier than the large increases in %Opal and $\%CaCO_3$, suggesting it is not an artefact of porewater chemistry and reflects changing bottomwater properties. Mg/Ca values were converted to BWT using the Mg/Ca-BWT relationship in equation 5.2 and $\delta^{18}O_{sw}$ was derived using the *Uvigerina* spp. α of Marchitto et al. (2014) and the $\delta^{18}O_{Uvi}$ record shown in figure 6.6. DIC and $[CO_3^{2-}]$ were calculated using equation 5.6 and the Li/Ca-ΔCO_3^{2-} relationship in 5.13 respectively. In order to assess the significance of reconstructed trends, a gaussian smooth at the 95% confidence level was fitted using a general additive model in the *mgcv* package in R (Figures 6.16, 6.17, 6.18 and 6.19).

From the glacial BWT of ∼0 °C, the temperature decreases to a minimum of ∼-0.5 °C from 18 to 16 ka, although this decrease is not significant. At 15.1 ka the BWT increases steadily and significantly by ∼2.5 °C, reaching the modern value at ∼11 ka. The timing of changes in $\delta^{18}O_{sw}$ do not necessarily relate to the changes in BWT. From a value of ∼0.7 ‰ $\delta^{18}O_{sw}$ increases after 20 ka to a maximum value of ∼1 ‰ at 18 ka. From this maximum value $\delta^{18}O_{sw}$ falls steadily, concurrent with the decrease in temperature, reaching a value of ∼0.6 ‰ at 15 ka. During the rapid rise in BWT $\delta^{18}O_{sw}$ shows no significant change, plateauing until 13 ka, after which there are large fluctuations and $\delta^{18}O_{sw}$ approaches a value close to modern. Both BWT and $\delta^{18}O_{sw}$ display higher variability after 11.2 ka.

From the glacial maximum in DIC/minimum in $[CO_3^{2-}]$ there is a rapid and significant loss of DIC from the deep-intermediate subarctic Pacific between 16-13 ka. The onset of the loss of DIC is concurrent with a slight warming of bottom waters, but precedes

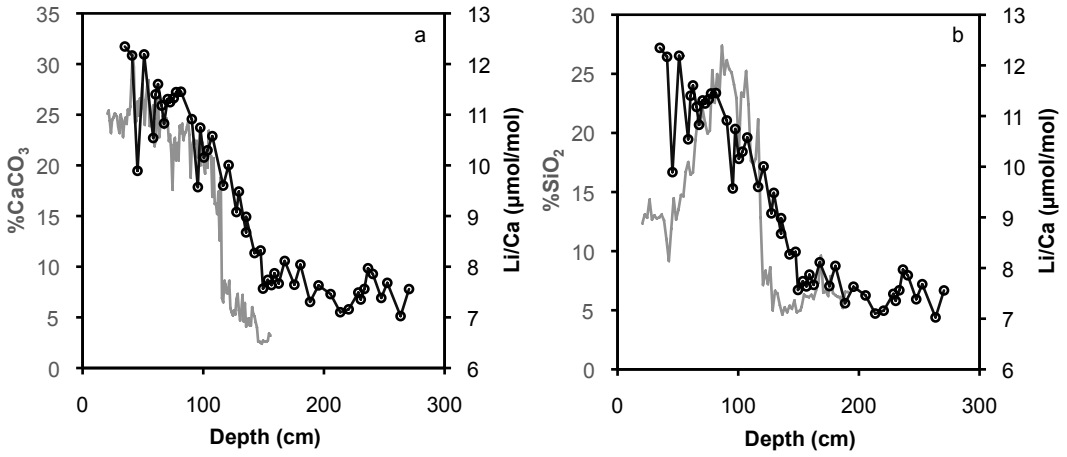

FIGURE 6.15: Downcore changes in *Uvigerina senticosa* Li/Ca in MD01-2416, versus $\%CaCO_3$ and %Opal in the core. The increase in Li/Ca precedes the large increases in $\%CaCO_3$ and %Opal, indicating it is not an artefact of porewater chemistry, and accurately reflects seawater properties.

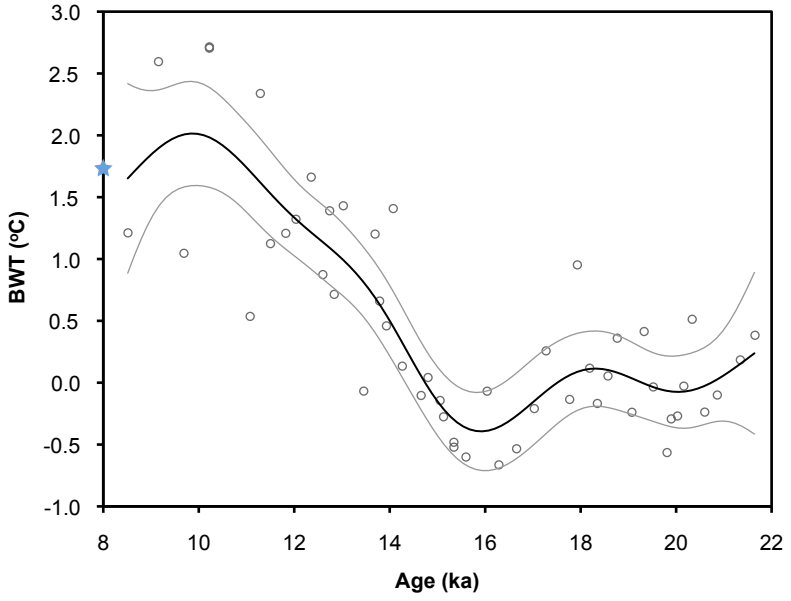

FIGURE 6.16: Deglacial BWT record from site MD01-2416 fitted with a gaussian smooth at the 95% confidence interval. Modern BWT at the site is shown by the blue star.

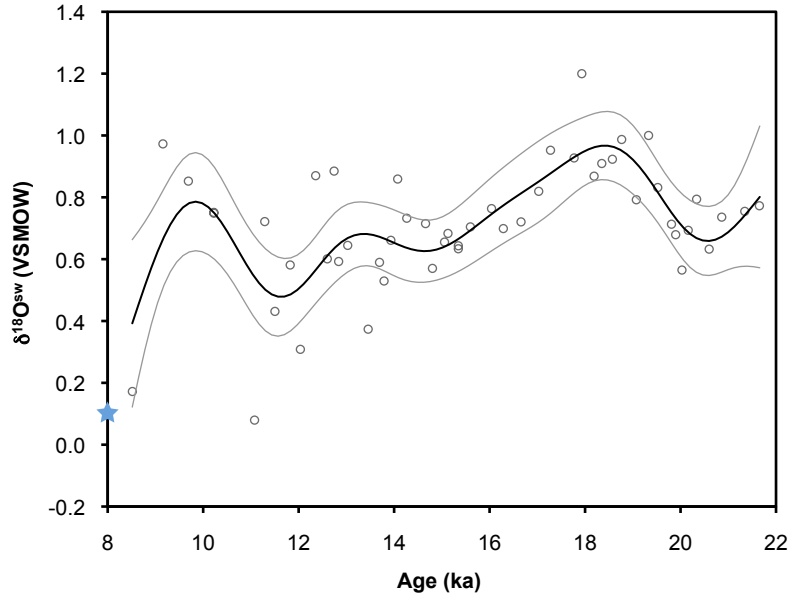

FIGURE 6.17: Deglacial $\delta^{18}O_{sw}$ (VSMOW) record from site MD01-2416 fitted with a gaussian smooth at the 95% confidence interval. Modern $\delta^{18}O_{sw}$ at the site is shown by the blue star.

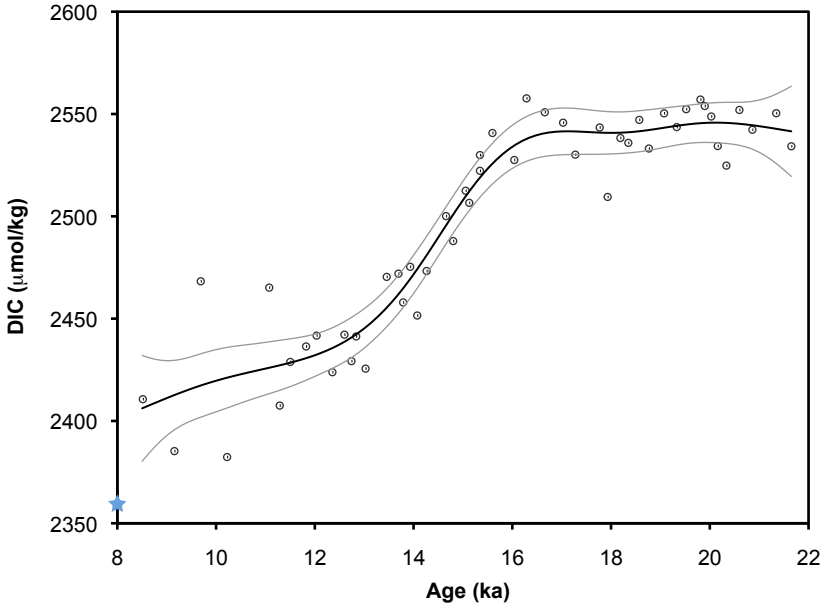

FIGURE 6.18: Deglacial DIC record from site MD01-2416 fitted with a gaussian smooth at the 95% confidence interval. Modern DIC at the site is shown by the blue star.

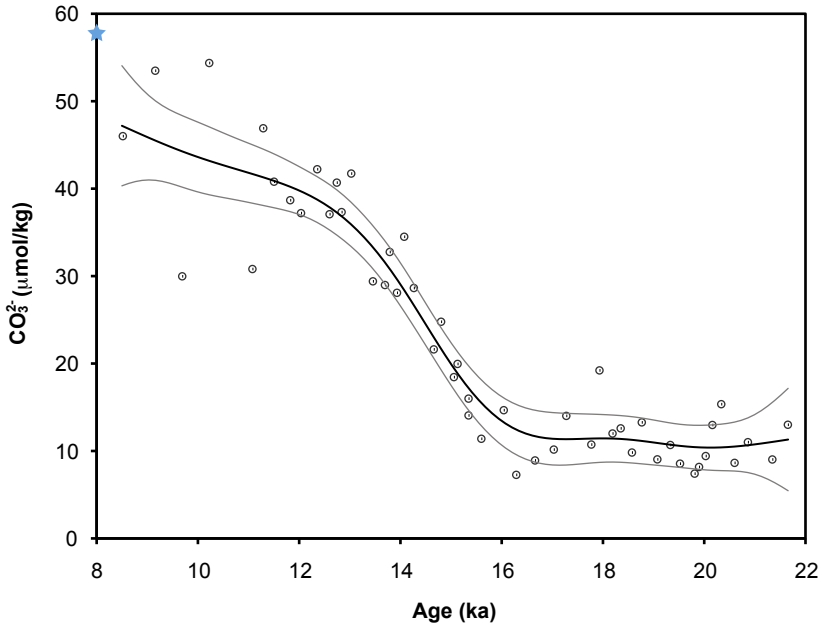

FIGURE 6.19: Deglacial $[CO_3^{2-}]$ record from site MD01-2416 fitted with a gaussian smooth at the 95% confidence interval. Modern $[CO_3^{2-}]$ at the site is shown by the blue star.

the rapid increase in BWT by ∼1000 years (Figure 6.20). Based on the direct DIC reconstruction, the loss of DIC beginning at ∼16 ka is ∼125 µmol/kg. Reconstructed $[CO_3^{2-}]$ shows a ∼30 µmol/kg loss, equivalent to a decrease in DIC of 250 µmol/kg using modern alkalinity. Both the DIC and $[CO_3^{2-}]$ reconstructions approach modern values in the later part of the deglaciation.

The large decrease in DIC is accompanied by an increase in $\Delta\Delta^{14}C$ (Figure 6.20), suggesting increased ventilation of the deep-intermediate subarctic Pacific at this time, and the transfer of an isolated deep-ocean DIC reservoir back to the intermediate depth ocean, and eventually to the atmosphere. The similarity of the benthic foraminiferal $\Delta^{14}C$ records from MD01-2416 and ODP 887, located at 3647 m water in the NE Pacific (Galbraith et al., 2007), indicate the deep and deep-intermediate North Pacific were ventilated simultaneously (Figure 6.21), with an increase in benthic foraminiferal $\delta^{13}C$ in core GGC37 (located at 3300 m in the NW Pacific) also suggesting ventilation of the deep North Pacific at this time (Keigwin, 1998). The transfer of DIC to the intermediate depths is marked by a decrease in oxygen there, as suggested by the high Mn/Ca values in core GGC27 (Figure 6.10), as well as laminated sediments in the Bering Sea (Cook et al., 2005), and an increase in suboxic benthic foraminifera species in the Santa Barbara basin (Cannariato et al., 1999).

The increase in ventilation observed at ∼16 ka within the deep and deep-intermediate

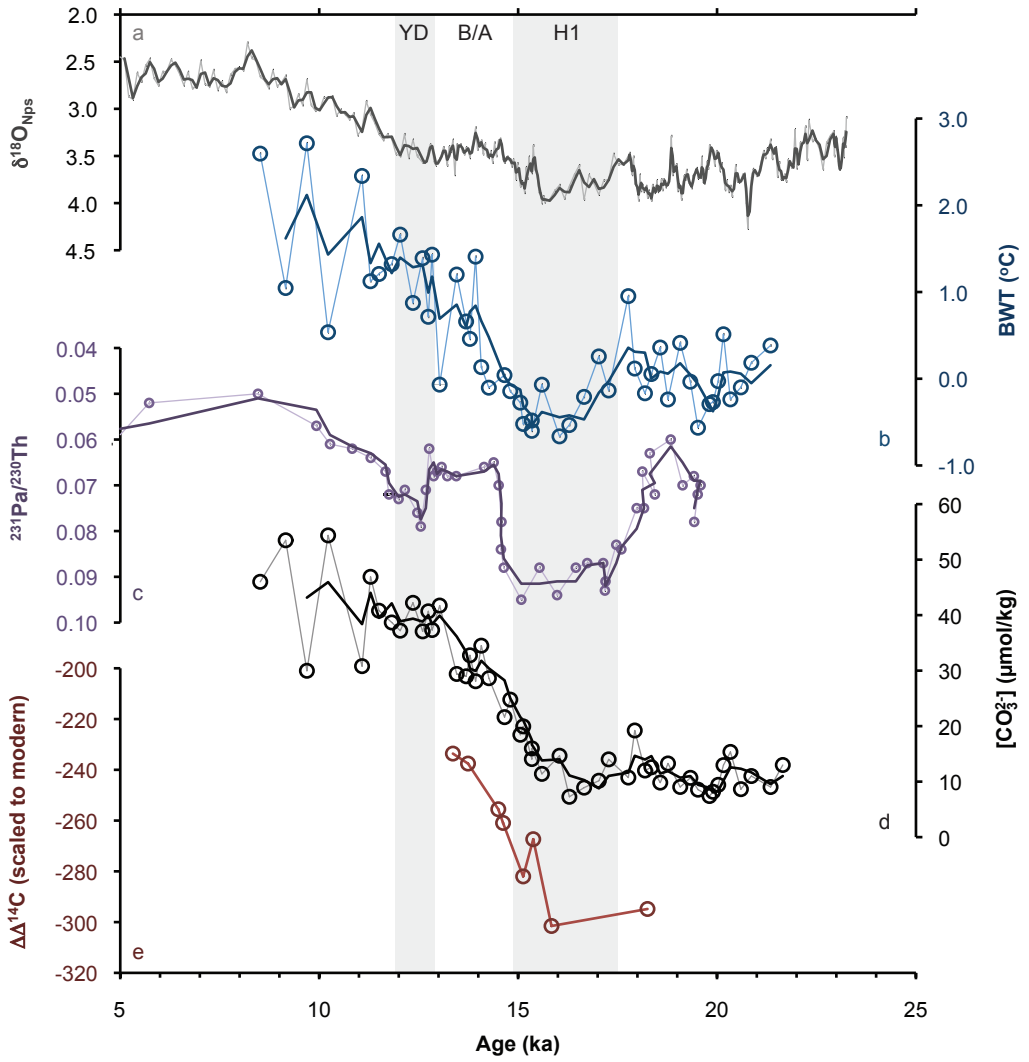

FIGURE 6.20: (a) *N. pachyderma* (s) $\delta^{18}O$ from MD01-2416 for stratigraphic reference (b) BWT from MD01-2416 (c) $^{231}Pa/^{230}Th$ from site OCE326-GGC5 in the North Atlantic (McManus et al., 2004) (d) $[CO_3^{2-}]$ from site MD01-2416 and (e) benthic $\Delta\Delta^{14}C$ (scaled to modern) from site MD01-2416. H1, B/A and YD are the Heinrich 1, Bolling-Allerod and Younger Dryas chronozones respectively.

North Pacific may be driven by better ventilated waters entering the Pacific basin from the south, or by the production of deepwaters within the North Pacific. Increased ventilation within MD01-2416 occurs later than the large increase in benthic foraminiferal $\Delta^{14}C$ in core MD02-2489, that has been taken as evidence for deepwater formation down to depths of ~3600 m within the NE Pacific during the Heinrich 1 stadial (H1) (Rae et al., 2014). Furthermore, the benthic foraminiferal $\Delta^{14}C$ data from MD02-2489 suggest a pulse of deepwater formation, rather than a steady state change in ventilation, as observed in MD01-2416 (Figure 6.21). At ~14.5 ka, a large negative benthic foraminiferal $\delta^{18}O$ excursion at a depth of ~2200m in the Bering Sea suggests

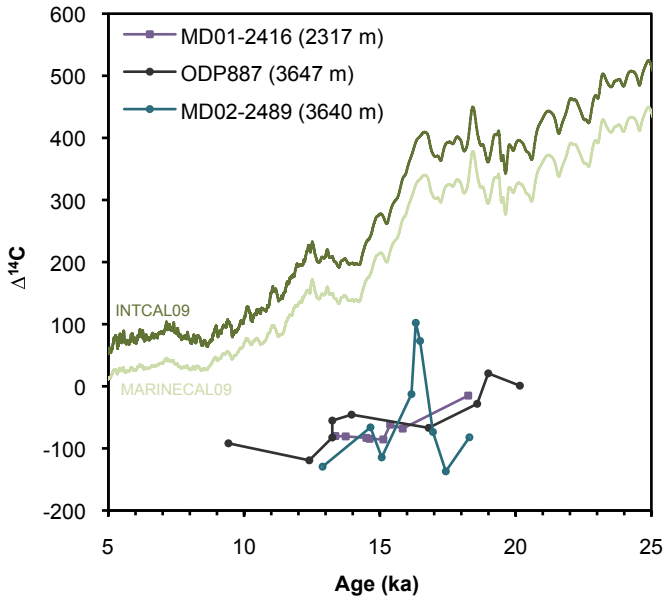

FIGURE 6.21: Deglacial benthic foraminiferal $\Delta^{14}C$ records from MD01-2416, calculated using the data of Gebhardt et al. (2008) and the age model developed in this study (purple), ODP887 (dark blue) (Galbraith et al., 2007), and MD02-2489 (turquoise) (Gebhardt et al., 2008), calculated using a new age model generated in this study by tying *N. pachyderma* (s) $\delta^{18}O$ in the core to the NGRIP $\delta^{18}O$ record on the GICC05 timescale (Andersen et al., 2004; Rasmussen et al., 2006). The INTCAL09 and MARINECAL09 curves are also shown (green and light green respectively) (Reimer et al., 2009).

the formation of deepwater within this basin (Figure 6.22), with an increase in benthic foraminiferal $\Delta^{14}C$ suporting increased ventilation of the Bering Sea at this time (Cook, M.S., 11^{th} International Conference on Paleoceanography, Barcelona, 2013). However, deepwater formation in the Bering Sea is unlikely to drive the ventilation of the deep and deep-intermediate open northwest Pacific as (i) the formation of deepwater in the Bering Sea lags the ventilation of the open northwest Pacific by ~1.5 ka (ii) after ~20 ka benthic foraminiferal $\delta^{18}O$ values in the deep-intermediate Bering Sea remain significantly lower than those in the deep and deep-intermediate open North Pacific for the duration of the deglaciation, suggesting a different (locally sourced) watermass occupied the Bering Sea compared to the open NW Pacific.

While the $\Delta\Delta^{14}C$ and DIC data show the deep-intermediate North Pacific does become better ventilated, DIC concentrations remain as high as the modern day, and the $\Delta\Delta^{14}C$ values remain as depleted in ^{14}C as at present, indicating that this is unlikely to be driven by transient, local deepwater production. The increase in ventilation appears to lead the onset of increased NADW production (as indicated by the sharp decrease in $^{231}Pa/^{230}Th$) (McManus et al., 2004), suggesting it is not driven by the reinvigoration

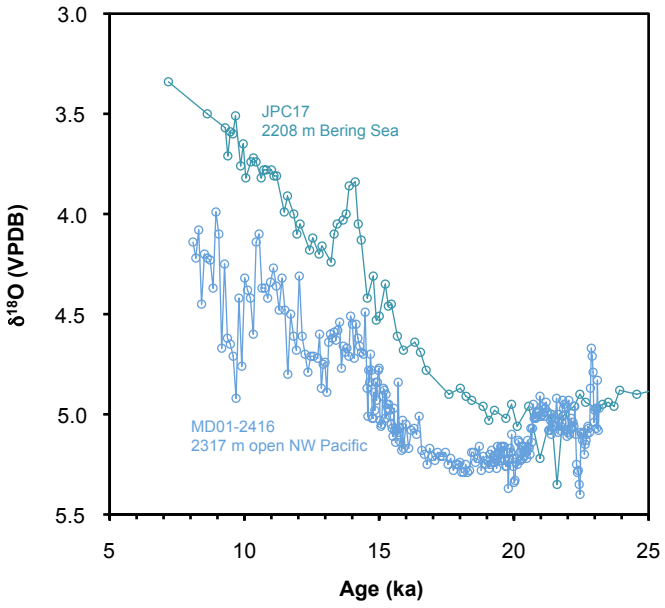

FIGURE 6.22: Deglacial *Uvigerina* spp. δ^{18}O records from MD01-2416 (light blue) (Gebhardt et al., 2008), and JPC17, located at 2208 m in the Bering Sea (turquoise) (Brunelle et al., 2007)

of AMOC during the Bolling Allerod. The rapid increase in ventilation of the deep-intermediate North Pacific occurs at the same time the benthic δ^{18}O records from the deep, and the deep-intermediate North Pacific become indistinguishable (Figure 6.6), suggesting a breakdown in salinity-driven, interior-ocean stratification, and a return to modern-like 'reversed' circulation within the interior North Pacific. This suggests the loss of DIC from the deep and deep-intermediate North Pacific at ~16 ka was driven by a breakdown in interior ocean stratification, and more recently ventilated deepwaters entering the Pacific basin from the south. The reduction in interior ocean stratification would have enabled the formation of PDW to resume through increased diapycnal mixing, reinstating a significant return-pathway of nutrients and DIC from the deep ocean to the intermediate depths and surface ocean. Fundamentally, this change represents a steady-state shift in the oceans ability to sequester DIC in the deep North Pacfic Ocean.

6.4 Conclusions and suggestions for further work

- The expansion of an ^{18}O depleted (low salinity) watermass to depths of >2300 m resulted in an increase in interior ocean stratification within the glacial subarctic Pacific, with a minimum of a three fold increase in the potential density gradient between 3300 m and 1000 m water depth during the LGM.

- Glacial water column profiles of DIC and $\Delta\Delta^{14}C$ show a both an increase in deep/deep-intermediate DIC concentrations of between ~200 - 400 μmol/kg, and a deepening of the DIC pool within the North Pacific, with the most poorly ventilated/DIC-rich waters located at either 2300 m or 3300 m, depending on the approach used to reconstruct DIC. The deepening of the DIC pool within the glacial North Pacific demonstrated within this study supports the nutrient deepening hypothesis of Boyle (1988) as a mechanism by which atmospheric CO_2 was lowered during glacial times, and by acting as a larger reservoir of DIC, highlights a significant role for the North Pacific Ocean in glacial-interglacial carbon cycling.

- While increased interior ocean stratification provides a viable mechanism by which a major return pathway of nutrients/DIC from the deep to intermediate depth/surface ocean in the modern ocean was reduced during glacial times, the relationship between stratification and DIC storage is not straightforward, with more, or as equally poorly ventilated waters at 2300 m as at 3300 m, despite considerably lower salinity ($^{18}O_{sw}$) at the shallower depth.

- An expansion of NPIW to depths of ~2000m had previously been proposed to explain the observation of an ^{18}O depleted and ^{13}C enriched watermass above ~2000 m during glacial times. While a watermass with lower salinity than within the deep ocean is indicated above 2300 m, DIC and $\Delta\Delta^{14}C$ reconstructions show it was as equally poorly ventilated as in the modern day, indicating a more distal source. Tentatively, this is suggested to be GNAIW, or the glacial equivalent of upper Circumpolar Deepwater.

- Reconstructed DIC/$[CO_3^{2-}]$ and $\Delta^{14}C$ shows the loss of between 125-250 μmol/kg of DIC from the deep-intermediate subarctic Pacific at ~16 ka, concurrent with a decrease in ventilation age, and 2 °C warming of bottom waters. Deep ocean $\Delta^{14}C$ and $\delta^{13}C$ records indicate increased ventilation of the deep North Pacific ocurred at a similar time during deglaciation. This denotes a significant transfer of DIC from the deep and deep-intermediate North Pacific Ocean to the intermediate depths, which is likely to have been released to the atmosphere through the surface ocean.

- The loss of DIC from the deep and deep-intermediate Pacific was likely driven by a reduction in interior ocean stratification, indicated by a reduction in the $\delta^{18}O_{Uvigerina}$ gradient between 2300m and 3300m, and more recently ventilated deepwaters entering the Pacific basin from the south. A breakdown in interior ocean stratification within the North Pacific would have reinstated a significant return-pathway of nutrients and DIC from the deep ocean to the intermediate

depths and surface ocean, and represents a steady-state shift in the oceans ability to sequester DIC in the deep North Pacfic Ocean, rather than a transient deep ocean ventilation event.

- The LGM density and DIC water column profiles presented in this study are currently based on a very sparse three point data set; greater coverage of benthic foraminiferal trace element/Ca ratio data is needed throughout the watercolumn in order to build up a more robust reconstruction of the physical and chemical structure of glacial water column.

- The successful approach of using paired Li/Ca and Mg/Ca ratios in *Uvigerina* spp. to reconstruct the temperature and carbonate chemistry of bottom waters over deglaciation in the deep-intermediate subarctic Pacific should be replicated within the deep and intermediate depth North Pacific. This would enable the nature and timing of the breakdown in physical and chemical stratification to be examined. Due to a paucity in deglacial material from the deep NW Pacific, a coring campaign is required before a deep ocean record can be generated.

- In order to generate a record of BWT and carbonate chemistry for the intermediate depth North Pacific using trace elements in benthic foraminifera, the issues of a contamination first have to be overcome. The persistance of contaminants following reductive cleaning suggests traditional foraminiferal trace element cleaning/analytical procedures are not suitable. However, the use of LA-ICP-MS to generate a downcore trace element record may offer a potential solution to the issues of contamination seen in this study, with LA-ICP-MS profiles allowing the foraminiferal and contaminatory signals to be seperated.

Chapter 7

Degacial CO_2 outgassing and surface ocean structure in the subarctic Pacific Ocean

7.1 Introduction

The leading hypotheses regarding changes in atmospheric CO_2 over glacial-interglacial cycles focus on the high latitude oceans (Sarmiento and Toggweiler, 1984; Broecker and Peng, 1989; Sigman and Boyle, 2000). Despite a highly stable upper watercolumn driven by a strong perennial halocline at ∼150 depth (Figure 1.6), tidal mixing brings the most nutrient rich deepwaters within the global ocean into the surface of the modern subarctic Pacific Ocean. Iron limitation results in incomplete nutrient utilisation, with summer PO_4^{3-} concentrations of >1.5 μmol/kg defining the subarctic Pacific as a high-nutrient low-chlorophyll zone (Figure 7.1), and resulting in annual flux of 4 moles/m^2/yr of CO_2 to the atmosphere (Figure 1.9) (Martin, 1990; Takahashi et al., 1993, 2002; Tsuda, 2003).

It is hypothesised that increased stratification of the subarctic Pacific (along with the Southern Ocean) during glacial times drove greater efficiency in the high-latitude biological pump, lowering atmospheric CO_2 (Sigman and Boyle, 2000; Sigman et al., 2010). Down core studies suggest both lower productivity and increased nutrient utilisation in the glacial subarctic Pacific (Kienast et al., 2004; Jaccard et al., 2005; Brunelle et al., 2010), taken as evidence for increased stratification of the watercolumn and a reduction in CO_2 outgassing (Sigman et al., 2004; Jaccard et al., 2005, 2010). Paramount to the high latitude nutrient utilisation theory is that over deglaciation an isolated deep ocean DIC reservoir is returned to the surface ocean and atmosphere

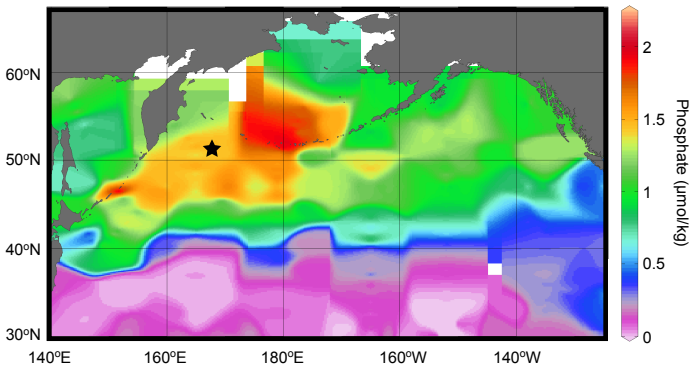

FIGURE 7.1: Summer phosphate concentrations at 25 m depth within the North Pacific, data from Key (2004). Location of MD01-2416 is indicated with a star.

(Sigman and Boyle, 2000; Jaccard et al., 2005; Sigman et al., 2010). Increases in $CaCO_3$ and opal demonstrate a rapid rise in productivity at ~15 ka (Kienast et al., 2004), taken to indicate overturning of the watercolumn, ventilation of the deep ocean, and the return of deeply sequested nutrients and DIC to the surface ocean (Jaccard et al., 2005). The cause of this productivity maximum remains enigmatic however, with above-Holocene productivity levels indicating the current Fe-limitation was overcome (Kienast et al., 2004; Lam et al., 2013).

While increased nutrient utilisation does suggest increased efficiency in the biological pump, there are no quantative constraints on the glacial carbonate chemistry of the subarctic Pacific, and secular changes in $\delta^{15}N$ relating to denitrification complicate interpretations of nutrient utilisation in the North Pacific over deglaciation (Brunelle et al., 2007, 2010). As the upwelling of nutrients is just one of multiple controls on productivity, evident by the high-nutrient low chlorophyll (HNLC) status of the subarctic Pacific today, increased productivity is not necessarily a direct indicator of increased upwelling. Furthermore, productivity records cannot discriminate between proportion of upwelled DIC pool that is remineralised as $CaCO_3$ or C_{org} and that which is released to the atmosphere as CO_2. Again, whilst increased stratification is implied by lower productivity and increased nutrient utilisation, the direct evidence for changes in watercolumn structure is extremely limited, with several records indicating that the salinity driven stratification only developed in the Holocene (Sarnthein et al., 2004; Riethdorf et al., 2013). As such, we do not know if pCO_2 was higher or lower in the glacial subarctic Pacific, how it changed over deglaciation, and how any potential changes may have related to stratification. This study aims to provide the first quantative reconstruction of deglacial pCO_2 within the subarctic Pacific, and assess the relationship between stratification, productivity, and surface ocean pCO_2 over deglaciation.

7.1.1 Multi-species approach to reconstructing upper water column structure

Planktonic tows in the northwestern Pacific show that *Neogloboquadrina pachyderma* (sinistral) is found below the pycnocline, with a maximum abundance between 60-80 m, whereas *Globigerina bulloides* is at a maximum abundance within the mixed layed (20-40 m) (Figure 7.2) (Kuroyanagi and Kawahata, 2004). The difference between *N. pachyderma* (s) and *G. bulloides* δ^{18}O closely follows the mixed layer thickness in the modern northeastern Pacific (Pak and Kennett, 2002) (Figure 7.2). Sediment trap studies in the North Atlantic suggest the greatest flux of *G. bulloides* and *N. pachyderma* occurs during late spring and summer (Jonkers et al., 2013a), whereas sediment traps in the western subarctic showed two seasonal *N. pachyderma* abundance peaks during the spring and autumn, roughly corresponding to the time of most, and least, stratification respectively (Kuroyanagi et al., 2011). As these fluxes are more or less equal, Kuroyanagi et al. (2011) concluded that the *N. pachyderma* δ^{18}O represents average annual oceanographic conditions at, or around, the pycnocline. No studies have been conducted into the growing season of *G. bulloides* in the North Pacific, but given their similarity in the North Atlantic, it is likely to be broadly similar to that of *N. pachyderma* in the North Pacific.

The δ^{18}O of many species of planktonic foraminifera is offset from inorganic calcite (Bemis et al., 2002), and while species-specific δ^{18}O-temperature relationships exist for both *N. pachyderma* (s) and *G. bulloides*, they are poorly constrained at low temperatures (von Langen et al., 2000; Spero et al., 2000). Kuroyanagi et al. (2011) suggested a -1‰ δ^{18}O offset from equilibrium calcite for *N. pachyderma* (s), whereas Jonkers et al. (2010) found no offset from equilibrium inorganic calcite. *G. bulloides* is thought to precipitate its test out of equilibrium, with culturing work generally showing the depletion in ^{18}O relative to equilibrium calcite, with the extent of disequilibrium varying with chamber size and $[CO_3^{2-}]$ (Spero and Lea, 1996; Spero et al., 1997). However, sediment trap data from the northeastern Pacific show *G. bulloides* with δ^{18}O that is both depleted and enriched (by up to ~2 ‰) in ^{18}O relative to calcite at equilibrium at different times of the year (Sautter and Thunell, 1989), and a ~0.4‰ enrichment has been found in the Southern Ocean (King and Howard, 2005). The variability in offset may relate to the extent of different phases of calcite within the test, with the calcification of gametogenic calcite potentially occuring via an altered mechanism or at a different depth within the water column (Hamilton et al., 2008). It can only be assumed that any offset from equilibrium has remained constant in the past.

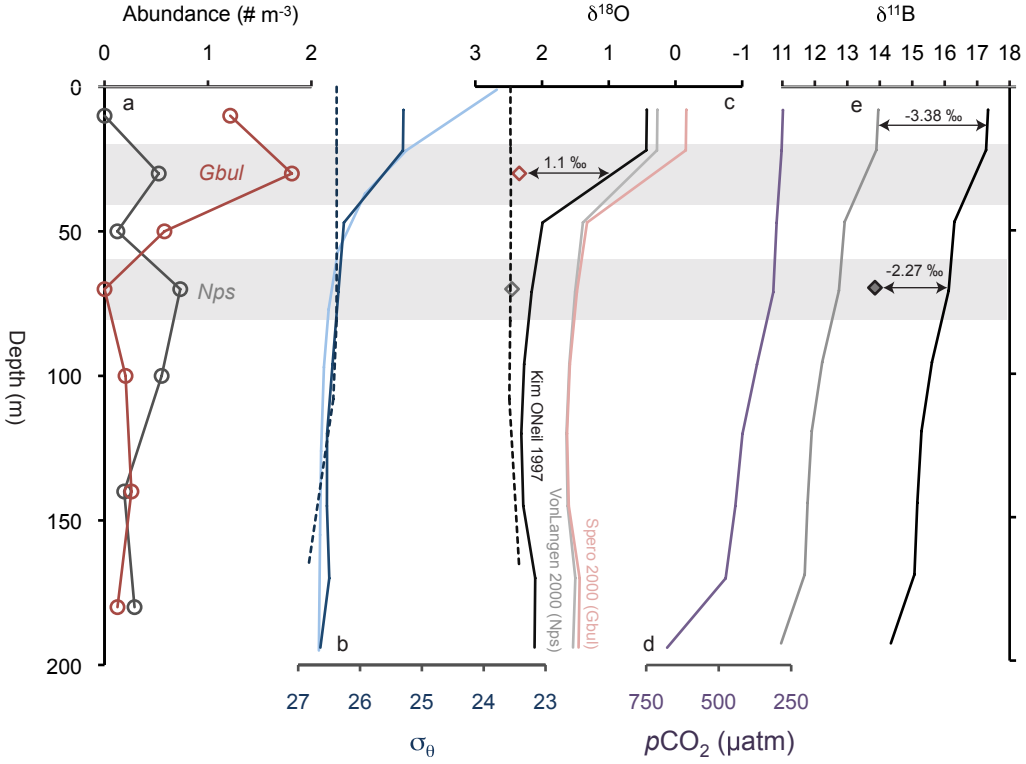

FIGURE 7.2: *N. pachyderma* (s) and *G. bulloides* habitat depth (a) Abundances of *N. pachyderma* (s) (*Nps*) and *G. bulloides* (*Gbul*) throughout the watercolumn in the north west Pacific based on planktonic tows. The interval with the maximum abundance of each species is shaded grey. Data from Kuroyanagi and Kawahata (2004) 'Site b', which although located further south than core MD01-2416 samples the Oyashio Current, and is thus representative of modern-day conditions at the core site, as indicated by the similarity in water column σ_θ profiles. (b) σ_θ for the Kuroyanagi and Kawahata (2004) 'Site b' (light blue) and the north western subarctic Pacific (dark blue), for both August (solid) and March (dashed). (c) $\delta^{18}O_{calcite}$ predicted in the northwestern subarctic Pacific using the species-specific fractionation factors of von Langen et al. (2000) for *N. pachyderma* (s) (light grey) and Spero et al. (2000) for *G. bulloides* (light red), and the equilibrium inorganic calcite relationship of Kim and ONeil (1997) for August (solid black) and March (dashed black). Core top $\delta^{18}O$ measurements of *N. pachyderma* (s) (open grey diamond) and *G. bulloides* (open red diamond) from the Detroit Seamounts (core VIN19-30BC). (d) pCO_2 based on GLODAP hydrographic data in the northwestern subarctic Pacific. (e) Subarctic Pacific $\delta^{11}B$ of $B(OH)_4^-$ (calculated using the parameters defined in the caption of figure 2.7) (black line), and with the -3.38‰ offset suggested for *N. pachyderma* by Yu et al. (2013b) (grey line). Coretop *N. pachyderma* (s) $\delta^{11}B$ from MD01-2416 is shown by the filled diamond.

The Mg/Ca of planktonic foraminifera is a widely applied proxy for water temperature (see section 2.2.1) (Elderfield and Ganssen, 2000; Lea, 2000; Anand, 2003), and calibration studies show a robust relationship between temperature and Mg/Ca in both *N. pachyderma* (s) and *G. bulloides* (Elderfield and Ganssen, 2000; Mashiotta et al., 1999). Core top samples have confirmed the *G. bulloides* Mg/Ca-temperature relationship of Mashiotta et al. (1999) is applicable in the North Pacific (Sagawa et al., 2005). While early culturing work indicated a minor influence of salinity ($5 \pm 3\%$ per PSU) (Lea et al., 1999), recent coretop studies suggested a much higher sensitivity of $15 - 30\%$ (Ferguson et al., 2008; Arbuszewski et al., 2010). Based on tropical species from the high-salinity waters of the low-latitude Atlantic and Mediterranean, however at least some of the 'excess-Mg' has been attributed to diagenisis (Boussetta et al., 2011; Sabbatini et al., 2011). Even if it is found to be high-Mg foraminiferal calcite, no study has ever indicated that salinity exerts such an strong influence on Mg uptake at low levels. Dissolution has also been shown to effect the Mg/Ca of planktonic foraminifera, with the recent study of Regenberg et al. (2014) indicating a much higher influence at low bottom water saturation states than the previous work of Brown and Elderfield (1996). The effect of dissolution can be assessed and corrected for using records of bottomwater ΔCO_3^{2-}. Mg/Ca derived temperatures can be used to deconvolve the effects of temperature and $\delta^{18}O_{sw}$ ($\sim$salinity) from foraminiferal $\delta^{18}O$ and, simultaneously using multiple species with different depth habitats allows past changes in upper ocean watercolumn structure to be reconstructed (Cléroux et al., 2008; Regenberg et al., 2009).

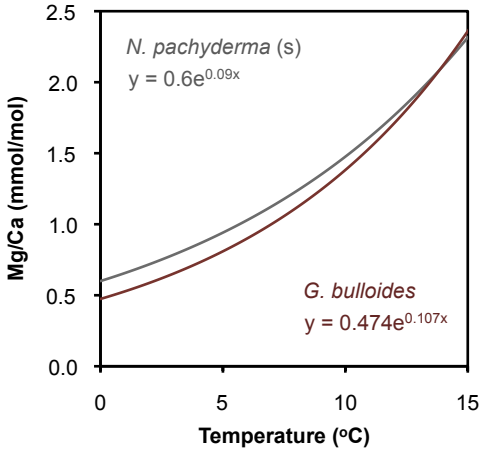

FIGURE 7.3: Mg/Ca temperature calibrations for *N. pachyderma* (grey) (Elderfield and Ganssen, 2000; Jonkers et al., 2013a) and *G. bulloides* (red) (Mashiotta et al., 1999).

7.1.2 Boron isotopes and B/Ca as proxies for the carbonate system

The theory underpinning the use of boron isotopes and B/Ca to reconstruct the pH of seawater is discussed in section 2.2.2. Briefly, boron is present in two species within seawater ($B(OH)_4^-$ and $B(OH)_3$), the proportions of which are pH dependent. Boron has two stable isotopes (^{11}B and ^{10}B); there is a large equilibrium fractionation of ~27‰ between $B(OH)_4^-$ and $B(OH)_3$ (Klochko et al., 2006), making the ratio of ^{11}B and ^{10}B ($\delta^{11}B$) in both species pH dependent. $B(OH)_4^-$ is thought to be the primary species incorporated into carbonates (Hemming and Hanson, 1992). As such both the $\delta^{11}B$, and B/Ca ratio (assuming a constant or knowable partition coefficent) of marine carbonates can be used to calculate seawater pH. Using $\delta^{11}B$ and/or B/Ca-derived pH and an estimation of alkalinity, past pCO_2 can be reconstructed (Palmer, 2003; Yu et al., 2007b; Foster, 2008a; Rae et al., 2011; Allen et al., 2012). The effects of temperature on carbonate and borate system speciation (K_B, K_1 and K_2), coupled with changes in the the HCO_3^- concentration of seawater can lead to significant variability in the $B(OH)_4^-/HCO_3^-$ of seawater that is unrelated to pH. This significantly alters the relationship between pH and foraminiferal B/Ca ratios, bringing considerably higher error into B/Ca derived pH (and pCO_2) reconstructions. Furthermore, dissolution has been shown to lower B/Ca in planktonic foraminifera (Coadic et al., 2013).

Culturing-work and core-top calibrations show species specific offsets from the $\delta^{11}B$ of inorganic calcite, as well as species-specific partition coefficents, and a temperature effect on B uptake in certain species (Yu et al., 2007b; Foster, 2008a; Yu et al., 2013b). Within the high latitude oceans the $\delta^{11}B$ of *Neogloboquadrina pachyderma* has been calibrated, suggesting a constant 3.38‰ offset from equilibrium (Figure 7.4) (Yu et al., 2013b). The partition coefficents (D_B) of *N. pachyderma* and *G. bulloides* have been calculated as 0.0015 and 0.0008 respectively (Figure 7.4), and neither show a dependence on temperature (Yu et al., 2007b, 2013b).

7.2 Materials and methods

Core MD01-2416 is located at 51.27 °N, 167.73 °E, 2317 m water depth on the Detroit Seamount. It is currently situated within the subarctic Pacific HNLC zone, making it well suited to track past changes in CO_2 outgassing in this region (Figure 7.1). The core has previously published *N. pachyderma* (s) and *G. bulloides* $\delta^{18}O$, and %Opal and $\%CaCO_3$ records (Gebhardt et al., 2008). For all $\delta^{18}O$, trace element, and $\delta^{11}B$ analysis *N. pachyderma* (s) were picked from the 150-250 μm size fraction and *G. bulloides* were picked from the >150 μm size fraction, to ensure samples were comparable to those of

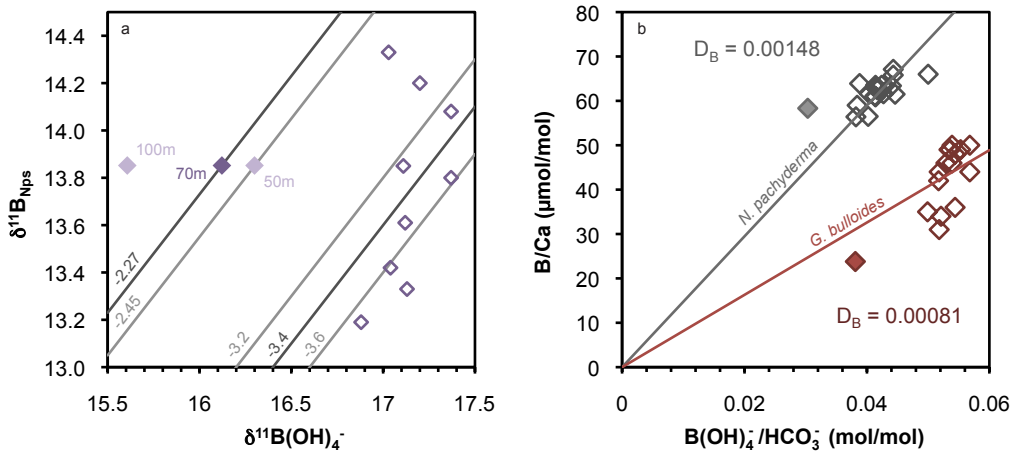

FIGURE 7.4: (a) *N. pachyderma* δ^{11}B (purple) and (b) *N. pachyderma* (s) (grey) and *G. bulloides* (red) B/Ca calibrations. Data from Yu et al. (2013b) are shown by the open diamonds, and filled diamonds are the coretop data from this study.

Gebhardt et al. (2008). Details of the age model generated for the core are given in section 6.2.1.

The *G. bulloides* δ^{18}O record of Gebhardt et al. (2008) was extended back to the LGM, with a 5cm sampling resolution between 200-250 cm depth. Several *N. pachyderma* δ^{18}O samples previously analysed by Gebhardt et al. (2008) were reanalysed at UCL to assess and correct for potential interlaboratory offsets. Details of the analytical procedure are given in section 5.2.3, and reproducibility of foraminiferal replicates is typically ±0.1 ‰, comparable to that of calcite standards. Newly generated δ^{18}O data is presented in the data appendix.

For trace element and δ^{11}B analysis the core was sampled at a 3-15 cm resolution. Between 20 - 50 monospecific *N. pachyderma* (s) and *G. bulloides* individuals were used for trace element analysis, except for samples that were subsequently utilised for δ^{11}B analysis, where a ∼5% split of the δ^{11}B sample was taken. δ^{11}B analysis requires significantly larger sample sizes, and ∼400 individual *N. pachyderma* (s) were used per analysis. *N. pachyderma* (s) was chosen for δ^{11}B analysis as it is the only high-latitude species with a published δ^{11}B calibration. However, 7 *G. bulloides* samples were also analysed as an initial investigation into the potential of using this species for paleo-CO_2 reconstruction. Around 80% of trace element samples were cleaned at UCL in a laminar flow hood fitted with a boron-free PTFE HEPA filter, following the the oxidative/reductive protocol of Boyle and Keigwin (1985) outlined in section 3.4. Around 20% of the samples (those subsequently used for δ^{11}B analysis) were cleaned in a class 100 clean lab at the National Oceanography Centre Southampton (NOCS) according to the 'Mg' method of Barker (2003) as detailed in Rae et al. (2011), which

omits the reductive step in order to avoid dissolution of the foraminiferal calcite and maximise sample size.

Cleaned foraminiferal samples were analysed after acidification for a suite of major and trace elements at Cardiff University or NOCS using a Thermo Finnigan Element II HR-ICP-MS by count ratio calibration against matrix matched standards (Lear et al., 2002). All samples were analysed against Cardiff's MCS A 2011 trace element standard. δ^{11}B was analysed at NOCS on a Thermo Finnigan Neptune MC-ICP-MS following the method of Foster (2008a) and Rae et al. (2011), which involves removing the Ca matrix prior to analysis using anionic exchange resin, and sample-standard bracketing to accurately correct for instrument induced mass fractionation. Reproducibility of this approach is ±0.25‰ at the 95% confidence interval. All trace element and δ^{11}B data is presented in the data appendix.

7.3 Results and discussion

7.3.1 Trace element contamination and cleaning procedures

N. pachyderma (s) and *G. bulloides* B/Ca and Mg/Ca ratios from samples cleaned by the oxidative only ('oxidative' from here on), and oxidative/reductive ('reductive') cleaning protocols (see sections 7.2 and 3.4 for details) were regressed against Al/Ca, Mn/Ca and U/Ca to asses the influence of clay, Mn-Fe oxyhyroxide and secondary carbonate overgrowth contamination (see table 7.1 and appendix A). U/Ca can be used as a contamination indicator as the activity of U increases significantly within porewaters under low oxygen conditions. U may be then be co-precipitated with Mg (and other trace elements) in secondary carbonate overgrowths that are also formed within porewaters. Different species and cleaning protocols were regressed seperately in order that species dependent inter-test trace element concentrations could be accounted for, and in order to assess the effects of the different cleaning procedures. All trace element/Ca data are shown against depth down core in figure 7.5.

Both reductively and oxidatively cleaned *N. pachyderma* (s) Mg/Ca ratios are strongly positively correlated with U/Ca. While the Mg/Ca values for the oxidatively and reductively cleaned valves display a very similar trend down core, and are constantly offset from each other by ~ 0.1 mmol/mol, U/Ca within the oxidatively cleaned samples is two orders of magnitude greater than in the reductively cleaned valves (note different scale for oxidative samples in figure 7.1). As such, while both the oxidative and reductive samples display a significant correlation to U/Ca, the relationships between U/Ca and

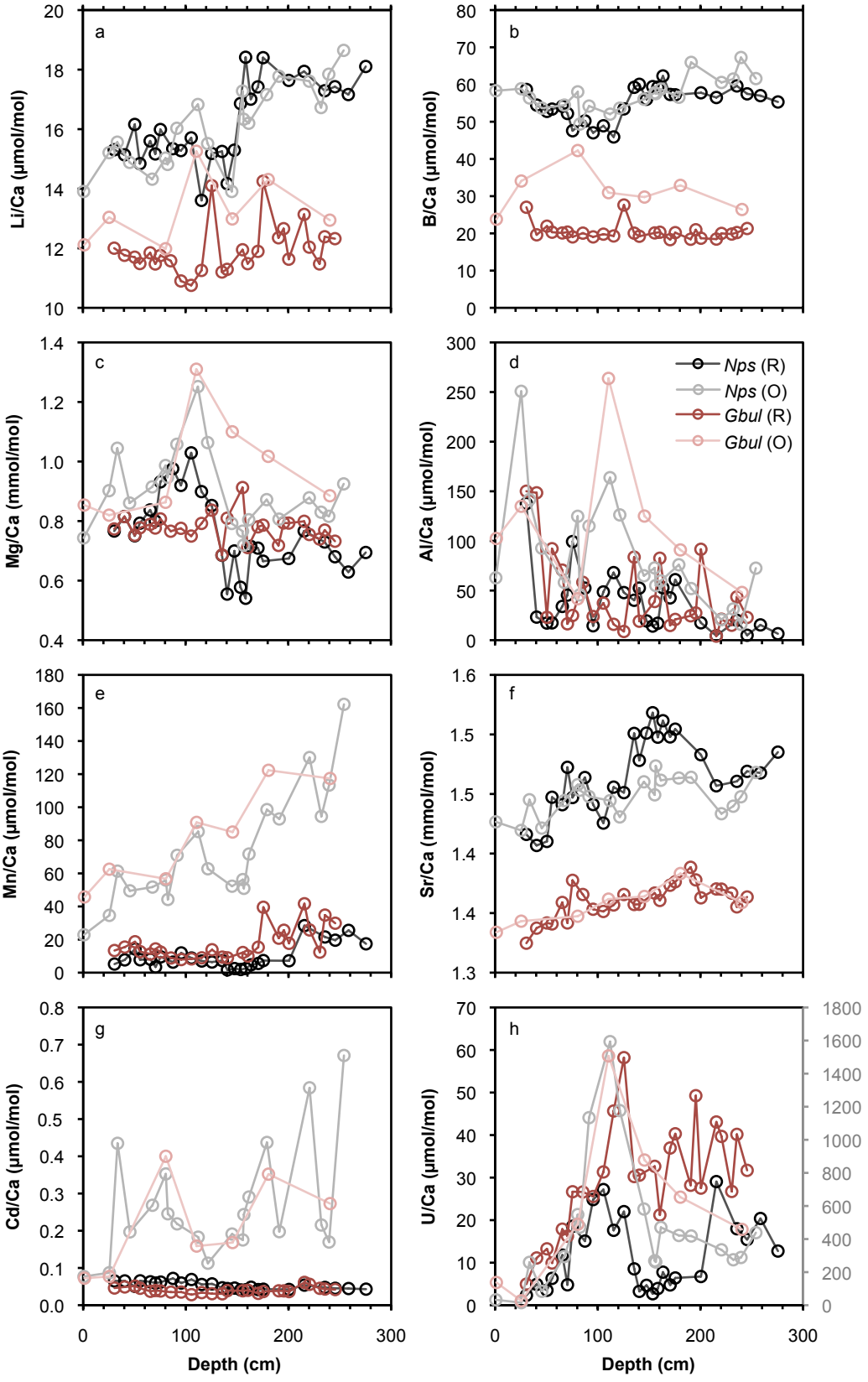

FIGURE 7.5: Reductively cleaned (R) and oxidatively cleaned (O) *N. pachyderma* (s) (black/grey) and *G. bulloides* (red/pink) (a) Li/Ca (b) B/Ca (c) Mg/Ca and (d) Al/Ca (e) Mn/Ca (f) Sr/Ca (g) Cd/Ca (h) Cd/Ca ratios plotted downcore. Note different scale (shown in grey) for oxidatively cleaned U/Ca.

TABLE 7.1: *p* values for correlations between contamination indicators and element/Ca ratios of interest. Significant correlations at the 95% interval are highlighted in bold. R is reductive cleaning and O is oxidative cleaning, see sections 7.2 and X for further details. Plots of the correlations are shown in appendix A

Species/cleaning		Li/Ca	B/Ca	Mg/Ca	Cd/Ca
N. pachyderma (s) R	Al/Ca	0.06	0.43	0.11	**0.04**
	Mn/Ca	**0.03**	0.95	0.89	0.67
	U/Ca	0.92	**0.01***	<**0.01**	0.11
N. pachyderma (s) O	Al/Ca	0.27	0.15	**0.01**	0.32
	Mn/Ca	<**0.01**	**0.02**	0.68	<**0.01**
	U/Ca	0.65	0.08	<**0.01**	0.75
G. bulloides R	Al/Ca	0.22	0.26	0.72	0.70
	Mn/Ca	<**0.01**	0.74	0.97	<**0.01**
	U/Ca	<**0.01**	0.99	0.30	0.26
G. bulloides O	Al/Ca	0.05	0.73	**0.03**	0.22
	Mn/Ca	0.15	0.72	0.39	0.33
	U/Ca	0.05	0.93	<**0.01**	0.74

*negative correlation

Mg/Ca are very different (Figure A.3). If the relationship between U/Ca and Mg/Ca was caused by a contaminant phase containing high concentrations of U and Mg, the relationship between Mg/Ca and U/Ca should be the same for both cleaning oxidatively and reductively cleaned samples, indicating this is not the cause of the correlation.

Mg/Ca in the oxidatively cleaned samples also shows a significant correlation with Al/Ca. The relationship between Mg/Ca and Al/Ca is caused by 5 samples with Al/Ca ratios over 100 µmol/mol. If these samples are excluded from the dataset the correlation between Mg/Ca and Al/Ca is not significant. The samples with Al/Ca over µmol/mol were corrected for the excess Mg, likely to be associated with clays using the relationship between Al/Ca and Mg/Ca in figure A.3. The correction is typically ∼10% (equivalent to ∼1 °C), and excluding these samples makes no difference to any of the conclusions drawn.

Excluding the 5 samples with Al/Ca ratios over µmol/mol, the Mg/Ca ratios for the oxidative samples are consistently higher than those for the reductive samples by 0.087 mmol/mol (10%). Reductive cleaning has been shown to lower the Mg/Ca of foraminiferal calcite by ∼10%, thought to be caused by the preferential dissolution of higher Mg phases of the foraminiferal calcite (Barker, 2003). 0.086 mmol/mol was

therefore added to all the reductively cleaned samples to correct for this offset, in order to match the cleaning protocol of the calibration study used to convert the Mg/Ca ratios to temperature (Elderfield and Ganssen, 2000). After corrrection, the oxidative (including the Al-corrected samples) and reductive samples show very good agreement with each other.

Reductively cleaned *G. bulloides* Mg/Ca shows no significant correlation to any of the contamination indicators, suggesting the influence of clays and Mn-Fe oxyhydroxides is minimal. In order to account for differences in cleaning method between this study and the *G. bulloides* calibration of Mashiotta et al. (1999) (which used oxidative cleaning only), a 10% correction factor was applied to the reductively cleaned *G. bulloides* Mg/Ca values. Oxidatively cleaned *G. bulloides* Mg/Ca is significantly correlated to both Al/Ca and U/Ca however. As such, the small number of oxidatively cleaned *G. bulloides* Mg/Ca datapoints are excluded from the study, except for the coretop sample which shows no sign of contamination.

B/Ca in reductively cleaned *N. pachyderma* (s) shows no correlation with Al/Ca or Mn/Ca, but does show a significant negative correlation with U/Ca. The negative correlation is highly unlikely to be due to contamination, and may be caused by a pH or $[CO_3^{2-}]$ control on both B/Ca and U/Ca. A negative relationship between $[CO_3^{2-}]$ and U/Ca has been found in both culture and coretop studies of benthic foraminifera (Raitzsch et al., 2011; Keul et al., 2013), possibly driven by the preferential uptake of smaller uranyl carbonate complexes, which are more abundant at low $[CO_3^{2-}]$ activity (see section 2.2.3). B/Ca in oxidatively cleaned *N. pachyderma* (s) shows a significant correlation with Mn/Ca. The effect of reductive cleaning on B/Ca has been found to be negligible (Yu et al., 2007a), and both the oxidative and reductively cleaned samples show similar values and trends downcore (Figure 7.5), despite the significantly higher Mn/Ca ratios of the oxidatively cleaned samples. In order to assess if Mn-Fe hydroxides are significantly influencing the B/Ca and $\delta^{11}B$ values, the amount of excess boron in each of the oxidatively cleaned samples was calculating by linearly interpolating between stratigraphically bracketing reductively cleaned samples. Although the amount of excess boron does generally increase with Mn/Ca, the relationship is not significant as the amount of B in Mn-Fe oxyhydroxides is generally low (Yu et al., 2007a; Foster, 2008a). However, the oxidatively cleaned B/Ca values are generally more scattered than those of reductively cleaned samples, and are thus excluded from the datset out of caution. There is no relationship between excess boron and $\delta^{11}B$, indicating negligible influence of contamination on the *N. pachyderma* $\delta^{11}B$ record. Neither the oxidatively or reductively cleaned *G. bulloides* B/Ca ratios show a significant correlation with any of the contamination indicators.

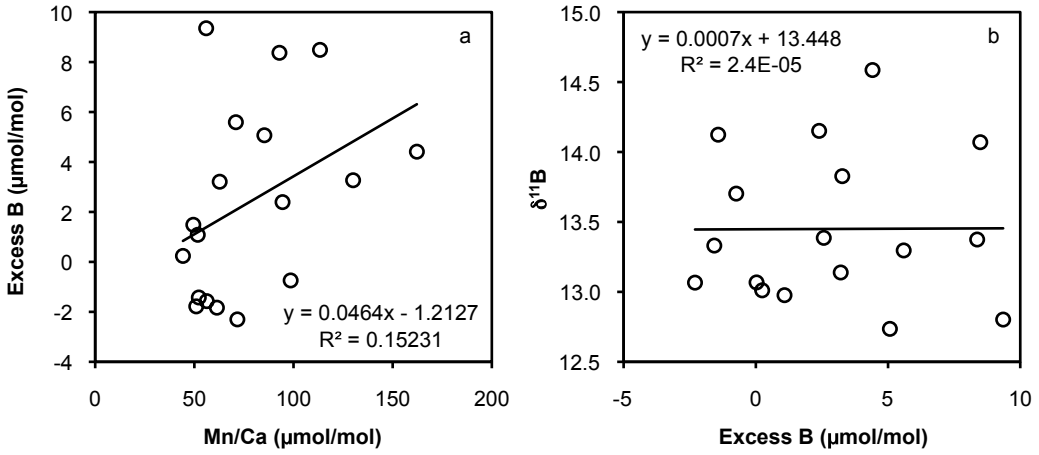

FIGURE 7.6: (a) Mn/Ca versus excess B (see text for details) in oxidatively cleaned *N. pachyderma* (s) and (b) the relationship between excess B and δ^{11}B.

7.3.2 Temperature and $\delta^{18}O_{sw}$

Mg/Ca ratios were converted to temperature using the calibration of Elderfield and Ganssen (2000) (recalculated by Jonkers et al. (2013b)) for *N. pachyderma* (s), and that of Mashiotta et al. (1999) for *G. bulloides* (which as been confirmed for the North Pacific by Sagawa et al. (2005). Error in both calibrations is equivalent to ±1 °C. Coretop (∼5 ka) Mg/Ca-temperature for *N. pachyderma* (s) shows good agreement with modern mean annual temperature at 70m water depth, and the *G. bulloides*-Mg/Ca temperature is close to mean annual temperature at 30m (Figure 7.7). Predicted $\delta^{18}O_{calcite}$ was calculated using modern hydrographic data from Key (2004) and Boyer et al. (2009), and the inorganic calcite fractionation factor (α) of Kim and ONeil (1997) and North Pacific salinity-$\delta^{18}O_{sw}$ relationship of LeGrande and Schmidt (2006). Coretop *N. pachyderma* (s) δ^{18}O matches mean annual predicted δ^{18}O at 70m depth (Figure 7.2), supporting Jonkers et al. (2010)'s assertion that *N. pachyderma* (s) precipitates calcite at or close to equilibrium, and reflects annual average conditions close to the pycnocline (Kuroyanagi et al., 2011). The δ^{18}O of *G. bulloides* is close to predicted δ^{18}O during winter conditions (-0.1‰), but 1.1 ‰ offset from equilibrium calcite predicted during the summer months. Given that the Mg/Ca-temperature relationship is better constrained than the δ^{18}O-temperature relationship in *G. bulloides*, and that this species has been widely demonstrated to precipitate its test out of equilibrium, the *G. bulloides* δ^{18}O data were corrected by 0.5 ‰ when calculating $\delta^{18}O_{sw}$. The 0.5 ‰ offset is based on the season/habitat depth indicated by the Mg/Ca temperature of the coretop, and its known habitat depth in the North Pacific (Kuroyanagi and Kawahata, 2004). This is similar to the offset found in the Southern Ocean (King and Howard, 2005), but very different to the results of laboratory cultures (Spero and Lea, 1996). The lack of consensus regarding the

nature and cause offsets from equilibrium in *G. bulloides* highlights the need for further (regional) planktonic tow and sediment-trap-based geochemical calibration studies, in order that this species may be fully utilised as a paleoceanographic recorder.

Downcore *N. pachyderma* (s) and *G. bulloides* $\delta^{18}O$, including the data generated in this study, are shown in figure 7.7 (note the *G. bulloides* $\delta^{18}O_{calcite}$ is not corrected for offsets from equilibrium in this figure). $\delta^{18}O_{sw}$ was calculated by removing the temperature component of the $\delta^{18}O_{calcite}$ with the Mg/Ca temperature, and correcting for the secular deglacial change in $\delta^{18}O_{sw}$ relating to ice volume by scaling the ~1‰ change in $\delta^{18}O_{sw}$ of Adkins (2002) to the sea level curve of Fairbanks (1989). This approach assumes that the ^{18}O depleted glacial meltwaters are instantaneously mixed within the ocean, which is a reasonable assumption for the surface ocean (within the ±1000 yr error of the age model), but has been demonstrated not to be the case for the deep ocean (Gebbie, 2012). $\delta^{18}O_{sw}$ is not converted to salinity, because although the direction of change within the $\delta^{18}O_{sw}$-salinity relationship will have remained constant over deglaciation, the exact relationship is likely to have changed.

Before discussion of changes in surface ocean structure, the potential effects of dissolution on the record must be considered. Regenberg et al. (2014) proposed a global Mg/Ca dissolution sensitivity of 0.054 μmol/mol/μmol/kg, below a ΔCO_3^{2-} threshold of 21.3 μmol/kg. The ΔCO_3^{2-} at the site is below this threshold in the modern ocean, and ΔCO_3^{2-} reconstructions show lower saturation during the LGM (see section 6.3.4). However, there are three lines of evidence that suggest dissolution is at most a minor factor within the Mg/Ca record. Firstly, using the dissolution sensitivity of Regenberg et al. (2014), the ~30 μmol/kg increase in deep ocean ΔCO_3^{2-} (Figure 6.19) would result in a 1.6 mmol/mol increase in Mg/Ca. This is five times higher than the observed increase in *N. pachyderma* (s) Mg/Ca, and thus would require a significant (~10 °C) cooling at this time to result in the observed trend. This seems highly unlikely as it occurs at a time when the rest of the Northern Hemisphere appears to be warming. Secondly, the correction of Regenberg et al. (2014) suggests dissolution should affect different species of planktonic foraminifera in a broadly similar manner, however the 0.3 mmol/mol increase in *N. pachyderma* (s) Mg/Ca is not seen in the *G. bulloides* record. If dissolution were a major factor in the Mg/Ca records, the Mg/Ca of both species should look broadly similar, in which case a cooling that exactly cancelled out the effect increased saturation state would be required to result in the observed *G. bulloides* Mg/Ca trend. Thirdly, the increased in *N. pachyderma* (s) Mg/Ca clearly leads the large increase in $\%CaCO_3$ within the core. Porewater saturation state will be the determining factor in the amount of dissolution that occurs (as the tests will be exposed to porewaters for much longer than bottomwaters), and thus if dissolution were a major factor in the record Mg/Ca would

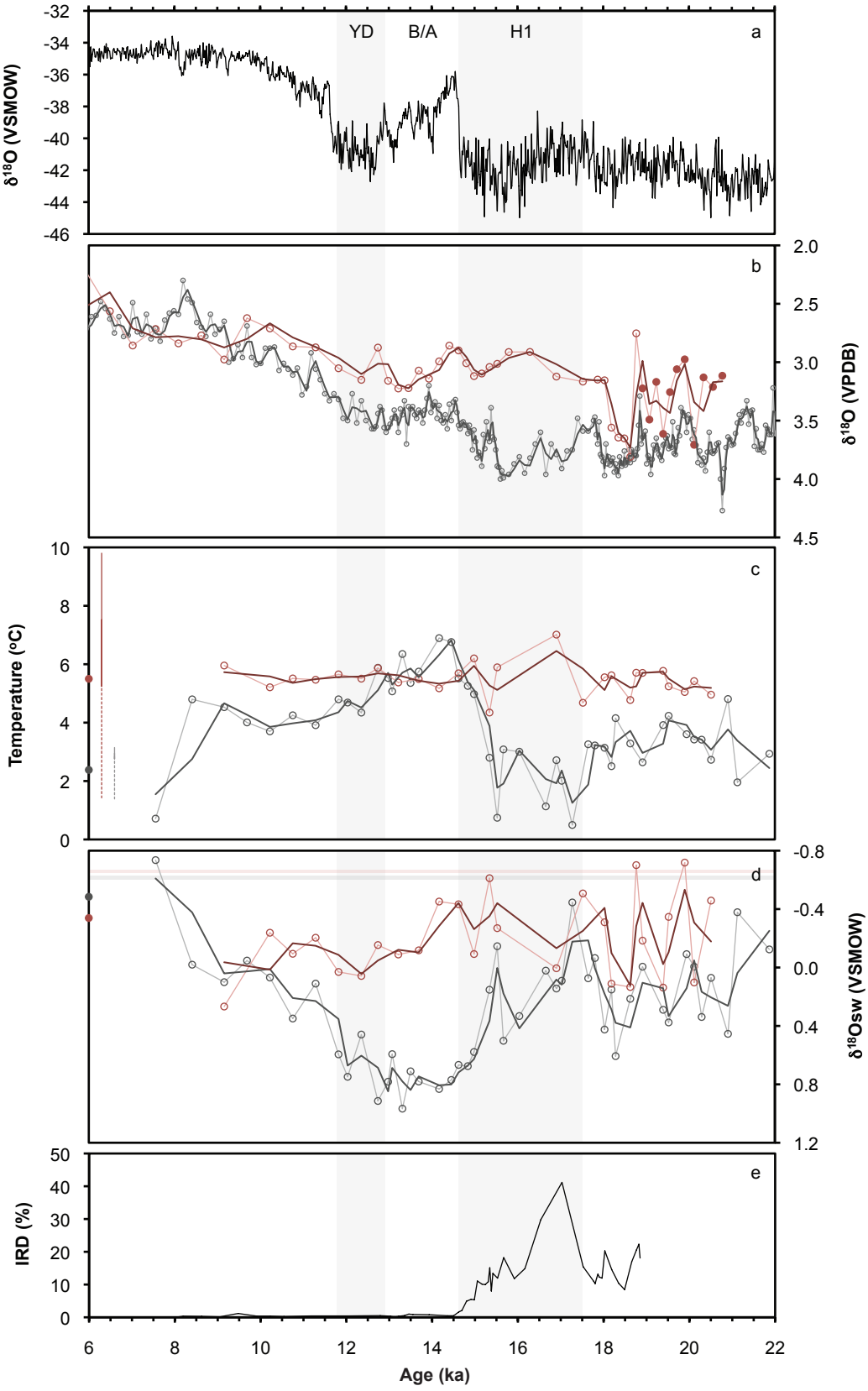

FIGURE 7.7: *N. pachyderma* (s) is shown in grey and *G. bulloides* is shown in red. Coretop values are shown by a solid circle on the y axis (a) NGRIP δ^{18}O on the GICC05 timescale (Rasmussen et al., 2006) (b) $\delta^{18}O_{calcite}$ (filled circles represent new data) (c) Temperature, with modern temperatures between 20-40 m depth (red) and 60-80 m depth (grey), and during summer (solid) and winter (dashed) indicated by the vertical lines (d) $\delta^{18}O_{seawater}$ (ice volume corrected), with the annual range of modern values at 30m (red) and 70m (grey) shown by the horizontal bar (e) %IRD data from Gebhardt et al. (2008).

be expected to change in step with $\%CaCO_3$. The absence of a significant influcence of dissolution on the Mg/Ca records indicates they can be used reliably to reconstruct past changes in water temperature.

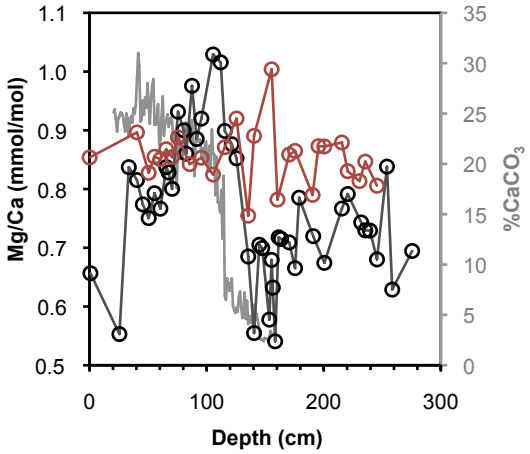

FIGURE 7.8: *N. pachyderma* (s) (black) and *G. bulloides* (red) Mg/Ca plotted downcore with $\%CaCO_3$ (grey). The $\%CaCO_3$ only extends to 155 cm.

The *N. pachyderma* (s) and *G. bulloides* temperature records clearly display different trends over deglaciation. While the *G. bulloides* record shows an almost constant temperature, suggesting temperatures similar to modern throughout deglaciation within the mixed layer, the *N. pachyderma* (s) record shows significant changes. From a baseline glacial temperature of of ~3 °C (that is similar to, or slightly higher than, modern), *N. pachyderma* (s) temperatures first decrease to ~2 °C at 17.5 ka (at the onset of the Heinrich 1 stadial), before rapidly increasing at 15.5 ka to a maximum of ~7 °C. The maximum temperature is higher than that observed in the *G. bulloides* record, although within error. From this maximum, temperature decreases steadily, but remains above modern until ~8 ka, when it decreases rapidly toward modern values. The pattern of change is similar to that observed in the more coastal North Pacific *N. pachyderma* (s) Mg/Ca temperature record of Riethdorf et al. (2013), which also shows cooling during H1, and warming at 15.5 ka.

While the relative stability of the *G. bulloides* record suggests similar temperatures in the mixed layer throughout deglaciation, changes in growing season and/or water depth must be considered. Rather than representing constant temperature in the mixed layer, it is possible than the lack of significant change results from shifting growing season/and or water depth to ensure optimum growth conditions. Thornalley et al. (2011) proposed that similar glacial and Holocene Mg/Ca temperatures for *G. bulloides* reflected habitat preference in the North Atlantic, where the site was influenced by alternating warm and cold surface ocean currents. *G. bulloides* become dominant in the fauna when summer

SST temperatures are >7 °C, but can tolerate a wide temperature range (Hilbrecht, 1996). What can be concluded from the seemingly constant deglacial temperature of ∼6 °C, and constant presence of *G. bulloides* through the record, is that over deglaciation at least some part of the mixed layer maintained a temperature of ∼6 °C at some point in the year; what proportion of the overall mixed layer this represents in the past is not known however. An argument against changing growth season/depth as a dominant factor in the *G. bulloides* Mg/Ca record comes from comparison of the $\delta^{18}O_{calcite}$ of *N. pachyderma* (s) and *G. bulloides*. Prior to ∼17 ka both species show large simultaneous fluctuations of >0.5‰. If changing depth habitat/growing season were a dominant control on the *G. bulloides* geochemical records then *N. pachyderma* (s) would also have to be changing growing season/habitat depth concurrently with *G. bulloides* for both species to show a similar pattern. Given the very different temperature preference of *N. pachyderma* (s) this seems highly unlikely, suggesting that the observed geochemical changes result from changes within the watercolumn, rather than being artefacts of foraminiferal habitat preference.

Prior to ∼17 ka sub-millenial scale variability is observed in both the *N. pachyderma* (s) and *G. bulloides* $\delta^{18}O_{calcite}$ records. However, greater magnitude is seen in the *G. bulloides* record (Figure 7.7). Separation of the temperature and $\delta^{18}O_{sw}$ components reveals that almost all of the millenial scale variability is driven by changes in $\delta^{18}O_{sw}$. Small changes can be seen in the *N. pachyderma* (s) temperature record, with subsurface waters cooling slightly as they become more ^{18}O depleted (fresher). These rapid and high magnitude fluctuations in $\delta^{18}O_{sw}$, observed in both *N. pachyderma* (s) and *G. bulloides* suggest large changes in the surface salinity of the North Pacific, equivalent to 2 PSU in the mixed layer and 1 PSU at the subsurface using the modern North Pacific salinity-$\delta^{18}O_{sw}$ relationship of LeGrande and Schmidt (2006). Such dynamic changes in salinity are remarkable for an ocean basin that is today defined by persistant low salinity to a depth of ∼200 m. Large fluctuations in the surface salinity of the North Pacific at this time may have been driven by changes in the freshwater flux associated with the East Asian monsoon, which today drives the permanent halocline (Warren, 1983; Emile-Geay, 2003). Inidcations of monsoon strength from the Hulu cave speleothem record indicate pronounced sub-millenial scale variability in the strength of the East Asian monsoon during early deglaciation (Wang et al., 2001b; Wu et al., 2009; Southon et al., 2012) (Figure 7.9), although due to the ±1000 yr error in the age model of this study, it is not possible to conclude wether these changes are synchonous with the changes in subarctic Pacfic $\delta^{18}O_{sw}$. It should also be noted, that while displaying large shifts, the $\delta^{18}O_{sw}$ of both the subsurface and mixed layer is considerably higher than modern through all of the deglaciation, with mixed layer values only becoming as ^{18}O depleted as the present day during the very peaks of the sub-millenial variability. The

general increase in $\delta^{18}O_{sw}$ suggests higher salinity within the surface and subsurface of the North Pacific during glacial times, and over the course of deglaciation.

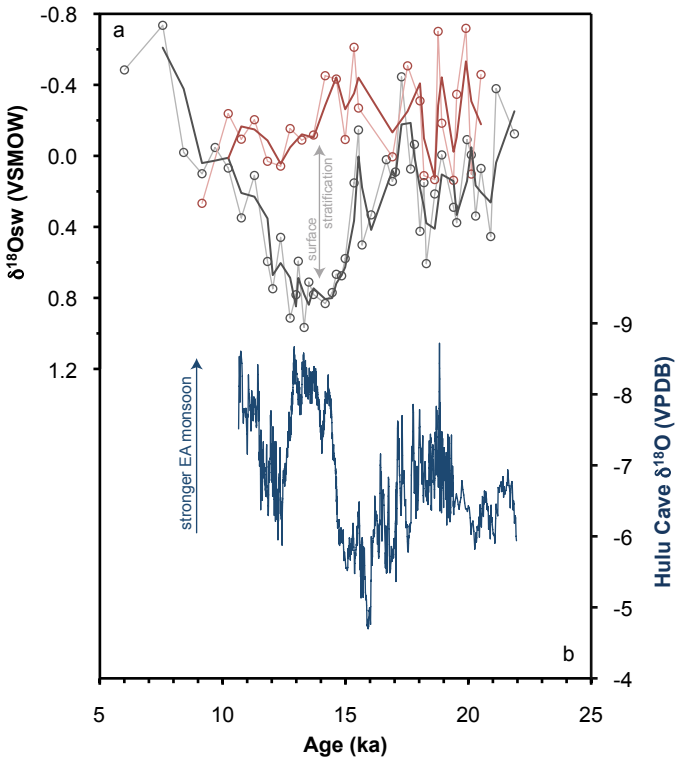

FIGURE 7.9: (a) *N. pachyderma* (s) (grey) and *G. bulloides* (red) $\delta^{18}O_{sw}$ and (b) the Hulu Cave speleothem $\delta^{18}O$ record (blue) (Wang et al., 2001b; Wu et al., 2009; Southon et al., 2012)

After ~17 ka the parallel $\delta^{18}O_{sw}$ variability within both the *N. pachyderma* (s) and *G. bulloides* records ceases, with the *G. bulloides* $\delta^{18}O_{sw}$ first decreasing, then steadily increasing into the early Holocene. Conversely, the *N. pachyderma* (s) $\delta^{18}O_{sw}$ increases to reach a maximum at ~14.5 ka, before decreasing into the early Holocene. This increase in *N. pachyderma* (s) $\delta^{18}O_{sw}$ is equivalent to a ~1.5 PSU increase in salinity using the modern North Pacific salinity-$\delta^{18}O_{sw}$ relationship of LeGrande and Schmidt (2006), and therefore represents a significant increase in salinity of the subsurface waters that coincides with the pronounced warming beginning at ~15.5 ka. The divergence in *N. pachyderma* (s) and *G. bulloides* $\delta^{18}O_{sw}$ at ~17 ka occurs following the deglacial minimum in *N. pachyderma* (s) $\delta^{18}O_{sw}$ that is coincidental with a large increase in ice rafted debris (IRD) within the core (Figure 7.7) (Gebhardt et al., 2008). Whether the source of ice was local or distant (Bigg et al., 2008), the large increase in IRD and minimum in *N. pachyderma* (s) $\delta^{18}O_{sw}$ is indicative of a massive release of freshwater into the North Pacific, which would have increased salinity stratification in the upper surface ocean. Thus, while the higher than modern day $\delta^{18}O_{sw}$ observed throughout

deglaciation supports previous studies that have concluded that the onset of the North Pacific halocline did not occur until the Holocene (Sarnthein et al., 2004; Riethdorf et al., 2013), the large difference in *N. pachyderma* (s) and *G. bulloides* $\delta^{18}O_{sw}$ shows a shallow but distinct halocline persisted from ~17 - 10 ka, reaching its maximum extent at ~14 ka, during a time of increased East Asian monsoon strength (Wang et al., 2001b; Wu et al., 2009; Southon et al., 2012) (Figure 7.9).

7.3.3 δ^{11}B constraints on CO_2 outgassing

The deglacial *N. pachyderma* (s) and *G. bulloides* δ^{11}B and B/Ca records are shown in figure 7.10. *N. pachyderma* (s) δ^{11}B ranges between ~13 and 14.5 ‰ (close to the range of $B(OH)_4^-$), and shows a general decrease over deglaciation. The δ^{11}B of *G. bulloides* varies between ~1 and 10 ‰, which is considerably below the δ^{11}B of $B(OH)_4^-$. The very low δ^{11}B values indicate the δ^{11}B of *G. bulloides* does not represent seawater $B(OH)_4^-$, and cannot be used to reconstruct pH; pH is in fact incalculable in this range. A negative offset cannot be driven by the incorporation of boric acid or by elevated pH during calcification as these would work to increase δ^{11}B (Zeebe et al., 2003; Foster, 2008b). As *G. bulloides* is symbiont barren, the low values may be caused by the effects of respiration on the foraminiferal microenvironment, or some other unknown vital effect.

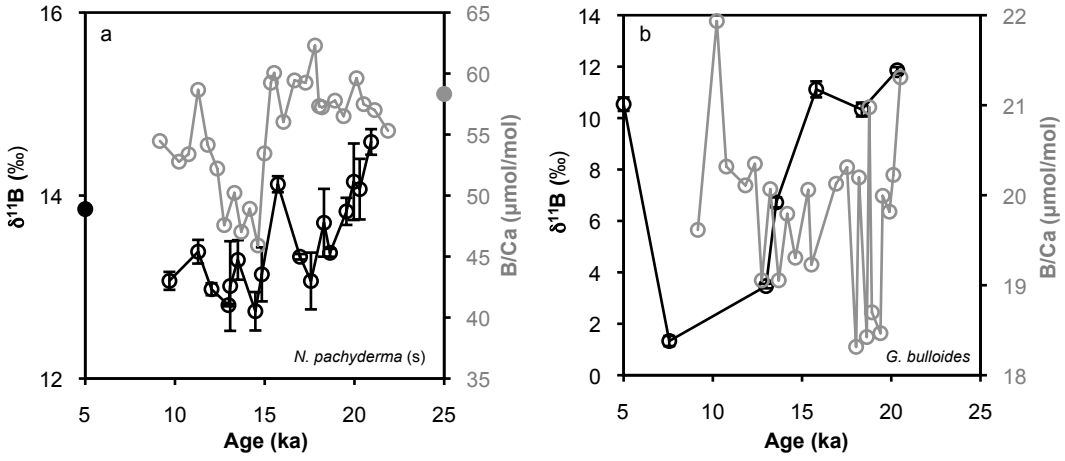

FIGURE 7.10: Downcore variations in δ^{11}B (black) and B/Ca (grey) in (a) *N. pachyderma* (s) and (b) *G. bulloides* in core MD01-2416. Coretop values are shown by solid circles.

B/Ca in *N. pachyderma* (s) varies between 45 - 60 µmol/mol, slightly lower than the range of deglacial values observed in the North Atlantic by Yu et al. (2013b). A prominent decrease in B/Ca occurs at ~15 ka. B/Ca in *G. bulloides* is markedly lower than in *N. pachyderma* (s), despite the higher pH of its habitat depth, as previously noted by Yu et al. (2007b) in relation to *Globorotalia inflata*. The range in values is also

lower than those observed in the coretop calibration of Yu et al. (2007b), and shows no trend over deglaciation.

The 3.38‰ offset of Yu et al. (2013b) was applied to the *N. pachyderma* (s) δ^{11}B values to correct to $\delta^{11}B(OH)_4^-$. The coretop value for the site shows a slightly lower offset of 2.27‰ (Figure 7.4), suggesting a regional calibration study should be conducted to confirm whether the relationship of Yu et al. (2013b) can be applied outside of the North Atlantic. However, to date the study of Yu et al. (2013b) is the only calibration study of this species. pH was calculated from corrected *N. pachyderma* (s) δ^{11}B using a seawater δ^{11}B value of 39.61 ‰ (Foster et al., 2010) and the experimentally-determined fractionation factor of 1.0272 (Klochko et al., 2006). The boric acid dissociation constant (K_B) was calculated with reconstructed temperatures and salinities (using the North Pacific salinity-$\delta^{18}O_{sw}$ relationship of LeGrande and Schmidt (2006)) using the constants of Dickson (1990b) and Millero (1995). Uncertainty in K_B was calculated using the temperature calibration error of ±1 °C, and a salinity error of ±2 PSU. The combined temperature and salinity uncertainty is equal to a pH error of ±0.02, which was combined with the analytical uncertainty to arrive at total pH error (typically ±0.04 pH units). Deglacial pH, derived from δ^{11}B values of *N. pachyderma* (s), is shown in figure 7.11.

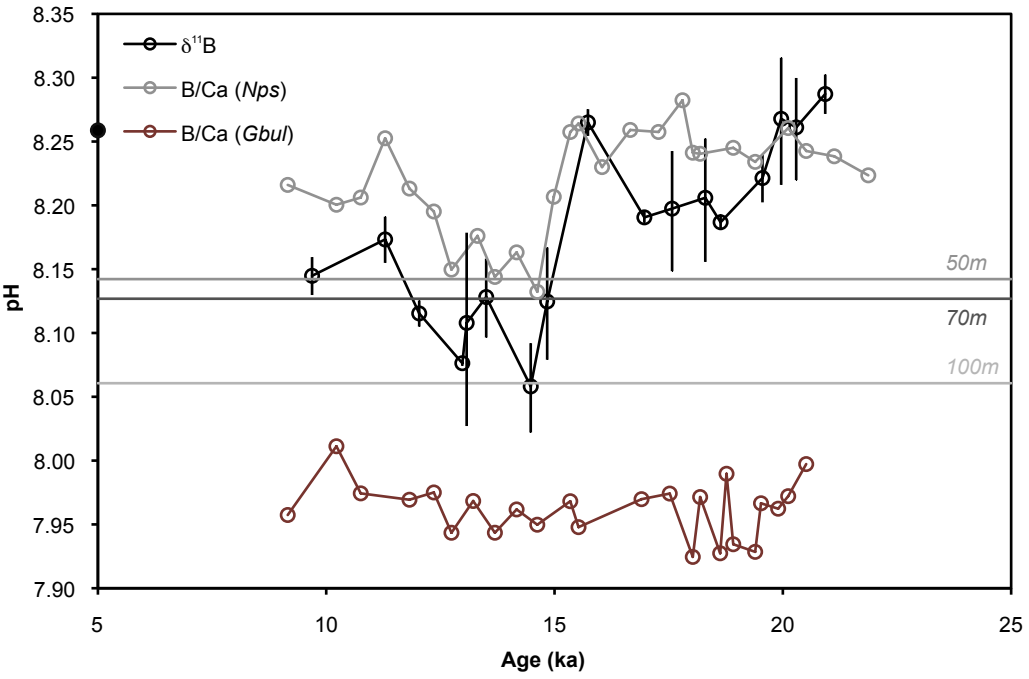

FIGURE 7.11: Deglacial pH in the subarctic Pacific ocean derived from *N. pachyderma* (s) δ^{11}B (black), *N. pachyderma* (s) B/Ca (grey) and *G. bulloides* B/Ca (red). The *N. pachyderma* (s) δ^{11}B coretop value is shown by the solid circle. See text for details. Pre-industrial pH between 50-100 m depth is shown by the horizontal grey lines.

B/Ca was converted to seawater $B(OH)_4^-/HCO_3^-$ using the partion coefficient of Yu et al. (2013b) for *N. pachyderma* (s) and Yu et al. (2007b) for *G. bulloides*. pH was calculated from $B(OH)_4^-/HCO_3^-$ using a pH-$B(OH)_4^-/HCO_3^-$ relationship based on carbonate system dissociation constants (K_1 and K_2) and K_B at a salinity of 33 PSU, and depth of 50 m, a DIC concentration of 2000 µmol/kg, and a temperature of 2.5 °C for *N. pachyderma* (s) and 7.5 °C for *G. bulloides* using the constants of Dickson (1990b) and Millero (1995). Altering the DIC between 1850-2250 µmol/kg (the range within the modern surface ocean) significantly alters the relationship between pH and $B(OH)_4^-/HCO_3^-$ (Figure 7.12). This is an unconstrained parameter that is likely to have varied in the past, and as such results in a large error in reconstructed pH from B/Ca ($> \pm 0.1$ pH unit). Deglacial B/Ca-derived pH for both *N. pachyderma* (s) and *G. bulloides* is shown in figure 7.11. However, due to the considerably larger error (which is not shown in the figure) most of the discussion will focus on the implications of the δ^{11}B-pH record.

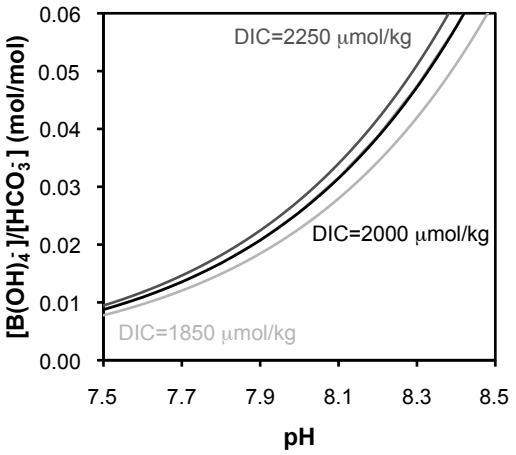

FIGURE 7.12: pH-$B(OH)_4^-/HCO_3^-$ relationship at DIC concentrations spanning the modern surface ocean range. Calculated at 33 PSU, 5 °C and 50 m depth using the constants of Dickson (1990b) and Millero (1995)

G. bulloides pH is very low, and indicates the partition coefficient of Yu et al. (2007b) is not applicable to the North Pacific, likely due to differences within the calcification process between regional genotypes (this is probably also the cause of varying offsets seen in δ^{18}O of this species). The *N. pachyderma* (s) δ^{11}B pH reconstruction shows higher pH during the LGM, which decreases markedly over deglaciation, and reaches pre-industrial values within the early Holocene. B/Ca-pH generally shows good agreement with the δ^{11}B-pH, however the δ^{11}B-pH record shows a greater range (0.25 pH units), and the B/Ca-pH record does not decrease until after ~15 ka, whereas the δ^{11}B-pH decreases earlier in deglaciation.

An additional parameter of the carbonate sytem is required to calculate pCO_2 from

pH, and alkalinity is widely used (Palmer, 2003; Foster, 2008a; Yu et al., 2013b). In the modern ocean alkalinity varies linearly with salinity as it is dependent on the charge balance of major conservative anions and cations in seawater (Zeebe and Wolf-Gladrow, 2001); as such alkalinity can be estimated from reconstructed salinity. $\delta^{18}O_{sw}$ was converted to salinity using the North Pacific salinity-$\delta^{18}O_{sw}$ relationship of LeGrande and Schmidt (2006). Alkalinity was calculated using reconstructed salinity and temperature and the Southern Ocean relationship of Lee et al. (2006) (Figure 7.13). The Southern Ocean relationship was used as the North Pacific relationship does not extend to the range of reconstructed salinity, and includes a longitudinal parameter to account for mixing that is unlikely to be constant over glacial-interglacial timescales. A very generous alkalinity error of ±150 μmol/kg was assigned, which is the range observed over the entire modern surface ocean (Figure 7.13). Typical uncertainty in reconstructed pCO_2 from quadratic propagation of total pH error (see above) and alkalinity error is ±35 ppmv. The effect of temperature (±1 °C) and salinity (±2 PSU) uncertainty on the carbonate system constants has a negligible effect on pCO_2 (±1.5 and ±5 ppmv respectively). As *N. pachyderma* (s) are found below the mixed layer some correction has to be made to account for the mixed layer pCO_2 gradient in order to derive surface ocean pCO_2. Takahashi et al. (1993) shows a 30 ppmv pCO_2 decrease in the mixed layer of the subarctic Pacific during the summer months. As *N. pachyderma* (s) most likely represent mean annual conditions and the surface ocean is well mixed in the winter a 15 ppmv correction is applied. Removing or doubling this offset makes no difference to any of the conclusions drawn.

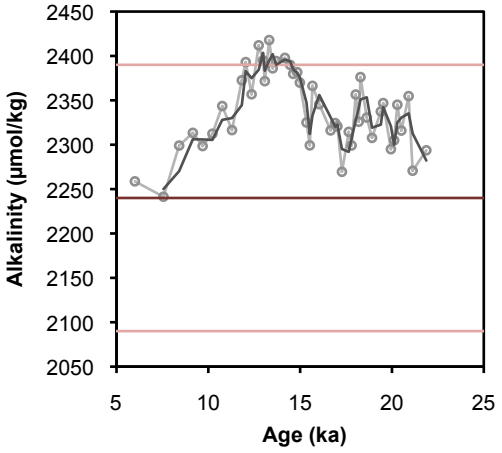

FIGURE 7.13: Reconstructed alkalinity over deglaciation (see text for details). Modern alkalinity at the site is shown by the dark red line, and the range in alkalinity within the modern surface ocean (±150 μmol/kg) is shown by the light red lines.

Deglacial pCO_2 in the subarctic Pacific is shown in Figure 7.14. Alkalinity has very little effect on the pCO_2 record, which is almost entirely driven by changes in pH. The data

show pCO_2 in the surface of the subarctic Pacific was ~90 ppmv lower during glacial times compared to the early Holocene. Over deglaciation pCO_2 within the subarctic Pacific increased significantly, reaching a maximum surface ocean pCO_2 of ~380 ppmv at 14.5 ka, resulting in significant flux of CO_2 the atmosphere (Figure 7.15). By 11 ka subarctic Pacific pCO_2 had decreased to a value of ~280 ppmv, again within error of equilibrium with the atmosphere. The pCO_2 reconstruction presented here supports the hypothesis of a more efficient biological pump in the subarctic Pacific during glacial times driving a reduced flux of CO_2 to the atmosphere, and the release of an isolated CO_2 reservoir back to the atmosphere over deglaciation (Sigman and Boyle, 2000; Jaccard et al., 2005). This record indicates a significant role for the subarctic Pacific in the deglacial CO_2 rise, with the greatest CO_2 flux from the subarctic Pacific occuring at a time of increasing atmospheric pCO_2 (Figure 7.15).

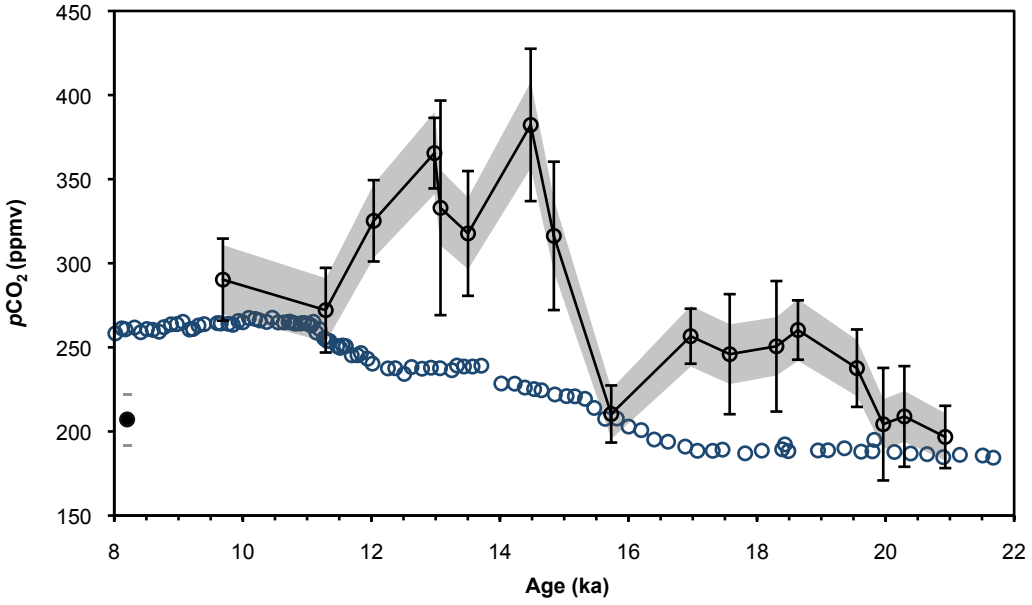

FIGURE 7.14: Deglacial pCO_2 in the subarctic Pacific. Atmospheric pCO_2 is shown by the blue circles (Monnin et al., 2001), and pCO_2 in the subarctic Pacific is shown in black. Uncertainty in pCO_2 associated with total pH error is shown by the error bars, while uncertainty in pCO_2 associated with alkalinity is given by the shaded grey area.

The relationship between CO_2 outgassing from the subarctic Pacific and atmospheric CO_2 is not straightforward. Figures 7.14 and 7.15 clearly demonstrate a significant release of CO_2 early in deglaciation, although no rise is seen in the atmosphere at this time. This suggests that increased CO_2 sequestration in other regions must have balanced the release of CO_2 from the subarctic Pacific, possibly mediated by Fe fertilisation, with an increased atmospheric dust flux implied by the NGRIP dust record at this time (Ruth et al., 2007). The pCO_2 record also suggests outgassing from the subarctic Pacific between 12 -13.5 ka (although lower than the preceeding and

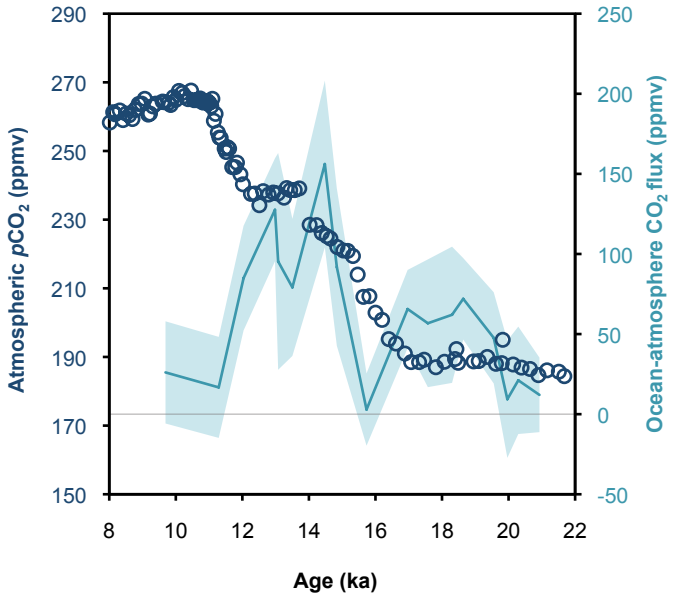

FIGURE 7.15: Deglacial pCO_2 flux from the subarctic Pacific to the atmosphere (turquoise line). Total pCO_2 error (shaded turquoise) is derived from quadratically propagating pCO_2 errors from total pH error and alkalinity error (see text for details). Atmospheric pCO_2 is shown by the blue circles (Monnin et al., 2001). Zero on the flux axis is marked with a horizontal grey line.

proceeding intervals), however atmospheric pCO_2 plateaus during this interval. It is possible that the high productivity observed within the subarctic Pacific at this time resulted in a higher proportion of the carbon returning back from the mixed layer to the intermediate depths, with widespread intermediate depth O_2 depletion observed during this interval (Cannariato et al., 1999; Cook et al., 2005; Chang et al., 2014) (Figure 7.16). However, such a high degree of disequilibrium (∼100 ppmv) is unlikely to have been entirely balanced by an increase in productivity. Instead, the release of CO_2 from the subarctic Pacific between 12 -13.5 ka may have been counteracted by the concurrent re-stratification of the Southern Ocean (Anderson et al., 2009). While one data point suggests a reduction in subarctic Pacific pCO_2 at ∼ 16 ka, a time of increasing atmospheric pCO_2, more data are needed before any conclusions can be drawn about this part of the record.

7.3.4 Controls on productivity and CO_2 outgassing over deglaciation

The similarity of the pH record and the *N. pachyderma* (s) $\delta^{18}O_{sw}$ record suggests salinity stratification of the upper water column may have acted as a control on nutrient upwelling and CO_2 degassing from the subarctic Pacific over deglaciation, with the period of lowest pH (and highest CO_2 flux out of the subarctic Pacific) occurring at

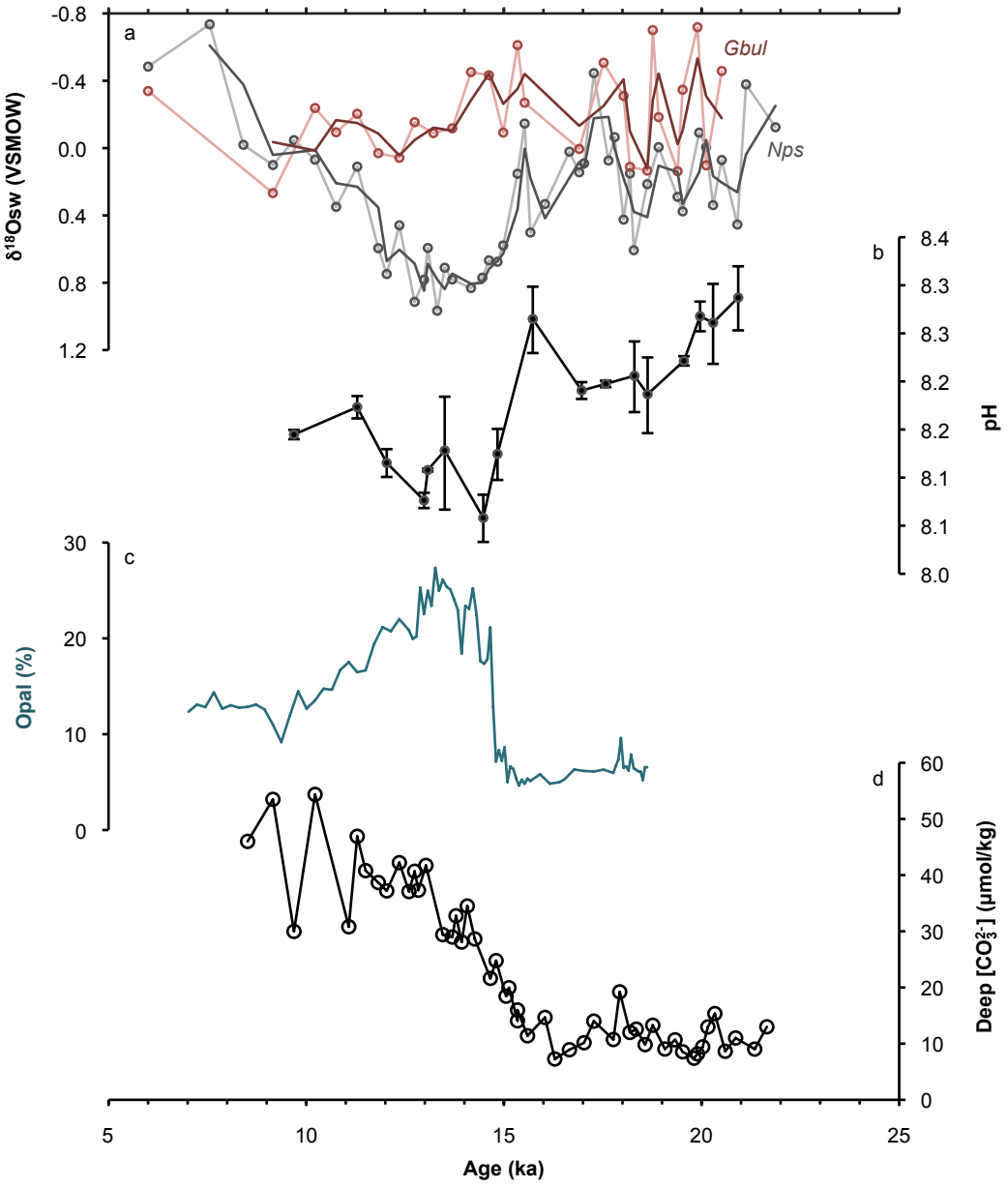

FIGURE 7.16: (a) *N. pachyderma* (s) (*Nps*) and *G. bulloides* (*Gbul*) $\delta^{18}O_{sw}$ (b) pH derived from the $\delta^{11}B$ of *N. pachyderma* (s) (see text for details) (c) %Opal, data from Gebhardt et al. (2008) (d) $[CO_3^{2-}]$ of the deep-intermediate subarctic Pacific (see section 6.3.4 for details).

the time of highest $\delta^{18}O_{sw}$ (highest subsurface salinity) (Figure 7.16). However, while subsurface salinity appears to have modulated changes in subarctic Pacific pCO_2 over deglaciation, the reduction in subsurface salinity during the LGM (coupled with similar temperatures to modern) indicates increased stratification of the upper water column is unlikely to be the cause of the observed increase in nutrient utilisation and decrease in pCO_2 within the glacial subarctic Pacific (Kienast et al., 2004; Jaccard et al., 2005; Brunelle et al., 2007). This poses a problem because reconstructions also show glacial intermediate waters were as similarly poorly ventilated as in the modern ocean (see section 6.3.3), thus the input of nutrients and DIC into the surface ocean would have remained at a similar level to, or been higher than, the levels observed at present; the data therefore argue against a salinity stratification driven mechanism to reduce nutrient/DIC input to the surface of the subarctic Pacific Ocean during glacial times, as previously proposed by Jaccard et al. (2005).

The high nutrient and DIC levels observed within the surface of the subarctic Pacific today are driven by a reduction in mixed layer stratification during the winter months (see σ_θ on figure 7.2), and tidal mixing processes along the Aleutian Island Archipelago, with the highest PO_4^{3-} concentrations found in the center of the island chain (Figure 7.1). Many of the eastern passes of the Aleutian Archipelago are <60 m deep, and the central passes, where most of the mixing occurs today, range between 160-450 m depth (with most only ~200 m) (Mordy et al., 2005). During the LGM sea level was ~120 m lower than the present day (Fairbanks, 1989), and many of these passes would have been exposed, or the water depth within them would have been considerably shallower. As such, the tidal mixing processes that drive the input of nutrients into the surface of the subarctic Pacific today, would have been significantly reduced. I propose that it was this reduction in tidal mixing, rather than salinity driven stratification that drove the observed increase in nutrient utilisation, and resultant decrease in pCO_2, within the glacial subarctic Pacific.

The effect of sea level on tidal mixing along the Aleutian Archipelago also provides a mechanism to explain the changes observed within the surface of the subarctic Pacific Ocean over deglaciation. Records of $[CO_3^{2-}]$ and $\Delta^{14}C$ show the deep-intermediate subarctic Pacific was ventilated at 16 ka (Figures 7.16 and 6.20). However, the large decrease in surface ocean pH, and increase in productivity indicated by the opal record, do not occur until 14.8 ka (Figure 7.16), and the large increase in $CaCO_3$ did not occur until 14.6 ka (Figure 7.17). Thus, there is clearly a lag of >1000 years between the loss of nutrients and DIC from the deep-intermediate ocean, and their input into the surface ocean, indicating the deglacial productivity maximum and reduction in pH of the surface

waters, was not a direct result of the ventilation of the deep/deep-intermediate North Pacific.

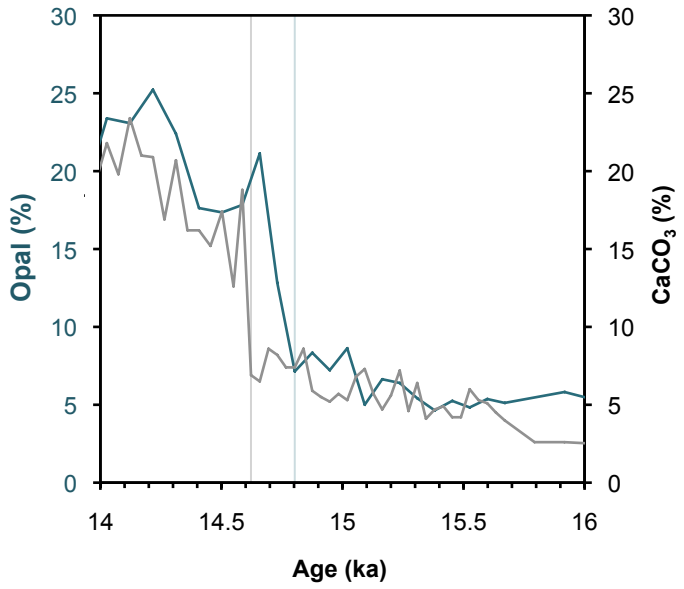

FIGURE 7.17: Variations in %Opal and %$CaCO_3$ between 14 and 16 ka. The onset of the large increase in %Opal (vertical green line) leads the onset of the %$CaCO_3$ increase (vertical grey line) by ∼200 years.

Over deglaciation, a rapid increase in sea level, known as meltwater pulse 1A (MWP 1A), is thought to represent the input of a significant volume of meltwater (possibly from Antarctica) into the oceans (Fairbanks, 1989; Weaver et al., 2003). Although the exact timing of MWP 1A is debated, several studies have placed it at ∼14.7 ka (Weaver et al., 2003; Kienast et al., 2003). Due to the similar timing of the rapid increase in sea level and the productivity maximum in the North Pacific, Mix et al. (1999) proposed the North Pacific deglacial productivity maximum was driven by increased Fe availability following the inundation of shelf seas (see also Davies et al. (2011)). Recent work has shown no change in Fe source during the productivity increase, suggesting this is unlikely to be the cause (Lam et al., 2013). However, by inundating the passes along the Aleutian island chain, the rise in sea level would have increased tidal mixing, and thus resulted in higher nutrient input to the surface ocean, providing a mechanism for the observed increase in productivity and reduction in pH. Furthermore, a strong but shallower halocline is also seen at this time, possibly driven by the increased strength of the East Asian monsoon (Figure 7.9), supporting Lam et al.'s (2013) assertion that a reduction in light limitation through transient stratification of the surface ocean may have played a role in the deglacial productivity maximum.

Much of the appeal of Jaccard et al.'s (2005) salinity stratification hypothesis lay in its simplicity; it provided a simple physical mechanism that could occur repeatedly and predictably over glacial-interclacial cycles, resulting in the repeating, predictable variations seen in atmospheric $p\mathrm{CO}_2$ over the past 800 ka. A mechanism based around the effects of sea level on tidal mixing along the Aleutian Archipelago retains this simplicity, providing a simple feedback mechanism between global climate, sea level, and atmospheric $p\mathrm{CO}_2$.

7.4 Conclusions

- The salinity of the North Pacific surface ocean was higher during the LGM, and throughout the last deglaciation, only reaching modern levels in the early Holocene. Dynamic, submillenial changes in surface salinity of ∼2 PSU are observed before ∼17 ka, possibly driven by variations in the strength of the East Asian monsoon. After ∼17 ka, a permanent, shallow halocline developed following significant meltwater input into the North Pacific, and at ∼14.5 ka, a maximum in mixed layer salinity stratification is coincidental with an inferred maximum in monsoonal flux.

- During the LGM temperatures of the subsurface North Pacific were similar, or slightly higher (∼1 °C) higher than at present. Following a rapid warming to a maximum of ∼6 °C at 14.5 ka, significantly warmer temperatures than modern persisted in the subsurface until 8 ka. The reconstruction of mixed layer temperature shows a remarkably similar temperature to modern throughout the course of deglaciation, although this may represent changes in the calcification season of *G. bulloides* to suit its habitat preference.

- This study presents the first direct evidence for a reduction of ∼90 ppmv in surface ocean $p\mathrm{CO}_2$ within the subarctic Pacific during glacial times, supporting the hypothesis that increased nutrient utilisation within the region led to a reduction in the flux of CO_2 to the atmosphere.

- Large disquilibria (>100 ppmv) with the atmosphere observed in the the subarctic Pacific $p\mathrm{CO}_2$ record over deglaciation indicate the region was a significant CO_2 source to the atmosphere, and highlights a major role for subarctic Pacific Ocean in the deglacial CO_2 rise. However, early release of CO_2 from the subarctic Pacific, at a time when no increase is seen in atmospheric $p\mathrm{CO}_2$, suggests a complex reorganisation of sources and sinks within the global carbon cycle over deglaciation.

- The large productivity spike observed at ∼14.8 ka within the North Pacific is concurrent with a shift to low-pH subsurface waters, indicating the input of nutrient rich deepwaters into the subsurface ocean. However, the increase in productivity lags the ventilation of the deep ocean by >1000 yrs.

- Due to the increase in surface and subsurface salinity observed within the North Pacific during the LGM, salinity-driven stratification of the upper water column does not seem likely to be the mechanism by which nutrient/DIC input into the surface ocean was reduced. Instead, I propose that lower sea levels reduced tidal mixing along Aleutian Archipelago, decreasing nutrient/DIC input into the surface of the subarctic Pacific, increasing the efficency of the biological pump, and reducing $p\mathrm{CO}_2$ during glacial times. Over deglaciation, a rapid rise in sea level at ∼14.7 ka increased tidal mixing of nutrient/DIC-rich intermediate waters into the surface ocean, driving the observed decrease in pH, and coupled with a maximum in mixed layer stratification, drove the deglacial productivity maximum.

- Recent methodological developments now allow $\delta^{15}\mathrm{N}$ to be measured on foraminiferal calcite (Ren et al., 2012). A study using paired analysis of $\delta^{15}\mathrm{N}$ and $\delta^{11}\mathrm{B}$ in planktonic foraminiferal calcite offers the potential to provide a fascinating elucidation of the relationship between nutrient utilisation and CO_2 within the high latitude oceans over glacial-interglacial cycles.

Chapter 8

Conclusions and further work

The overarching aim of this thesis has been to examine the role of the North Pacific Ocean in the deglacial CO_2 rise, using trace elements, oxygen isotopes and boron isotopes in biogenic carbonates. Specifically, by reconstructing the physical properties (temperature and $\delta^{18}O$) and carbonate chemistry ($DIC/[CO_3^{2-}]$ and pCO_2) of the surface and interior subarctic Pacific over deglaciation, this thesis seeked to examine the physical mechanisms underpinning implied deglacial variations in the efficiency of the biological pump, and the concequences of these changes on deep ocean carbon storage and CO_2 outgassing. Before applying trace element/Ca proxies down core, the potential influence of contaminants on Mg/Ca ratios in marine ostracod genus Krithe was examined, and a core-top calibration study was carried out to determine the controls on the uptake of Li, B, Mg and Sr in benthic foraminifera Uvigerina peregrina. Detailed conclusions are given at the end of each respective chapter, and a summary of the findings is given below.

Cleaning experiments were carried out to assess the influence of contamination and cleaning procedures on Mg/Ca ratios in the marine ostracod genus *Krithe* (Chapter 4). Mg bearing clays and Fe-Mn oxyhydroxide overgrowths can exert a significant influence on the Mg/Ca of *Krithe* valves, leading to bias and variability with BWT reconstructions. Sonication in methanol lowers Mg/Ca by 1.6 mmol/mol (11%)(1.5 °C) due to the removal of clays, emphasising that this is a critical step in the preparation of *Krithe* valves for Mg/Ca analysis. Reduction with hydrous hydrazine/ammonium citrate decreases Mg/Ca by 0.9 mmol/mol (7%), equivalent to a decrease in reconstructed temperature of 1 °C, due both to the removal of Fe-Mn oxyhydroxide overgrowths, and the partial dissolution of the valve surface. While future work should aim to better constrain the effects of partial dissolution of the valve surface and determine the optimum

exposure time to the reducing reagents, the lowest inter-valve Mg/Ca variability of ±0.6 mmol/mol (5%) (±0.6 °C) was achieved following reductive cleaning, demonstrating its potential to improve the precision of BWT reconstructions based on *Krithe* Mg/Ca. Future *Krithe* Mg/Ca studies should employ the full cleaning procedure outlined in this study, and further coretop data from *Krithe* that have been cleaned according to this protocol should be generated to improve the *Krithe* Mg/Ca-temperature calibration.

A core top calibration study was carried out to determine the controls on the uptake of Li, B, Mg and Sr in benthic foraminiferal species *Uvigerina peregrina* over a wide range of BWTs and carbonate ion saturation states (Chapter 5). The study indicates the uptake of Mg in *Uvigerina peregrina* is mainly controlled by temperature, and ΔCO_3^{2-} does not affect Mg/Ca in this species, demonstrating it can reliably be used as a proxy for bottom water temperature in the past. Li uptake is controlled by both temperature and seawater carbonate chemistry. The temperature sensitivity of Li uptake appears to be close to that of inorganic calcite, and if the effects of temperature are accounted for by normalisation to a constant temperature (Li/Ca_{TN}), a strong correlation is observed with several carbonate system parameters, but most significantly with DIC. Mg/Ca temperature can be used to correct Li/Ca ratios for the effects of temperature, enabling it to be used as a proxy for past bottom water DIC concentrations. Sr/Ca and B/Ca also show a highly significant relationships with several carbonate system parameters, implying they can be used as proxies for bottom water carbonate chemistry in the past. A Rayleigh distillation model and inorganic calcite trace element partition coefficients can adequately explain the observed Li/Ca and Sr/Ca data. A DIC control, on the rate of calcification or vacuole flushing rate (either directly, or through ΔCO_3^{2-}), provides a viable mechanism for Li and Sr incorporation within *Uvigerina peregrina*. Porewater chemistry and dissolution appear to have a limited effect on *Uvigerina peregrina* Li/Ca and Sr/Ca ratios, indicating they can effectively be used to reconstruct past bottomwater chemistry. Further core top data from bottom waters with a ΔCO_3^{2-} between 10-50 μmol/kg are needed to confirm the relationships presented in this study.

Subarctic Pacific LGM water column profiles of BWT, $^{18}O_{sw}$, and DIC were generated using *Uvigerina* spp. Mg/Ca, Li/Ca and $\delta^{18}O_{calcite}$ measurements, and previously published data were collated to form an LGM $\Delta\Delta^{14}C$ watercolumn profile of the North Pacific. Down core *Uvigerina senticosa* Mg/Ca, Li/Ca, $\delta^{18}O_{calcite}$ and $\Delta^{14}C$ data were used to reconstruct changes in BWT, $^{18}O_{sw}$, DIC and $\Delta\Delta^{14}C$ for the deep-intermediate subarctic Pacific over deglaciation (Chapter 6). The LGM water column profiles show the expansion of an ^{18}O depleted (low salinity) watermass to depths of >2300 m (possibly GNAIW), which resulted in an increase in interior ocean stratification within the glacial

subarctic Pacific. The DIC and $\Delta\Delta^{14}C$ profiles indicate both an increase in deep/deep-intermediate DIC concentrations of between ~200 - 400 μmol/kg, and a deepening of the DIC pool within the North Pacific, supporting the nutrient deepening hypothesis of Boyle (1988) as a mechanism by which atmospheric CO_2 was lowered during glacial times. The increase in DIC within the deep and deep-intermediate North Pacific Ocean signifies DIC storage within this basin played a significant role in loweric atmospheric CO_2 during glacial times. While increased interior ocean stratification provides a viable mechanism by which a major return pathway of nutrients/DIC from the deep to intermediate depth/surface ocean in the modern ocean was reduced during glacial times, the relationship between stratification and DIC storage is not straightforward, with more, or as equally poorly ventilated waters at 2300 m as at 3300 m, despite considerably lower salinity ($^{18}O_{sw}$) at the shallower depth.

Between 125-250 μmol/kg of DIC was released from the deep-intermediate subarctic Pacific at ~16 ka, concurrent with a decrease in ventilation age, and 2 °C warming of bottom waters. The loss of DIC from the deep-intermediate Pacific was likely driven by a reduction in interior ocean stratification, and more recently ventilated deepwaters entering the Pacific basin from the south. A breakdown in interior ocean stratification within the North Pacific would have reinstated a significant return-pathway of nutrients and DIC from the deep ocean to the intermediate depths and surface ocean, and represents a steady-state shift in the oceans ability to sequester DIC in the deep North Pacfic Ocean, rather than a transient deep ocean ventilation event. The LGM density and DIC water column profiles presented in this study are currently based on a very sparse three point data set; greater coverage of benthic foraminiferal trace element/Ca ratio data is needed throughout the watercolumn in order to build up a more robust reconstruction of the physical and chemical structure of glacial water column. Due to a paucity in deglacial material from the deep NW Pacific, a coring campaign is required before a deep ocean record of BWT and DIC from paired Li/Ca and Mg/Ca ratios in *Uvigerina* spp. can be generated.

Deglacial changes in upper ocean structure and pCO_2 within the subarctic Pacific were reconstructed using Mg/Ca ratios and $\delta^{18}O$ in *N. pachyderma* and *G. bulloides*, and $\delta^{11}B$ in *N. pachyderma* (Chapter 7). The results indicate the salinity of the North Pacific surface ocean was higher during the LGM, and throughout the last deglaciation, only reaching modern levels in the early Holocene. Dynamic, submillenial changes in surface salinity of ~2 PSU are observed before ~17 ka, and a permanent, shallow halocline developed after ~17 ka. Meltwater input and variations in the strength of the East Asian monsoon appear to be major drivers of North Pacific salinity over deglaciation. During the LGM the temperature of the subsurface North Pacific was similar to present, and

between 8 - 14.5 ka the temperature was significantly higher than modern. There was a reduction of ∼90 ppmv in surface ocean $p\mathrm{CO}_2$ within the subarctic Pacific during glacial times, supporting the hypothesis that increased nutrient utilisation led to a reduction in the flux of CO_2 to the atmosphere. Large disequilibria with the atmosphere (>100 ppmv) observed in the the subarctic Pacific $p\mathrm{CO}_2$ record over deglaciation indicate the region was a significant CO_2 source to the atmosphere, and highlights a major role for subarctic Pacific Ocean in the deglacial CO_2 rise. However, an early release of CO_2 also suggests a complex reorganisation of sources and sinks within the global carbon cycle over deglaciation. Due to the increase in surface and subsurface salinity observed within the North Pacific during the LGM, salinity-driven stratification of the upper water column does not seem likely to be the mechanism responsible for decreasing nutrient/DIC input into the surface ocean. An alternate mechanism is provided by lower glacial sea levels, which would have worked to reduce tidal mixing along the Aleutian Archipelago, and decreased nutrients and $p\mathrm{CO}_2$ within the surface ocean. Over deglaciation, a rapid rise in sea level at ∼14.7 ka increased tidal mixing of nutrient/DIC-rich intermediate waters into the surface ocean, driving the observed decrease in pH. This nutrient upwelling, coupled with an increase in mixed layer stratification, resulted in the deglacial productivity maximum. A study using paired analysis of $\delta^{15}\mathrm{N}$ and $\delta^{11}\mathrm{B}$ in planktonic foraminiferal calcite would allow the relationship between nutrient utilisation and CO_2 within the high latitude oceans to be assessed over glacial-interglacial cycles.

Appendix A

Correlations between contamination indicators and trace elements in planktonic foraminifera

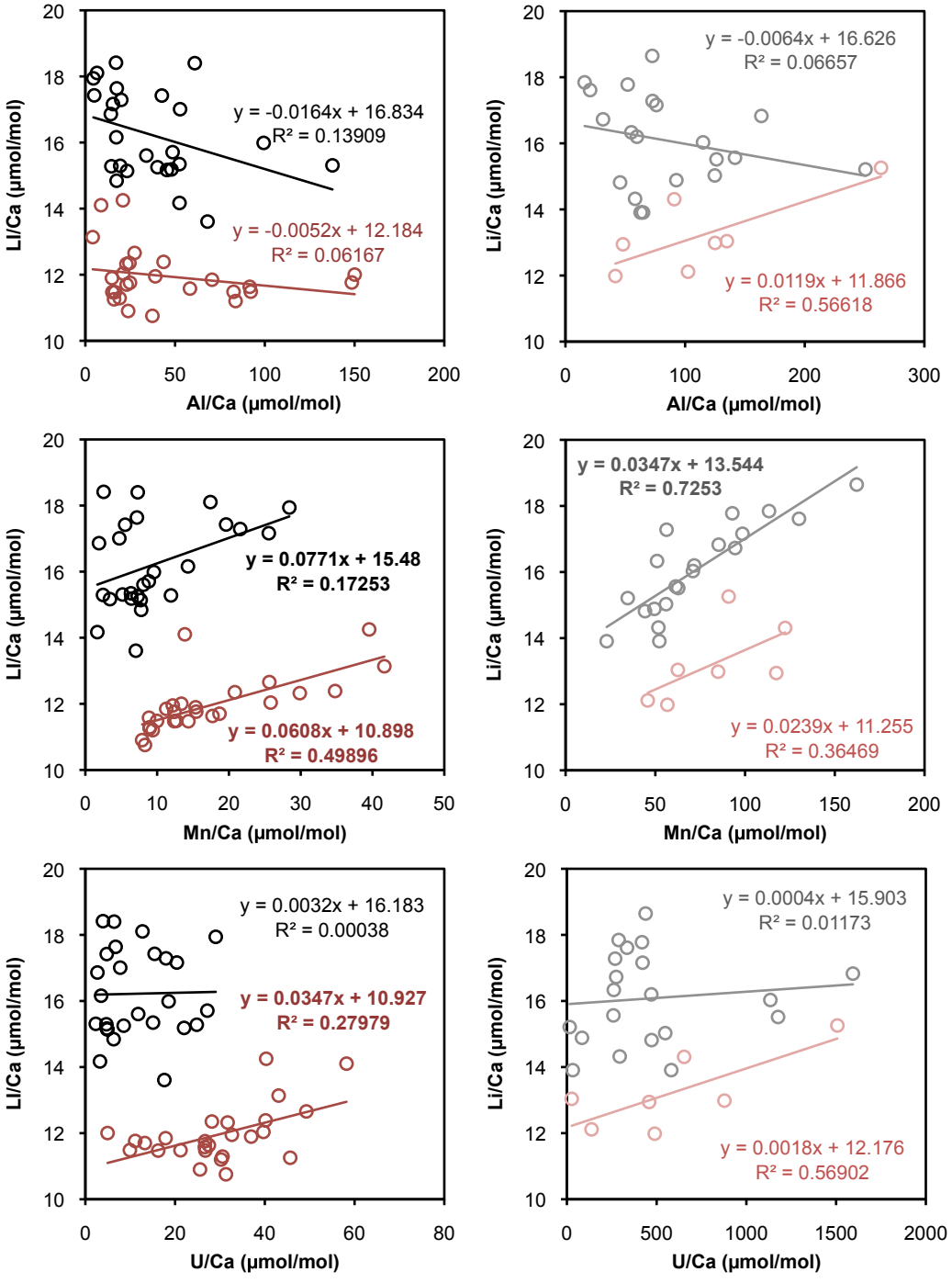

FIGURE A.1: Reductively (dark) and oxidatively (light) cleaned *N. pachyderma* (s) (black/grey) and *G. bulloides* (red/pink) Li/Ca against Al/Ca, Mn/Ca and U/Ca. Significant correlations to the 95% confidence interval are shown in bold.

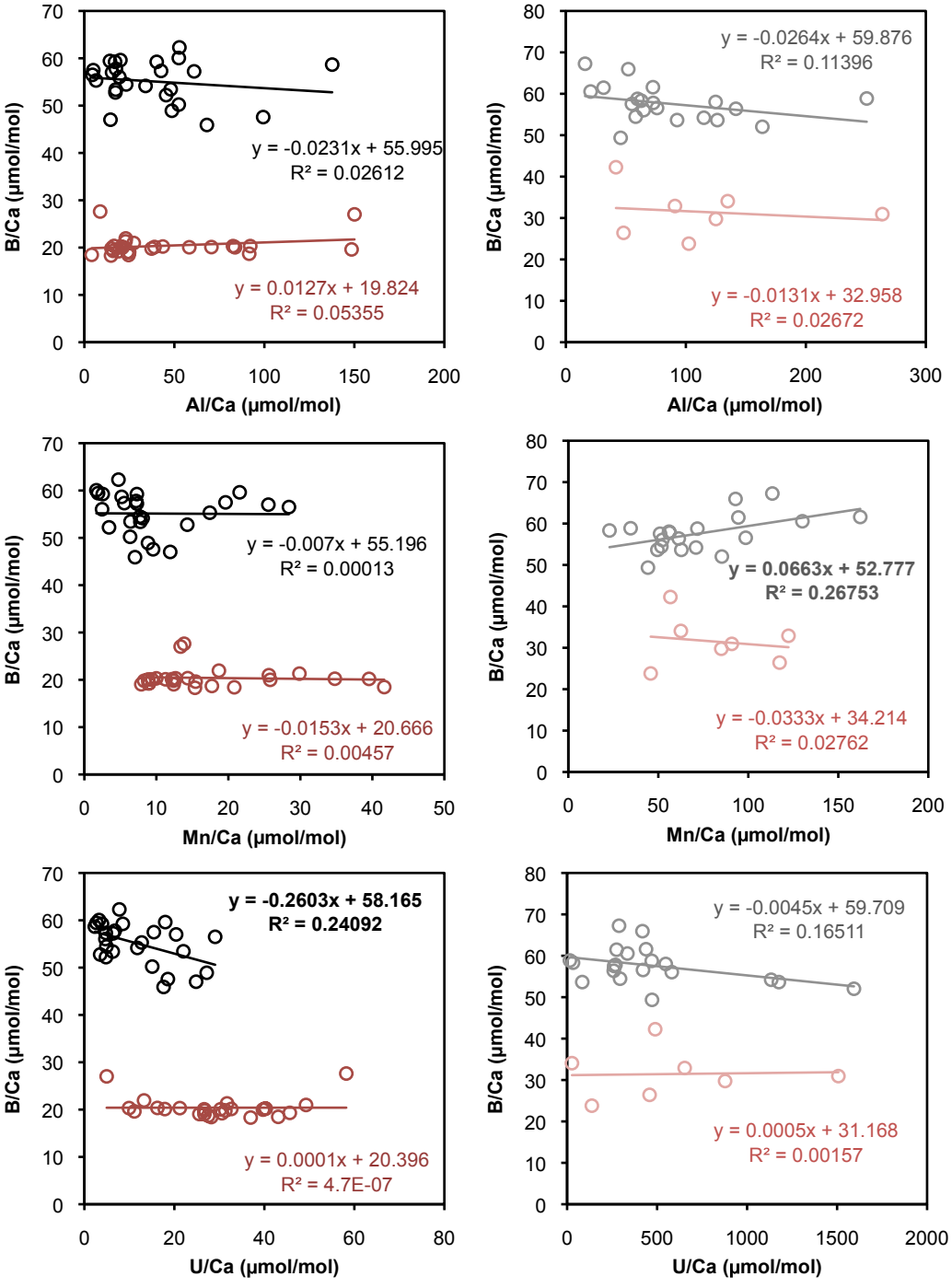

FIGURE A.2: Reductively (dark) and oxidatively (light) cleaned *N. pachyderma* (s) (black/grey) and *G. bulloides* (red/pink) B/Ca against Al/Ca, Mn/Ca and U/Ca. Significant correlations to the 95% confidence interval are shown in bold.

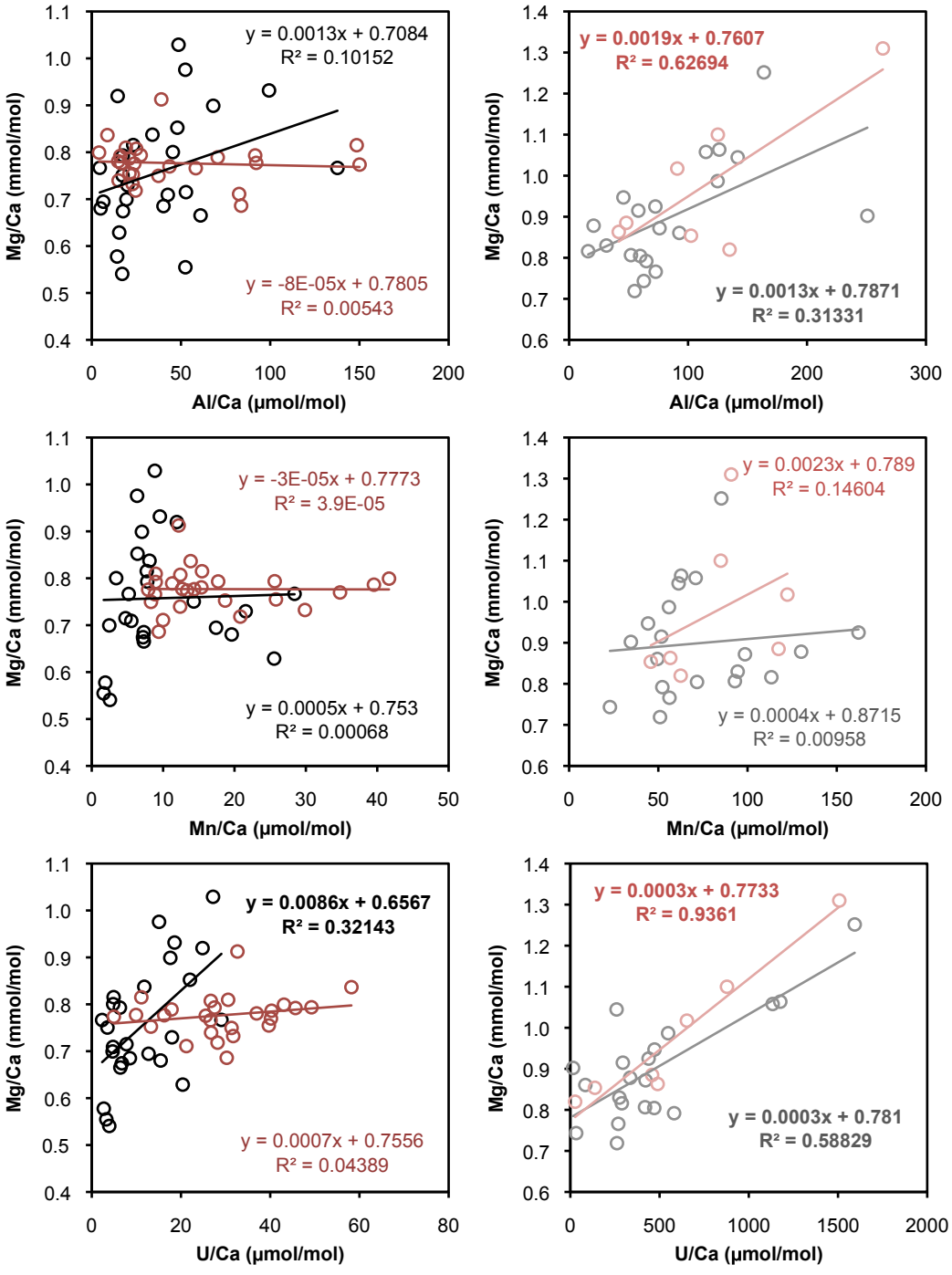

FIGURE A.3: Reductively (dark) and oxidatively (light) cleaned *N. pachyderma* (s) (black/grey) and *G. bulloides* (red/pink) Mg/Ca against Al/Ca, Mn/Ca and U/Ca. Significant correlations to the 95% confidence interval are shown in bold.

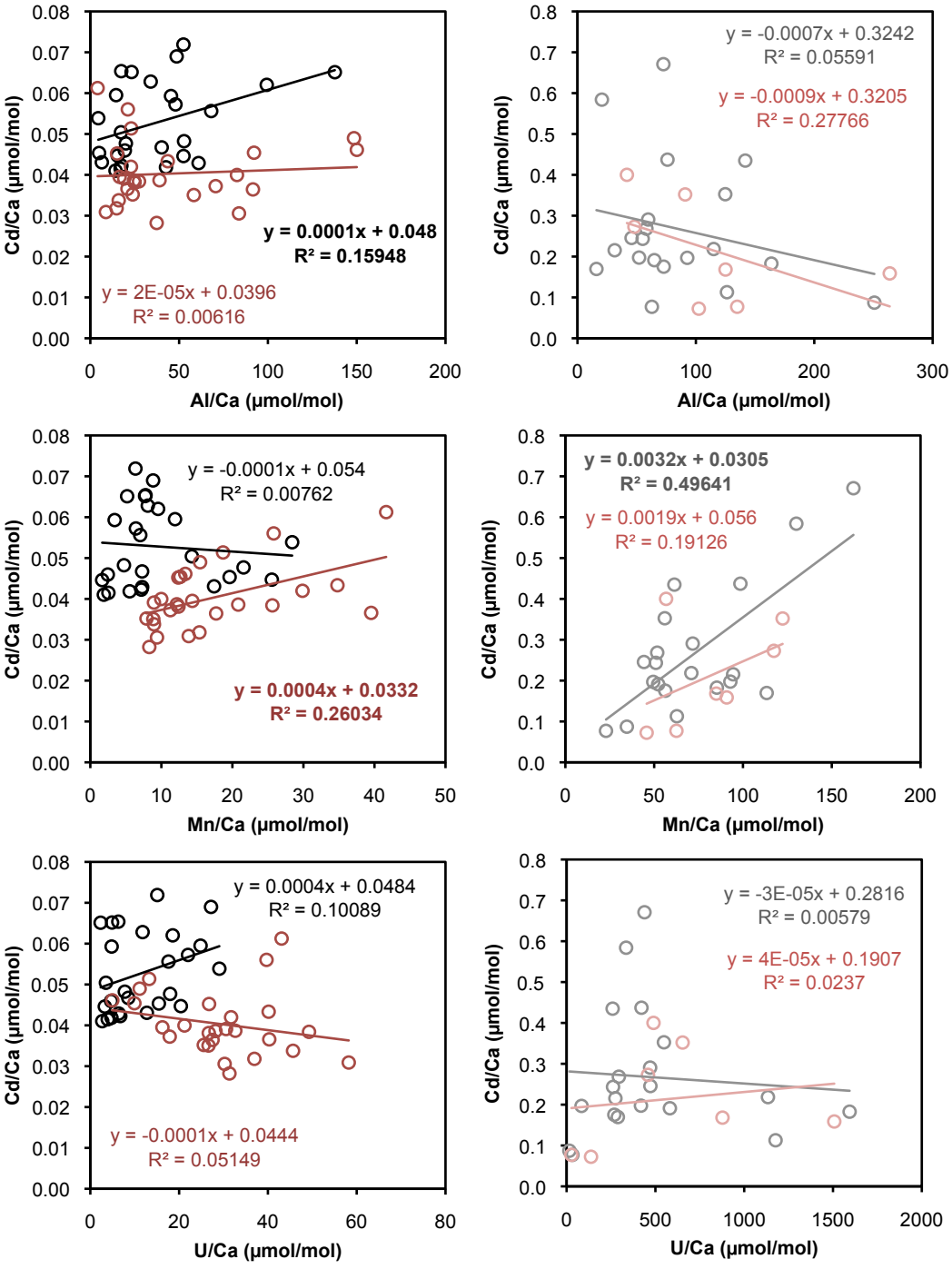

FIGURE A.4: Reductively (dark) and oxidatively (light) cleaned *N. pachyderma* (s) (black/grey) and *G. bulloides* (red/pink) Cd/Ca against Al/Ca, Mn/Ca and U/Ca. Significant correlations to the 95% confidence interval are shown in bold.

Bibliography

Adkins, J. F. (2002). The Salinity, Temperature, and delta 18O of the Glacial Deep Ocean. *Science*, 298(5599):1769–1773.

Adkins, J. F. (2013). The role of deep ocean circulation in setting glacial climates. *Paleoceanography*, pages 10.1002–palo.20046.

Ahagon, N. (2003). Mid-depth circulation in the northwest Pacific during the last deglaciation: Evidence from foraminiferal radiocarbon ages. *Geophys. Res. Lett*, 30(21):2097.

Al-Ammar, A., Gupta, R. K., and Barnes, R. M. (1999). Elimination of boron memory effect in inductively coupled plasma-mass spectrometry by addition of ammonia. *Spectrochimica Acta Part B: Atomic Spectroscopy*, 54(7):1077–1084.

Allen, K. A., Hönisch, B., Eggins, S. M., and Rosenthal, Y. (2012). Environmental controls on B/Ca in calcite tests of the tropical planktic foraminifer species Globigerinoides ruber and Globigerinoides sacculifer. *Earth and Planetary Science Letters*, 351-352(C):270–280.

Anand, P. (2003). Calibration of Mg/Ca thermometry in planktonic foraminifera from a sediment trap time series. *Paleoceanography*, 18(2):10.1029–2002PA000846.

Andersen, K. K., Azuma, N., Barnola, J. M., Bigler, M., Biscaye, P., Caillon, N., Chappellaz, J., Clausen, H. B., Dahl-Jensen, D., Fischer, H., Fluckiger, J., Fritzsche, D., Fujii, Y., Goto-Azuma, K., Grønvold, K., Gundestrup, N. S., Hansson, M., Huber, C., Hvidberg, C. S., Johnsen, S. J., Jonsell, U., Jouzel, J., Kipfstuhl, S., Landais, A., Leuenberger, M., Lorrain, R., Masson-Delmotte, V., Miller, H., Motoyama, H., Narita, H., Popp, T., Rasmussen, S. O., Raynaud, D., Röthlisberger, R., Ruth, U., Samyn, D., Schwander, J., Shoji, H., Siggard-Andersen, M. L., Steffensen, J. P., Stocker, T., Sveinbjörnsdóttir, A. E., Svensson, A., Takata, M., Tison, J. L., Thorsteinsson, T., Watanabe, O., Wilhelms, F., and White, J. W. C. (2004). High-resolution record of Northern Hemisphere climate extending into the last interglacial period. *Nature*, 431(7005):147–151.

Anderson, O. R. and Faber, W. W. (1984). An estimation of calcium carbonate deposition rate in a planktonic foraminifer Globigerinoides sacculifer using 45 Ca as a tracer; a recommended procedure for improved accuracy. *The Journal of Foraminiferal Research*, 14(4):303–308.

Anderson, R., Ali, S., Bradtmiller, L., Nielsen, S., Fleisher, M., Anderson, B., and Burckle, L. (2009). Wind-driven upwelling in the Southern Ocean and the deglacial rise in atmospheric CO2. *Science*, 323(5920):1443.

Anderson, R. F. (1982). Concentration, vertical flux, and remineralization of particulate uranium in seawater. *Geochimica et Cosmochimica Acta*, 46(7):1293–1299.

Arbuszewski, J., deMenocal, P., Kaplan, A., and Farmer, E. C. (2010). On the fidelity of shell-derived δ18Oseawater estimates. *Earth and Planetary Science Letters*, 300(3-4):185–196.

Archer, D., Lyle, M., Rodgers, K., and Froelich, P. (1993). What controls opal preservation in tropical deep-sea sediments. *Paleoceanography*, 8(1):7–21.

Archer, D. and Maier-Reimer, E. (1994). Effect of deep-sea sedimentary calcite preservation on atmospheric CO_2 concentration. *Nature*, 367:260–263.

Archer, D., Winguth, A., Lea, D., and Mahowald, N. (2000). What caused the glacial/interglacial atmospheric pCO2 cycles. *Rev. Geophys*, 38(2):159–189.

Augustin, L., Barbante, C., Barnes, P. R. F., Marc Barnola, J., Bigler, M., Castellano, E., Cattani, O., Chappellaz, J., Dahl-Jensen, D., Delmonte, B., Dreyfus, G., Durand, G., Falourd, S., Fischer, H., Flückiger, J., Hansson, M. E., Huybrechts, P., Jugie, G., Johnsen, S. J., Jouzel, J., Kaufmann, P., Kipfstuhl, J., Lambert, F., Lipenkov, V. Y., Littot, G. C., Longinelli, A., Lorrain, R., Maggi, V., Masson-Delmotte, V., Miller, H., Mulvaney, R., Oerlemans, J., Oerter, H., Orombelli, G., Parrenin, F., Peel, D. A., Petit, J.-R., Raynaud, D., Ritz, C., Ruth, U., Schwander, J., Siegenthaler, U., Souchez, R., Stauffer, B., Peder Steffensen, J., Stenni, B., Stocker, T. F., Tabacco, I. E., Udisti, R., van de Wal, R. S. W., van den Broeke, M., Weiss, J., Wilhelms, F., Winther, J.-G., Wolff, E. W., and Zucchelli, M. (2004). Eight glacial cycles from an Antarctic ice core. *Nature*, 429(6992):623–628.

Barbante, C., Barnola, J. M., Becagli, S., Beer, J., Bigler, M., Boutron, C., Blunier, T., Castellano, E., Cattani, O., Chappellaz, J., Dahl-Jensen, D., Debret, M., Delmonte, B., Dick, D., Falourd, S., Faria, S., Federer, U., Fischer, H., Freitag, J., Frenzel, A., Fritzsche, D., Fundel, F., Gabrielli, P., Gaspari, V., Gersonde, R., Graf, W., Grigoriev, D., Hamann, I., Hansson, M., Hoffmann, G., Hutterli, M. A., Huybrechts, P., Isaksson,

E., Johnsen, S., Jouzel, J., Kaczmarska, M., Karlin, T., Kaufmann, P., Kipfstuhl, S., Kohno, M., Lambert, F., Lambrecht, A., Lambrecht, A., Landais, A., Lawer, G., Leuenberger, M., Littot, G., Loulergue, L., Lüthi, D., Maggi, V., Marino, F., Masson-Delmotte, V., Meyer, H., Miller, H., Mulvaney, R., Narcisi, B., Oerlemans, J., Oerter, H., Parrenin, F., Petit, J. R., Raisbeck, G., Raynaud, D., Röthlisberger, R., Ruth, U., Rybak, O., Severi, M., Schmitt, J., Schwander, J., Siegenthaler, U., Siggaard-Andersen, M. L., Spahni, R., Steffensen, J. P., Stenni, B., Stocker, T., Tison, J. L., Traversi, R., Udisti, R., Valero-Delgado, F., van den Broeke, M. R., van de Wal, R. S. W., Wagenbach, D., Wegner, A., Weiler, K., Wilhelms, F., Winther, J. G., and Wolff, E. (2006). One-to-one coupling of glacial climate variability in Greenland and Antarctica. *Nature*, 444(7116):195–198.

Barker, S. (2003). A study of cleaning procedures used for foraminiferal Mg/Ca paleothermometry. *Geochemistry, Geophysics, Geosystems*, 4(9):10.1029–2003GC000559.

Barker, S., Cacho, I., Benway, H., and Tachikawa, K. (2005). Planktonic foraminiferal Mg/Ca as a proxy for past oceanic temperatures: a methodological overview and data compilation for the Last Glacial Maximum. *Quaternary Science Reviews*, 24(7-9):821–834.

Barnes, C. E. and Cochran, J. K. (1990). Uranium removal in oceanic sediments and the oceanic U balance. *Earth and Planetary Science Letters*, 97(1):94–101.

Bemis, B., Spero, H. J., Bijma, J., and Lea, D. (1998). Reevaluation of the oxygen isotopic composition of planktonic foraminifera: Experimental results and revised paleotemperature equations. *Paleoceanography*, 13(2):150–160.

Bemis, B., Spero, H. J., and Thunell, R. (2002). Using species-specific paleotemperature equations with foraminifera: a case study in the Southern California Bight. *Marine Micropaleontology*, 46(3-4):405–430.

Bentov, S. and Erez, J. (2006). Impact of biomineralization processes on the Mg content of foraminiferal shells: A biological perspective. *Geochem. Geophys. Geosyst*, 7(1):10.1029–2005GC001015.

Benway, H. M., Haley, B. A., Klinkhammer, G. P., and Mix, A. C. (2003). Adaptation of a flowthrough leaching procedure for Mg/Ca paleothermometry. *Geochemistry, Geophysics, Geosystems*, 4(2):10.1029–2002GC000312.

Bigg, G. R., Clark, C. D., and Hughes, A. L. C. (2008). A last glacial ice sheet on the Pacific Russian coast and catastrophic change arising from coupled ice–volcanic interaction. *Earth and Planetary Science Letters*, 265(3-4):559–570.

Boussetta, S., Bassinot, F., Sabbatini, A., Caillon, N., Nouet, J., Kallel, N., Rebaubier, H., Klinkhammer, G. P., and Labeyrie, L. (2011). Diagenetic Mg-rich calcite in Mediterranean sediments: Quantification and impact on foraminiferal Mg/Ca thermometry. *Marine Geology*, 280(1-4):195–204.

Boyer, T. P., Antonov, J. I., Baranova, O. K., and Garcia, H. E. (2009). Boyer: World Ocean Database 2009. *NOAA Atlas NESDIS*.

Boyle, E. (1981). Cadmium, Zinc, Copper, and Barium in Foraminifera Tests. *Earth and Planetary Science Letters*, 53(1):11–35.

Boyle, E. and Huested, S. (1983). Aspects of the surface distributions of copper, nickel, cadmium, and lead in the North Atlantic and North Pacific. In Wong, C. S., editor, *Trace Metals in Sea Water*. Springer, New York.

Boyle, E. and Keigwin, L. (1985). Comparison of Atlantic and Pacific Paleochemical Records for the Last 215,000 Years - Changes in Deep Ocean Circulation and Chemical Inventories. *Earth and Planetary Science Letters*, 76:135–150.

Boyle, E. A. (1983). Manganese carbonate overgrowths on foraminifera tests. *Geochimica et Cosmochimica Acta*, 47(10):1815–1819.

Boyle, E. A. (1988). Vertical oceanic nutrient fractionation and glacial/interglacial CO2 cycles. *Nature*, 331(6151):55–56.

Boyle, E. A. (1992). Cadmium and δ^{13}C paleochemical ocean distributions during the stage 2 glacial maximum. *Annual Review of Earth and Planetary Sciences*, (20):245–287.

Boyle, E. A., Sclater, F., and Edmond, J. M. (1976). On the marine geochemistry of cadmium. *Nature*, 263(5572):42–44.

Branson, O., Redfern, S. A. T., Tyliszczak, T., Sadekov, A., Langer, G., Kimoto, K., and Elderfield, H. (2013). Earth and Planetary Science Letters. *Earth and Planetary Science Letters*, 383(C):134–141.

Broecker, W. and Barker, S. (2007). A 190 drop in atmosphere's Δ^{14}C during the "Mystery Interval" (17.5 to 14.5 kyr). *Earth and Planetary Science Letters*, 256:90–99.

Broecker, W. and Peng, T. (1987). The role of CaCO3 compensation in the glacial to interglacial atmospheric CO2 change. *Global Biogeochemical Cycles*, 1(1):15–29.

Broecker, W. S. (1982). Ocean chemistry during glacial time. *Geochimica et Cosmochimica Acta*, 46(10):1689–1705.

Broecker, W. S. and Henderson, G. M. (1998). The sequence of events surrounding Termination II and their implications for the cause of glacial-interglacial CO 2 changes. *Paleoceanography*, 13(4):352–364.

Broecker, W. S., Peacock, S. L., Walker, S., Weiss, R., Fahrbach, E., Schroeder, M., Mikolajewicz, U., Heinze, C., Key, R., and Peng, T. H. (1998). How much deep water is formed in the Southern Ocean? *Journal of Geophysical Research*, 103(15):833–815.

Broecker, W. S. and Peng, T. H. (1982). Tracers in the sea. *Columbia University*.

Broecker, W. S. and Peng, T. H. (1989). The cause of the glacial to interglacial atmospheric CO2 change: a polar alkalinity hypothesis. *Global Biogeochemical Cycles*, 3(3):215–239.

Bronk Ramsey, C. (2013). Recent and Planned Developments of the Program OxCal. *Radiocarbon*, 55(3–4):720–730.

Brown, S. J. and Elderfield, H. (1996). Variations in Mg/Ca and Sr/Ca ratios of planktonic foraminifera caused by postdepositional dissolution: Evidence of shallow Mg-dependent dissolution. *Paleoceanography*, 11:1–9.

Bruland, K. W. (1983). Trace elements in seawater. In Riley, J. P. and Chester, R., editors, *Chemical Oceanography*, pages 147–220. Academic, London.

Brunelle, B., Sigman, D., Cook, M., Keigwin, L., Haug, G., Plessen, B., Schettler, G., and Jaccard, S. (2007). Evidence from diatom-bound nitrogen isotopes for subarctic Pacific stratification during the last ice age and a link to North Pacific denitrification changes. *Paleoceanography*, 22(1):doi:10.1029–2005PA001205.

Brunelle, B. G., Sigman, D. M., Jaccard, S. L., Keigwin, L. D., Plessen, B., Schettler, G., Cook, M. S., and Haug, G. H. (2010). Glacial/interglacial changes in nutrient supply and stratification in the western subarctic North Pacific since the penultimate glacial maximum. *Quaternary Science Reviews*, 29(19-20):2579–2590.

Bryan, S. P. and Marchitto, T. M. (2008). Mg/Ca–temperature proxy in benthic foraminifera: New calibrations from the Florida Straits and a hypothesis regarding Mg/Li. *Paleoceanography*, 23(2):10.1029–2007PA001553.

Bryan, S. P. and Marchitto, T. M. (2010). Testing the utility of paleonutrient proxies Cd/Ca and Zn/Ca in benthic foraminifera from thermocline waters. *Geochem. Geophys. Geosyst*, 11(1):10.1029–2009GC002780.

Busenberg, E. and Plummer, L. N. (1985). Kinetic and thermodynamic factors controlling the distribution of SO32 and Na+ in calcites and selected aragonites. *Geochimica et Cosmochimica Acta*, 49:713–725.

Cadot, H. M. and Kaesler, R. L. (1977). Magnesium content of calcite in carapaces of benthic marine Ostracoda. *The Paleontological Institute, The University of Kansas*, 87:1–23.

Cannariato, K., Kennett, J., and Behl, R. (1999). Biotic response to late Quaternary rapid climate switches in Santa Barbara Basin: Ecological and evolutionary implications. *Geology*, 27(1):63–66.

Catanzaro, E. J., Champion, C. E., Garner, E. L., Marinenko, G., Sappenfield, K., and Shields, W. (1970). Boric acid: isotopic and assay standard reference materials. *NBS (US) Special Publication*, 260:1–70.

Chan, L.-H., Alt, J. C., and Teagle, D. A. H. (2002). Lithium and lithium isotope profiles through the upper oceanic crust: a study of seawater–basalt exchange at ODP Sites 504B and 896A. *Earth and Planetary Science Letters*, 201(1):187–201.

Chan, L. H. and Edmond, J. M. (1988). Variation of lithium isotope composition in the marine environment: A preliminary report. *Geochimica et Cosmochimica Acta*, 52:1711–1717.

Chan, L.-H., Leeman, W. P., and Plank, T. (2006). Lithium isotopic composition of marine sediments. *Geochem. Geophys. Geosyst*, 7(6):10.1029–2005GC001202.

Chang, A. S., Pedersen, T. F., and Hendy, I. L. (2014). Effects of productivity, glaciation and ventilation on late Quaternary sedimentary redox and trace element accumulation on the Vancouver Island margin, western Canada. *Paleoceanography*, pages 10.1002–2013PA002581.

Chave, K. E. (1954). Aspects of the biogeochemistry of magnesium 1. Calcareous marine organisms. *The Journal of Geology*, 62:266–283.

Chave, K. E. (1984). Physics and Chemistry of Biomineralization. *Annual Review of Earth and Planetary Sciences*, 12:293–305.

Chikamoto, M., Matsumoto, K., and Yamanaka, Y. (2009). Influence of export rain ratio changes on atmospheric CO 2 and sedimentary calcite preservation. *Journal of Oceanography*, 65(2):209–221.

Chivas, A. R., De Deckker, P., and Shelley, G. (1983). Magnesium, strontium and barium partitioning in non marine ostracod shells and their use in paleoenvironment reconstructions - a preliminary study. In Maddocks, R. F., editor, *In Applications of Ostracoda*, pages 238–249. University of Houston, Houston.

Cléroux, C., Cortijo, E., Anand, P., Labeyrie, L., Bassinot, F., Caillon, N., and Duplessy, J.-C. (2008). Mg/Ca and Sr/Ca ratios in planktonic foraminifera: Proxies for upper water column temperature reconstruction. *Paleoceanography*, 23(3):10.1029–2007PA001505.

Coadic, R., Bassinot, F., Dissard, D., Douville, E., Greaves, M., and Michel, E. (2013). A core-top study of dissolution effect on B/Ca in Globigerinoides sacculiferfrom the tropical Atlantic: Potential bias for paleo-reconstruction of seawater carbonate chemistry. *Geochem. Geophys. Geosyst*, pages 10.1029–2012GC004296.

Coggon, R. M., Teagle, D. A. H., Smith-Duque, C. E., Alt, J. C., and Cooper, M. J. (2010). Reconstructing Past Seawater Mg/Ca and Sr/Ca from Mid-Ocean Ridge Flank Calcium Carbonate Veins. *Science*, 327(5969):1114–1117.

Coles, G. P., Whatley, R. C., and Moguilevsky, A. (1994). The ostracod genus *Krithe* from the Tertiary and Quaternary of the North Atlantic. *Palaeogeography*, 37:71–120.

Cook, M., Keigwin, L., and Sancetta, C. (2005). The deglacial history of surface and intermediate water of the Bering Sea. *Deep Sea Research Part II: Topical Studies in Oceanography*, 52:2163–2173.

Corliss, B. (1991). Morphology and microhabitat preferences of benthic foraminifera from the northwest Atlantic Ocean. *Marine Micropaleontology*, 17(3-4):195–236.

Correge, T. (1993). Preliminary results of paleotemperature reconstruction using the magnesium to calcium ratio of deep-sea ostracode shells from the late Quaternary of Site 822, Leg 133 (western Coral Sea). *Proceedings of the Ocean Drilling Program Scientific Results*, 133:175–180.

Cronin, T. M., Dowsett, H. J., Dwyer, G. S., Baker, P. A., and Chandler, M. A. (2005). Mid-Pliocene deep-sea bottom-water temperatures based on ostracode Mg/Ca ratios. *Marine Micropaleontology*, 54(3-4):249–261.

Cronin, T. M., Dwyer, G. S., Farmer, J., Bauch, H. A., Spielhagen, R. F., Jakobsson, M., Nilsson, J., Briggs Jr, W. M., and Stepanova, A. (2012). Deep Arctic Ocean warming during the last glacial cycle. *Nature Geoscience*, 5(9):631–634.

Davies, M. H., Mix, A. C., Stoner, J. S., Addison, J. A., Jaeger, J., Finney, B., and Wiest, J. (2011). The deglacial transition on the southeastern Alaska Margin: Meltwater input, sea level rise, marine productivity, and sedimentary anoxia. *Paleoceanography*, 26(2):PA2223.

Dawber, C. F. and Tripati, A. (2012). Relationships between bottom water carbonate saturation and element/Ca ratios in coretop samples of the benthic foraminifera *Oridorsalis umbonatus*. *Biogeosciences*, 9(8):3029–3045.

de Baar, H. J. W., Saager, P. M., Nolting, R. F., and van der Meer, J. (1994). Cadmium versus phosphate in the world ocean. *Marine Chemistry*, 46(3):261–281.

de Nooijer, L., Langer, G., Nehrke, G., and Bijma, J. (2009). Physiological controls on seawater uptake and calcification in the benthic foraminifer Ammonia tepida. *Biogeosciences*, 6:2669–2675.

De Nooijer, L., Spero, H. J., Erez, J., Bijma, J., and Reichart, G. J. (2014). Earth-Science Reviews. *Earth Science Reviews*, 135(C):48–58.

De Nooijer, L., Toyofuku, T., and Kitazato, H. (2009). Foraminifera promote calcification by elevating their intracellular pH. *Proceedings of the National Academy of Sciences*, 106(36):15374–15378.

de Villiers, S. (1999). Seawater strontium and Sr/Ca variability in the Atlantic and Pacific oceans. *Earth and Planetary Science Letters*, 171(4):623–634.

de Villiers, S., Greaves, M., and Elderfield, H. (2002). An intensity ratio calibration method for the accurate determination of Mg/Ca and Sr/Ca of marine carbonates by ICP-AES. *Geochemistry, Geophysics, Geosystems*, 3:10.1029–2001GC000169.

Dekens, P. S. (2002). Core top calibration of Mg/Ca in tropical foraminifera: Refining paleotemperature estimation. *Geochem. Geophys. Geosyst*, 3(4):10.1029–2001GC000200.

Delaney, M., WH Be, A., and Boyle, E. A. (1985). Li, Sr, Mg, and Na in foraminiferal calcite shells from laboratory culture, sediment traps, and sediment cores. *Geochimica et Cosmochimica Acta*, 49(6):1327–1341.

Dickson, A. G. (1990a). Standard potential of the reaction: , and and the standard acidity constant of the ion HSO4 in synthetic sea water from 273.15 to 318.15 K. *The Journal of Chemical Thermodynamics*, 22(2):113–127.

Dickson, A. G. (1990b). Thermodynamics of the dissociation of boric acid in synthetic seawater from 273.15 to 318.15 K. *Deep Sea Research Part A. Oceanographic Research Papers*, 37(5):755–766.

Djogic, R., Sipos, L., and Branica, M. (1986). Characterization of uranium (VI) in seawater. *Limnology and Oceanography*, 31(5):1122–1131.

DOE (1994). Handbook of methods for the analysis of the various parameters of the carbon dioxide system in sea water. ORNL/CDIAC-74.

Driessens, F. and Verbeeck, R. (1981). Metastable states in calcium phosphate-aqueous phase equilibrations. *Journal of Crystal Growth*, 53(1):55–62.

Dugdale, R. C., Wischmeyer, A. G., Wilkerson, F. P., Barber, R. T., Chai, F., Jiang, M. S., and Peng, T. H. (2002). Meridional asymmetry of source nutrients to the equatorial Pacific upwelling ecosystem and its potential impact on ocean–atmosphere CO 2 flux; a data and modeling approach. *Deep Sea Research Part II: Topical Studies in Oceanography*, 49(13):2513–2531.

Dwyer, G., Cronin, T. M., Baker, P. A., and Rodriguez-Lazaro, J. (2000). Changes in North Atlantic deep-sea temperature during climatic fluctuations of the last 25,000 years based on ostracode Mg/Ca ratios. *Geochemistry, Geophysics, Geosystems*, 1(162):45–57.

Dwyer, G. S., Cronin, T. M., and Baker, P. A. (2002). Trace elements in marine ostracodes. In Holmes, J. A. and Chivas, A. R., editors, *The Ostracoda: Applications in Quaternary Research*, pages 205–225. Geophysical Monograph Series, Washington D.C.

Dwyer, G. S., Cronin, T. M., Baker, P. A., Raymo, M. E., Buzas, J. S., and Correge, T. (1995). North-Atlantic Deep-Water Temperature-Change During Late Pliocene and Late Quaternary Climatic Cycles. *Science*, 270(5240):1347–1351.

Dymond, J. and Lyle, M. (1985). Flux comparisons between sediments and sediment traps in the eastern tropical Pacific: Implications for atmospheric CO, variations during the Pleistocene. *OCEANOGRAPHY*, 30(4):699–712.

Elderfield, H., Bertram, C. J., and Erez, J. (1996). A biomineralization model for the incorporation of trace elements into foraminiferal calcium carbonate. *Earth and Planetary Science Letters*, 142(3):409–423.

Elderfield, H. and Ganssen, G. (2000). Past temperature and δ^{18}O of surface ocean waters inferred from foraminiferal Mg/Ca ratios. *Nature*, 405(6785):442–445.

Elderfield, H., Greaves, M., Barker, S., Hall, I. R., Tripati, A., Ferretti, P., Crowhurst, S., Booth, L., and Daunt, C. (2010). A record of bottom water temperature and seawater δ^{18}O for the Southern Ocean over the past 440kyr based on Mg/Ca of benthic foraminiferal Uvigerina spp. *Quaternary Science Reviews*, 29(1-2):160–169.

Elderfield, H., Yu, J., Anand, P., Kiefer, T., and Nyland, B. (2006). Calibrations for benthic foraminiferal Mg/Ca paleothermometry and the carbonate ion hypothesis. *Earth and Planetary Science Letters*, 250(3-4):633–649.

Elmore, A. C., Sosdian, S., Rosenthal, Y., and Wright, J. D. (2012). A global evaluation of temperature and carbonate ion control on Mg/Ca ratios of ostracoda genus Krithe. 13(9):10.1029–2012GC004073.

Elrod, V. A. (2004). The flux of iron from continental shelf sediments: A missing source for global budgets. *Geophys. Res. Lett*, 31(12):L12307.

Emile-Geay, J. (2003). Warren revisited: Atmospheric freshwater fluxes and "Why is no deep water formed in the North Pacific". *Journal of Geophysical Research*, 108(C6):10.1029–2001JC001058.

Erez, J. (2003). The source of ions for biomineralization in foraminifera and their implications for paleoceanographic proxies. In *Review of Mineral Geochemistry*, pages 115–149. Hebrew Univ Jerusalem, Inst Earth Sci, IL-91904 Jerusalem, Israel.

Fairbanks, R. (1989). A 17, 000-year glacio-eustatic sea level record: influence of glacial melting rates on the Younger Dryas event and deep-ocean circulation. *Nature*, 342(6250):637–642.

Fairbanks, R., Mortlock, R., Chiu, T., Cao, L., Kaplan, A., Guilderson, T., Fairbanks, T., Bloom, A., Grootes, P., and Nadeau, M. (2005). Radiocarbon calibration curve spanning 0 to 50,000 years BP based on paired 230Th/234U/238U and 14C dates on pristine corals. *Quaternary Science Reviews*, 24(16-17):1781–1796.

Farmer, J. R., Cronin, T. M., and Dwyer, G. S. (2012). Ostracode Mg/Ca paleothermometry in the North Atlantic and Arctic oceans: Evaluation of a carbonate ion effect. *Paleoceanography*, 27(2):10.1029–2012PA002305.

Ferguson, J. E., Henderson, G. M., Kucera, M., and Rickaby, R. E. M. (2008). Systematic change of foraminiferal Mg/Ca ratios across a strong salinity gradient. *Earth and Planetary Science Letters*, 265(1-2):153–166.

Foster, G. L. (2008a). Seawater pH, pCO2 and [CO23] variations in the Caribbean Sea over the last 130 kyr: A boron isotope and B/Ca study of planktic foraminifera. *Earth and Planetary Science Letters*, 271(1-4):254–266.

Foster, G. L. (2008b). Seawater pH, pCO2 and [CO23] variations in the Caribbean Sea over the last 130 kyr: A boron isotope and B/Ca study of planktic foraminifera. *Earth and Planetary Science Letters*, 271(1-4):254–266.

Foster, G. L., Pogge von Strandmann, P. A. E., and Rae, J. W. B. (2010). Boron and magnesium isotopic composition of seawater. *Geochem. Geophys. Geosyst*, 11(8):10.1029–2010GC003201.

Froelich, P. N., Klinkhammer, G. P., and Bender, M. L. (1979). Early oxidation of organic matter in pelagic sediments of the eastern equatorial Atlantic: suboxic diagenesis. *Geochimica et Cosmochimica Acta*, 43:1075–1090.

Gaffey, S. J. and Bronnimann, C. E. (1993). Effects of bleaching on organic and mineral phases in biogenic carbonates. *Journal of Sedimentary Petrology*, 63:752–754.

Galbraith, E., Jaccard, S., Pedersen, T., Sigman, D., Haug, G., Cook, M., Southon, J., and Francois, R. (2007). Carbon dioxide release from the North Pacific abyss during the last deglaciation. *Nature*, 449(7164):890–893.

Galbraith, E., Kienast, M., Jaccard, S., Pedersen, T., Brunelle, B., Sigman, D., and Kiefer, T. (2008). Consistent relationship between global climate and surface nitrate utilization in the western subarctic Pacific throughout the last 500 ka. *Paleoceanography*, 23(2):10.1029–2007PA001518.

Garrels, R. M. and Christ, C. L. (1965). Solutions, minerals, and equilibria. *Freeman Cooper Co.*

Gebbie, G. (2012). Tracer transport timescales and the observed Atlantic-Pacific lag in the timing of the Last Termination. *Paleoceanography*, 27(3):10.1029–2011PA002273.

Gebhardt, H., Sarnthein, M., Grootes, P., Kiefer, T., Kuehn, H., Schmieder, F., and Röhl, U. (2008). Paleonutrient and productivity records from the subarctic North Pacific for Pleistocene glacial terminations I to V. *Paleoceanography*, 23(4):21.

Greaves, M. (2005). Accuracy, standardization, and interlaboratory calibration standards for foraminiferal Mg/Ca thermometry. *Geochem. Geophys. Geosyst*, 6(2):10.1029–2004GC000790.

Hain, M. P., Sigman, D. M., and Haug, G. H. (2011). Shortcomings of the isolated abyssal reservoir model for deglacial radiocarbon changes in the mid-depth Indo-Pacific Ocean. *Geophys. Res. Lett*, 38(4):L04604.

Haley, B. A. and Klinkhammer, G. P. (2002). Development of a flow-through system for cleaning and dissolving foraminiferal tests. *Chemical Geology*, 185(1):51–69.

Hall, J. and Chan, L. (2004). Li/Ca in multiple species of benthic and planktonic foraminifera: thermocline, latitudinal, and glacial-interglacial variation 1. *Geochimica et Cosmochimica Acta*, 68(3):529–545.

Hamilton, C. P., Spero, H. J., Bijma, J., and Lea, D. W. (2008). Geochemical investigation of gametogenic calcite addition in the planktonic foraminifera Orbulina universa. *Marine Micropaleontology*, 68(3-4):256–267.

Harris, D. C. (2010). *Quantitative Chemical Analysis*. W. H. Freeman, New York, 6th edition.

Hart, S. R. and Staudigel, H. (1982). The control of alkalies and uranium in seawater by ocean crust alteration. *Earth and Planetary Science Letters*, 58(2):202–212.

Hastings, D. W., Emerson, S. R., and Erez, J. (1996). Vanadium in foraminiferal calcite: Evaluation of a method to determine paleo-seawater vanadium concentrations. *Geochimica et Cosmochimica Acta*, 60:3701–3715.

Haug, G. and Sigman, D. (2009). Palaeoceanography: Polar twins. *Nature Geoscience*, 2(2):91–92.

Hemming, N. G. and Hanson, G. N. (1992). Boron isotopic composition and concentration in modern marine carbonates. *Geochimica et Cosmochimica Acta*, 56(1):537–543.

Hendy, I., Kennett, J., Roark, E., and Ingram, B. (2002). Apparent synchroneity of submillennial scale climate events between Greenland and Santa Barbara Basin, California from 30-10 ka. *Quaternary Science Reviews*, 21(10):1167–1184.

Herguera, J., Jansen, E., and Berger, W. (1992). Evidence for a Bathyal front at 2000-m depth in the glacial Pacific, based on a depth transect on Ontong Java Plateau. *Paleoceanography*, 7(3):273–288.

Herguera, J. C., Herbert, T., Kashgarian, M., and Charles, C. (2010). Intermediate and deep water mass distribution in the Pacific during the Last Glacial Maximum inferred from oxygen and carbon stable isotopes. *Quaternary Science Reviews*, 29(9-10):1228–1245.

Hilbrecht, H. (1996). Extant planktic foraminifera and the physical environment in the Atlantic and Indian Oceans - Mitteilungen aus dem Geologischen Institut der Eidgen. Technischen Hochschule und der Universität Zürich. *Neue Folge*, (300):9.

Hintz, C., Shaw, T., Bernhard, J., Chandler, G., McCorkle, D., and Blanks, J. (2006a). Trace/minor element:calcium ratios in cultured benthic foraminifera. Part II: Ontogenetic variation. *Geochimica et Cosmochimica Acta*, 70(8):1964–1976.

Hintz, C. J., Shaw, T. J., Chandler, G. T., McCorkle, D. C., Bernhard, J. M., and Blanks, J. K. (2006b). Calcite saturation state effects on cultured benthic foraminiferal trace-element distribution coefficients. *AGU Fall Meeting Abstracts*, 1:1080.

Holmes, J. A. (2008). Sample-size implications of the trace-element variability of ostracod shells. *Geochimica et Cosmochimica Acta*, 72(12):2934–2945.

Horikawa, K., Asahara, Y., Yamamoto, K., and Okazaki, Y. (2010). Intermediate water formation in the Bering Sea during glacial periods: Evidence from neodymium isotope ratios. *Geology*, 38(5):435–438.

Horne, D. J., Cohen, A., and Martens, K. (2002). Taxonomy, morphology and biology of Quaternary and living ostracoda. In *The Ostracoda: applications in Quaternary Research*, pages 5–36. American Geophysical Union, Washington, D. C.

Hughen, K., Lehman, S., Southon, J., Overpeck, J., Marchal, O., Herring, C., and Turnbull, J. (2004). 14C activity and global carbon cycle changes over the past 50,000 years. *Science*, 303(5655):202.

Huh, Y., Chan, L.-H., Zhang, L., and Edmond, J. M. (1998). Lithium and its isotopes in major world rivers: implications for weathering and the oceanic budget. *Geochimica et Cosmochimica Acta*, 62(12):2039–2051.

Insua, T. L., Spivack, A. J., Graham, D., D'Hondt, S., and Moran, K. (2014). Reconstruction of Pacific Ocean bottom water salinity during the Last Glacial Maximum. *Geophys. Res. Lett*, 41(8):2914–2920.

Ishikawa, T. and Nakamura, E. (1993). Boron isotope systematics of marine sediments. *Earth and Planetary Science Letters*, 117:567–580.

Ito, E., De Deckker, P., and Eggins, S. M. (2003). Ostracodes and their shell chemistry: implications for paleohydrologic and paleoclimatologic applications. *Paleontological Society Papers*, 9:119.

Jaccard, S., Haug, G., Sigman, D., Pedersen, T., Thierstein, H., and Rohl, U. (2005). Glacial/interglacial changes in subarctic North Pacific stratification. *Science*, 308(5724):1003.

Jaccard, S. L., Galbraith, E. D., Sigman, D. M., and Haug, G. H. (2010). A pervasive link between Antarctic ice core and subarctic Pacific sediment records over the past 800kyrs. *Quaternary Science Reviews*, 29(1-2):206–212.

Jaccard, S. L., Galbraith, E. D., Sigman, D. M., Haug, G. H., Francois, R., Pedersen, T. F., Dulski, P., and Thierstein, H. R. (2009). Subarctic Pacific evidence for a glacial deepening of the oceanic respired carbon pool. *Earth and Planetary Science Letters*, 277(1-2):156–165.

Jickells, T. D. and Spokes, L. J. (2001). Atmospheric iron inputs to the oceans. In Turner, D. R. and Hunter, K. A., editors, *The biochemistry of Iron in Seawater*, pages 85–118. John Wiley & Sons, New Jersey.

Jin, Z., Bickle, M., Chapman, H., Yu, J., Greaves, M., Wang, S., and Chen, S. (2006). An experimental evaluation of cleaning methods for fossil ostracod Mg/Ca and Sr/Ca determination. *Journal of Paleolimnology*, 36(2):211–218.

Jonkers, L., Brummer, G.-J. A., Peeters, F. J. C., van Aken, H. M., and De Jong, M. F. (2010). Seasonal stratification, shell flux, and oxygen isotope dynamics of left-coiling N. pachydermaand T. quinquelobain the western subpolar North Atlantic. *Paleoceanography*, 25(2):PA2204.

Jonkers, L., Jiménez-Amat, P., Mortyn, P. G., and Brummer, G.-J. A. (2013a). Earth and Planetary Science Letters. *Earth and Planetary Science Letters*, 376(C):137–144.

Jonkers, L., Jiménez-Amat, P., Mortyn, P. G., and Brummer, G.-J. A. (2013b). Earth and Planetary Science Letters. *Earth and Planetary Science Letters*, 376(C):137–144.

Joyce, T. M., Warren, B. A., and Talley, L. D. (1986). The geothermal heating of the abyssal subarctic Pacific Ocean. *Deep Sea Research Part A. Oceanographic Research Papers*, 33(8):1003–1015.

Katz, A. (1973). The interaction of magnesium with calcite during crystal growth at 25–90 °C and one atmosphere. *Geochimica et Cosmochimica Acta*, 37(6):1563–1586.

Keigwin, L. (1998). Glacial-age hydrography of the far northwest Pacific Ocean. *Paleoceanography*, 13(4):323–339.

Kelley, J. J. and Hood, D. W. (1971). Carbon dioxide in the Pacific Ocean and Bering Sea: Upwelling and mixing. *Journal of Geophysical Research*, 76(3):745–752.

Kesling, R. V. (1951). The morphology of ostracod molt stages. *Illinois Biological Monographs*, 21:1–126.

Keul, N., Langer, G., de Nooijer, L. J., Nehrke, G., Reichart, G.-J., and Bijma, J. (2013). Incorporation of uranium in benthic foraminiferal calcite reflects seawater carbonate ion concentration. *Geochem. Geophys. Geosyst*, 14(1):102–111.

Key, R. M. (2004). A global ocean carbon climatology: Results from Global Data Analysis Project (GLODAP). *Global Biogeochemical Cycles*, 18(4):10.1029–2004GB002247.

Keyser, D. and Walter, R. (2010). Calcification in ostracodes. *Revista Española de Micropaleontologia*, 36(1):1–11.

Kiefer, T., Lorenz, S., Schulz, M., Lohmann, G., Sarnthein, M., and Elderfield, H. (2002). Response of precipitation over Greenland and the adjacent ocean to North Pacific warm spells during Dansgaard-Oeschger stadials. *Terra Nova*, 14(4):295–300.

Kienast, M., Hanebuth, T. J. J., Pelejero, C., and Steinke, S. (2003). Synchroneity of meltwater pulse 1a and the Bølling warming: New evidence from the South China Sea. *Geology*, 31(1):67.

Kienast, S., Hendy, I., Crusius, J., Pedersen, T., and Calvert, S. (2004). Export Production in the Subarctic North Pacific over the Last 800 kyrs: No Evidence for Iron Fertilization? *Journal of Oceanography*, 60(1):189–203.

Kim, S. and ONeil, J. (1997). Equilibrium and nonequilibrium oxygen isotope effects in synthetic carbonates. *Geochimica et Cosmochimica Acta*, 61(16):3461–3475.

King, A. L. and Howard, W. R. (2005). δ18O seasonality of planktonic foraminifera from Southern Ocean sediment traps: Latitudinal gradients and implications for paleoclimate reconstructions. *Marine Micropaleontology*, 56(1-2):1–24.

Klinkhammer, G. P. and Palmer, M. R. (1991). Uranium in the oceans: Where it goes and why. *Geochimica et Cosmochimica Acta*, 55(7):1799–1806.

Klochko, K., Kaufman, A. J., Yao, W., Byrne, R. H., and Tossell, J. A. (2006). Experimental measurement of boron isotope fractionation in seawater. *Earth and Planetary Science Letters*, 248(1-2):276–285.

Knox, F. and McElroy, M. B. (1984). Changes in atmospheric CO2: Influence of the marine biota at high latitude. *Journal of Geophysical Research*, 89(D3):4629–4637.

Kovanen, D. J. and Easterbrook, D. J. (2002). Paleodeviations of radiocarbon marine reservoir values for the northeast Pacific. *Geology*, 30(3):243.

Koziol, A. M. and Newton, R. C. (1995). Experimental determination of the reactions magnesite + quartz = enstatite+ CO_2 and magnesite = periclase + CO_2, and enthalpies of formation of enstatite and magnesite. *American Mineralogist*, 80(11-12):1252–1260.

Krestou, A., Xenidis, A., and Panias, D. (2003). Mechanism of aqueous uranium (VI) uptake by natural zeolitic tuff. *Minerals Engineering*, 16(12):1363–1370.

Ku, T. L., Knauss, K. G., and Mathieu, G. G. (1977). Uranium in open ocean: concentration and isotopic composition. *Deep-sea Research*, 24(11):1005–1017.

Kuile, B. and Erez, J. (1987). Uptake of inorganic carbon and internal carbon cycling in symbiont-bearing benthonic foraminifera. *Marine Biology*, 94(4):499–509.

Kuile, B., Erez, J., and Padan, E. (1989a). Competition for inorganic carbon between photosynthesis and calcification in the symbiont-bearing foraminifer Amphistegina lobifera. *Marine Biology*, 103(2):253–259.

Kuile, B., Erez, J., and Padan, E. (1989b). Mechanisms for the uptake of inorganic carbon by two species of symbiont-bearing foraminifera. *Marine Biology*, 103(2):241–251.

Kuroyanagi, A. and Kawahata, H. (2004). Vertical distribution of living planktonic foraminifera in the seas around Japan. *Marine Micropaleontology*, 53(1-2):173–196.

Kuroyanagi, A., Kawahata, H., and Nishi, H. (2011). Seasonal variation in the oxygen isotopic composition of different-sized planktonic foraminifer Neogloboquadrina pachyderma(sinistral) in the northwestern North Pacific and implications for reconstruction of the paleoenvironment. *Paleoceanography*, 26(4):10.1029–2011PA002153.

Lam, P. J., Robinson, L. F., Blusztajn, J., Li, C., Cook, M. S., McManus, J. F., and Keigwin, L. D. (2013). Transient stratification as the cause of the North Pacific productivity spike during deglaciation. *Nature Geoscience*, 6(8):622–626.

Lea, D. (2000). Climate Impact of Late Quaternary Equatorial Pacific Sea Surface Temperature Variations. *Science*, 289(5485):1719–1724.

Lea, D. and Boyle, E. (1991). Barium in Planktonic-Foraminifera. In *Geochimica et Cosmochimica Acta*, pages 3321–3331.

Lea, D., Mashiotta, T., and Spero, H. (1999). Controls on magnesium and strontium uptake in planktonic foraminifera determined by live culturing. *Geochimica et Cosmochimica Acta*, 63(16):2369–2379.

Lear, C., Elderfield, H., and Wilson, P. A. (2000). Cenozoic deep-sea temperatures and global ice volumes from Mg/Ca in benthic foraminiferal calcite. *Science*, 287:269–272.

Lear, C., Elderfield, H., and Wilson, P. A. (2003). A Cenozoic seawater Sr/Ca record from benthic foraminiferal calcite and its application in determining global weathering fluxes. *Earth and Planetary Science Letters*, 208(1-2):69–84.

Lear, C., Rosenthal, Y., and Slowey, N. (2002). Benthic foraminiferal Mg/Ca-paleothermometry: A revised core-top calibration. *Geochimica et Cosmochimica Acta*, 66(19):3375–3387.

Lear, C. H., Mawbey, E. M., and Rosenthal, Y. (2010). Cenozoic benthic foraminiferal Mg/Ca and Li/Ca records: Toward unlocking temperatures and saturation states. *Paleoceanography*, 25(4).

Lear, C. H. and Rosenthal, Y. (2006). Benthic foraminiferal Li/Ca: Insights into Cenozoic seawater carbonate saturation state. *Geology*, 34(11):985.

Lee, K., Tong, L. T., Millero, F. J., Sabine, C. L., Dickson, A. G., Goyet, C., Park, G.-H., Wanninkhof, R., Feely, R. A., and Key, R. M. (2006). Global relationships of total alkalinity with salinity and temperature in surface waters of the world's oceans. *Geophys. Res. Lett*, 33(19):L19605.

LeGrande, A. N. and Schmidt, G. A. (2006). Global gridded data set of the oxygen isotopic composition in seawater. *Geophys. Res. Lett*, 33(12):L12604.

Levy, M., Bopp, L., Karleskind, P., Resplandy, L., Ethe, C., and Pinsard, F. (2013). Physical pathways for carbon transfers between the surface mixed layer and the ocean interior. *Global Biogeochemical Cycles*, pages 10.1002–gbc.20092.

Li, Y. H. (2000). *A compendium of geochemistry: from solar nebula to the human brain.* Princeton University Press, Princeton, New Jersey.

Lourantou, A., Lavrič, J. V., Kohler, P., Barnola, J.-M., Paillard, D., Michel, E., Raynaud, D., and Chappellaz, J. (2010). Constraint of the CO 2rise by new atmospheric carbon isotopic measurements during the last deglaciation. *Global Biogeochemical Cycles*, 24(2):10.1029–2009GB003545.

Lund, D. C., Mix, A. C., and Southon, J. (2011). Increased ventilation age of the deep northeast Pacific Ocean during the last deglaciation. *Nature Geoscience*, 4(11):771–774.

Lüthi, D., Le Floch, M., Bereiter, B., Blunier, T., Barnola, J., Siegenthaler, U., Raynaud, D., Jouzel, J., Fischer, H., and Kawamura, K. (2008). High-resolution carbon dioxide concentration record 650,000–800,000 years before present. *Nature*, 453(7193):379–382.

Lynch-Stieglitz, J., Curry, W. B., and Slowey, N. (1999). A geostrophic transport estimate for the Florida Current from the oxygen isotope composition of benthic foraminifera. *Paleoceanography*, 14(3):360–373.

Lynch-Stieglitz, J., Stocker, T. F., Broecker, W. S., and Fairbanks, R. G. (1995). The influence of airsea exchange on the isotopic composition of oceanic carbon: Observations and modeling. *Global Biogeochemical Cycles*, 9(4):653–665.

Lynn, D. and Bonatti, E. (1965). Mobility of manganese in diagenesis of deep-sea sediments. *Marine Geology*, 3(6):457–474.

Mackenzie, F. T. and Garrels, R. M. (1966). Chemical mass balance between rivers and oceans. *American Journal of Science*, 264:507–525.

Marchitto, T., Lehman, S., Ortiz, J., Fluckiger, J., and van Geen, A. (2007a). Marine radiocarbon evidence for the mechanism of deglacial atmospheric CO2 rise. *Science*, 316(5830):1456.

Marchitto, T., Lynch-Stieglitz, J., and Hemming, S. (2005). Deep Pacific CaCO3 compensation and glacial-interglacial atmospheric CO2. *Earth and Planetary Science Letters*, 231(3-4):317–336.

Marchitto, T. M., Bryan, S. P., Curry, W. B., and McCorkle, D. C. (2007b). Mg/Ca temperature calibration for the benthic foraminifer Cibicidoides pachyderma. *Paleoceanography*, 22(1).

Marchitto, T. M., Curry, W. B., Lynch-Stieglitz, J., Bryan, S. P., Cobb, K. M., and Lund, D. C. (2014). Improved oxygen isotope temperature calibrations for cosmopolitan benthic foraminifera. *Geochimica et Cosmochimica Acta*, 130(C):1–11.

Marinov, I., Gnanadesikan, A., Sarmiento, J., Toggweiler, J., Follows, M., and Mignone, B. (2008). Impact of oceanic circulation on biological carbon storage in the ocean and atmospheric pCO2, Global Biogeochem. *Global Biogeochemical Cycles*, 22:10.1029–2007GB002958.

Marinov, I., Gnanadesikan, A., Toggweiler, J. R., and Sarmiento, J. L. (2006). The Southern Ocean biogeochemical divide. *Nature*, 441(7096):964–967.

Marriott, C. S., Henderson, G. M., Belshaw, N. S., and Tudhope, A. W. (2004a). Temperature dependence of delta Li-7, delta Ca-44 and Li/Ca during growth of calcium carbonate. *Earth and Planetary Science Letters*, 222(2):615–624.

Marriott, C. S., Henderson, G. M., Crompton, R., Staubwasser, M., and Shaw, S. (2004b). Effect of mineralogy, salinity, and temperature on Li/Ca and Li isotope composition of calcium carbonate. *Chemical Geology*, 212(1-2):5–15.

Marshall, J. and Speer, K. (2012). Closure of the meridional overturning circulation through Southern Ocean upwelling. *Nature Geoscience*, 5(3):171–180.

Martin, J. H. (1990). Glacial-interglacial CO2 change: The iron hypothesis. *Paleoceanography*, 5(1):1–13.

Martin, J. H. and Michael Gordon, R. (1988). Northeast Pacific iron distributions in relation to phytoplankton productivity. *Deep Sea Research Part A. Oceanographic Research Papers*, 35(2):177–196.

Martin, J. M. and Meybeck, M. (1979). Elemental Mass-Balance of Material Carried by Major World Rivers. *Marine Chemistry*, 7(3):173–206.

Martin, P., Lea, D., Rosenthal, Y., Shackleton, N., Sarnthein, M., and Papenfuss, T. (2002). Quaternary deep sea temperature histories derived from benthic foraminiferal Mg/Ca. *Earth and Planetary Science Letters*, 198(1-2):193–209.

Martin, P. A. (2002). A simple evaluation of cleaning procedures on fossil benthic foraminiferal Mg/Ca. *Geochemistry, Geophysics, Geosystems*, 3(10):10.1029–2001GC000280.

Mashiotta, T. A., Lea, D. W., and Spero, H. J. (1999). Glacial–interglacial changes in Subantarctic sea surface temperature and δ^{18}O-water using foraminiferal Mg. *Earth and Planetary Science Letters*, 170(4):417–432.

Matsumoto, K., Oba, T., Lynch-Stieglitz, J., and Yamamoto, H. (2002). Interior hydrography and circulation of the glacial Pacific Ocean. *Quaternary Science Reviews*, 21(14-15):1693–1704.

McCorkle, D. C., Corliss, B., and Farnham, C. (1997). Vertical distributions and stable isotopic compositions of live (stained) benthic foraminifera from the North Carolina and California continental margins. *Deep-Sea Research Part I*, 44(6):983–1024.

McKee, B. A., DeMaster, D. J., and Nittrouer, C. A. (1987). Uranium geochemistry on the Amazon shelf: evidence for uranium release from bottom sediments. *Geochimica et Cosmochimica Acta*, 51:2779–2786.

McKenzie, K. G., Majoran, S., Emami, V., and Reymant, R. A. (1989). The Krithe Problem - 1st Test of Peypouquets Hypothesis, with a Redescription of Krithe-Praetexta-Praetexta (Crustacea, Ostracoda). *Palaeogeography, Palaeoclimatology, Palaeoecology*, 74:343–354.

McManus, J. F., Francois, R., Gherardi, J.-M., Keigwin, L. D., and Brown-Leger, S. (2004). Collapse and rapid resumption of Atlantic meridional circulation linked to deglacial climate changes. *Nature*, 428(6985):834–837.

Michalopoulos, P. and Aller, R. C. (1995). Rapid clay mineral formation in Amazon delta sediments: reverse weathering and oceanic elemental cycles. *Science*, 270:614–617.

Millero, F. J. (1995). Thermodynamics of the carbon dioxide system in the oceans. *Geochimica et Cosmochimica Acta*, 59(4):661–677.

Millero, F. J., Graham, T. B., Huang, F., Bustos-Serrano, H., and Pierrot, D. (2006). Dissociation constants of carbonic acid in seawater as a function of salinity and temperature. *Marine Chemistry*, 100(1-2):80–94.

Millero, F. J. and Roy, R. N. (1997). A Chemical equilibrium model for the carbonate sysem in natural waters. *Croatica chemica acta*, 70(1):1–38.

Mix, A. C., Lund, D. C., Pisias, N. G., Bodén, P., Bornmalm, L., Lyle, M., and Pike, J. (1999). Rapid climate oscillations in the Northeast Pacific during the last deglaciation reflect Northern and Southern Hemisphere sources. In *Mechanisms of Global CLimate Change at Millennial Time Scales*, pages 127–148. American Geophysical Union, Washington, D. C.

Monnin, E., Indermuhle, A., Dallenbach, A., Fluckiger, J., Stauffer, B., Stocker, T., Raynaud, D., and Barnola, J. (2001). Atmospheric CO2 concentrations over the last glacial termination. *Science*, 291(5501):112.

Mordy, C. W., Stabeno, P. J., Ladd, C., Zeeman, S., Wisegarver, D. P., Salo, S. A., and Hunt, G. L. (2005). Nutrients and primary production along the eastern Aleutian Island Archipelago. *Fisheries Oceanography*, 14(s1):55–76.

Morse, J. W. and Mackenzie, F. T. (1990). *Geochemistry of Sedimentary Carbonates*. Elsevier, New York.

Nehrke, G., Keul, N., Langer, G., de Nooijer, L., Bijma, J., and Meibom, A. (2013). A new model for biomineralization and trace element signatures of foraminifera tests. *Mineralogical Magazine*, 77(5):1818–1868.

Nürnberg, D., Bijma, J., and Hemleben, C. (1996). Assessing the reliability of magnesium in foraminiferal calcite as a proxy for water mass temperatures. *Geochimica et Cosmochimica Acta*, 60:803–814.

Ohkouchi, N., Kawahata, H., Murayama, M., Okada, M., Nakamura, T., and Taira, A. (1994). Was deep water formed in the North Pacific during the Late Quaternary? Cadmium evidence from the Northwest Pacific. *Earth and Planetary Science Letters*, 124(1):185–194.

Ohkushi, K., Itaki, T., and Nemoto, N. (2003). Last Glacial-Holocene change in intermediate-water ventilation in the Northwestern Pacific. *Quaternary Science Reviews*, 22(14):1477–1484.

Okazaki, Y., Sagawa, T., Asahi, H., Horikawa, K., and Onodera, J. (2012). Ventilation changes in the western North Pacific since the last glacial period. *Climate of the Past*, 8(1):17–24.

Okazaki, Y., Timmermann, A., Menviel, L., Harada, N., Abe-Ouchi, A., Chikamoto, M., Mouchet, A., and Asahi, H. (2010). Deepwater Formation in the North Pacific During the Last Glacial Termination. *Science*, 329(5988):200.

Okumura, M. and Kitano, Y. (1986). coprecipitation of alkali-metal ions with calcium-carbonate. *Geochimica et Cosmochimica Acta*, 50(1):49–58.

Oomori, T., Kaneshima, H., Maezato, Y., and Kitano, Y. (1987). Distribution coefficient of Mg2+ ions between calcite and solution at 10–50 °C. *Marine Chemistry*, 20(4):327–336.

Pak, D. and Kennett, J. (2002). A foraminiferal isotopic proxy for upper water mass stratification. *The Journal of Foraminiferal Research*, 32(3):319.

Palmer, M. R. (2003). A 23,000-Year Record of Surface Water pH and PCO2 in the Western Equatorial Pacific Ocean. *Science*, 300(5618):480–482.

Palmer, M. R. and Edmond, J. M. (1993). Uranium in river water. *Geochimica et Cosmochimica Acta*, 57(20):4947–4955.

Pena, L. D. (2005). Identification and removal of Mn-Mg-rich contaminant phases on foraminiferal tests: Implications for Mg/Ca past temperature reconstructions. *Geochemistry, Geophysics, Geosystems*, 6(9):10.1029–2005GC000930.

Pena, L. D., Cacho, I., Calvo, E., Pelejero, C., Eggins, S., and Sadekov, A. (2008). Characterization of contaminant phases in foraminifera carbonates by electron microprobe mapping. *Geochemistry, Geophysics, Geosystems*, 9(7):10.1029–2008GC002018.

Peterson, C. D., Lisiecki, L. E., and Stern, J. V. (2014). Deglacial whole-ocean δ13C change estimated from 480 benthic foraminiferal records. *Paleoceanography*, (29):549–563.

Rae, J. W. B., Foster, G. L., Schmidt, D. N., and Elliott, T. (2011). Boron isotopes and B/Ca in benthic foraminifera: Proxies for the deep ocean carbonate system. *Earth and Planetary Science Letters*, 302(3-4):403–413.

Rae, J. W. B., Sarnthein, M., Foster, G. L., Ridgwell, A., Grootes, P. M., and Elliott, T. (2014). Deep water formation in the North Pacific and deglacial CO 2rise. *Paleoceanography*, 29(6):645–667.

Raitzsch, M., Kuhnert, H., Hathorne, E. C., Groeneveld, J., and Bickert, T. (2011). U/Ca in benthic foraminifers: A proxy for the deep-sea carbonate saturation. *Geochemistry, Geophysics, Geosystems*, 12(6):10.1029–2010GC003344.

Ramsey, M. H., Thompson, M., and Walton, S. J. (1987). Self-matrix effects as a cause of calibration curvature in inductively coupled plasma atomic emission spectrometry. *Journal of Analytical Spectrometry*, 2(1):33.

Rasmussen, S. O., Andersen, K. K., Svensson, A. M., Steffensen, J. P., Vinther, B. M., Clausen, H. B., Siggaard-Andersen, M. L., Johnsen, S. J., Larsen, L. B., Dahl-Jensen, D., Bigler, M., Röthlisberger, R., Fischer, H., Goto-Azuma, K., Hansson, M. E., and Ruth, U. (2006). A new Greenland ice core chronology for the last glacial termination. *Journal of Geophysical Research*, 111(D6).

Rathbuml, A. E. and Corliss, B. (1994). The ecology of living (stained) deep-sea. *Paleoceanography*, 9(1):87–150.

Redfield, A. C., Ketchum, B. H., and Richards, F. A. (1963). Redfield: The influence of organisms on the composition of sea-water. In Hill, M. N., editor, *The Sea,; ideas and observations*, pages 26–77. Interscience, New York.

Regenberg, M., Regenberg, A., Garbe-Schönberg, D., and Lea, D. W. (2014). Global dissolution effects on planktonic foraminiferal Mg/Ca ratios controlled by the calcite-saturation state of bottom waters. *Paleoceanography*, pages 10.1002–2013PA002492.

Regenberg, M., Steph, S., Nürnberg, D., Tiedemann, R., and Garbe-Schönberg, D. (2009). Calibrating Mg/Ca ratios of multiple planktonic foraminiferal species with δ18O-calcification temperatures: Paleothermometry for the upper water column. *Earth and Planetary Science Letters*, 278(3-4):324–336.

Reichart, G.-J., Jorissen, F., Anschutz, P., and Mason, P. R. D. (2003). Single foraminiferal test chemistry records the marine environment. *Geology*, 31(4):355.

Reimer, P. (2013). IntCal13 and Marine13 Radiocarbon Age Calibration Curves 0–50,000 Years cal BP. *Radiocarbon*, 55(4):1869–1887.

Reimer, P. J., Baillie, M. G. L., Bard, E., Bayliss, A., Beck, J. W., Blackwell, P. G., Ramsey, C. B., Buck, C. E., Burr, G. S., Edwards, R. L., Friedrich, M., Grootes, P. M., Guilderson, T. P., Hajdas, I., Heaton, T. J., Hogg, A. G., Hughen, K. A., Kaiser, K. F., Kromer, B., McCormac, F. G., Manning, S. W., Reimer, R. W., Richards, D. A., Southon, J. R., Talamo, S., Turney, C. S. M., van der Plicht, J., and Weyhenmeyer, C. E. (2009). IntCal09 and Marine09 radiocarbon age calibration curves, 0-50,000 yeard cal BP. *Radiocarbon*, (51):1111–1150.

Reiss, Z. (1957). The Bilamellidea, nov. superfam., and remarks on Cretaceous globoraliids. *Contrib Cushman Found Foraminiferal Res*, VIII:127–145.

Ren, H., Sigman, D. M., Chen, M.-T., and Kao, S.-J. (2012). Elevated foraminifera-bound nitrogen isotopic composition during the last ice age in the South China Sea and its global and regional implications. *Global Biogeochemical Cycles*, 26(1):10.1029–2010GB004020.

Ridgwell, A., Hargreaves, J. C., Edwards, N. R., Annan, J. D., Lenton, T. M., Marsh, R., Yool, A., and Watson, A. (2007). Marine geochemical data assimilation in an efficient Earth System Model of global biogeochemical cycling. *Biogeosciences*, 4(1):87–104.

Ridgwell, A. J., Kennedy, M. J., and Caldeira, K. (2003). Carbonate deposition, climate stability, and Neoproterozoic ice ages. *Science*, 302(5646):859–862.

Riethdorf, J.-R., Max, L., Nürnberg, D., Lembke-Jene, L., and Tiedemann, R. (2013). Deglacial development of (sub) sea surface temperature and salinity in the subarctic northwest Pacific: Implications for upper-ocean stratification. *Paleoceanography*, pages 10.1002–palo.20014.

Riley, J. P. and Chester, R. (1971). *Introduction to marine chemistry*. Academic Pr, San Diego.

Rosenfeld, A. (1979). Structure and secretion of the carapace in some living ostracodes. *Lethaia*, 12(4):353–360.

Rosenthal, Y. (2004). Interlaboratory comparison study of Mg/Ca and Sr/Ca measurements in planktonic foraminifera for paleoceanographic research. *Geochem. Geophys. Geosyst*, 5(4):10.1029–2003GC000650.

Rosenthal, Y., Boyle, E., and Slowey, N. (1997). Temperature control on the incorporation of Mg, Sr, F and Cd into benthic foraminiferal shells from Little Bahama Bank: prospects for thermocline paleoceanography. *Geochimica et Cosmochimica Acta*, 61(17):3633–3643.

Rosenthal, Y., Field, M. P., and Sherrell, R. M. (1999). Precise determination of element/calcium ratios in calcareous samples using sector field inductively coupled plasma mass spectrometry. *Analytical Chemistry*, 71:3248–3253.

Russell, A. D., Hönisch, B., Spero, H. J., and Lea, D. W. (2004). Effects of seawater carbonate ion concentration and temperature on shell U, Mg, and Sr in cultured planktonic foraminifera. *Geochimica et Cosmochimica Acta*, 68(21):4347–4361.

Ruth, U., Bigler, M., and Röthlisberger, R. (2007). Ice core evidence for a very tight link between North Atlantic and east Asian glacial climate. *Geophysical Research Letters*, 34:10.1029–2006GL027876.

Ruttenberg, K. C. (1993). Reassessment of the oceanic residence time of phosphorus. *Chemical Geology*, 107(3-4):405–409.

Sabbatini, A., Bassinot, F., and Boussetta, S. (2011). Further constraints on the diagenetic influences and salinity effect on Globigerinoides ruber (white) Mg/Ca

thermometry: Implications in the Mediterranean Sea. *Geochemistry, Geophysics, Geosystems*, (12):doi:10.1029–2011GC003675.

Sagawa, T. and Ikehara, K. (2008). Intermediate water ventilation change in the subarctic northwest Pacific during the last deglaciation. *Geophys. Res. Lett*, 35(24):10.1029–2008GL035133.

Sagawa, T., Toyoda, K., and Oba, T. (2005). Sea surface temperature record off central Japan since the Last Glacial Maximum using planktonicforaminiferal Mg/Ca thermometry. *Journal of Quaternary Science*, 21:63–73.

Sarmiento, J. L., Gruber, N., Brzezinski, M. A., and Dunne, J. P. (2004). High-latitude controls of thermocline nutrients and low latitude biological productivity. *Nature*, 427(6969):56–60.

Sarmiento, J. L. and Toggweiler, J. R. (1984). A new model for the role of the oceans in determining atmospheric pCO 2. *Nature*, 308(5960):621–624.

Sarnthein, M., Gebhardt, H., Kiefer, T., Kucera, M., Cook, M., and Erlenkeuser, H. (2004). Mid Holocene origin of the sea-surface salinity low in the subarctic North Pacific. *Quaternary Science Reviews*, 23(20-22):2089–2099.

Sarnthein, M., Schneider, B., and Grootes, P. M. (2013). Peak glacial ^{14}C ventilation ages suggest major draw-down of carbon into the abyssal ocean. *Climate of the Past Discussions*, 9(1):925–965.

Sautter, L. R. and Thunell, R. (1989). Seasonal succession of planktonic foraminifera; results from a four-year time-series sediment trap experiment in the Northeast Pacific. *The Journal of Foraminiferal Research*, 19(4):253–267.

Schmitt, J., Schneider, R., Elsig, J., Leuenberger, D., Lourantou, A., Chappellaz, J., Kohler, P., Joos, F., Stocker, T., and Leuenberger, M. (2012a). Carbon isotope constraints on the deglacial CO2 rise from ice cores. *Science*, 336(6082):711–714.

Schmitt, J., Schneider, R., Elsig, J., Leuenberger, D., Lourantou, A., Chappellaz, J., Kohler, P., Joos, F., Stocker, T., Leuenberger, M., and Fischer, H. (2012b). Carbon Isotope Constraints on the Deglacial CO2 Rise from Ice Cores. *Science*, 336(6082):711–714.

Schneider von Deimling, T., Held, H., Ganopolski, A., and Rahmstorf, S. (2006). Climate sensitivity estimated from ensemble simulations of glacial climate. *Climate Dynamics*, 27:149–163.

Schrag, D. P., Hampt, G., and Murray, D. (1996). Pore fluid constraints on the temperature and oxygen isotopic composition of the glacial ocean. *Science*, 272(5270):1930.

Schwarcz, H. P., Agyei, E. K., and McMullen, C. C. (1969). Boron isotopic fractionation during clay adsorption from seawater. *Earth and Planetary Science Letters*, 6:1–5.

Serno, S., Winckler, G., Anderson, R. F., Hayes, C. T., Ren, H., Gersonde, R., and Haug, G. H. (2014). Using the natural spatial pattern of marine productivity in the Subarctic North Pacific to evaluate paleoproductivity proxies. *Paleoceanography*.

Seyfried, Jr, W. E., Janecky, D. R., and Mottl, M. (1984). Alteration of the oceanic crust: implications for geochemical cycles of lithium and boron. *Geochimica et Cosmochimica Acta*, 48:557–569.

Shackleton, N. (1967). Oxygen Isotope Analyses and Pleistocene Temperatures Re-assessed. *Nature*, 215(5096):15–17.

Shevenell, A. E., Kennett, J., and Lea, D. (2004). Middle Miocene Southern Ocean Cooling and Antarctic Cryosphere Expansion. *Science*, 305(5691):1766–1770.

Siegenthaler, U. and Wenk, T. (1984). Rapid atmospheric CO2 variations and ocean circulation. *Nature*, 308(5960):624–626.

Sigman, D. and Boyle, E. (2000). Glacial/interglacial variations in atmospheric carbon dioxide. *Nature*, 407(6806):859–869.

Sigman, D., Jaccard, S., and Haug, G. (2004). Polar ocean stratification in a cold climate. *Nature*, 428(6978):59–63.

Sigman, D. M., Hain, M. P., and Haug, G. H. (2010). The polar ocean and glacial cycles in atmospheric CO2 concentration. *Nature*, 466(7302):47–55.

Slowey, N. C. and Curry, W. B. (1995). Glacial-interglacial differences in circulation and carbon cycling within the upper western North Atlantic. *Paleoceanography*, 10:715–732.

Southon, J., Noronha, A. L., Cheng, H., Edwards, R. L., and Wang, Y. (2012). Quaternary Science Reviews. *Quaternary Science Reviews*, 33(C):32–41.

Spero, H., Bijma, J., Lea, D., and Bemis, B. (1997). Effect of seawater carbonate concentration on foraminiferal carbon and oxygen isotopes. *Nature*, 390:497–499.

Spero, H. and Lea, D. (1996). Experimental determination of stable isotope variability in Globigerina bulloides: implications for paleoceanographic reconstructions. *Marine Micropaleontology*, 28(3-4):231–246.

Spero, H. J., Mielke, K. M., von Langen, P. J., and Lea, D. (2000). Calibrating the oxygen isotope paleothermometer: do species-specific offsets work in application mode? . *Eos Transactions AGU*.

Spivack, A. J. and Edmond, J. M. (1987). Boron Isotope Exchange Between Seawater and the Oceanic-Crust. *Geochimica et Cosmochimica Acta*, 51(5):1033–1043.

Spivack, A. J., Palmer, M. R., and Edmond, J. M. (1987). The Sedimentary Cycle of the Boron Isotopes. *Geochimica et Cosmochimica Acta*, 51(7):1939–1949.

Stoffyn-Egli, P. and Mackenzie, F. T. (1984). Mass balance of dissolved lithium in the oceans. *Geochimica et Cosmochimica Acta*, 48:859–872.

Swanson, K. M. and Van der Lingen, G. J. (1994). Podocopid ostracod dissolution description of a new paleoenvironmental tool, with examples from the eastern Tasman Sea. In van der Kingen, G. J., Swanson, K. M., and Muir, R. J., editors, *Evolution of the Tasman Sea Basin*, pages 245–260. Balkema, Rotterdam.

Swart, P. K. and Hubbard, J. (1982). Uranium in scleractinian coral skeletons. *Coral Reefs*, 1:13–19.

Tagliabue, A., Sallée, J.-B., Bowie, A. R., Lévy, M., Swart, S., and Boyd, P. W. (2014). Surface-water iron supplies in the Southern Ocean sustained by deep winter mixing. *Nature Geoscience*, 7(4):314–320.

Takahashi, T., Olafsson, J., Goddard, J. G., Chipman, D. W., and Sutherland, S. (1993). seasonal-variation of co_2 and nutrients in the high-latitude surface oceans - a comparative study. *Global Biogeochemical Cycles*, 7(4):843–878.

Takahashi, T., Sutherland, S., Sweeney, C., Poisson, A., Metzl, N., Tilbrook, B., Bates, N., Wanninkhof, R., Feely, R., and Sabine, C. (2002). Global sea-air CO2 flux based on climatological surface ocean pCO2, and seasonal biological and temperature effects. *Deep Sea Research Part II: Topical Studies in Oceanography*, 49(9-10):1601–1622.

Talley, L. (1993). Distribution and formation of North Pacific intermediate water. *Journal of Physical Oceanography*, 23:517–517.

Talley, L. (2002). Ocean Circulation. In MacCracken, M. C. and Perry, J. S., editors, *Encyclopedia of Global Environmental Change*, pages 557–579.

Talley, L. D. (2013). Closure of the global overturning circulation through the Indian, Pacific, and Southern Oceans: Schematics and transports. *OCEANOGRAPHY*, 26(1):80–97.

Tang, J., Köhler, S. J., and Dietzel, M. (2008). Sr2+/Ca2+ and 44Ca/40Ca fractionation during inorganic calcite formation: I. Sr incorporation. *Geochimica et Cosmochimica Acta*, 72(15):3718–3732.

Tang, J., Niedermayr, A., Köhler, S. J., Böhm, F., Ksakürek, B., Eisenhauer, A., and Dietzel, M. (2012). Ca fractionation during inorganic calcite formation: III. Impact of salinity/ionic strength. *Geochimica et Cosmochimica Acta*, 77(C):432–443.

Tans, P. P., Fung, I. Y., and Takahashi, T. (1990). Observational constraints on the global atmospheric C02 budget. *Science*, 247:1431–1438.

Thornalley, D. J. R., Elderfield, H., and McCave, I. N. (2011). Global and Planetary Change. *Global and Planetary Change*, 79(3-4):163–175.

Tsuda, A. (2003). A Mesoscale Iron Enrichment in the Western Subarctic Pacific Induces a Large Centric Diatom Bloom. *Science*, 300(5621):958–961.

Turekian, K. K. (1969). The oceans, streams, and atmosphere. In Wedepohl, K. H., editor, *Handbook of geochemistry VI*, pages 297–323. Springer-Verlag, Heidelberg.

Turpen, J. and Angell, R. (1971). Aspects of molting and calcification in the ostracod Heterocypris. *Biological bulletin*, 140(2):331–338.

Uppström, L. R. (1974). The boron/chloninity ratio of deep-sea water from the Pacific Ocean. *Deep Sea Research and Oceanographic Abstracts*, 21:161–162.

Vetter, L., Spero, H. J., Russell, A. D., and Fehrenbacher, J. S. (2013). LA-ICP-MS depth profiling perspective on cleaning protocols for elemental analyses in planktic foraminifers. *Geochemistry, Geophysics, Geosystems*, 14(8):2916–2913.

Von Damm, K. L., Edmond, J. M., and Grant, B. (1985). Chemistry of submarine hydrothermal solutions at 21 N, East Pacific Rise. *Geochimica et Cosmochimica Acta*, 49:2197–2220.

von Langen, P. J., Lea, D., and Spero, H. J. (2000). Effects of temperature on oxygen isotope and Mg/Ca values in *Neogloboquadrina pachyderma* shells determined by live culturing . *Eos Transactions AGU*.

Wang, Y., Cheng, H., Edwards, R. L., An, Z., Wu, J., Shen, C., and Dorale, J. (2001a). A high-resolution absolute-dated late Pleistocene monsoon record from Hulu Cave, China. *Science*, 294(5550):2345.

Wang, Y., Cheng, H., Edwards, R. L., An, Z. S., Wu, J. Y., Shen, C., and Dorale, J. (2001b). A high-resolution absolute-dated late Pleistocene monsoon record from Hulu Cave, China. *Science*, 294(5550):2345–2348.

Warren, B. (1983). Why is no deep water formed in the North Pacific? *Journal of Marine Research*, 41(2):327–347.

Warren, B. A. (1973). Transpacific hydrographic sections at lats. 43 °S and 28 °S: the SCORPIO expedition—II. deep water. *Deep Sea Research and Oceanographic Abstracts*, 20(1):9–38.

Weaver, A. J., Saenko, O. A., Clark, P. D., and Mitrovicia, J. X. (2003). Meltwater Pulse 1A from Antarctica as a Trigger of the Bolling-Allerod Warm Interval. *Science*, 299(5613):1709–1713.

Wilkinson, B. H. and Algeo, T. J. (1989). Sedimentary carbonate record of calcium-magnesium cycling. *American Journal of Science*, 289:1158–1194.

Williams, R. J. P. (2008). Some fundamental features of biomineralization. *Geological Society, London, Special Publications*, 303(1):33–44.

Wu, J., Wang, Y., Cheng, H., and Edwards, L. R. (2009). An exceptionally strengthened East Asian summer monsoon event between 19.9 and 17.1 ka BP recorded in a Hulu stalagmite. *Science in China Series D: Earth Sciences*, 52(3):360–368.

Yasuda, I. (1997). The origin of the North Pacific Intermediate Water. *Journal of Geophysical Research-Oceans*, 102:893–909.

Yu, J. (2005). Determination of multiple element/calcium ratios in foraminiferal calcite by quadrupole ICP-MS. *Geochem. Geophys. Geosyst*, 6(8):Q08P01.

Yu, J., Anderson, R. F., Jin, Z., Rae, J. W. B., Opdyke, B. N., and Eggins, S. M. (2013a). Quaternary Science Reviews. *Quaternary Science Reviews*, 76(C):39–52.

Yu, J., Broecker, W. S., Elderfield, H., Jin, Z., McManus, J., and Zhang, F. (2010). Loss of Carbon from the Deep Sea Since the Last Glacial Maximum. *Science*, 330(6007):1084–1087.

Yu, J. and Elderfield, H. (2007). Benthic foraminiferal B/Ca ratios reflect deep water carbonate saturation state. *Earth and Planetary Science Letters*, 258(1-2):73–86.

Yu, J., Elderfield, H., Greaves, M., and Day, J. (2007a). Preferential dissolution of benthic foraminiferal calcite during laboratory reductive cleaning. *Geochemistry, Geophysics, Geosystems*, 8(6):10.1029–2006GC001571.

Yu, J., Elderfield, H., and Hönisch, B. (2007b). B/Ca in planktonic foraminifera as a proxy for surface seawater pH. *Paleoceanography*, 22(2):PA2202.

Yu, J., Elderfield, H., Jin, Z., Tomascak, P., and Rohling, E. J. (2014). Quaternary Science Reviews. *Quaternary Science Reviews*, 98(C):1–6.

Yu, J., Thornalley, D. J. R., Rae, J. W. B., and McCave, N. I. (2013b). Calibration and application of B/Ca, Cd/Ca, and δ 11B in Neogloboquadrina pachyderma(sinistral) to constrain CO 2uptake in the subpolar North Atlantic during the last deglaciation. *Paleoceanography*, pages 10.1002–palo.20024.

Zeebe, R. E. (2007). Modeling CO2 chemistry, δ13C, and oxidation of organic carbon and methane in sediment porewater: Implications for paleo-proxies in benthic foraminifera. *Geochimica et Cosmochimica Acta*, 71(13):3238–3256.

Zeebe, R. E. and Sanyal, A. (2002). Comparison of two potential strategies of planktonic foraminifera for house building: Mg2+ or H+ removal? *Geochimica et Cosmochimica Acta*, 66(7):1159–1169.

Zeebe, R. E. and Wolf-Gladrow, D. (2001). *CO2 in Seawater: Equilibrium, Kinetics, Isotopes: Equilibrium, Kinetics, Isotopes*. Elsevier Oceanography Series. Elsevier.

Zeebe, R. E., Wolf-Gladrow, D. A., Bijma, J., and Honisch, B. (2003). Vital effects in foraminifera do not compromise the use of δ 11B as a paleo-pH indicator: Evidence from modeling. *Paleoceanography*, 18(2):10.1029–2003PA000881.